



HAL
open science

Matière Organisée Hybride Organique-Inorganique

Rénal Backov

► **To cite this version:**

Rénal Backov. Matière Organisée Hybride Organique-Inorganique. Matériaux. Université Sciences et Technologies - Bordeaux I, 2003. tel-00593471

HAL Id: tel-00593471

<https://theses.hal.science/tel-00593471>

Submitted on 16 May 2011

HAL is a multi-disciplinary open access archive for the deposit and dissemination of scientific research documents, whether they are published or not. The documents may come from teaching and research institutions in France or abroad, or from public or private research centers.

L'archive ouverte pluridisciplinaire **HAL**, est destinée au dépôt et à la diffusion de documents scientifiques de niveau recherche, publiés ou non, émanant des établissements d'enseignement et de recherche français ou étrangers, des laboratoires publics ou privés.

N° d'ordre : 250

Habilitation à Diriger les Recherches

Présentée à

L'UNIVERSITE BORDEAUX I

Par **Rénal BACKOV**

Matière Organisée Hybride Organique-Inorganique

soutenue le 20 novembre 2003

Devant le Jury composé de :

Président : **Philippe Barois** (*Directeur de recherches, CRPP UPR-CNRS 8641*)

Rapporteur : **Jacques Livage** (*Professeur, Collège de France, LCMC UMR-7574*)

Rapporteur : **Mir Wais Hosseini** (*Professeur, Université Louis Pasteur, LCCO UMR 7513*)

Rapporteur : **Hervé Arribart** (*Directeur des recherches, Compagnie de Saint-Gobain*)

Examineur : **Didier Roux** (*Directeur de recherches, CRPP UPR-CNRS 8641*)

Examineur : **Clément Sanchez** (*Directeur de recherches, LCMC UMR-CNRS-7574*)

-2003-

CURRICULUM VITAE

BACKOV Rénal

Né le 20/05/68

Marié.

e-mail : backov@crpp.u-bordeaux.fr

Parcours professionnel, études de 3^{ème} cycle :

- **06/09/01** Maître de Conférences, 31^{ème} Section, Université Bordeaux-1,

Centre de Recherches Paul Pascal (C.R.P.P.)

C.N.R.S. U.P.R. 8641

Avenue Albert Schweitzer, Pessac, 33600 FRANCE.

-**1998/01** Chercheur Associé: University of Florida, Gainesville, FL, Etats-Unis

(Equipe de M. le Professeur Daniel R. Talham)

- Cristallisation d'oxalate de calcium et photoréduction de Pt^{II} à l'interface de monocouches de Langmuir et films de Langmuir-Blodgett.

- Magnétisme associé aux solides et solides mous.

- Mésophases lyotropes organiques-inorganiques.

- Systèmes organométalliques (matériaux 1D, 2D, 3D et en échelles).

-**1997/98** A.T.E.R.: USTL Montpellier II, 32^{ème} section, chimie minérale.

(L. A. M. M. I. U.M.R. 5072 U. S. T. L. Montpellier II)

-**1994/97** Doctorat : Synthèse et caractérisation d'hybrides organiques-inorganiques obtenus par intercalation de molécules électroactives dans le phosphate de zirconium.

Soutenu le 17 Décembre 1997, **mention très honorable.**

allocataire M.E.S.R. / MONITEUR (32^{ème} Section)

(L. A. M. M. I. U.M.R. 5072 U. S. T. L. Montpellier II)

Jury : M le Professeur J. V. Zanchetta	Président (Montpellier)
M le Professeur J. Rozière	Directeur de thèse (Montpellier)
M ^{elle} D. J. Jones (D. R.)	Co-directeur de thèse (Montpellier)
M le Professeur R. Clément	Rapporteur (Orsay)
M le Professeur F. Béguin	Rapporteur (Orléans)
M P. Batail (D. R.)	Examineur (Nantes)
M le Professeur J. M. Fabre	Examineur (Montpellier)

-**1993/94** D.E.A.: Matériaux de l'électronique et de l'ionique du solide (bourse rectorale)

mention T. Bien, major de promotion.

Stage de D.E.A.: Etude des propriétés de conduction dans le système

V₂O_{5(x)}B₂O_{3(1-x)}. Evaluation de la symétrie locale de l'ion V⁴⁺ par Résonance Paramagnétique Electronique.

(L.P.C.M.C. U.M.R. 5617 U.S.T.L. Montpellier II)

COMPETENCES DEVELOPPEES EN RECHERCHE

THEMATIQUES ABORDEES

- 1- Solides hybrides organiques-inorganiques de basse dimensionnalité.
- 2- Mésophases lyotropes hybrides organiques-inorganiques.
- 3- Technique de Langmuir-blodgett et croissance anisotrope de particules métalliques.
- 4- Monocouches de Langmuir et phénomènes de biominéralisation à l'interface air-liquide.
- 5- Conductivité de polarisation et systèmes vitreux.
- 6- Magnétisme associé aux hybrides organiques-inorganiques, systèmes organométalliques et films LB
- 7- Solides hybrides organiques-inorganiques à structures hiérarchisées : chimie des formes

CHIMIE DE LA MATIERE ORGANISEE

*** Etat solide:** Synthèses de matériaux hybrides de basses dimensionnalités.

- synthèses hydrothermales
- synthèses par chimie douce
- phosphates de métaux tétravalents
- phosphonates de Cuivre, Vanadyl
- hydroxyacétate et hydroxyphosphonate de cuivre, hydroxycarboxylates de cuivre, de nickel et de Cobalt
- hydroxydes doubles lamellaires
- dimères organométalliques, matériaux 1D, matériaux en échelle, matériaux à structures ouvertes
- perovskites à base de Cuivre, Cadmium

*** Solide mou :** Films de Langmuir-Blodgett, monocouches de Langmuir, mésophases lyotropes.

- formation de nanoparticules, macroparticules métalliques
- étude des interactions à l'interface entre une monocouche de Langmuir et espèces en croissance
- élaboration de films de Langmuir-Blodgett à propriétés magnétiques
- chimie sol-gel, films auto-supportés, phases lyotropes, matériaux hiérarchisés.

TECHNIQUES DE CARACTERISATION EMPLOYEES

- diffraction de RX sur poudre
- diffraction de RX aux petits angles
- XPS
- spectrophotométrie de flamme
- spectroscopie de vibration (IR, Raman, diffusion inélastique incohérente de neutrons)
- EXAFS/XANES
- spectroscopie électronique
- spectroscopie Mössbauer (^{119}Sn)
- RMN ^{13}C , ^{31}P , ^1H
- RPE
- SQUID (susceptibilité magnétique continue et alternative)
- technique de Van der Paw (conductivité en courant continu)
- conductivité de polarisation
- mesure du coefficient de Seebeck (pouvoir thermoélectrique)
- SEM, TEM-TED
- microscope à angle de Brewster (BAM)
- ATG-ATD
- microscopie en polarisation croisée (cristaux liquides)

ENCADREMENTS- RESPONSABILITES COLLECTIVES

Responsabilités :

01/présent

Recherches :

-Prise en charge de l'équipe du Professeur D.R. Talham pendant son séjour sabbatique en France (un an 1998/1999).

Durant la première année de mon stage post-doctorale Daniel Talham, invité en séjour sabbatique en France (5 mois au CRPP-Bordeaux et 7 mois IMN-Nantes), m'a demandé de le substituer à Gainesville en veillant sur son équipe américaine, ce, sur un plan exclusivement scientifique. Les responsabilités administratives et financières étant gérées entre ce dernier et son administration par courrier électronique.

A l'époque, cette équipe était constituée de deux stagiaires post-doctoraux, de cinq étudiants de thèse et d'autres stagiaires de niveau "bachelor degree" équivalent au diplôme de Maîtrise. En plus de mes travaux de recherches (biominéralisation, synthèse de nanoparticules et microparticules en milieu confiné, mésophases lyotropes), j'étais spécialement en charge de Jonathan Woodward (thèse sur la réalisation de polymères de coordination à propriétés magnétiques de spin) tout en devant suivre les travaux de Jeff Culp (autre étudiant de thèse) qui s'intéressait alors aux matériaux lamellaires mixtes cobalt-cuivre à bases de phényle phosphonates. En fin de première année de stage post-doctorale mais également sur toute la période suivante j'étais en charge d'Eduardo Perez-Cordero, étudiant de thèse, dont la thèse était centrée sur la réalisation de mésophases lyotropes organiques-inorganiques à bases de Pérovskites lamellaires et autres hydroxydes doubles lamellaires.

Cette période très enrichissante mais également assez éprouvante m'a permis d'appréhender *in situ* les réalités de la gestion d'une équipe de recherche où les paramètres de compétences scientifiques mais également de relations humaines sont mises à rudes épreuves, et ceci, surtout dans un pays comme les Etats-Unis où les notions de compétitivité et de production scientifique, poussées à l'extrême, amènent bien souvent des situations assez tendues entre jeunes étudiants ou étudiantes de thèse !

- Responsable de l'activité CRPP : biomimétisme, biotectonique et biominéralisation

- * Morphogénèses minérales et fluides complexes
- * Morphogénèses minérales sous cisaillement
- * Minéralisation et mousses
- * Minéralisation et phases lamellaires
- * Minéralisation et instabilités hydrodynamiques
- * Systèmes poreux et réactivité

- Participation à une proposition de thématique dans le cadre du réseau d'excellence Européen (PCRDT-6) : matériaux hybrides organiques-inorganiques et magnétisme. Direction nationale : Marc Drillon (*Coordinateur CRPP : R. Clérac*).

- Participation à une proposition de thématique dans le cadre du réseau d'excellence Européen (PCRDT-6) : matériaux hybrides organiques-inorganiques et biomatériaux. Direction nationale : Clément Sanchez (*Coordinateur CRPP : R. Backov*)

- Participation ACI "Jeunes Chercheurs 2002": Couplage entre la structure d'un fluide complexe et une instabilité hydrodynamique : du problème académique aux applications. N° d'ident: 2046 (*Chef de projet: Sébastien Manneville*)

- Co-organisateur de l'école Galerne 2003 "matériaux hybrides organiques-inorganiques" Bordeaux, septembre 2003. Co-organisateurs : Mondain-Monval Olivier (CRPP), Zakri Cécile (CRPP), Duguet Etienne (ICMCB), Marie-Hélène Delville (ICMCB), Monat Treguet (ICMCB).

- Prise en charge de l'équipe du Professeur D.R. Talham pendant son séjour sabbatique en France 1998-1999

Enseignements :

- Responsable du module 6 : "Formulation de matériaux à base de milieux dispersés." Option 3^{ème} année Ingénieur, ENSCPB.

Encadrements au C.R.P.P. depuis Septembre 2001:

- **Stagiaire Post-doctoral** : Formation de coques de silice mésostructurées obtenues par chimie sol-gel et procédé d'émulsion, procédés d'encapsulation. Mirérialisation aux interfaces SAM. (1 an 2002/03- **Giulia Fornasieri**) co-encadrement (à 50% avec Philippe Poulin)

- **Thèse** "chimie douce et matière molle : mousses inorganiques". (Thèse débutée le 1^{er} Octobre 2003 – **Florent Carn**)

- **Thèse** "Matériaux hybrides organiques-inorganiques à propriétés magnétiques".
Co-encadrée à 50% avec Rodolphe Clérac. (*HDR détenue par Philippe Barois, responsable administratif*)
(Thèse débutée le 1^{er} Octobre 2002 –**Lolita Lecren**)

- **Thèse** "Matériaux structurés hybrides organiques-inorganiques". Co-encadrée à 50% avec Olivier Mondain-Monval. (Thèse débutée le 1^{er} Septembre 2001–**Alexandre Desforges**)

- **DEA** –Polymères : chimie sol-gel et mousses
Co-encadrée à 50% avec Annie Colin.
(6 mois d'encadrement 2003 –**Florent Carn**)

- **DEA** –Polymères : Matériaux hybrides organiques-inorganiques et nanostructuration.
Co-encadrée à 25% avec Serge Ravaine, Eric Cloutet et Henry Cramail. (6 mois d'encadrement 2003–**Anne de Cuendias**)

- **DEA** -ENSCP: Conceptualisation de matériaux hybrides organiques-inorganiques par procédé d'émulsification. Co-encadrée à 50% avec Philippe Poulin. (6 mois d'encadrement 2002- **Doreau Nicolas**)

- **DEA** –PCMC : Matériaux hiérarchisés hybrides organiques-inorganiques et propriétés magnétiques. Co-encadrée à 50% avec Rodolphe Clérac.
(6 mois d'encadrement 2002 -**Lolita Lecren**)

- **DESS granulats et colloïdes**: Nanoparticules d'or encapsulées dans une structure sphérulite, générées par photoréduction du complexe $[\text{AuCl}_4]$. Co-encadrée à 50% avec Chrystel Faure
(7 semaines d'encadrement 2002- **Delage Céline**)

- **DESS granulats et colloïdes**: Nanoparticules d'or encapsulées dans une structure sphérulite, générées par photoréduction du complexe $[\text{AuCl}_4]^{2-}$. Co-encadrée à 50% avec Chrystel Faure
(7 semaines d'encadrement 2002- **Tawl Karine**)

- **Maîtrise Chimie -Physiques**: Des mousses solides ! Vers une synthèse de renfort pour pneumatiques. Co-encadrée à 50% avec Annie Colin.
(4 mois d'encadrement 2002- **Saadi Zoubida**)

- **Maîtrise Chimie -Physiques**: Nanoparticules d'or encapsulées dans une structure sphérulite, générées par photoréduction du complexe $[AuCl_4]$. Co-encadrée à 50% avec Chrystel Faure
(4 mois d'encadrement 2003- **Meyre Marie-Edith**)

- **Licence Professionnelle de Chimie Industrielle** : Mise en forme de silices mésostructurées sous flux laminaire. (4 semaines d'encadrement 2003- **Gaëlle Petit**)

- **Licence Professionnelle de chimie Industrielle** : Mise en forme de silices mésostructurées sous flux laminaire.(4 semaines d'encadrement 2003- **Julien Laguéri**)

- **Licence Professionnelle de Chimie Industrielle** : Formation de coques de silice mesostructurées obtenues par chimie sol-gel et procédé d'émulsion.
(4 semaines d'encadrement 2002- **Stéphane Jautard**)

- **Licence Professionnelle de chimie Industrielle** : Formation de coques de silice mesostructurées obtenues par chimie sol-gel et procédé d'émulsion.
(4 semaines d'encadrement 2002- **Julie Sarsiat**)

Encadrements à l'Université de Floride : 1998/2001

- "**Ph.D student**" (University of Florida): synthesis and characterization of new mineral liquid crystals based on perovskite structures (*deux ans d'encadrement*-**Eduardo E. Perez-Cordero**)

- "**Ph.D student**" (University of Florida) synthesis and characterization of new ladder materials based on $M_xCl_y(CH_3CN)_z$ / M= Ni, Co, Mn, Fe. (*trois mois d'encadrement*- **Chen Liu**)

- "**Ph.D student**" (University of Florida) :chemical and physical characterization of hybrid organic -inorganic low-dimensional coordination polymers. (*trois ans et six mois d'encadrement*- **Jonathan Woodward**)

- "**Bachelor degree student**" (University of Florida): synthesis and characterization of new mineral liquid crystals based on layered double hydroxides structures. (*un an d'encadrement*- **Sarah Lane**)

- "**Undergraduated student**" (University of Florida): synthesis and characterization of polyaromatic electroactive molecules.(*un an d'encadrement*-**David Zipp**)

Encadrements à l'Université Montpellier II : 1995/1997

- **Maîtrise**: simulation de courbes de conductivité obtenues pour des matériaux lamellaires hybrides organiques-inorganiques.
(2 mois d'encadrement- **Lionel Nicole**)

- **D.E.A**: intercalation de composés aminés dans des hexacyanoferrates de Cuivre et de Potassium.
(6 mois d'encadrement- **Gaëlle Derien**)

- **D.E.A**: intercalation de pérylène dans les phosphates de Zirconium α -ZrP et δ -ZrP.
(6 mois d'encadrement- **Thibaud Mourgues**)

- **Maîtrise** : synthèse d'hexacyanoferrate de Cuivre et de Potassium.
(2 mois d'encadrement- **Lydie Tchikaya**)

- **IUT** (mesures physiques): réalisation d'une cellule de conductivité de Van der Pauw (méthodes des quatre points), applications à quelques matériaux hybrides organiques-inorganiques conducteurs électroniques.
(6 mois d'encadrement-**Thibaud Gaultier**)
- **Licence de chimie** : intercalation de dipropargylamine dans le phosphate de Titane γ -TiP. (2 mois d'encadrement)

MCF (Université Bordeaux -I)

Cours : Licence professionnelle (13 H ETD): «Les colloïdes durs »

Chapitre 1 : des colloïdes durs au procédé sol-gel

- I-1 Introduction et quelques définitions
- I-2 Polymérisation-structuration
- I-3 Les grandeurs fractales
- I-4 Du monomère au gel

Chapitre II : colloïdes et sols de particules " les non-silicates"

- II-1 Chimie des précurseurs inorganiques : les métaux de transition
 - II-1-1 L'hydrolyse
 - II-1-2 Condensation
 - a) olation
 - b) oxolation
 - II-1-3 Espèces polymères et gélotion
 - II-1-4 Un exemple d'étude structurale : V_2O_5
- II-2 Chimie des précurseurs inorganiques : les alkoxydes de métaux de transition
 - II-2-1 Mécanismes d'hydrolyse et condensation
 - II-2-2 Rôle du catalyseur
 - II-2-3 Structures des produits de condensation

Chapitre III : colloïdes et sols de particules " les silicates"

- III-1 Introduction
- III-2 Les silices en solutions aqueuses
- III-3 Mécanismes d'hydrolyse et condensation
 - III-3-1 Comportement global
 - III-3-2 Les précurseurs moléculaires

Chapitre IV : évolution structurale d'un gel pendant le processus de solidification. Formation de films par procédés de "dip-coating" et "spin-coating"

- IV-1 Introduction
- IV-2 Structures de gels poreux : Xérogels et Aérogels
- IV-3 Formation de films par "dip-coating"
- IV-4 Formation de films par "spin-coating"

Chapitre V : colloïdes durs, chimie sol-gel et applications

- V-1 Films et revêtements de surface
 - V-1-1 Revêtements de surface
 - V-1-2 Films pour l'électronique
 - V-1-3 Films protecteurs
 - V-1-4 Films poreux
- V-2 Les monolithes
- V-3 Poudres, grains et sphères
- V-4 Les composites
- V-5 Les membranes et gels poreux

Cours : DESS - granulats et colloïdes (7 H ETD): «chimie sol-gel»

Cours : ENSCPB- 3^{ème} année (7 H ETD):

«matériaux obtenus par procédés sol-gel et matière molle : chimie des formes»

«Biomatériaux»

Chapitre I : Introduction aux biomatériaux

Chapitre II : Matériaux cholestériques à base de chitine et collagène

Chapitre III : Phosphate de calcium et calcification biologique

Chapitre IV : Bio-silification

«Matériaux poreux et mise en forme »

Chapitre I : Introduction aux matériaux bio-inspirés

Chapitre II : Les stratégies de synthèse

Chapitre III : Les principales empreintes organiques

Chapitre IV : Structures à bases de silice

Chapitre V : Exemples de micro-moulages et auto-assemblages

Travaux dirigés : chimie générale (DEUG TC1A)

Travaux dirigés : thermodynamique, approche microscopique (DEUG TC3A)

Travaux dirigés : mécanique quantique et spectroscopie (DEUG TC3A)

Travaux pratiques : chimie-physique, mécanique quantique et spectroscopie (DEUG TC3A)

Travaux pratiques : thermodynamique, Licence chimie-physiques.

Travaux pratiques : rhéologie, granulométrie, comportements de polymères en solutions, Licence professionnelle.

A.T.E.R. (USTL Montpellier II) 1997/1998

Cours, TP et TD réalisés au cours du monitorat.

TP de Licence "Chimie Fondamentale" : synthèses et caractérisations de quelques complexes de Werner (Cobalt et Chrome), étude de ces composés par spectroscopie électronique et infrarouge.

TD de DEUG 2^{ème} Période BPC2 : nomenclature, formalisme de LEWIS, VSEPR, réactions acido-basiques.

MONITORAT (USTL Montpellier II) 1994/1997

Cours : D.E.U.G. 4^{ème} période

Introduction à la théorie des groupes:

- notion de symétrie
- éléments et opérations de symétrie
- les groupes ponctuels
- les représentations non dégénérées
- rappel sur les matrices
- les représentations dégénérées
- les modes normaux de vibration (activité IR, Raman)
- spectrométrie, transformée de Fourier, interféromètre de Michelson

Travaux dirigés : D.E.U.G. 2^{ème} période

Oxydoréduction:

- nombres d'oxydation
- potentiels d'électrodes
- équation de NENRST

Chimie descriptive:

- formalisme de LEWIS.
- géométrie moléculaire par la théorie V.S.E.P.R.

Travaux pratiques: D.E.U.G. 2^{ème} période

- Semi-micro analyse qualitative.
- Aluns de chrome et de potassium.
- Les complexes.
- Dosage colorimétrique du cuivre II.
- Préparation d'un sel double et d'un sel complexe.
- Les halogènes.
- Préparation et dosage d'une Schoenite

PUBLICATIONS, BREVETS, PROCEEDINGS (38)

Publications (22) :

- ** Palladium nanoparticles generation within microcellular polymeric foam (polyHIPES)
A. Desforges, H. Deleuze, **R. Backov** , O. Mondain-Monval.
J. Chem. Soc; chem. Comm. (soumis)
- ** Inorganic monoliths hierarchically textured via concentrated direct emulsion and micellar templates.
A. Colin, M.-F. Achard, F. Carn, H. Deleuze, **R. Backov**.
J. Chem. Soc; chem. Comm. (soumis)
- ** Mesoporous mineral capsules generation from reverse emulsion and sol-gel processes.
G. Fornasieri, S. Badaire, **R. Backov**, O. Mondain-Monval, C. Zakri, P. Poulin
Nature Mat., **2004** (soumis).
- ** Spontaneous generation of gold nanoparticles within onion mesophases.
C. Faure, O. Regev, D. Roux, **R. Backov**
Adv. Mat. (soumis)
- ** Structural, thermal and magnetic properties investigation of three transition metal-4,4'-bipyridine coordination polymers : [Ni(4,4'-bipy)₃(H₂O)₂](ClO₄)₂·1.4(4,4'bipy)·3H₂O, [Co(4,4'-bipy)₃(H₂O)₂](ClO₄)₂·1.4(4,4'bipy)·3H₂O and [Cu(4,4'-bipy)₃(DMSO)₂](ClO₄)₂·2(4,4'bipy)·W Woodward, **R. Backov**, H. Honuki, M.W. Meisel, D.R. Talham
olyhedron, **2003**, 22, 2821.
- ** Presence of lipids in urine, crystals and stones: Implication for the formation of kidney stones.
S. R. Khan, P. A. Glenton, **R. Backov** and D. R. Talham.
Kidney International **2002**, 62, 2062.
- ** Lyotropic phase from hybrid organic-inorganic layered copper hydroxides.
R. Backov, A. N. Morgan, S. Lane, E.E. Perez-Cordero, K. Williams, M.W. Meisel, C. Sanchez, D. R. Thalam.
Mol. Cryst. Liq. Cryst. **2002**, 376, 127.
- ** [Ni(terpy)(H₂O)]-*trans*-[Ni-μ-(CN)₂(CN)₂]_n, a one-dimensional linear tetracyanonicolate chain.
J. D. Woodward, **R. Backov**, K. A. Abboud, D. R. Talham.
Acta. Cryst. C. **2001**, C57, 1027.
- ** Layered mixed-metal phenylphosphonates, Co_xMn_{1-x}(O₃PC₆H₅).H₂O: Structure and magnetic properties.
J. T. Culp, G. E. Fanucci, B. C. Watson, **R. Backov**, H. Ohnuki, M. W. Meisel, D. R. Talham
J. Solid State Mat. **2001**, 159, 362.
- ** The magnetic spin ladder (C₅H₁₂N₂)₂CuBr₄: high field magnetization and scaling near quantum criticality.
B. C. Watson, V. N. Koto, M. W. Meisel, D. W. Hall, G. E. Granroth, W. T. Montfrooij, S. E. Nagler, D. A. Jensen, **R. Backov**, M. A. Petruska, G. E. Fanucci, D. R. Talham.
Phys. Rev. Letter **2001**, 86, 5168.

- ** Multiple bilayer dipalmitoylphosphatidylserine (DPPS) LB films stabilized with transition metals ions.
G. E. Fanucci, **R. Backov**, R. Fu, D. R. Talham.
Langmuir **2001**, *17*, 1660.
- ** Calcium oxalate monohydrate precipitation at phosphatidylglycerol Langmuir monolayers.
R. Backov, C. M. Lee, S. R. Khan, C. Mingotaud, G. E. Fanucci, D. R. Talham.
Langmuir **2000**, *16*, 6013.
- ** Magnetic phase diagram of the quasi-2D mixed metal phenylphosphonates.
G. E. Fanucci, J.T. Culp, B. C. Watson, **R. Backov**, H. Ohnuki, D. R. Talham, M. W. Meisel.
Physica B **2000**, *284-8*, 1499.
- ** DC and AC conductivities of $V_2O_5(x)B_2O_3(1-x)$ oxide glasses.
H. el Mkami, B. Deroide, **R. Backov**, J. V. Zanchetta.
J. Phys. Chem. Solids **2000**, *61*, 819.
- ** Precipitation of calcium oxalate monohydrate at phospholipid monolayers.
R. Backov, S. R. Khan, K. Byer, C. Mingotaud, C. Nixon, D. R. Talham.
J. Am. Soc. Nephrology **1999**, *10*, S359.
- ** Photoluminescence properties of fullerene C_{60} in microporous VPI5-Zeolite.
A. Lamrate, J. M. Jannot, L. C. de Ménorval, **R. Backov**, J. Rozière, J. L. Sauvajol, J. Allègre,
B.P. Séta.
Synth. Metals **1999**, *103*, 2426.
- ** Non linear optics in zirconium phosphate layered phases.
Th. Coradin, **R. Backov**, D. J. Jones, J. Rozière, R. Clément.
Mol. Cryst. Liq. Cryst. **1998**, *311*, 275.
- ** Growth of calcium oxalate monohydrate at phospholipid Langmuir monolayers.
S. Whipps, S. R. Khan, F. J. O'palko, **R. Backov**, D. R. Talham.
J. Cryst. Growth **1998**, *192*, 243.
- ** Intercalation and post-synthesis oxidation of basic electroactive TTF-type molecules in zirconium phosphate.
R. Backov, L. Binet, J. M. Fabre, D. J. Jones, J. Rozière.
Mol. Cryst. Liq. Cryst. **1998**, *311*, 239.
- ** Evidence of confinement of fullerene C_{60} in microporous zeolite.
A. Lamrate, J. M. Jannot, A. Elmidaoui, **R. Backov**, J. Rozière, L. C. de Ménorval, J. L. Sauvajol,
J. Allègre, P. Séta.
Chem. Phys. Lett. **1998**, *295*, 257.
- ** Two-dimensional organic-inorganic intercalation hybrids of tetrathiafulvalene in zirconium phosphate.
R. Backov, B. Bonnet, D. J. Jones, B. Mula, J. Rozière.
Mol. Cryst. Liq. Cryst. **1998**, *311*, 233.
- ** Assembly of partially oxidized tetrathiafulvalene in layered phosphates. Formation of highly conducting organic-inorganic hybrid by intercalation.
R. Backov, B. Bonnet, D. J. Jones, J. Rozière.
Chem. Mater. **1997**, *9*, 1812.

** Assembly of TTF in modified layered zirconium phosphates under controlled oxidation conditions
R. Backov, D. J. Jones, J. Rozière.
J. Chem. Soc., Chem. Comm. **1996**, 599.

Brevets (5) :

** Monolithes inorganiques obtenus par chimie sol-gel en milieu confiné mousses et « macro-empreintes ».
A. Colin, F. Carn, **R. Backov**.
Brevet français, **2003**, n° de dépôt FR03-09085.

** Monolithes inorganiques à structures hiérarchisées obtenus par chimie sol-gel en émulsion directe concentrée.
A. Colin, **R. Backov**.
Brevet français, **2003**, n° de dépôt FR03-03774.

** Matériaux hybrides associant une matrice organique poreuse de types poly(hipe) à des nanoparticules métalliques générées *in situ*. Propriétés en catalyse supportée "hydrogénation".
A. Desforges, **R. Backov**, H. Deleuze, O. Mondain-Monval.
Brevet français, **2003**, n° de dépôt FR03-05427.

** Nanoparticules d'or générées dans des structures multilamellaires de type "oignons"
C. Faure, **R. Backov**.
Brevet français, **2002**, n° de dépôt FR02-15153.
Extension Internationale, **2003** : PCT/FR03/03464.

** Capsules minérales mésoporeuses obtenues par un procédé de chimie sol-gel en émulsion inverse (eau dans huile).
S. Badaire, **R. Backov**, O. Mondain-Monval, C. Zakri, P. Poulin
Brevet français, **2002**, n° de dépôt FR02-07505.

Proceedings (10)

10- Involvement of cellular membranes and their lipids in nucleation of stone forming crystals.
S. R. Khan, J. M. Fasano, **R. Backov**, D. R. Talham.
Mat. Res. Soc. Symp. Proc. **2000**, 599, 269.

09- The features of self-assembling organic bilayers important to the formation of anisotropic inorganic materials in microgravity conditions.
D. R. Talham, **R. Backov** and J. H. Adair.
NASA Microgravity Materials Science Conference Proceedings, **2002**, 120.

08- Magnetic phase diagram of a quasi-2D mixed metal phenylphosphonates.
J. Culp, G. E. Fanucci, H. Ohnuki, **R. Backov**, M. Orendac, A. Ferher, B. C. Watson,
J. R. Maloney, D. R. Talham and M. W. Meisel.
Bull. Am. Phys. Soc. **2000**, 45, 1033.

07- The magnetic spin ladder $(C_5H_{12}N_2)_2CuBr_4$: high field magnetization and scaling near quantum criticality.
B.C. Watson, V. N. Koto, M. W. Meisel, D. W. Hall, G. E. Granroth, W. T. Montfrooij,
S. E. Nagler, D. A. Jensen, **R. Backov**, M. A. Petruska, G. E. Fanucci, D. R. Talham.
NHMFL 2000 Annual Review, Cond-Mat, **2000**, 2, 214.

- 06-** Characterization of the novel low dimensional system $(\text{CH}_3)_2\text{NH}_2\text{CuCl}_3$.
B. C. Watson, J. R. Maloney, J. M. Sock, M.W. Meisel, D. W Hall , G. E. Granroth,
S. E. Nagler , D. A. Jensen, **R. Backov**, M. A. Petruska, D. R. Talham.
NHMFL 2000 Annual Review, Cond-Mat, **2000**, 2, 213.
- 05-** Magnetic studies of two $S=1/2$ ladder-like compounds, BPCP and MCCL.
B. C. Watson, A. N. Morgan, M.W. Meisel, D. A. Jensen, **R. Backov**, M. A. Petruska,
D. R. Talham, D. W Hall, G. E. Granroth, S. E. Nagler.
Bull. Am. Phys. Soc. **2000**, 45, 586.
- 04-..** Lipids in urine, crystals and stones: do they have a role in the formation of kidney stones?
Khan S.R., Glenton P.A., **Backov R.**, Talham D.R.
B.J.U. International 90, **2002**, (Supplément 2), 257.
- 03-** Following the polymerization and graphitization of acetylenic guest molecules using INS.
.Aptel, **R. Backov**, D. J. Jones and J. Rozière.
ISIS experimental report, Rutherford Appleton Laboratory, RB 6425, **1996**.
- 02-** Controlled oxidation and assembly of TTF in modified layered zirconium phosphate. INS of new electronic conductors.
R. Backov, P. Aitchison, B. Ammundsen, D. J. Jones and J. Rozière.
ISIS experimental report, Rutherford Appleton Laboratory, RB 7939, **1997**.
- 01-** Assembly of TTF in layered zirconium phosphate. INS of new organic electronic conductors.
R. Backov, B. Ammundsen, J. Rozière and D. J. Jones.
ISIS experimental report, Rutherford Appleton Laboratory, RB 8762, **1998**.
- 11-** Direct observation of calcium oxalate monohydrate precipitation at phospholipid monolayers with Brewster angle microscopy.
I. O. Benitez, **R. Backov**, S.R. Khan, D.R. Talham.
Mat. Res. Soc. Symp. Proc. **2003**, 774, O.59.

COMMUNICATIONS (59)

Communications orales invitées (8)

Congrés internationaux(2)

- 02-** Soft matter and “chimie douce”: hierarchically organized materials
G. fornasieri, S. Badaire, A. Desforges, A. Colin, C. Faure, P. Poulin,
O. Mondain-Monval, **R. Backov**.
Euromat 2003, Lausanne, Suisse, Septembre 2003.
- 01-** Nucleation of calcium oxalate monohydrate at phospholipid monolayers.
R. Backov, S. R. Khan, K. Byer, C. Mingotaud, C. Nixon and D. R. Talham.
International Finlayson Congres on Urology, Gainesville, U.S.A., Janvier 1999.

Séminaires (6)

- 06-** Soft matter and “chimie douce”: hierarchically organized materials
G. Fornasieri, S. Badaire, A. Desforges, A. Colin, C. Faure, P. Poulin,
O. Mondain-Monval, **R. Backov**
2003 Hokkaido University-Bordeaux University Bilateral Joint Symposium
Supramolecular assemblies, biological molecules and materials, Mars, 2003.
- 05-** Chimie douce et matière molle : approche biomimétique pour de nouveaux matériaux
R. Backov
Séminaire, Saint-Gobain Recherches, Aubervilliers, France, Juin 2003.
- 04-** Matériaux hybrides organiques-inorganiques obtenus par chimie douce.
R. Backov
Séminaire, Saint-Gobain Recherches, Aubervilliers, France, Mai 2001.
- 03-** Tunable properties of hybrid organic -inorganic solid state materials obtained by “chimie douce”.
R. Backov
Inorganic Division Seminar, University of Florida, Gainesville, USA Novembre 2000.
- 02-** Matériaux hybrides organiques-inorganiques à propriétés contrôlées obtenus par chimie douce.
R. Backov
Séminaire, Centre de Recherches Paul Pascal, Pessac, France, Mai 2001.
- 01-** Matériaux hybrides organiques-inorganiques à propriétés contrôlées.
R. Backov
Séminaire, LAMMI, Université des Sciences et Techniques du Languedoc, Montpellier, France,
Mai, 2002.

Congrès Internationaux (28)

Communications orales (14)

- 17-** Microcellular polymeric materials from concentrated emulsions: Synthesis and application properties.
H. Deleuze, A. Desforges, **R. Backov**, O. Mondain-Monval.
International Symposium on Polymers in Dispersed Media. Colloids from preparation to applications.
ENS-Lyon, Gerland, France, Avril 2004.
- 16-** Growth of calcium oxalate monohydrate at phospholipid monolayers.
D.R. Talham, I.O. Benitez, **R. Backov**, S.R. Khan.
A.C.S. national meeting, Nouvelle orléans, Mars 2003.
- 15-** Direct observation of calcium oxalate monohydrate precipitation at phospholipid monolayers with Brewster angle microscopy.
I. O. Benitez, **R. Backov**, S.R. Khan, D.R. Talham.
Mat. Res. Soc. Symposium, San Francisco, U.S.A., Avril 2003.
- 14-** Assembly of electroactive organic species in layered phosphates.
R. Backov, R. Fourcade, D.J. Jones, B. Mula, J. M. Fabre and J. Rozière.
MRS Spring Meeting-Symposium V, Interfacial Effects and Organization of Inorganic -Organic Composite Solids, San Francisco, U. S. A., Mars 1997.

- 13- Highly conducting two-dimensional organic-inorganic intercalation hybrids of tetrathiafulvalene in zirconium phosphate.
R. Backov, B. Bonnet, D. J. Jones, B. Mula and J. Rozière.
International Symposium on Intercalation Chemistry, Arcachon, Mai 1997.
- 12- Assembly of electroactive monomers and polymers in layered host substrats.
R. Backov, B. Bonnet, D.J. Jones and J. Rozière.
Material Chemistry 3, Royal Society of Chemistry, Exeter, U. K., Juillet 1997.
- 11- Assembly of electroactives molecules in inorganic ion exchangers.
R. Backov, D.J. Jones and J. Rozière.
International Congres Symposium ICSM'98, Montpellier, Juillet 1998.
- 10- Novel two-dimensional magnetic copper arrays assembled in Langmuir-Blodgett films.
G.E. Fanucci, M. Petruska, **R. Backov**, D. R. Talham, B. C. Watson and M. W. Meisel.
American Physical Society Meeting, Atlanta, U.S.A., Mars 1999.
- 09- Magnetic phase diagram of the quasi-2D mixed metal phenylphosphonates.
G. E. Fanucci, J. T. Culp, B. C. Watson, **R. Backov**, D. R. Talham and M. W. Meisel.
22nd International Low Temperature Conference, Helsinky, Finlande, Août 1999.
- 08- Involvement of cellular membranes and their lipids in nucleation of stone forming crystals.
S. R. Khan, J. M. Fasano, **R. Backov**, D. R. Talham,
M.R.S Fall-Meeting, Boston, Symposium DD: Mineralization in Natural and Synthetic Biomaterials
U.S.A. , Novembre 1999.
- 07- Magnetic Studies of two S=1/2 ladder-like compounds, BPCP and MCCL.
B. C. Watson, A. N. Morgan, M. W. Meisel, D. A. Jensen, **R. Backov**,
M. A. Petruska and D. R. Talham
Am. Phys. Soc. meeting, Mineapolis, USA, Mars 2000.
- 06- Evidence of frustration induced precursor phase in a quasi-2D mixed metal phenylphosphonate.
J. T. Culp, G. E. Fanucci, **R. Backov**, B. C. Watson, H. Ohnuki, M. W. Meisel and D. R. Talham
Am. Phys. Soc. meeting, Mineapolis, USA, Mars 2000.
- 05- A new class of mineral liquid crystals.
R. Backov, J. T. Culp and D. R. Talham.
7th International Conference on Molecular based Magnets, San Antonio, Texas USA,
Septembre 2000.
- 04- A new class of mineral liquid crystals.
D. R. Talham, **R. Backov**, J. T. Culp
2000 International Chemical Congres of pacific basin Societies, Honolulu, HI, USA
Décembre 2000.
- 03- A new class of mineral liquid crystals.
D.R. Talham, **R. Backov**, J. T. Culp
2nd International Conference on Inorganic Materials, Santa Barbara, USA, Septembre 2000.

02- A new class of mineral liquid crystals: nematic phases based on nanoparticles of organic-inorganic layered solids.

R. Backov, E.E. Perez-Cordero and D. R. Talham.

Particules 2001, Orlando, Février 2001, U. S. A,

01- Nucleation of Calcium oxalate at Langmuir monolayers.

S.R. Khan SR, **R. Backov**, D.R. Talham, 1st International and 11th National Chemistry Conference, April 10-14, 2001, Peshawar University, Peshawar, Pakistan.

Communications Locales (4)

Communications orales (1)

01-. Chimie douce et matière molle : organisations aux grandes échelles.

R. Backov, G. Fornasieri, S. Badaire, A. Desforges, A. Colin, C. Faure, P. Poulin, O. Mondain-Monval, S. Manneville, Z. Saadi, K. Tawl, N. Doreau, C. Delage.

Journées CRPP-Curie, Pessac, Octobre 2002.

Communications par affiches (3)

03-. Intercalation et polymerisation in situ de propargylamine et aminoacétonitrile dans le phosphate lamellaire de titane.

G. Aptel, R. Backov, D.J. Jones et J. Rozière.

02-. Intercalation de TTF dans des phosphates lamellaires de métaux IV par échange cationique ou oxydation contrôlée..

R. Backov, D.J. Jones et J. Rozière.

Journée de l'école doctorale « matière condensée », Montpellier, Juin 1996.

01-. Intercalation de TTF fonctionnalisés dans des phosphates de zirconium lamellaires.

R. Backov, D.J. Jones, J. Rozière, L. Binet et J.M. Fabre

Journée de l'école doctorale « matière condensée », Montpellier, Juin 1997

SYNTHESE D'ACTIVITE

BACKOV Rénal

"Matière organisée hybride organique-inorganique"

-SOMMAIRE-

I- <u>PREAMBULE</u>	21
II- <u>INTRODUCTION</u>	22
III- <u>TRAVAUX POST-DOCTORAUX</u>	24
III-1 SYSTEMES BIDIMENSIONNELS ET PROPRIETES MAGNETIQUES DE SPIN .24	
III-1-a Phénylphosphonates 2D de métaux transitionnels: Systèmes polycristallins.....	24
III-1-b Phosphonates 2D de métaux transitionnels: Films de Langmuir-Blodgett.....	25
III-2 CRISTAUX, INGENIERIE SUPRAMOLECULAIRE ET PROPRIETES MAGNETIQUES DE SPIN	28
III-2-a Matériaux 3D à structures ouvertes.....	29
III-2-b Matériaux en échelles.....	31
III-3 MONOCOUCHEs DE LANGMUIR ET FILMS de LANGMUIR-BLODGETT: DEUX SYSTEMES STRUCTURANTS	35
III-3-a Films de Langmuir-Blodgett Phospholipidiques: RMN ³¹ P.....	36
III-3-b Monocouches de Langmuir et procédé de biominéralisation	39
III-3-c Films de Langmuir-Blodgett: nano- et microparticules métalliques	42
III-4 SYSTEMES BIDIMENSIONNELS, MESOPHASES LYOTROPES ET MISE EN FORME AUX GRANDES ECHELLES	43
IV- <u>RECHERCHES ACTUELLES</u>	48
IV-1 BIOMIMETISME, BIOTECTONIQUE et BIOMINERALISATION	48
IV-1-a Morphogénèses minérales et fluides complexes	49
IV-1-b Morphogénèses minérales sous cisaillement.....	51
IV-1-c Minéralisation et mousses.....	52
IV-1-d Minéralisation et phases lamellaires.....	54
IV-1-e Systèmes poreux et réactivité.....	57
V- <u>PERSPECTIVES GLOBALES</u>	61
VI- <u>REMERCIEMENTS ET CONCLUSION</u>	65
VII- <u>LISTE DE PUBLICATIONS CHOISIES</u>	65
VIII- <u>REFERENCES</u>	66

I- PREAMBULE

Les travaux de recherches décrits dans ce document s'articulent autour du domaine des matériaux hybrides organiques-inorganiques et sont en partie illustrés avec la figure 1. Dans ce cadre, ont été abordés des thèmes traitant de la chimie du solide mais également de la matière molle, ces deux approches s'entrecroisant ou bien même se complétant en fonction de la spécificité de la recherche abordée. Cette utilisation de deux domaines de compétence explique le choix du titre de ce rapport d'activité, "Matière organisée hybride organique-inorganique" qui a été préféré à celui de "Matériaux hybrides organiques-inorganiques" trop exclusif de la chimie du solide.

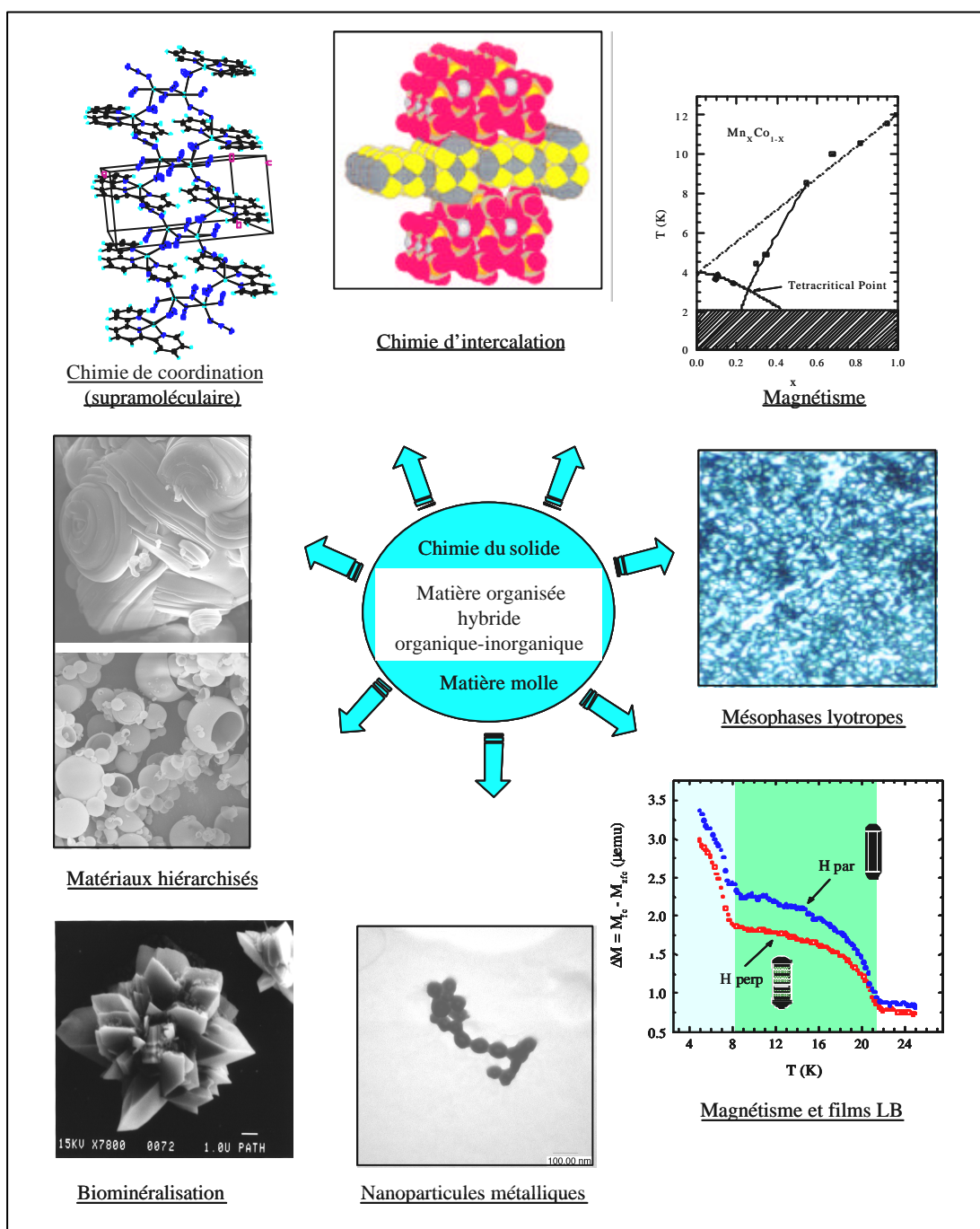


Figure 1. Illustrations des thèmes abordés, articulés autour de la matière organisée hybride organique-inorganique.

II- INTRODUCTION

Un matériau hybride organique-inorganique est obtenu, comme son nom l'indique, par l'association de deux entités de nature différente, organique et inorganique. Le chimiste pourra obtenir un matériau spécifique où une synergie existe entre les propriétés de ces deux systèmes de base. De cette synergie pourra naître des propriétés exaltées, inhibées voire combinées dans le cas d'une polyfonctionnalité.^[1] La réalisation de tels matériaux a été facilitée, avec une amélioration du contrôle des processus réactionnels, par un concept de "chimie douce"^[1-3] où les synthèses sont réalisées, la plupart du temps, dans des conditions proches de la température ambiante et de la pression atmosphérique. Cette notion assez récente de chimie douce est applicable à la fois aux systèmes de basses dimensionnalités (chimie d'intercalation par exemple)^[2] mais également aux systèmes plus ou moins désorganisés (chimie sol-gel par exemple).^[3] La structuration d'un matériau hybride organique-inorganique doit être basée sur l'interpénétration de deux réseaux étendus organiques et inorganiques, organisés ou non. Ceci est une distinction par rapport aux matériaux composites où l'interpénétration des réseaux de bases n'est plus une condition *sine qua non* mais où une simple juxtaposition ou association de composés devient une condition nécessaire et suffisante. Cependant, lorsque les entités de bases atteignent des dimensions nanométriques on parle alors de nanocomposites, qui, par effet de taille, sont classés dans la familles des hybrides organiques-inorganiques.

Récemment, un nouveau concept de "chimie supramoléculaire"^[4] ou de "chimie au-delà de la molécule", basé sur des processus de reconnaissances moléculaires associés à l'intervention de liaisons faibles, a permis une nouvelle avancée dans la structuration et polyfonctionnalité des matériaux synthétisés, qu'ils soient purement organiques ou hybrides organiques-inorganiques. Dans ce contexte, la structuration d'entités organiques et inorganiques s'opérant à l'échelle supramoléculaire nous pouvons, pour les échelles supramoléculaires les plus grandes, obtenir des réseaux étendus interpénétrés organiques-inorganiques. Dès lors, certains matériaux supramoléculaires peuvent être définis comme des matériaux hybrides organiques-inorganiques. Pour des structurations supramoléculaires aux échelles les plus faibles, "agrégats moléculaires", ces matériaux sont alors assez proches de ceux inhérents à la chimie de coordination.

Les notions décrites précédemment avec très certainement une trop grande simplicité laissent néanmoins entrevoir le formidable potentiel de créativité associé à la chimie et physico-chimie des matériaux hybrides organiques-inorganiques. L'état de l'art actuel, le volume conséquent de références bibliographiques et donc l'engouement des chercheurs, font de la science associée à cette classe de matériaux non pas seulement un axe de recherche particulier, mais au-delà, lui confèrent les caractéristiques d'une véritable discipline au même titre que, par exemple, la thermodynamique ou la mécanique quantique. Par ailleurs, la polyvalence des thèmes associés à cette discipline est un atout formidable pour compléter des thèmes de recherche "frontières" comme la biologie, la biochimie, etc. A titre d'exemple, une bonne compréhension des processus de chimie douce et de physico-chimie de la matière molle permet de réaliser des matériaux hybrides organiques-inorganiques spécifiques basés sur des méthodologies de biominéralisation, biotectonique et biomimétisme.^[5] Dans ce cadre une phase organique organisée sert d'entité structurante à un minéral en croissance. Des organisations à plusieurs échelles, en utilisant des systèmes thermodynamiques (émulsions, mésophases lyotropes, etc.), des stimuli mécaniques (cisaillement, transfert sur un substrat solide, etc.) ou combinaison des deux, permettent la réalisation de matériaux hiérarchiquement structurés.^[5,6] Ces classes de matériaux sont étudiées depuis un certain nombre d'années par les biologistes, leurs connaissances et avancées dans ce domaine, mais également leurs limites et leurs demandes pour une réalisation rationnelle de matériaux à architectures et texturations contrôlées, ont induit la rencontre de cette communauté avec celle grandissante de la matière organisée hybride organique-inorganique. La réalité de cette communion scientifique a permis de mettre en avant une

nouvelle approche dans la conceptualisation de matériaux nouveaux, celle de la "chimie des formes".^[7] Ces efforts communs, aux chimistes et physico-chimistes, dans le but d'obtenir un plus grand contrôle de l'organisation sur toute une gamme d'échelle, passent indubitablement par une étude minutieuse des spécificités de réactivités aux interfaces organo-minérales, qui devient de ce fait une problématique de taille où, comme nous le verrons ultérieurement, bon nombre de paramètres sont impliqués de manière partitive ou coopérative dans ces procédés de germination, nucléation et croissance minérales *via* un substrat organique.

C'est dans le contexte décrit ci-dessus que se sont développées et se développent actuellement mes recherches, dont un panel est proposé avec la figure 1.

Ce sont mes travaux de thèse, effectués au LAMMI-UMR CNRS 5072, sous la direction de Jacques Rozière professeur à l'Université Montpellier II, qui m'ont permis de découvrir la discipline des matériaux hybrides organiques-inorganiques. L'objectif de ce travail a été l'étude de l'intercalation de molécules électroactives de type tétrathiafulvalène dans l'espace interfoliaire de phosphates acides de métaux du groupe 4 et 14, avec comme perspectives l'assemblage et l'organisation de ces molécules pour former *in situ* des fils moléculaires conducteurs. Au-delà de la réalisation de matériaux hybrides organiques-inorganiques un intérêt particulier a été porté sur le contrôle des stœchiométries obtenues et donc sur les propriétés physico-chimiques qui en découlent, la conductivité électronique en l'occurrence.^[8-11] Pendant ces études j'ai pu collaborer avec mon collègue Thibaud Coradin actuellement chargé de recherches au LCMC-UMR CNRS 7574 qui à cette période réalisait sa thèse au LCI-UMR CNRS 420 sous la direction de René Clément professeur à l'Université de Paris XI. Ce travail nous a permis d'obtenir, par intercalation de molécules chromophores dans l'espace interlamellaire de phosphates de zirconium de formes α et γ , des matériaux hybrides organiques-inorganiques présentant des propriétés d'optique non linéaire (ONL) de second ordre.^[12] L'apparition de cette propriété d'ONL est générée par le caractère non-centrosymétrique associé à l'agencement des molécules invitées, cette configuration étant elle-même induite par l'effet de confinement offert par le système d'accueil. Pendant mes travaux de thèse j'ai également collaboré avec Patrick Séta directeur de recherches CNRS (LMPM-UMR CNRS 5635). Cette collaboration nous a permis de mettre en évidence l'effet de confinement de fullerènes C_{60} au sein de cavités zéolitiques d'une matrice à structure ouverte de type VPI-5.^[13] Lors de cette étude nous nous sommes intéressés aux propriétés photoluminescentes de ces matériaux d'insertion hybrides organiques-inorganiques, et avons pu spécifier le temps de vie associé à la fluorescence des molécules de C_{60} confinées.^[14]

L'ensemble des travaux brièvement énoncés précédemment ne sera pas traité dans ce document.

III- TRAVAUX POST-DOCTORAUX

III-1 SYSTEMES BIDIMENSIONNELS ET PROPRIETES MAGNETIQUES DE SPIN.

III-1-a Phénylphosphonates 2D de métaux transitionnels: Systèmes polycristallins.

Toutes les propriétés des systèmes étudiés pendant mes années de thèse découlent d'entités organiques insérées ou intercalées, la partie inorganique ne jouant qu'un simple rôle de réseau hôte structurant. En fait, s'il est possible de contrôler les propriétés d'un matériau hybride organique-inorganique en se focalisant essentiellement sur la partie organique, nous pouvons également obtenir des matériaux à propriétés contrôlées en ne jouant qu'avec la partie inorganique. Cette démarche est décrite dans les lignes suivantes avec une étude portant sur des matériaux lamellaires à base de phénylphosphonates mixtes de Cobalt et de Manganèse.

Ce travail a été réalisé en collaboration avec Jeffrey T. Culp et Gail E. Fanucci, à l'Université de Floride (Gainesville-USA) dans l'équipe du Professeur Daniel R. Talham avec qui j'ai effectué mon stage post-doctoral. Les mesures magnétiques ont été effectuées par l'équipe du Professeur Marck W. Meisel, ainsi que toutes les mesures de magnétisme associées aux films de Langmuir-Blodgett et matériaux magnétiques à structures ouvertes qui seront décrits ultérieurement. Ces travaux ont permis la réalisation de deux articles et de deux communications.

Les phénylphosphonates de métaux transitionnels sont des matériaux lamellaires dont la structure est bien référencée.^[15] Des groupements phényles pointent dans l'espace interfolaire, alors que les entités phosphonates assurent une connectivité intrafeuillet *via* la présence de métaux de transition. Ces métaux de transition, lorsqu'ils présentent des électrons de valence non appariés, vont induire des propriétés magnétiques où les interactions de spin sont modulées par des ponts "oxo" inhérents aux groupements phosphonates.^[15] L'idée de ce travail était d'associer Mn(II) et Co(II) dans la connectivité intrafeuillet, l'un et l'autre de ces éléments de transition correspondant respectivement à des modèles d'interaction de spin de types Heisenberg et Ising.^[16] La répartition statistique de ces éléments transitionnels au sein de la structure permet de considérer les feuillets comme de véritables solutions solides.^[17] Dans cette étude nous avons réalisé toute une série de composés répondant globalement à la stœchiométrie suivante : $Mn_xCo_{1-x}(O_3PC_6H_5).H_2O$. Pour x étant égale à zéro nous obtenons le phénylphosphonate de Manganèse associé à une température de Néel $T_N(11,7K)$ ^[18a] légèrement supérieure à T_N^* (11,5K), cette dernière température caractéristique variant avec la force du champ magnétique imposé. Ceci met en évidence un ordre faiblement ferromagnétique au-dessous de ces températures caractéristiques. Pour x étant égale à un, nous obtenons le phénylphosphonate de Cobalt caractérisé par un comportement antiferromagnétique associé à une température de Néel de 3,9K.^[18b] Pour les systèmes mixtes Mn/Co, un exemple des comportements magnétiques est proposé sur la figure 2-a. Ces mesures ont été effectuées pour tous les composés réalisés et un diagramme de phase a pu être élaboré, indiqué sur la figure 2-b.^[18] Ce diagramme met en évidence un écart à la théorie du champ moyen, avec un écart maximum pour la composition contenant 25% de Manganèse, ceci définissant un point "tétracritique"^[17,19] Cette stœchiométrie de 25% en Manganèse apparaît en fait comme un seuil de percolation où, pour un réseau plan cubique centré, le Cobalt possède au moins un Manganèse comme premier voisin, ce dernier dominant l'environnement magnétique local.^[18b]

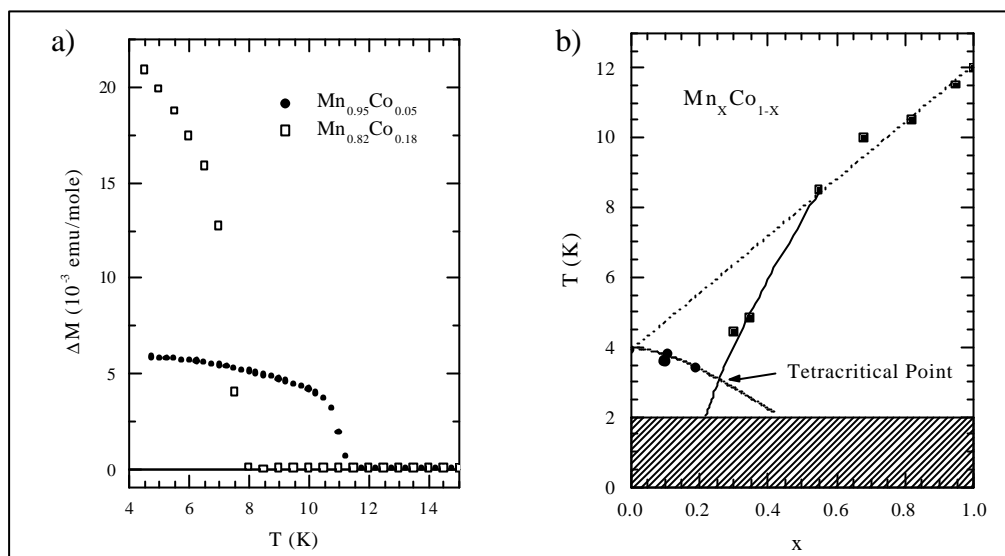


Figure 2. a) Comportements magnétiques de deux systèmes mixtes $\text{Mn}_x\text{Co}_{1-x}(\text{O}_3\text{PC}_6\text{H}_5)\cdot\text{H}_2\text{O}$, b) diagramme de phases associé au système $\text{Mn}_x\text{Co}_{1-x}(\text{O}_3\text{PC}_6\text{H}_5)\cdot\text{H}_2\text{O}$.

Dans le cadre de ce travail, nous avons également essayé, en vain, de mettre en évidence la présence d'un état vitreux de spin prédit par des études antérieures.^[20] En effet, pour des compositions proches et températures légèrement supérieures au point dit "tétracritique", et en se focalisant sur la partie réelle de la susceptibilité alternative associée aux matériaux étudiés, les températures de transition de spin ordre-désordre ne montrent aucune variation notable entre 17 Hz et 1,5 kHz.^[18b]

III-1-b Phosphonates 2D de métaux transitionnels: Films de Langmuir-Blodgett.

Tous les travaux décrits précédemment sont réalisés par le biais de l'obtention de matériaux polycristallins qui de ce fait n'offrent aucune anisotropie macroscopique, permettant de ségréguer les contributions axiales et transversales d'une propriété physico-chimique particulière (conduction, optique, magnétisme, etc.). Généralement cette anisotropie est obtenue en travaillant sur des monocristaux adéquats. La technique de Langmuir-Blodgett, permettant de mettre en forme des matériaux en tirant parti d'une interface plane liquide/air, apparaît comme une méthode élégante où cette anisotropie macroscopique peut être envisagée. Dans les lignes suivantes seront décrits succinctement la formation de films de Langmuir-Blodgett (films LB) à base de phosphonates de Cuivre ou de vanadyle ainsi que leur comportement magnétique.

Ce travail a été effectué dans l'équipe de Daniel R. Talham avec Gail E. Fanucci, actuellement chercheur post-doctoral à l'Université de Virginie (USA) dans l'équipe animée par David S. Cafiso. Ce travail a permis de réaliser pour le moment une communication.

La technique de Langmuir-Blodgett permet de mettre en forme des matériaux bidimensionnels. Elle consiste dans un premier temps à disperser un tensioactif à la surface d'un liquide remplissant une cuve dite de "Langmuir". Dans une seconde étape, il s'agit d'organiser la monocouche déposée en la compressant à l'aide d'une simple, voire d'une double barrière disposée à la surface de la cuve. Enfin, pour une tension superficielle désirée, il est possible de déposer de manière séquencée sur un substrat solide des films de Langmuir-Blodgett (LB). Le principe de cette technique est décrit sur la figure 3. Les travaux, concernant la réalisation de films LB purement organiques ou hybrides organiques-inorganiques sont considérables.^[20] Dans le cas de matériaux

hybrides, il a été possible de recréer à l'interface liquide/air des structures organiques-inorganiques, récurrentes de celles existant à l'état solide, présentant des propriétés magnétiques analogues avec l'avantage d'obtenir des films et non plus des matériaux polycristallins.^[21] C'est dans cette optique que s'inscrit ce travail, avec la réalisation de matériaux à base d'octadécylphosphonate de cuivre (Cu-ODPA) et de vanadyle (VO^{2+}) (VO-ODPA).

En chimie du solide, les phosphonates de cuivre correspondent à plusieurs phases cristallographiques. Ces différences de structures sont fortement corrélées à leur état d'hydratation. Le composé $\text{Cu}(\text{R-PO}_3)$ non hydraté possède un ordre magnétique de spin à basse température.^[22] Sur la figure 4-a, nous pouvons constater des interactions antiferromagnétiques de spin associées à une aimantation spontanée et positive vers 8K (figure 4-b).

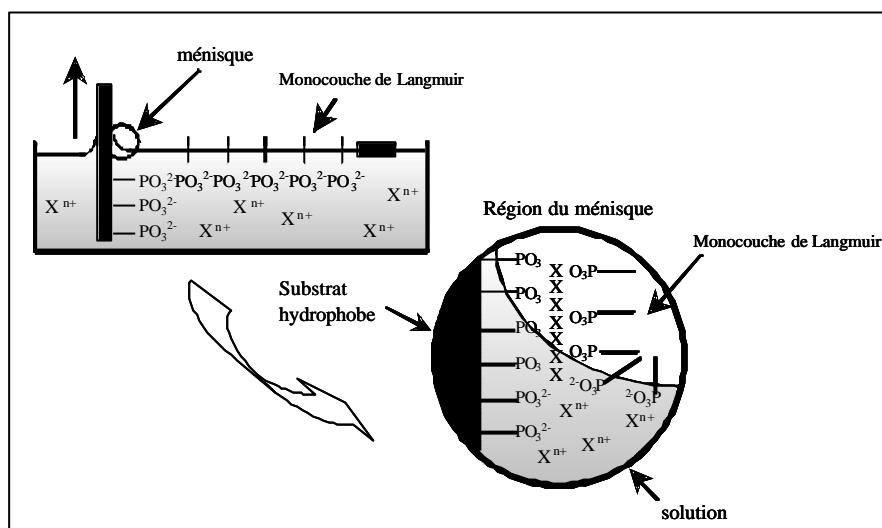


Figure 3. Schéma décrivant la technique de Langmuir-Blodgett.

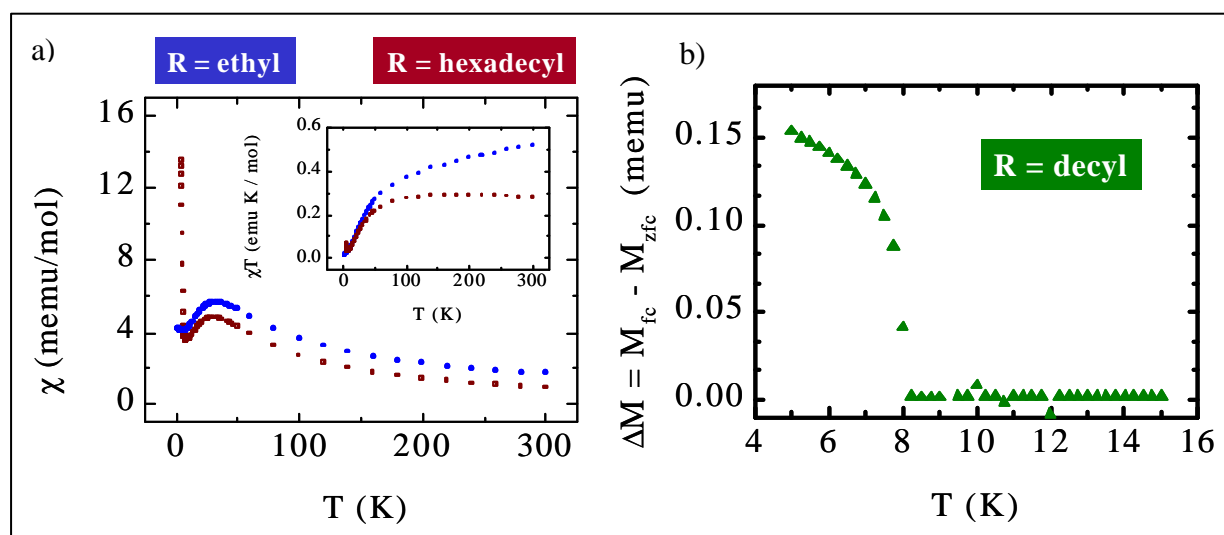


Figure 4. Comportements magnétiques de spin de certains phosphonates de cuivre polycristallins.

Cette aimantation spontanée est envisageable car les interactions de spin sont "antiferromagnétiques angulées" ou faiblement ferromagnétiques et induisent de ce fait un moment magnétique net positif.

Sur la figure 5-b, nous pouvons constater que le composé octadécylphosphonate de cuivre (Cu-ODPA) présente également cette transition de phase magnétique vers 8K. Cette transition à basse température est dédoublée par une seconde transition à une température de l'ordre de 16K. Ces

deux températures de transition de phases sont également présentes pour le film LB Cu-ODPA (figure 5-a).

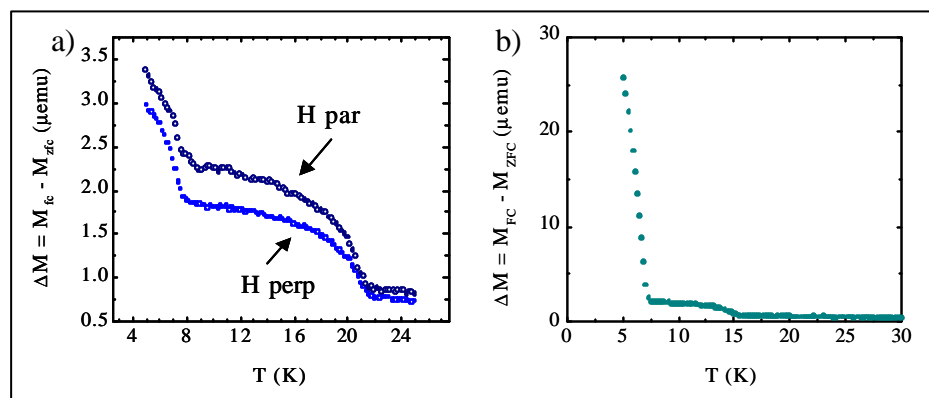


Figure 5. Comportements magnétiques de spin du composé à base d'octadécylphosphonate de cuivre, a) film LB, b) système polycristallin.

Comme l'indiquent les diffractogrammes de rayons X, le système polycristallin est biphasé (figure 6). Ceci pourrait expliquer le comportement magnétique de spin observé. En effet, il a été démontré, que pour certains hydroxycarboxylates de cuivre à longues chaînes alkyles, des interactions de spin interfeuillet pourraient exister, si la longueur de cohérence des domaines magnétiques intrafeuillet est assez grande pour induire des interactions de spin d'un feuillet à l'autre.^[22d] Dans ce contexte, la distance interfeuillet associée à l'agencement des chaînes alkyles devient un paramètre pouvant générer de nouveaux comportements magnétiques.

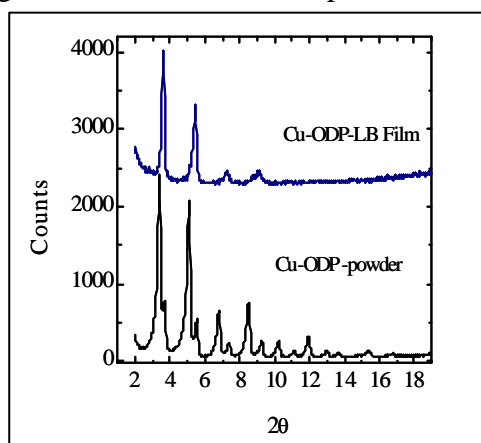


Figure 6. Diffractogrammes de rayons X des composés d'octadécylphosphonates de cuivre : film LB et composé polycristallin.

Nous pouvons constater que le film LB Cu-ODPA possède une seule distance interfeuillet tout en étant cependant caractérisé par deux transitions magnétiques de spin, une première à 8K et une seconde pour une température supérieure de 21K (figure 5-a). Dans le cas du film (LB), nous avons donc un matériau biphasé au niveau de la structure intrafeuillet et non plus au niveau des distances interfeuillet.

Dans une autre étude, nous avons également essayé de transposer les comportements magnétiques de systèmes polycristallins à base d'ions vanadyles (VO^{2+}) vers des films LB. Dans l'état solide deux matériaux présentent des interactions antiferromagnétiques. Dans le composé à base de phénylphosphonate de vanadyle les interactions de spin sont induites *via* les groupes phosphonates ($(\text{VO})\text{-O-P-O}(\text{VO})$),^[22a,b,c] alors que dans le cas du composé à base de méthylphosphonate de cuivre, les interactions d'échange sont obtenues *via* des ponts oxo inhérents aux groupes phosphonates $(\text{VO})\text{-O}(\text{VO})$.^[22a,b,c] Nous avons donc élaboré un nouveau film LB à base

d'octadécylphosphonate de cuivre, en espérant retranscrire ces comportements magnétiques. Le film LB (VO-ODPA) ne montre pas de comportement magnétique mettant en avant des interactions d'échange. En effet, l'évolution de sa susceptibilité magnétique en fonction de la température est reproduite par une loi de Curie (figure 7-a) et sa courbe d'aimantation en fonction d'une augmentation d'un champ magnétique imposé est caractéristique d'une fonction de Brillouin (figure 7-b). Ces deux comportements, mettent en évidence l'existence de spin 1/2 sans interaction. De plus, en jouant sur l'anisotropie macroscopique offerte par la nature des films LB, l'évolution de la largeur de raie à mis hauteur du signal RPE, caractéristique des ions V^{4+} (sonde paramagnétique locale) en fonction de l'orientation de l'échantillon, ne montre pas la signature caractéristique d'un échange de spin.

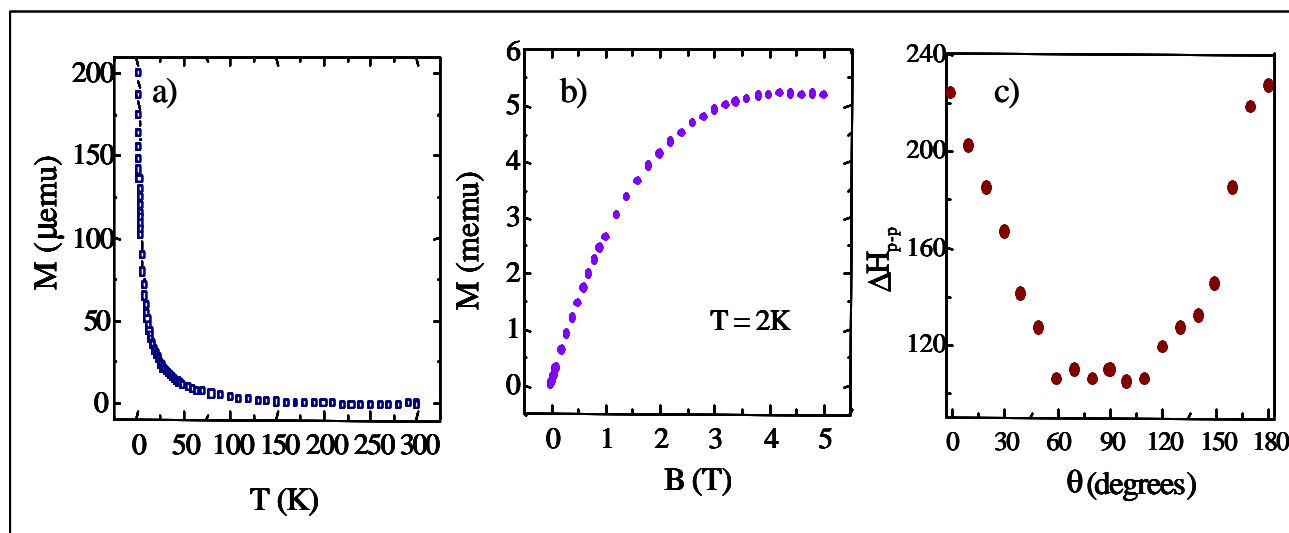


Figure 7. Comportement magnétique d'un film LB à base d'octadécylphosphonate de vanadyde.

III-2 CRISTAUX, INGENIERIE SUPRAMOLECULAIRE ET PROPRIETES MAGNETIQUES DE SPIN.

Dans les travaux décrits précédemment, les matériaux étudiés étaient soit polycristallins, soit mis en forme par le biais d'une interface air/liquide, ceci dans le cas particulier des films LB. Cette organisation contrôlée d'édifices à base moléculaire se retrouve également dans un thème récent à la frontière de la chimie de coordination. Cet axe de recherche repose sur une organisation prédéterminée, et de ce fait contrôlée, de l'agencement moléculaire au sein d'un motif unité caractéristique d'une maille cristallographique. S'agissant d'organisation contrôlée de briques molécules nous sommes bien en phase avec les concepts de chimie supramoléculaire, décrits en introduction. Cependant cette chimie, s'adressant dans ce cas à la réalisation de cristaux à structures prédéterminées, préfère parler de : "cristaux obtenus par ingénierie supramoléculaire".^[23] Ceci débouche sur une nouvelle philosophie d'appréhender la chimie de coordination. En effet, il ne s'agira plus de rechercher une dualité structure-propriété où la structure est une finalité en soit, mais bien d'envisager en priorité une spécificité des propriétés souhaitées dont devra découler dans une seconde étape, un agencement cristallographique à caractère supramoléculaire. C'est dans ce contexte que s'inscrivent les travaux décrits dans les deux paragraphes suivants.

Ces travaux ont été réalisés à l'Université de Floride, dans l'équipe de Daniel R. Talham, principalement dans le cadre de la thèse de Jonathan Woodward (soutenue le 10 Juillet 2002).^[24] Ces travaux ont, pour le moment, permis de réaliser deux articles et une communication.

L'acquisition des données cristallographiques a été réalisée avec l'aide précieuse de Khalil Abboud, Professeur à l'Université de Gainesville.

III-2-a Matériaux 3D à structures ouvertes.

Pour les raisons énoncées ci-dessus, la conception rationnelle de matériaux hybrides organiques-inorganiques à structures ouvertes connaît actuellement un essor considérable. Ceci étant induit par le formidable potentiel de propriétés contrôlées associées à cette catégorie de matériaux. Nous pouvons citer par exemples des propriétés d'échanges ioniques,^[25] propriétés d'insertions (réseaux hôtes-molécules invitées),^[26] propriétés de catalyse,^[27] propriétés d'optique non-linéaire^[28] ou bien encore de magnétisme^[29] ou de conductivité électronique.^[30]

Dans ce cadre nous avons réalisé trois nouveaux matériaux à structure ouverte correspondants aux stoechiométries suivantes: $[\text{Ni}(4,4'\text{-bipy})_3(\text{H}_2\text{O})_2](\text{ClO}_4)_2 \cdot 1.4(4,4'\text{-bipy}) \cdot 3(\text{H}_2\text{O})$ [**1**], $[\text{Co}(4,4'\text{-bipy})_3(\text{H}_2\text{O})_2](\text{ClO}_4)_2 \cdot 1.4(4,4'\text{-bipy}) \cdot 3(\text{H}_2\text{O})$ [**2**], et $[\text{Cu}(4,4'\text{-bipy})_3(\text{DMSO})_2](\text{ClO}_4)_2 \cdot 2(4,4'\text{-bipy})$ [**3**].^[31] Les composés **1** et **2** iso-structuraux ont été obtenus par synthèses en conditions hydrothermales. Le matériau **3** à été obtenu par cristallisation en solution de diméthylsulfoxyde. La structure globale de ces matériaux est hiérarchisée où l'unité de base est une chaîne à connectivité iono-covalente, ces chaînes sont connectées les unes aux autres *via* des liaisons hydrogènes et interactions π (induites par le caractère aromatique des molécules de 4,4' bipyridine) pour former des feuillets. Ces feuillets présentent des cavités hydrophobes, l'empilement des feuillets et la présence de ces cavités, génèrent la formation de canaux. La stabilité structurales de ces matériaux est associée à la présence de molécules invitées (DMSO, 4,4' bipyridine et contre-ions perchlorates). Quelques représentations de la structure du composé **1** sont proposées sur la figure 8.

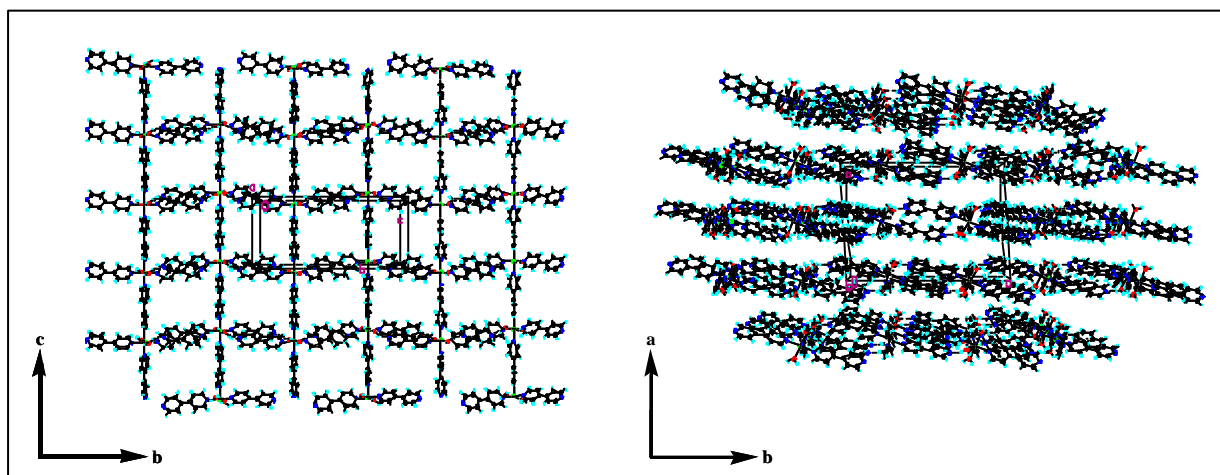


Figure 8. Quelques représentations de la structure du composé : $[\text{Ni}(4,4'\text{-bipy})_3(\text{H}_2\text{O})_2](\text{ClO}_4)_2 \cdot 1.4(4,4'\text{-bipy}) \cdot 3(\text{H}_2\text{O})$.
Groupe d'espace = C2/c, $a = 17.5698 \text{ \AA}$, $b = 11.4101 \text{ \AA}$, $c = 24.479 \text{ \AA}$, $\beta = 93.064^\circ$,
 $V = 4900.4 \text{ \AA}^3$, $Z = 4$.

Le composé **3** n'est pas iso-structural de **1** et **2**, quelques représentations cristallographiques sont données sur la figure 9.

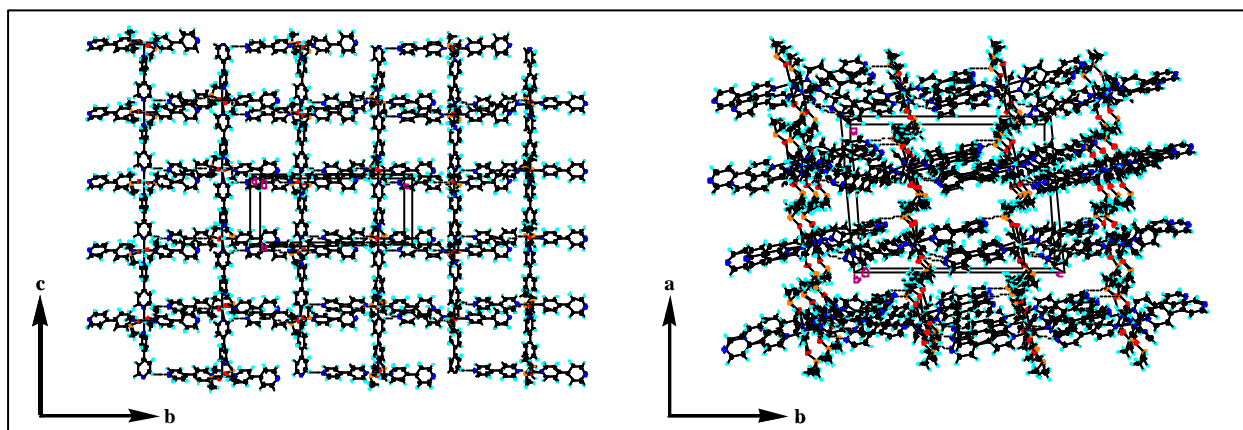


Figure 9. Quelques représentations de la structure du composé : $[\text{Cu}(4,4'\text{-bipy})_3(\text{DMSO})_2](\text{ClO}_4)_2 \cdot 2(4,4'\text{-bipy})$. Groupe d'espace = Cc, $a = 19.0931 \text{ \AA}$, $b = 11.1949 \text{ \AA}$, $c = 25.607 \text{ \AA}$, $\beta = 94.810^\circ$, $V = 5454.0 \text{ \AA}^3$, $Z = 4$.

La première différence structurale majeure existant entre le composé **3** et les deux homologues **1** et **2**, est la présence de diméthylsulfoxyde dans la première sphère de coordination du cuivre. La seconde différence de taille, est l'absence de liaisons hydrogène inter-chaînes pour le matériau **3**, et enfin les cycles aromatiques des molécules de bipyridine coordonnant le cuivre sont bien moins coplanaires et caractérisés par un angle de distorsion de $61,4^\circ$. Il existe également quelques différences mineures (angles de liaison et distances inter-atomiques) sur lesquelles nous ne nous étendrons pas dans ce document.^[24]

Nous nous sommes intéressés aux propriétés magnétiques de ces matériaux. L'ensemble de leurs propriétés magnétiques sont similaires mettant en avant de faibles interactions d'échange entre centres métalliques pour les composés **1** et **2**, et pas d'interaction au-dessus de 2K pour le composé **3**. Un exemple de comportement magnétique pour le composé **1** est proposé sur la figure 10.

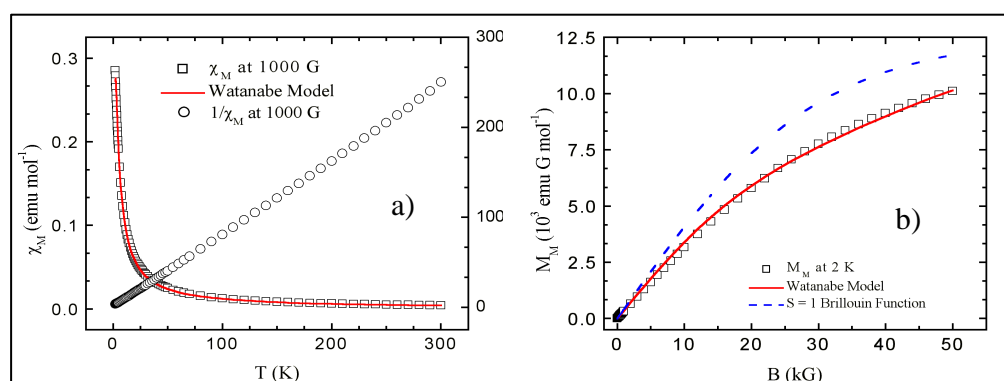


Figure 10. Comportement magnétique du composé $[\text{Ni}(4,4'\text{-bipy})_3(\text{H}_2\text{O})_2](\text{ClO}_4)_2 \cdot 1.4(4,4'\text{-bipy}) \cdot 3(\text{H}_2\text{O})$.

Le comportement de la susceptibilité magnétique molaire en fonction de la température peut être simulé en utilisant un modèle de champ moléculaire d'ions isolés, corrigé par le modèle de Watanabe, introduisant un paramètre d'anisotropie.^[x] Nous obtenons une constante de couplage J/k_B égale à -0.42K , signifiant de faibles interactions antiferromagnétiques entre centres métalliques. La courbe d'aimantation à 2K nous permet de déterminer un paramètre axial de structure fine (D/k_B) égal à $6,74 \text{ K}$. Le comportement magnétique du composé **1** est indiqué sur la figure 11. La valeur de la susceptibilité paramagnétique molaire prise à la température ambiante est de $1,19 \cdot 10^{-3} \text{ emu/mol}$. Cette valeur expérimentale corrobore tout à fait celle attendue ($1,33 \cdot 10^{-3} \text{ emu/mol}$) pour des centres métalliques à spin $\frac{1}{2}$ sans interaction. La dépendance en température de la susceptibilité molaire à 1000G, s'ajuste parfaitement à une loi de Curie et la dépendance en champ de l'aimantation est très

bien ajustée par une fonction de Brillouin. Ces deux comportements suggèrent que les centres métalliques sont non couplés, même à une température de 2K.

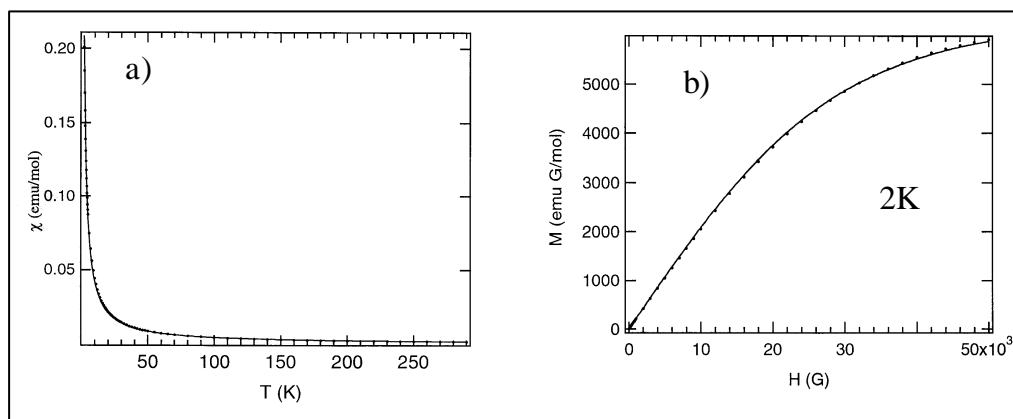


Figure 11. Comportement magnétique du composé $[\text{Cu}(4,4'\text{-bipy})_3(\text{DMSO})_2](\text{ClO}_4)_2 \cdot 2(4,4'\text{-bipy})$.

Dans un tout autre contexte, les cavités intrinsèques à ces matériaux leur confèrent des propriétés d'inclusion. Ces propriétés d'insertion ont été testées avec des molécules sondes, de types triphénylphosphine (TPPO), triméthylphosphine (TMPO) et caractérisées qualitativement par RMN du ^{31}P . Ce travail ne sera pas traité dans ce document, mais constitue une partie de la thèse Jonathan Woodward (thèse soutenue en Juillet 2002) et de Bhavin Abadjaru (thèse en cours à l'Université de Floride, sous la direction de Clifford Bowers, Professeur à l'Université de Gainesville).

III-2-b Matériaux en échelles.

Une autre problématique abordée, centrée sur le comportement magnétique de composés cristallins, traite de la synthèse et caractérisation de matériaux en échelles (échelles atomiques et/ou de spin). Dans cette problématique, il faut associer une délocalisation de spin à une dimensionnalité de structure limitée et contrôlée. Il faut donc utiliser des ligands adéquats jouant un rôle de briques moléculaires, permettant d'induire ou d'inhiber l'extension du polymère de coordination. Plusieurs briques moléculaires peuvent être employées pour s'orienter vers une réalisation spécifique de matériaux en échelles. Dans le cadre de ces travaux nous nous sommes essentiellement intéressés aux ligands azidure (N_3^-) et ter-pyridine. Les cristallisations ont lieu en solvant polaire (DMSO) en utilisant le sel $\text{Cu}(\text{ClO}_4)_2 \cdot 5\text{H}_2\text{O}$. En fonction des conditions de synthèse et en jouant principalement avec le rapport $[\text{Cu}(\text{II})/\text{N}_3^-]$ deux types de matériaux en échelle, ont été obtenus avec comme motifs de base un tétramère et pentamère de Cuivre nommés respectivement C4 et C5. Ces deux unités de base sont décrites dans la figure 12.

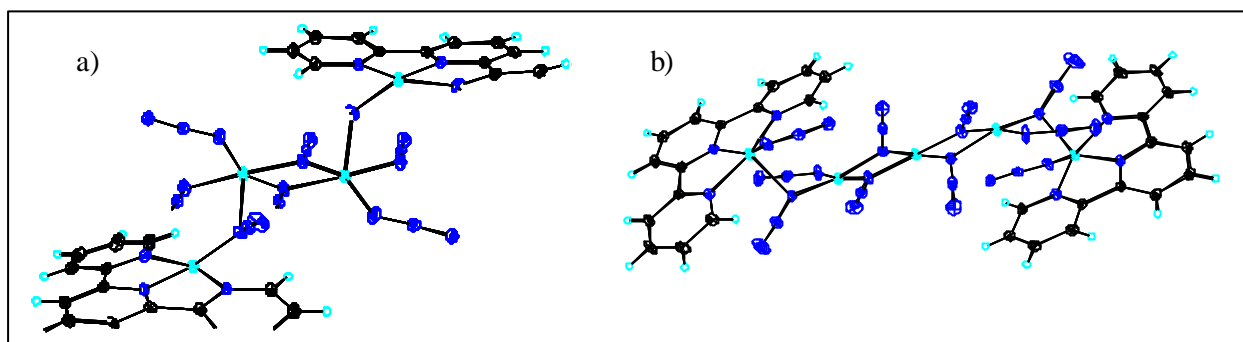


Figure 12. Unité de base des composés a) $[\text{Cu}_2(\text{terpy})_2-\mu_2-(\text{N}_3)_4][\text{Cu}_2-\mu_2-(\text{N}_3)_2(\text{N}_3)_2]$, (**C4**) et b) $[\text{Cu}_2(\text{terpy})_2-\mathbf{m}(\text{N}_3)_2(\text{N}_3)_2][\text{Cu}_3-\mathbf{m}(\text{N}_3)_4(\text{N}_3)_2]$, (**C5**).

La figure 13-b met bien en évidence une structuration en échelle du composé **C4**, les échelles s'alignant le long de l'axe cristallographique a. La connectivité entre "jambes" et "barreaux" est assurée par des monomères $[\text{Cu}(\text{terpy})(\text{N}_3)_2]$, les barreaux des échelles sont associés aux dimères $[\text{Cu}_2(\text{N}_3)_4]$. Ces échelles sont agencées dans le plan cristallographique (a,b) et forment ainsi des feuilletts. La figure 13-a met en évidence une légère inter-pénétration des échelles mitoyennes par le biais d'interactions π - π des cycles aromatiques inhérents aux molécules de ter-pyridine. Dans ce composé il est important de noter l'absence d'ion perchlorate, qui de ce fait ne participent pas à l'électroneutralité du composé.

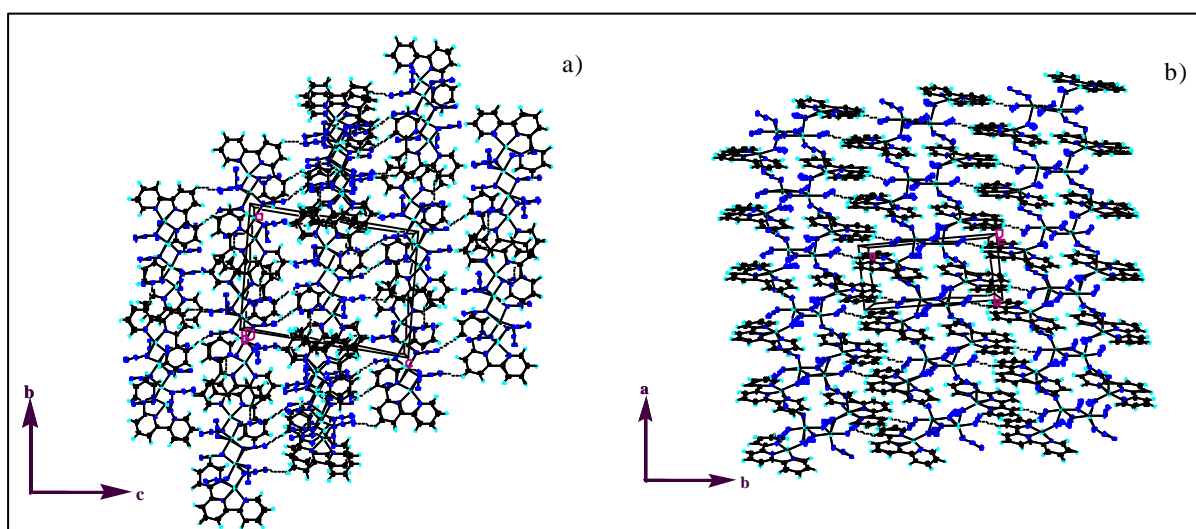


Figure 13. Quelques représentations de la structure du composé $[\text{Cu}_2(\text{terpy})_2-\mu_2-(\text{N}_3)_4][\text{Cu}_2-\mu_2-(\text{N}_3)_2(\text{N}_3)_2]$ **C4**. Groupe d'espace = $P2_1/n$, $a = 14.4872 \text{ \AA}$, $b = 7.1430 \text{ \AA}$, $c = 18.454 \text{ \AA}$, $\beta = 95.719^\circ$, $V = 1900.2 \text{ \AA}^3$, $Z = 4$.

Le matériau **C5** est également un polymère de coordination structuré en échelle (figure 14). Cette structuration en échelle est basée sur une superposition de pentamères $[\text{Cu}_5(\text{terpy})_2(\text{N}_3)_{10}]$. La connectivité entre "jambes" et "barreaux" est assurée par des monomères $[\text{Cu}(\text{terpy})(\text{N}_3)_2]$. Les unités pentamériques se superposent suivant l'axe cristallographique a. L'agencement des échelles induit une structure en feuilletts coplanaires au plan (a,c) (figure 14-a). Nous pouvons constater que dans ce cas également les échelles mitoyennes sont interpénétrées, cette caractéristique est induite par des interactions π - π propres aux cycles aromatiques des entités ter-pyridine.

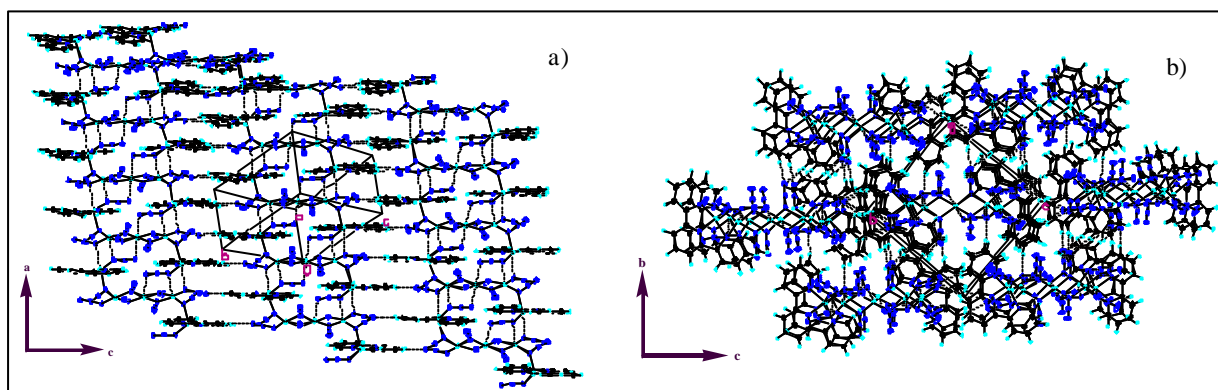


Figure 14. Quelques représentations de la structure du composé $[\text{Cu}_2(\text{terpy})_2\text{-}m(\text{N}_3)_2(\text{N}_3)_2][\text{Cu}_3\text{-}m(\text{N}_3)_4(\text{N}_3)_2]$ **C5**. Groupe d'espace = P-1, $a = 6.6035 \text{ \AA}$, $b = 12.660 \text{ \AA}$, $c = 13.110 \text{ \AA}$, $\alpha = 88.682^\circ$, $\beta = 76.278^\circ$, $\gamma = 82.819^\circ$, $V = 1056.4 \text{ \AA}^3$, $Z = 2$.

Les détails cristallographiques des composés C4 et C5 ne seront pas mentionnés dans ce document (distances inter-atomiques, angles de liaisons), seuls quelques détails seront donnés pour expliciter simplement leur comportement magnétique.

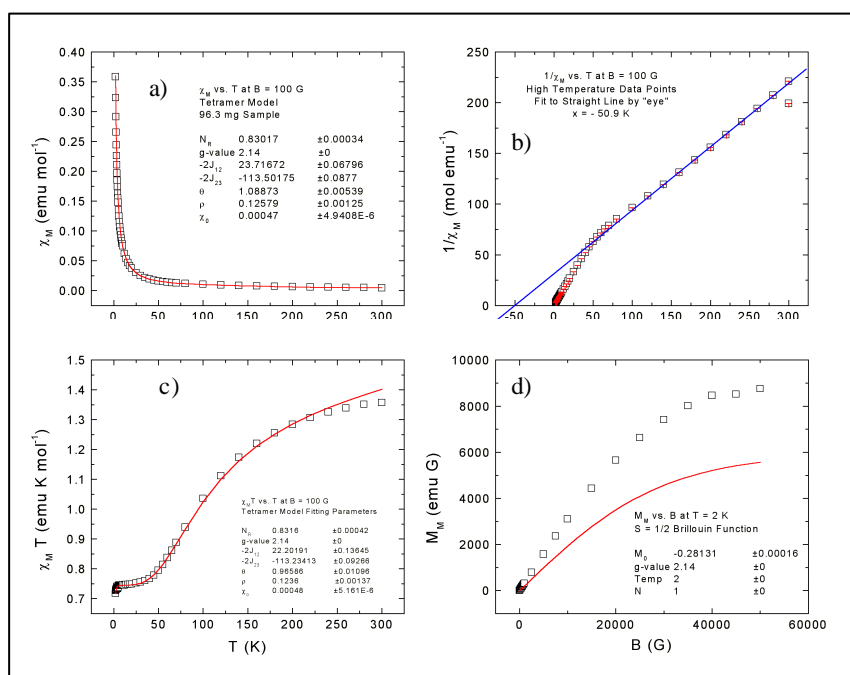


Figure 15. Comportement magnétique du composé $[\text{Cu}_2(\text{terpy})_2\text{-}\mu_2\text{-(N}_3)_4][\text{Cu}_2\text{-}\mu_2\text{-(N}_3)_2(\text{N}_3)_2]$ **C4**

Nous pouvons constater que la susceptibilité magnétique molaire du composé C4 augmente quand la température décroît. Cette phénoménologie est identique que ce soit pour des mesures avec, ou sans champ appliqué. Ceci met en évidence l'absence d'un ordre magnétique de spin de la température ambiante à 2K. L'inverse de la susceptibilité magnétique portée en fonction de la température met en évidence un comportement dominant de caractère antiferromagnétique (l'extrapolation des données hautes températures sur l'axe des abscisses indique une température négative égale à $-46,32 \text{ K}$) (figure 15-b). La décroissance de $\chi_M * T$ en fonction de la température (de 300 K à 50 K) (figure 15-c) confirme le caractère antiferromagnétique des interactions dominantes. Au-dessous de 5 K une seconde diminution de la valeur de $\chi_M * T$ est observée (avec une pente plus importante que précédemment), mettant ainsi en évidence de faibles interactions

antiferromagnétiques au sein du matériau C4. La courbe d'aimantation à 2 K (figure 15-d) indique une augmentation de l'aimantation avec la valeur du champ appliqué, nous pouvons observer le début d'une seconde aimantation vers 40 kG.

Pour le composé C4 l'interaction dominante antiferromagnétique est celle induite par les dimères $[\text{Cu}_2(\text{N}_3)_4]$ constitutifs des barreaux de l'échelle. Cependant les angles de liaison Cu-N-Cu égaux à 103° devraient induire une interaction d'échange ferromagnétique. En effet il existe un angle limite de 108° (angle d'orthogonalité où les contributions antiferromagnétiques et ferromagnétiques s'annulent mutuellement et au-dessous duquel les interactions sont annoncées ferromagnétiques).^[32] Les raisons de cette anomalie associée aux interactions d'échanges intradimère $[\text{Cu}_2(\text{N}_3)_4]$ ne sont pas bien claires pour le moment. Cependant des calculs *ab-initio* reliant la structure de ce composé à son comportement magnétique sont en cours d'étude *via* une collaboration avec Mike Whangbo, Professeur à l'Université de Caroline du Nord. Les interactions dimères-monomères entre le dimère central $[\text{Cu}_2(\text{N}_3)_4]$ et les deux monomères adjacents $[\text{Cu}(\text{terpy})(\text{N}_3)_2]$ assurant la connectivité "barreaux-jambes" sont faibles mais non négligeables. Les interactions inter-tétramères, malgré de faibles distances Cu-N (jambes de l'échelle), sont nulles. Ceci s'explique par la valeur de l'angle Cu-N-Cu (107°) très proche de la condition d'orthogonalité (108°). De ce fait le composé C4 ne peut pas être considéré comme un matériau à échelles de spin.

Le comportement magnétique du composé C5 est proposé sur la figure suivante.

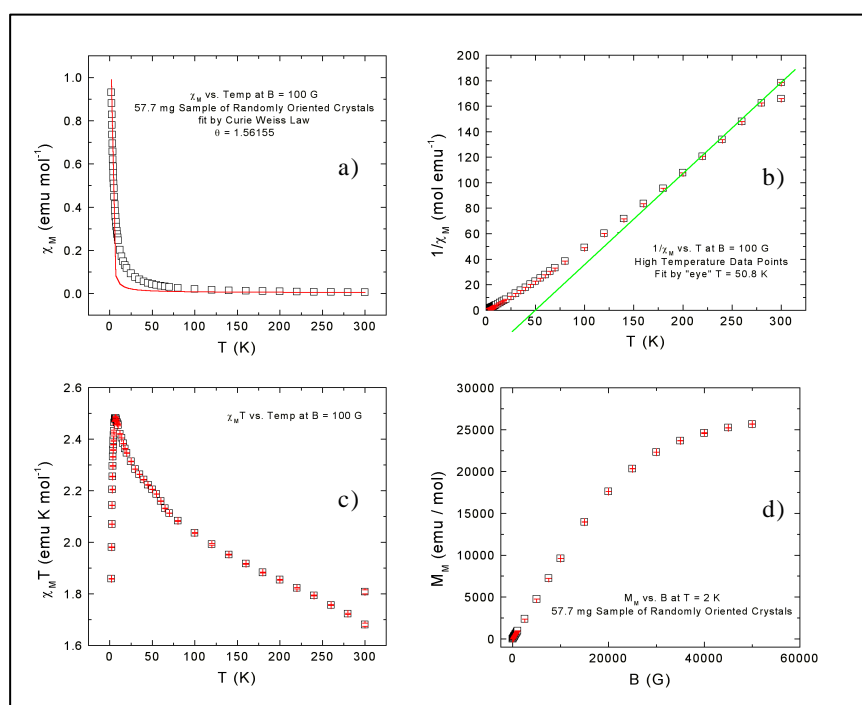


Figure 16. Comportement magnétique du composé $[\text{Cu}_2(\text{terpy})_2\text{-}m(\text{N}_3)_2(\text{N}_3)_2]$ $[\text{Cu}_3\text{-}m(\text{N}_3)_4(\text{N}_3)_2]$ C5.

Comme C4 le composé C5 ne présente pas d'ordre magnétique à longues distances et ceci pour une gamme de température allant de la température ambiante à 2K. L'inverse de la susceptibilité magnétique en fonction de la température intercepte (par extrapolation des valeurs à haute température) l'axe des ordonnées à une température positive de 47 K (fig.16-b). Ceci suggère que les interactions dominantes de spin sont ici de caractère ferromagnétique. Ce comportement aux hautes températures est également confirmé avec la pente positive de la courbe $\chi_M T$ reportée en fonction de la température (fig.16-c). Nous observons sur cette courbe un maximum vers 6,5K (2,48 emu K mol⁻¹). Au-dessous de cette température de 6,5K le produit $\chi_M T$ décroît en fonction de la

température ceci traduisant la présence d'interactions antiferromagnétiques faibles. La courbe d'aimantation augmente avec la valeur du champ imposé et commence à saturer vers 30 kG en atteignant une valeur seuil de 26000 emu G mol⁻¹. Dans ce composé trois types d'échanges ont été considérés : l'unité centrale Cu₃N₆ de chaque pentamère est supposée induire les interactions de super-échange dominant le comportement magnétique du matériau, le couplage entre le trimère central et les deux monomères terminaux (Cu(terpy)(N₃)₂) et enfin le couplage inter-pentamères. Le couplage trimère-monomères est médié *via* des groupements azidures en site de coordination basal et apical respectivement pour un cuivre terminal et un cuivre central, cette configuration ne permettant pas de bons couplages. Les interactions inter-pentamères sont médiées par de longues liaisons Cu-N associées à des ponts azidures asymétriques de types tête-tête et tête-bêche, cette configuration ne permet pas de bons échanges de spin.

Le composé C5 peut donc être considéré comme un empilement de trimères en interactions faibles. Aux hautes températures C5 possède un comportement paramagnétique, les spins non appariés associés à chaque pentamère ne sont pas couplés et sont distribués aléatoirement le long de l'échelle. Lorsque la température décroît, le couplage intrapentamère peut avoir lieu car l'énergie thermique devient insuffisante pour peupler les états excités. Une augmentation du produit $\chi_M \cdot T$ est observée au début des interactions d'échange de spins ferromagnétiques induites par un angle Cu-N-Cu de 101°. On remarque deux pentes bien distinctes, mettant peut être en avant deux constantes de couplages différentes. A la température de 6,5 K l'état fondamental S= 5/2 est complètement peuplé, le composé C5 consiste alors en un empilement de pentamères à interactions ferromagnétiques. A plus basses températures, la décroissance du produit $\chi_M \cdot T$ annonce les interactions faibles inter-pentamères.

Ces comportements magnétiques ont été modélisés dans la thèse de Jonathan Woodward (University of Florida), ces études ne seront pas traitées dans ce document.

III-3 MONOCOUCHE DE LANGMUIR ET FILMS DE LANGMUIR-BLODGETT: DEUX SYSTEMES STRUCTURANTS.

Ces travaux se focalisent principalement sur la formation d'entités inorganiques aux interfaces de substrats organiques bidimensionnels inhérents aux monocouches de Langmuir et films de Langmuir-Blodgett. Nous nous sommes intéressés à la formation de systèmes continus hybrides organiques-inorganiques à base de phospholipides et complexes de métaux transitionnels, mais également à la formation de particules métalliques et minérales. Dans ces trois cas de figures, les méthodologies employées ainsi que les techniques de caractérisations utilisées sont brièvement décrites sur la figure 17.

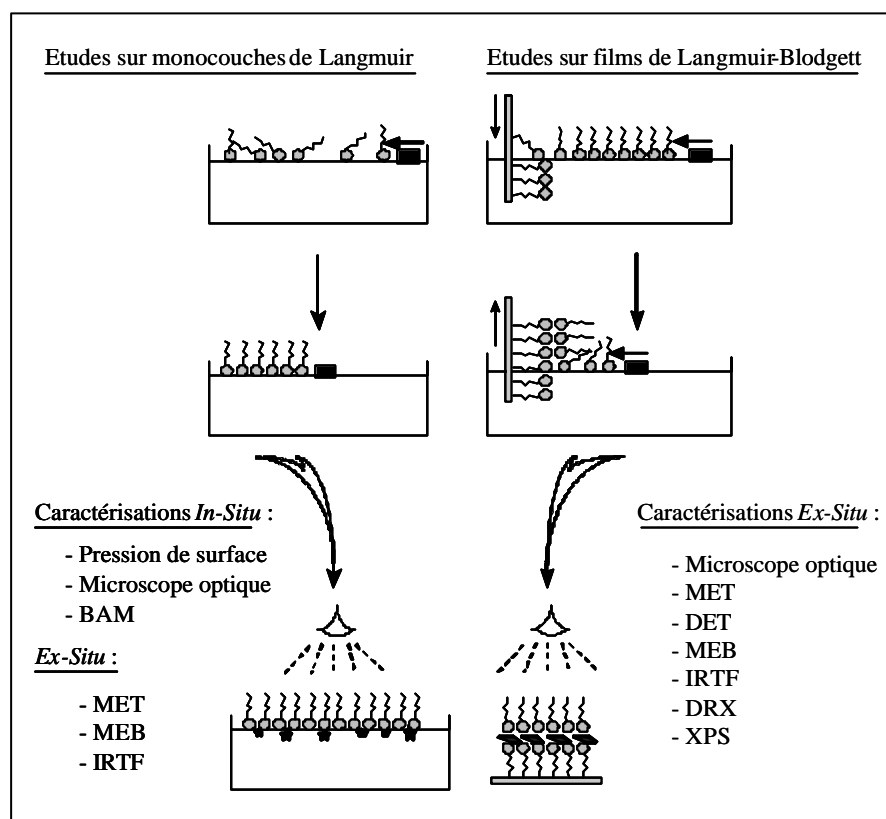


Figure 17. Schématisation des méthodologies employées et techniques de caractérisation utilisées.

III-3-a Films de Langmuir-Blodgett Phospholipidiques: RMN ³¹P

Dans les travaux décrits précédemment, les problématiques associées à l'obtention d'une matière organisée hybride organique-inorganique n'intéressent essentiellement que les communautés propres aux chimistes et physico-chimistes. L'étude présentée dans cette partie s'adresse aux chimistes et physico-chimistes, mais de plus trouve des intérêts pratiques pour les biologistes et biochimistes. En effet, ce travail a permis d'obtenir les premiers films LB structurés à base de phosphatidylsérine (DPPS) et stabilisés par des cations de métaux transitionnels Pt(II), Cd(II), Pd(II), Au(III).^[33] Dans ce contexte, la RMN devient un outil indispensable pour évaluer la structure et au-delà, toutes interactions d'une membrane phospholipidique associée à d'autres composantes propres au monde du vivant, Cholestérol, protéines etc. Pour opérer avec succès, il faut à la fois ne pas dénaturer l'aspect membranaire de l'objet étudié tout en obtenant une quantité de manière raisonnable permettant d'obtenir un signal RMN satisfaisant. Pour atteindre ce double objectif, il est fait appel à des dépôts de membranes sur des supports de mica, ces supports étant accolés les un aux autres afin d'augmenter la quantité de matière organique à analyser. Ce procédé est assez long, demande une très grande minutie et dans le meilleur des cas n'empêche pas une dégradation partielle des structures étudiées.

Ce travail a été effectué dans l'équipe de Daniel R. Talham avec Gail E. Fanucci. La spectroscopie RMN a été réalisée par Riqiang Fu, Chercheurs au "National High Magnetic Field Laboratory" de Tallahassee en Floride. Cette étude a permis la réalisation d'un article.

En règle générale la déposition séquentielle de bicouches phospholipidiques par utilisation de la technique LB est une tâche très difficile et seulement quelques succès ont été obtenus avec des dérivés de la molécule de phosphatidyléthanolamine.^[34] Cette difficulté de transférer verticalement

sur supports solides ces entités phospholipidiques est attribuée à de faibles interactions de leurs parties polaires ou hydrophiles, interactions qui parfois même sont de nature répulsive.^[35] Dans le but d'améliorer ces interactions et donc de permettre une structuration en bicouches, des cations calcium et uranyle ont été utilisés pour stabiliser la partie hydrophile et anionique de l'acide dipalmitolphosphatidique.^[35] C'est dans ce même effort que se situe notre étude avec comme entité amphiphile la molécule de dipalmitolphosphatidylsérine (DPPS).^[33] Pour stabiliser les interactions intermoléculaires à l'interface eau/air différents sels métalliques ont été dissous en solution aqueuse: K_2PdCl_4 , K_2PtCl_4 , $K_2Pt(CN)_4$, $KAuCl_4$ et $Cd(ClO_4)_2$. Par spectroscopie infrarouge à transformée de Fourier (IRTF), nous pouvons évaluer le caractère homogène de chaque transfert en suivant les intensités relatives des modes normaux de vibration associées aux élongations symétriques et asymétriques des groupements (CH_2) comme l'indique la figure 18.

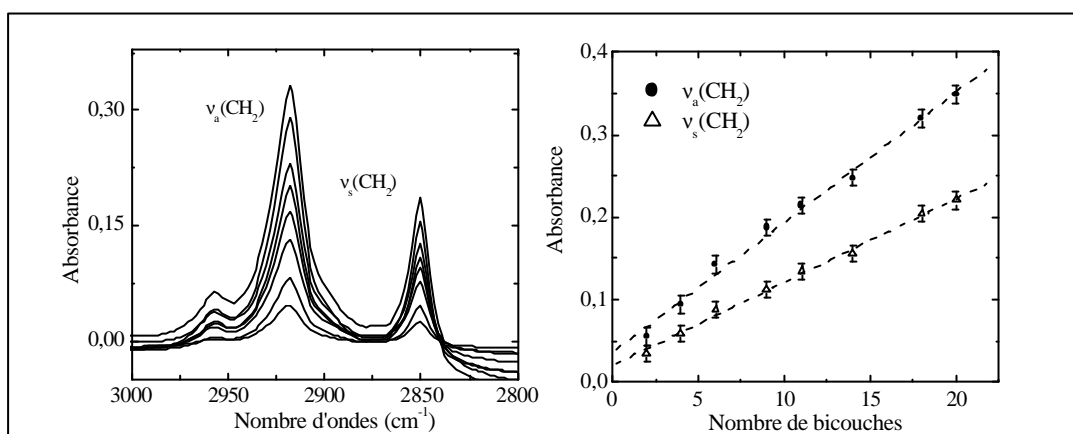


Figure 18. Evolution des intensités des vibrations d'élongations symétriques et asymétriques en fonction du nombre de bicouches déposées.

Par une étude de spectroscopie infrarouge polarisée, en se focalisant sur les vibrations d'élongations caractéristiques des groupements (CH_2), l'angle des chaînes alkyles avec la perpendiculaires au substrat a été évalué à 39° . Le caractère bidimensionnel des matériaux transférés est révélé par diffraction des rayons X, avec une distribution caractéristique des harmoniques définissant une distance interfoliaire de 56\AA . Les stœchiométries des matériaux déposés ont été déterminée par XPS, pour le film hybride DPPS-Pt(II), sur lequel nous avons centré notre étude, la composition suivante a été obtenue: $[(DPPS^-)]_2Pt(II)(H_2O)](DPPS)_4$. De toutes ces analyses, résumées ci-dessus, une configuration possible de l'agencement des phospholipides au sein des films a pu être avancée (figure 19).

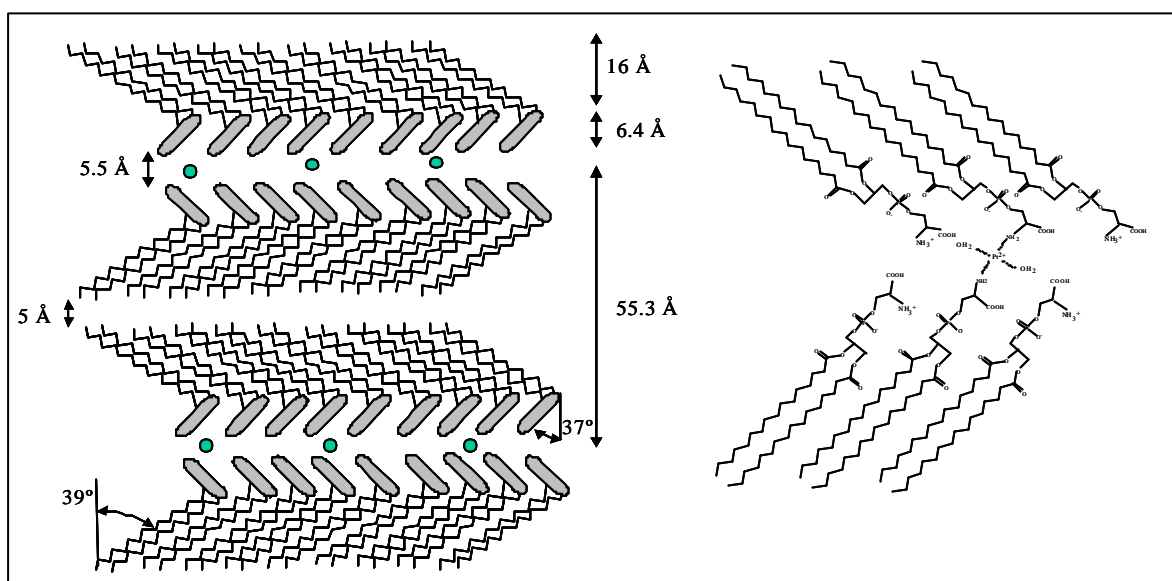


Figure 19. Représentation schématique des bicouches phospholipidiques associées au système $[(DPPS^-)_2Pt(II)(H_2O)](DPPS)_4$.

Suivant cette stratégie de mise en forme, nous avons pu réaliser jusqu'à cent dépôts de bicouches phospholipidiques organisées, ayant ainsi assez de matière organique pour obtenir un spectre RMN du ^{31}P (figure 20).

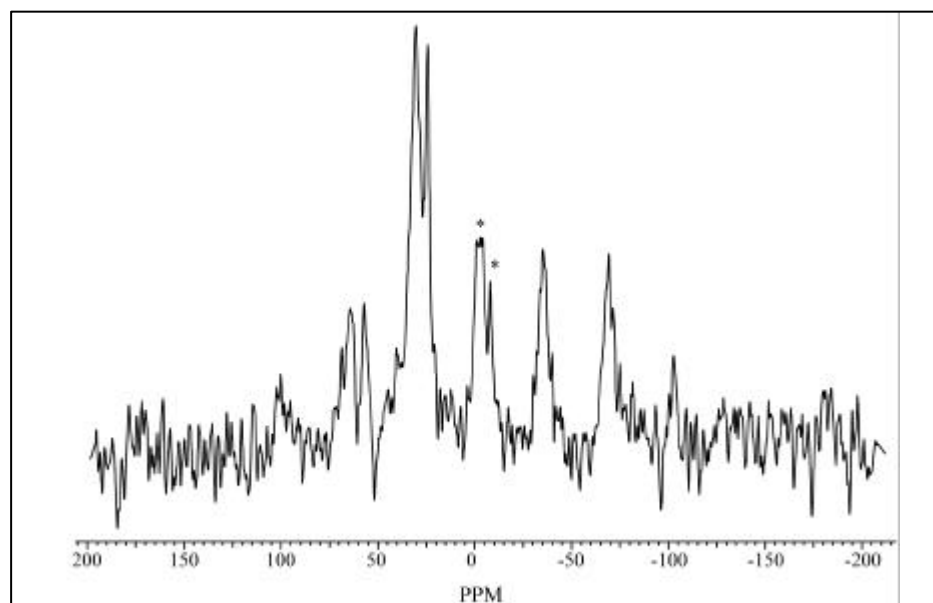


Figure 20. Spectre RMN ^{31}P du composé $[(DPPS^-)_2Pt(II)(H_2O)](DPPS)_4$.

Ce spectre RMN MAS en cross-polarisation $^1H/^{31}P$ a été obtenu en soixante-douze heures. Nous pouvons détecter deux signaux associés aux résonances isotropes suivantes: $\delta_{iso} = -2,9 \pm 0,2$ ppm et $\delta_{iso} = -7,7 \pm 0,1$ ppm (avec comme référence $NH_4H_2PO_4$). La présence de ces deux signaux met en évidence la présence de deux types de DPPS. Le signal donnant un déplacement à $-2,9$ ppm est à la même position, possède la même symétrie en ayant le même nombre d'harmoniques ou "spinning side bands" que la poudre de DPPS initiale. Ceci implique qu'une grande partie des entités de DPPS se trouve sous une forme identique à celle du zwitterion phospholipidique de départ. Le signal plus

petit centré à -7,7 ppm est caractéristique d'une autre forme de DPPS en interaction avec le cation transitionnel Pt^{2+} . En effet, il a été démontré que la présence de ce signal est caractéristique d'une augmentation de la structuration des phospholipides, cette organisation résultant sans doute des interactions phospholipides-complexes inorganiques.^[36]

III-3-b Monocouches de Langmuir et procédé de biominéralisation.

Ce travail s'inscrit dans une thématique frontière entre la mise en forme de minéraux via une interface organique et la médecine, en particulier le domaine de la néphrologie, science s'intéressant aux problématiques liées à la formation de calculs rénaux. Ces calculs rénaux sont en fait des matériaux hybrides organiques-inorganiques où coexistent des substances minérales (Oxalate de calcium, Phosphate de calcium) associées à des entités organo-biologiques (phospholipides, lipides, protéines, cholestérol, carbohydrates, etc.). Des exemples de calculs rénaux sont proposés sur la figure 23. Dans ce contexte, certains chercheurs spécialistes de néphrologie ont émis une hypothèse où les structures organiques pouvaient servir de sites de nucléation préférentiels pour une entité minérale en croissance.^[37] Cette nucléation hétérogène pouvant être exaltée ou inhibée par différents facteurs explicités dans les lignes suivantes, mais relevant tous d'une problématique de spécificité de réactivité aux interfaces organo-minérales.^[37,7a]

Ces travaux ont été réalisés aux Etats-Unis, dans l'équipe de Daniel R. Talham, en collaboration avec Saeed R. Khan, Professeur à l'université de Floride (College of Medecin - Shands hospital), spécialistes des maladies rénales et ont permis la réalisation de quatre articles, un proceeding et cinq communications.

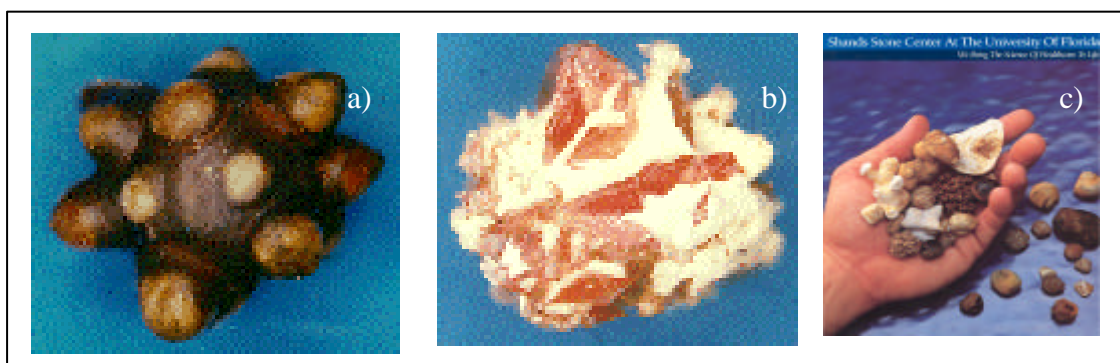


Figure 23. a) Calculs rénaux composés à 97% d'oxalate de calcium mono-hydraté et 3% de composés organique, b)calculs rénaux composés de 69% d'oxalate de calcium mono-hydraté, 28% de phosphate de calcium, c) quelques exemples de tailles critiques associées aux calculs rénaux.

Dans ce contexte, les monocouches de Langmuir apparaissent comme des systèmes simples où les paramètres impliqués, dans cette phénoménologie de nucléation hétérogène aux interfaces organo-minérales, peuvent être ségrégués et étudiés. Dans une première étude^[x] trois phospholipides différents ont été étudiés, avec comme spécificité la charge de leur tête polaire. Ces phospholipides sont les suivants : Dipalmitolphosphatidylglycérol (DPPG), dipalmitolphosphatidylcholine (DPPC) et dipalmitolphosphatidylsérine (DPPS), le caractère anionique de leur tête polaire évoluant comme tel : DPPG> DPPS=DPPG.

Nous nous sommes en particulier intéressés à la formation d'oxalate de calcium monohydraté (COM) $\text{CaC}_2\text{H}_2\cdot\text{H}_2\text{O}$, ce minéral étant le constituant inorganique majoritaire des calculs rénaux. Dans toutes les études suivantes, trois types de morphologies sont obtenues en fonction du type de facettes nucléées et de l'état d'agrégation des cristallites attachés aux monocouches, ces différences sont indiquées sur la figure 24.

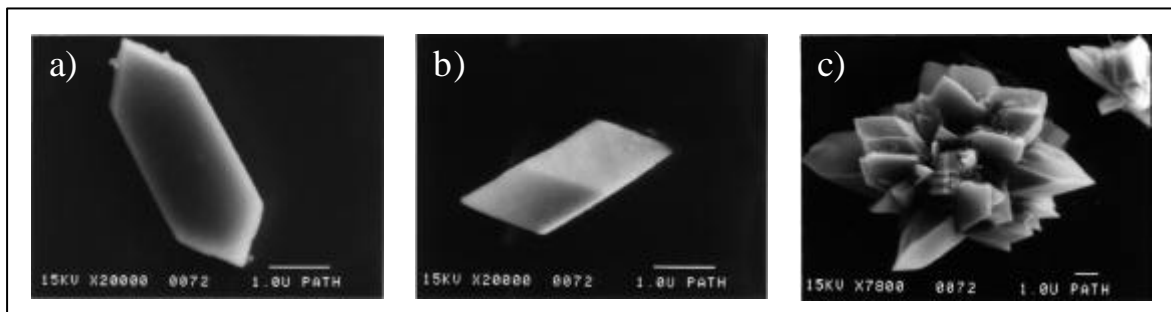


Figure 24. Différentes morphologies des cristaux de COM : a) face (10-1), b) face (010), c) agrégats.

Nous avons ensuite comptabilisé le nombre et distingué les types de cristaux attachés aux monocouches en utilisant la microscopie électronique à balayage (MEB), ceci pour des solutions sursaturées en oxalate de calcium à concentration différentes RS5 et RS10.^[x] Nous avons observé une plus grande quantité de cristaux nucléés sous la monocouche de DPPG par rapport aux monocouches de DPPC et DPPS. Nous avons pu démontrer l'influence spécifiques des ions calcium sur l'agencement des monocouches phospholipides. Les ions Ca^{2+} jouent en fait un rôle "liant" entre la monocouche organique et le réseau inorganique en croissance.^[38] Les monocouches de DPPG possédant un fort caractère anionique auront une interaction préférentielle avec les ions calcium, optimisant ainsi la formation d'oxalate de calcium monohydraté. Nous avons également remarqué une cristallisation à caractère hétérogène, où, dans tous les cas, un maximum de cristaux est observé avec la face (10-1) attachée aux monocouches. Ceci est expliqué par le fait que cette face (10-1) est riche en ions calcium.^[x] Cette première série d'étude a permis de mettre en évidence l'importance des densités de charge anionique (nature phospholipidique) sur les phénomènes de nucléation hétérogène aux interfaces entre cristaux de COM et monocouches phospholipidiques.

Dans une seconde étude, nous nous sommes intéressés aux effets de l'organisation d'une monocouche (structure phospholipidique) sur les phénomènes de nucléation.^[39] Pour ce faire, quatre phospholipides de même charge anionique (phosphatidylglycérol) mais avec des parties hydrophobes différentes, ont été utilisés (dipalmitolphosphatidylglycérol (DPPG), dimiristolphosphatidylglycérol (DMPG), oléole-palmitolphosphatidylglycérol (POPG), dioléolphosphatidyl-DL-glycérol (DOPG). Les comportements globaux sont représentés sur la figure 25. Trois analyses peuvent être menées de front : quatre phospholipides à une pression de surface de 20 mN/m, quatre phospholipides à une surface moyenne de $95 \text{ \AA}^2/\text{molécule}$ et enfin l'étude de l'effet de ces deux conditions limites sur un même surfactant. Dans ce dernier cas, on observe une augmentation du taux de nucléation aux faibles tensions superficielles. Ceci est induit par une augmentation de la fluidité des monocouches qui peuvent alors accommoder préférentiellement leurs paramètres de maille à ceux de l'espèce minérale en croissance. Ceci correspond à une épitaxie, mais s'agissant de matière molle c'est le substrat qui s'accommode au réseau minéral en croissance et non l'inverse. Ce phénomène, d'exaltation du taux de nucléation, est accru pour le DPPG. Il faut noter que pour une surface moyenne de $95 \text{ \AA}^2/\text{molécule}$ la monocouche DPPG possède une structure biphasée où s'associent une phase très désorganisée (analogue à l'état gazeux) et une phase un peu moins désorganisée (analogue à un état liquide).

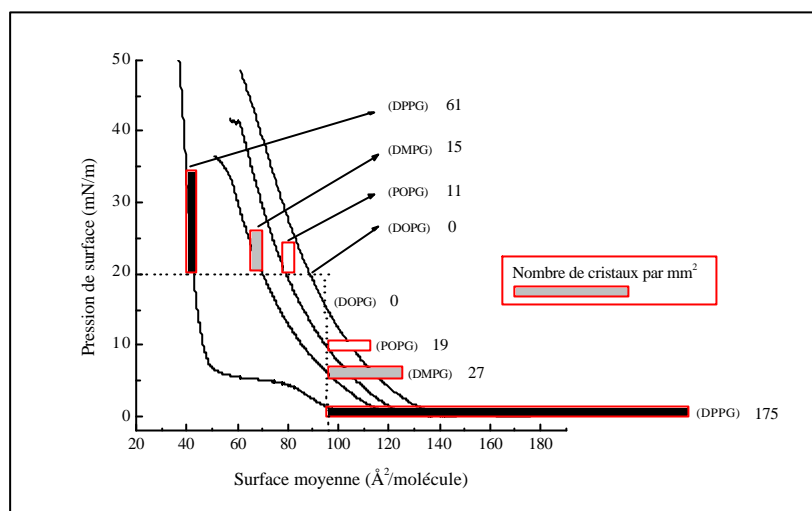


Figure 25. Taux de nucléation associés aux différents phospholipides utilisés dans deux conditions limites (tension superficielle de 20 mN/m et Surface moyenne de 95 Å²/molécule).

Une observation de la structure de la monocouche par microscopie à angle de Brewster (figure 26), nous a permis de mettre en évidence un autre paramètre important.

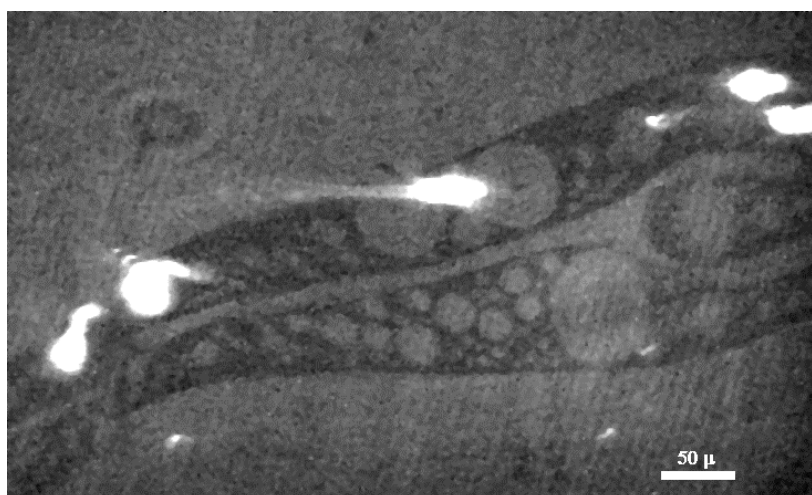


Figure 26. Image de Brewster caractéristique d'une monocouche de DPPG à une tension superficielle de 95 Å²/molécule.

On constate en effet qu'une nucléation préférentielle a lieu aux interfaces entre les deux phases citées précédemment. En fait, cette interface spécifique de la monocouche de DPPG agit comme une zone de défauts qui exalte le taux de nucléation.

Lors de ces études quatre paramètres de nucléation hétérogène ont été globalement identifiés : Structure, nature, fluidité et défauts inhérents aux types de monocouches étudiés. Ces travaux mettent en évidence une action partitive de ces paramètres et non pas coopérative.^[39] Dans ce contexte, des études similaires ont été menées avec adjonction de cholestérol, qui, au-delà d'une concentration seuil, limite le taux de nucléation.^[40] Ces études sont à poursuivre en y associant d'autres composés biologiques comme des polysaccharides, protéines, etc. D'autre part, dans ces études, la morphologie des cristaux ainsi observés est caractéristique de la méthode utilisée qui, par nature, est de caractère bidimensionnelle. Ceci implique une certaine différence de morphologie entre les calculs rénaux (fig. 23) et les cristaux de COM observés dans nos études (fig. 24). Dans le

but d'améliorer la part "bio-mimétique" de nos études, des travaux sont envisagés avec des structures "oignons" où entités organique et inorganique seront cette fois-ci réellement imbriquées (partie IV-1d2) de ce document).

III-3-c Films de Langmuir-Blodgett: nano- et microparticules métalliques.

Dans cet axe de recherche nous essayons de déterminer comment l'espace interfoliaire de films de Langmuir-Blodgett peut à la fois induire la formation de particules métalliques et diriger leur croissance par effet de confinement. Dans ce cadre le système organique apparaît comme un microréacteur jouant le double rôle de structurant et de stabilisant pour une entité inorganique en croissance.

Ces travaux ont été réalisés à l'Université de Floride, dans l'équipe de Daniel R. Talham en collaboration avec James Adair, professeur à l'Université de Pennsylvanie et la N.A.S.A. pour des études de "mise en forme" sous conditions de microgravité. Ces travaux ont permis la réalisation d'un proceeding et cinq communications.

La nano-structuration d'entités inorganiques par le biais de phases structurantes connaît depuis une vingtaine d'années un essor considérable. Cet intérêt est induit par la miniaturisation croissante des composants électroniques mais également à un effet quantique de taille générant des comportements physico-chimiques exotiques.^[41] Dans le but d'améliorer le contrôle des procédés de morphogenèse associés à la réalisation de nano-objets, plusieurs types de systèmes moléculaires organisés ont été utilisés : membranes,^[42] micelles,^[43] vésicules,^[44] monocouches de Langmuir et films de langmuir-Blodgett.^[45] Dans ce dernier exemple, nous nous sommes intéressés à la formation de nano-particules de platine en utilisant différents surfactants à fonctionnalités spécifiques : benzyldiméthylstéarylammonium (BDSA) (ammonium quaternaire), l'octadécylamine (ODA) (amine primaire), dipalmitophosphatidylsérine (DPPS) (zwitterion phospholipidique) et hexadécylaniline (HDA) (amine primaire polymérisable). L'apport de platine émane du complexe $[\text{PtCl}_4]^{2-}$, l'étape de réduction est catalysée par irradiation sous lampe UV (lampe au mercure de 450 W). En plaçant les échantillons à une distance de dix centimètres de la source UV, nous obtenons des nanoparticules, représentées sur la Figure 27.

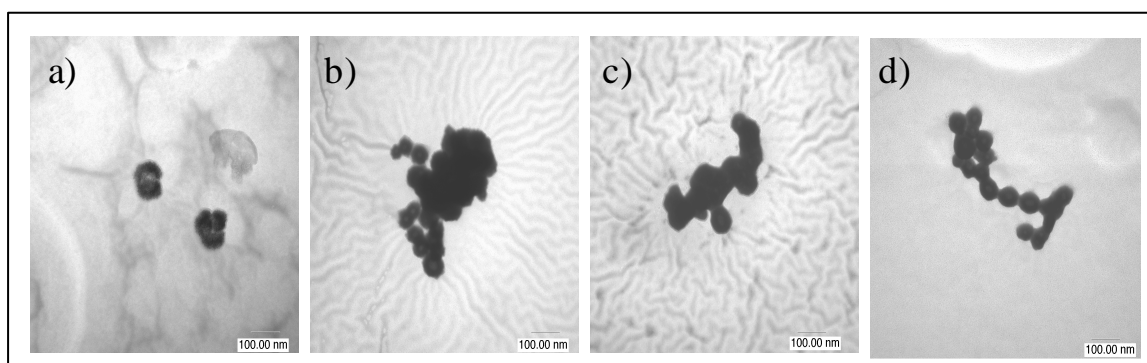


Figure 27. Images MET des nanoparticules métalliques associées aux films LB à bases de : a) DPPC, b) DPPS, c) HDA et d) ODA.

Nous observons que ces nano-objets (80-100 nm) ont une morphologie dans tous les cas sphérique avec une forte tendance à l'aggrégation. Nous n'avons pas d'objet anisotrope plat, que pourrait induire la bidimensionnalité des films LB. De plus, des caractérisations par XPS et diffraction de rayons-X par transmission mettent en évidence la présence de platine zéro-valent pour les systèmes Pt/ODA, Pt/HDA, Pt/DPPS, alors que le système Pt/BDSA est associé à la présence de différents oxydes de platine. Ceci s'explique par la présence d'amines primaires, pour les films LB à

bases de ODA, HDA et DPPS, qui se déprotonnent pendant l'étape de réduction du Pt(II) stabilisant ainsi les nanoparticules métalliques néoformées. Les molécules de BDSA possèdent des ammoniums quaternaires n'offrant pas cette spécificité. Des études quantitatives montrent que très peu de nano-objets sont synthétisés à partir de DPPS, ceci étant dû à la faible interaction entre sa partie zwitterionique polaire et le complexe $[PtCl_4]^{2-}$.

Dans une seconde série d'expériences, nous avons rapproché les films LB à 1 centimètre la source UV, ce qui a pour conséquence d'augmenter légèrement la température associée aux réactions de réductions, qui passe de 25°C à 45°C. Les particules élaborées dans ces conditions sont présentées sur la figure 28.

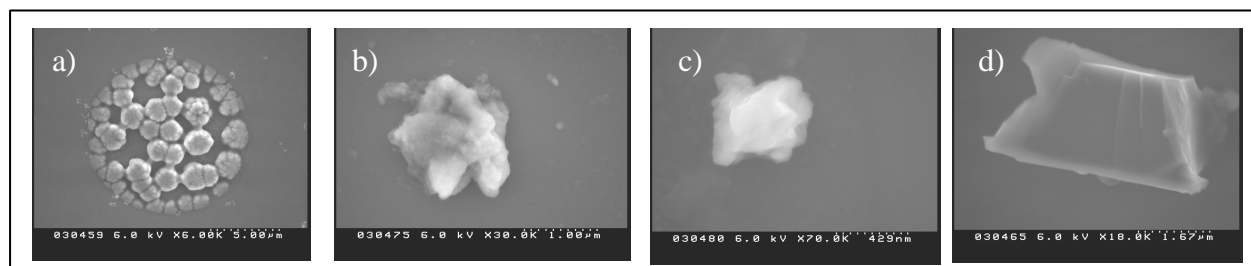


Figure 28. Images MEB des particules métalliques associées aux films LB à bases de : a) BDSA, b) HDA, c) DPPSA et d) ODA.

Nous pouvons donc constater que les particules sont globalement de tailles micrométrique. Dans le cas où des films LB à base de BDSA sont utilisés, nous obtenons des particules colloïdales, tout comme précédemment sous forme de différents oxydes métalliques. Dans le cas des films LB constitués à partir de DPPS, nous observons les plus petits objets qui restent de tailles nanoscopiques, la faible interaction entre sa tête polaire et le complexe de platine utilisé lors de l'étape de transfert ne permettant pas un apport de matière conséquent, inhibant de ce fait la réalisation d'objets micrométriques. Pour les films LB à base d'HDA, nous observons des particules de platine à morphologie chaotique. Des études couplées de RX et d'IRTF mettent en évidence une polymérisation de l'aniline (IRTF analogue au sel d'émeraude) avec le traitement UV, ayant pour conséquence de dénaturer la structure 2D du film LB. Enfin, pour le système ODA/Pt, nous observons bien des objets anisotropes à morphologie en feuillets caractéristique induite par la structure bidimensionnelle inhérente aux films de Langmuir-Blodgett.

III-4 SYSTEMES BIDIMENSIONNELS, MESOPHASES LYOTROPES ET MISE EN FORME AUX GRANDES ECHELLES.

Dans les travaux cités précédemment les propriétés physico-chimiques des matériaux finaux pré-existent dans une des deux entités de départ qu'elle soit organique ou inorganique (conductivité, ONL, magnétisme de spin et nucléaire). Il est possible de réaliser des hybrides organiques-inorganiques où la propriété physico-chimique résultante émane de l'association des entités de départ sans être pré-indiquée dans aucun de ces composants. Dans ce cadre nous sommes intéressés à la formation de mésophases lyotropes en partant de systèmes polycristallins de basse dimensionnalité et en les dispersant dans un solvant approprié.

Ce travail a été réalisé dans l'équipe de Daniel R. Talham, sur une collaboration engagée avec Clément Sanchez directeur de recherches CNRS (LMMC, UMR-CNRS, Université de Paris VI). Cette étude a permis la réalisation d'un article et de quatre communications. (une thèse est en cours à Gainesville sur ce sujet)

Les cristaux liquides sont le plus souvent de composition purement organique. L'alignement préférentiel aux grandes échelles des unités constitutives est lié à la présence d'une anisotropie de forme. Dans la plupart des cas, s'agissant de phases organiques une entité mésogène est associée à un corps rigide à caractère poly-aromatique.^[46] Leurs propriétés thermotrope et/ou lyotrope se révèlent par l'apparition de magnifiques textures observées en microscopie sous analyseurs et polariseurs croisés.^[47] Ces textures sont donc biréfringentes et doivent répondre à un stimulus externe (champs magnétique, élongation mécanique, etc.) par un alignement des domaines biréfringents avec le champ de force appliqué.

Ces comportements ont été également observés au début du XX^{ème} siècle pour des systèmes minéraux.^[48] Récemment ces études sont redevenues à l'ordre du jour avec l'observation et l'interprétation de comportements "cristaux liquides" associés aux phases V_2O_5 ,^[49] aux phases de Chevrel échangées au lithium,^[50] aux structures bohémite^[51] etc.^[52] Ce comportement s'explique, brièvement, par une dispersion de particules minérales anisotropes et hydrophiles dans un solvant polaire, ceci, au-delà d'une concentration seuil. Pour limiter les forces de répulsions inter-particules et augmenter la concentration seuil décrite précédemment, il est possible d'enrober des particules minérales par un polymère hydrophobe et de disperser ces composites dans un solvant non polaire comme le toluène. L'apparition des premiers systèmes hybrides organique-inorganique à comportement "cristal liquide" n'est que très récente.^[53] C'est dans ce contexte que s'établit l'axe de recherche décrit dans les lignes suivantes.

Notre étude est basée tout d'abord sur la réalisation de nouveaux hydroxy-carboxylates de cuivre, cobalt et nickel polycristallins, dont les propriétés magnétiques de spin sont très bien référencées.^[x] Par ailleurs, des dispersions d'hydroxy-stéarate de cuivre dans du toluène à différentes fractions massiques sont représentées sur la figure 29.

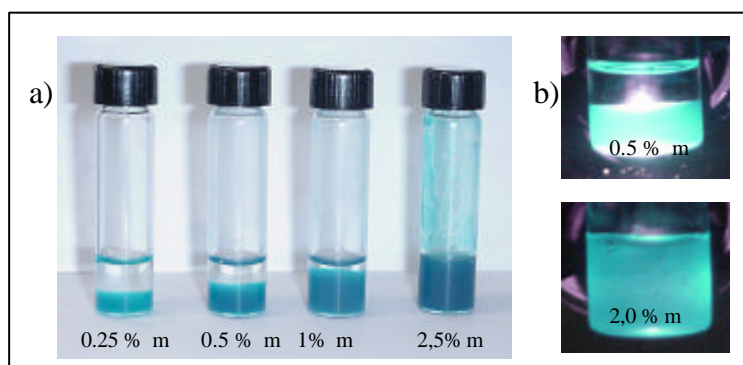


Figure 29. Dispersions d'une poudre d'hydroxystéarate de cuivre à différentes fractions massiques. a) Sans polarisateurs croisés, b) avec polariseurs croisés.

Nous observons donc des systèmes biphasés (dispersion-solvant) pour les faibles pourcentages massiques, au-delà de 2% massique un gel se forme. Comme l'indique les clichés en polariseurs croisés, suspension et gel ont des propriétés biréfringentes, sans doute caractéristique du système polycristallin de départ. Une observation au microscope optique en polariseurs croisés révèle une texture et un comportement assez intéressants, comme l'indique la figure 30.

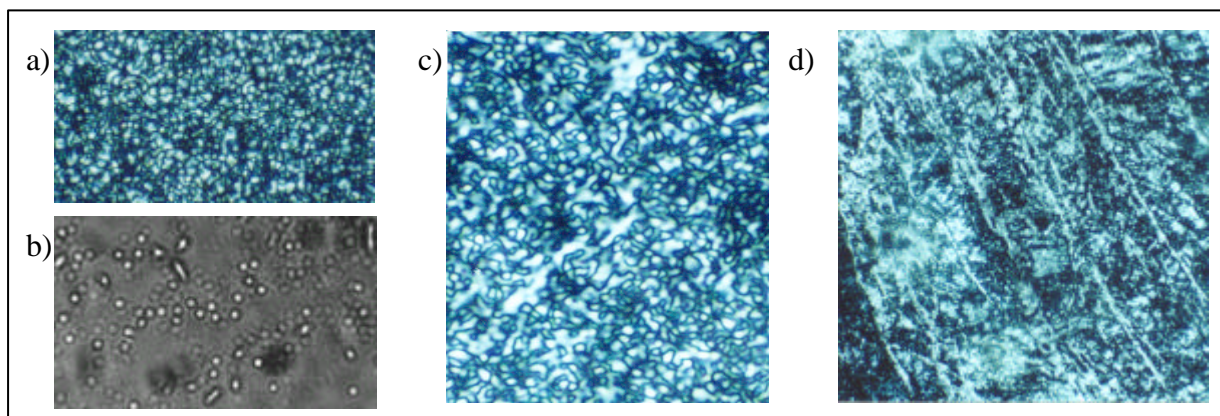


Figure 30. Observation d'un gel d'hydroxystéarate de cuivre/toluène (2% massique) en microscopie à polarisateurs croisés. a) système de départ (grossissement X 20), b) gouttes biréfringents observées à une température légèrement inférieure au point éclaircissant (grossissement x 40), c) systèmes après recuit (grossissement X 20), d) système de départ étiré entre lame et lamelle (grossissement X 20).

La première constatation observable sur le système de départ est une association de zones biréfringentes (fig. 30a). Ces zones biréfringentes ont un comportement thermotrope et sont associées à un point de clarification à 68°C. Au-dessous de ce point éclaircissant les premiers domaines biréfringents réapparaissent sous la forme de petites gouttelettes (fig. 30b). D'autre part, un recuit induit une augmentation de taille des domaines biréfringents (fig. 30c). Finalement, ce système peut être étiré entre lame et lamelle (fig. 30d). L'ensemble de ce comportement est analogue à certains cristaux liquides de caractéristique nématique.^[47] Nous avons également observé, sous loupe binoculaire entre polariseurs croisés, une augmentation de la biréfringence en compressant un gel entre deux lames de microscope à l'aide d'une spatule (figure 31).

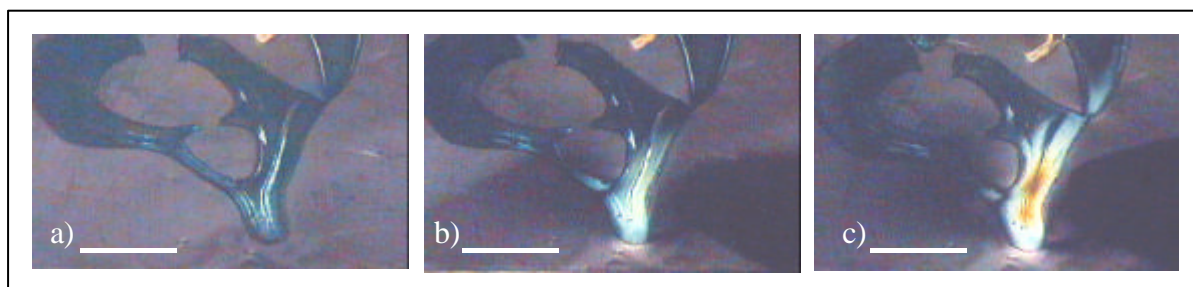


Figure 31. Observation d'un gel d'hydroxystéarate de cuivre/toluène (2,5% massique) sous loupe binoculaire à polariseurs croisés. a) sans pression, b) avec une légère pression inférieure au point éclaircissant, c) avec une pression forte. La barre correspond à 3 mm.

Cette expérience met en évidence une augmentation de la biréfringence, et donc une augmentation de l'agencement préférentiel des domaines sur une grande échelle de l'ordre du millimètre. D'autre part, après recuit et en se replaçant au dessous de la température du point éclaircissant, par trempe rapide jusqu'à température ambiante nous sommes parvenus à figer l'agencement des particules d'hydroxycarboxylate de cuivre (figure 32). Nous remarquons que les particules anisotropes sont alignées le long d'un axe préférentiel, comme le serait la répartition d'entités anisotropes dans un cristal liquide classique "nématique"^[46]

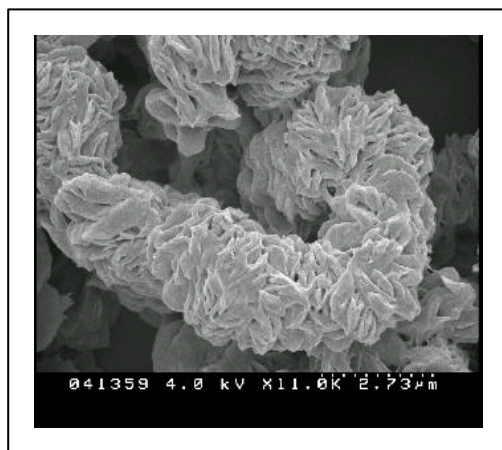


Figure 32. Agencement des particules d'hydroxystéarate de cuivre observées par MEB après recuit.

La phénoménologie décrite ci-dessus n'est pas associée à une augmentation de l'espace interlamellaire du composé d'hydroxystéarate de cuivre. De ce fait, ce comportement n'est pas dû à un gonflement des feuillets par diffusion de toluène. Un autre comportement intéressant est la formation de films translucides auto-supportés à partir de gels décrits précédemment, déposés goutte à goutte sur une feuille de Mylar et laissés sécher à l'air (Figure 33).

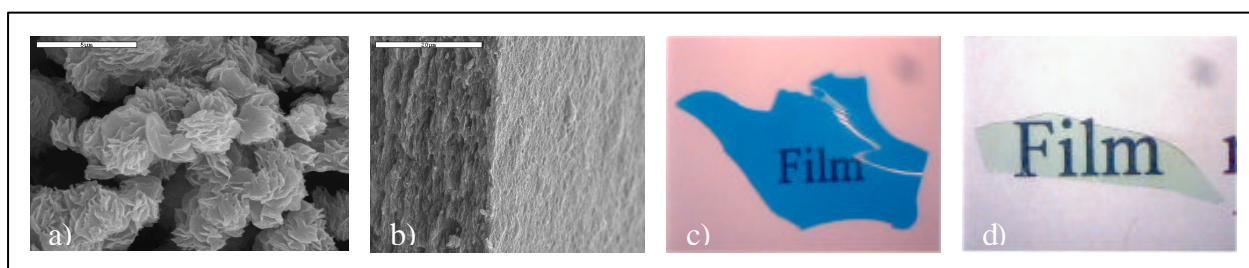


Figure 33. a) Particules d'hydroxystéarate de cuivre observées par MEB, b) arrête d'un film d'hydroxystéarate de cuivre observée par MEB montrant l'agencement préférentiel des particules, c) films d'hydroxystéarate de cuivre déposé sur une feuille de papier, d) films d'hydroxystéarate de nickel déposé sur une feuille de papier.

Ce comportement est récurrent pour un ensemble de composés, associés aux hydroxycarboxylate de cuivre.^[53b] Nous avons également essayé d'étendre cette phénoménologie à d'autres systèmes lamellaires, comme les pérovskites et hydroxydes doubles lamellaires (fig. 34). D'autre part sur un plan plus phénoménologique, la figure 29 met en évidence des systèmes biphasés correspondant à un équilibre entre un solvant et une dispersion. Ceci est une distinction par comparaison aux systèmes minéraux étudiés à l'heure actuelle, où est observé un équilibre biphasique entre une solution isotrope et une phase biréfringente.^[53a] Ceci implique l'existence d'une force attractive supplémentaire associée aux matériaux décrits dans ce document qui inhibe une transition de premier ordre "solution isotrope-phase biréfringente". Ceci pourrait être dû à une interaction hydrophobe entre les chaînes alkyles constitutives des composés. Cette hypothèse reste à vérifier. Ce travail est actuellement en cours d'étude par Eduardo E. Perez-Cordero dans le cadre de sa thèse dirigée par Daniel R. Talham. Les travaux concernant les hydroxydes doubles lamellaires ont été réalisés par Sarah Laine, dans le cadre de son "Master degree" co-encadré avec Daniel R. Talham et sont repris dans sa thèse qu'elle effectue au sein de la même équipe.

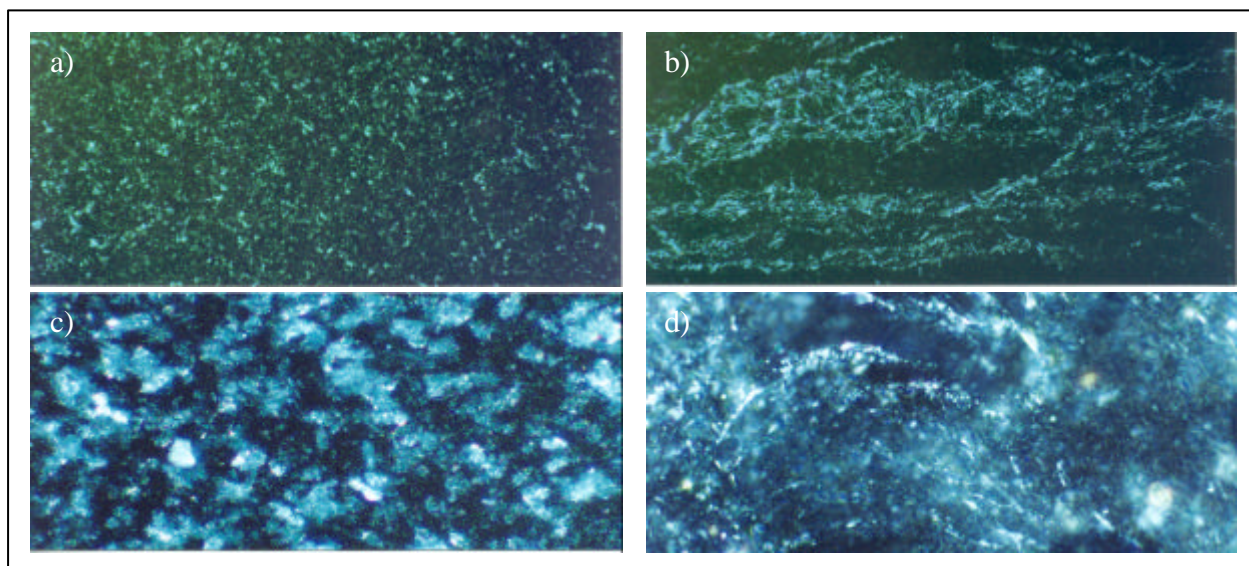


Figure 34. a) Images obtenus en microscopie entre polariseurs et analyseurs croisés (grossissement X20). a) Péroovskite $(C_6H_{13}NH_3)_2CuCl_4$, b) $(C_6H_{13}NH_3)_2CuCl_4$ après étirement entre lame et lamelle, c) HDL $Zn_{0.74}Cr_{0.26}(OH)_2(CH_3(CH_2)_{11}SO_4)_{0.29} \cdot 0.65 H_2O$, d) $Zn_{0.74}Cr_{0.26}(OH)_2(CH_3(CH_2)_{11}SO_4)_{0.29} \cdot 0.65 H_2O$ après étirement entre lame et lamelle.

IV- RECHERCHES ACTUELLES.

IV-1 BIOMIMÉTISME, BIOTECTONIQUE et BIOMINÉRALISATION.

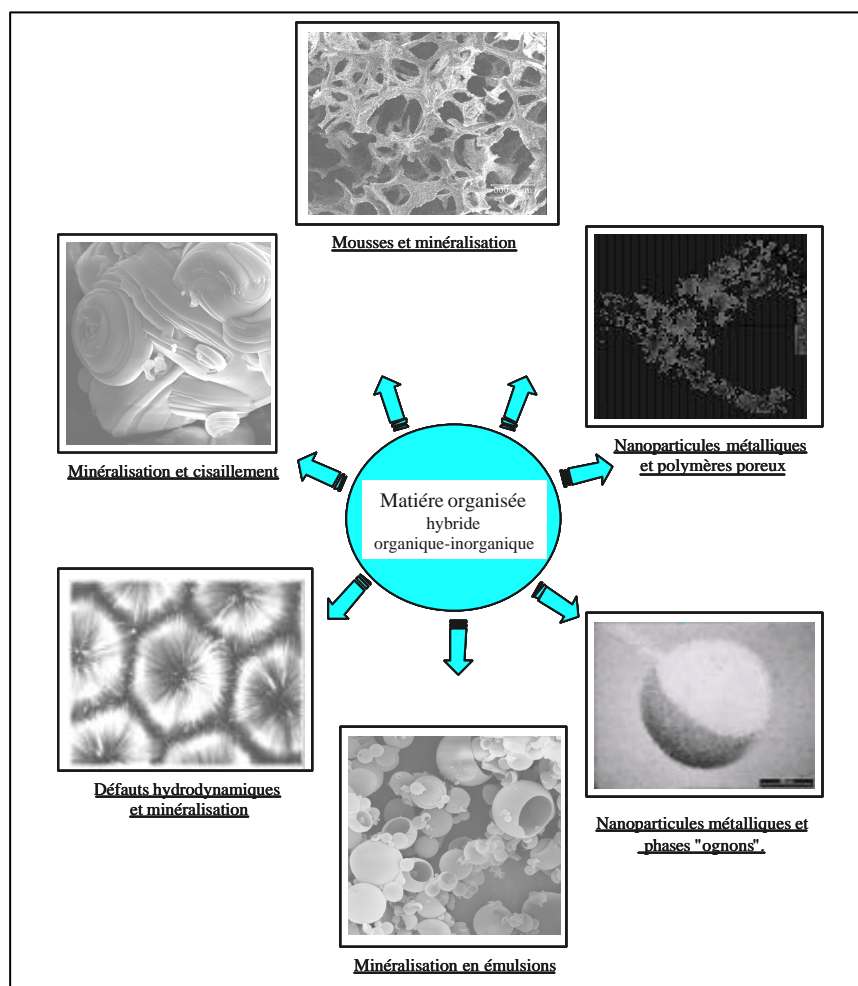


Figure 35. Illustrations des thèmes abordés au CRPP, articulés autour de la matière organisée hybride organique-inorganique.

La synthèse de matériaux inorganiques par utilisation de procédés de biominéralisation connaît aujourd'hui un essor considérable. Cette systématique s'inspire des processus de biominéralisation propres au "monde du vivant".^[5-7] Dans ces systèmes biologiques, l'association de solutions minérales sursaturées (ou de monomères minéraux polymérisables) et de surfaces organiques à caractère membranaire permet la réalisation de systèmes organo-minéraux hiérarchiquement structurés. Ces structurations et texturations impliquent une organisation étape par étape des matériaux, allant de l'échelle atomique à celle du macroscopique ; la structure de type abalone illustre parfaitement cette organisation. Un défi offert aux scientifiques est la réalisation en laboratoire de telles architectures par mimétisme des modèles de construction moléculaire que nous inspire le "monde du vivant". A travers ces diverses approches nous essayons de contrôler les structures, textures et morphologies (aux grandes échelles) des objets organiques-inorganiques réalisés au C.R.P.P.

A cette volonté de réaliser des biomatériaux "sur mesure" nous associons une approche plus fondamentale visant à identifier et expliciter les mécanismes associés à la morphogenèse de ces architectures. Dans ce cadre, des systèmes modèles sont utilisés comme par exemple les monocouches de Langmuir et monocouches auto-assemblées sur substrats.

Ces travaux de recherches sont menés au C.R.P.P. et reposent sur l'activité de thème

"biomimétisme, biotectonique et biominéralisation". Le Centre de Recherche Paul Pascal possède une solide expertise en réalisation et caractérisation de la matière molle (cristaux liquides, émulsions, mousses, et toutes autres structures de fluides complexes en règle générale). Répondant à une requête de son comité d'évaluation, le CRPP a créé une interface entre la matière molle et la chimie douce dans le but de développer de nouveaux thèmes de recherches où la matière molle servira d'empreinte à un composé inorganique en croissance. Ce nouveau thème de recherches, précédemment cité est effectif depuis septembre 2001, année de mon recrutement et est supporté par une jeune équipe polyvalente comprenant les personnalités suivantes : Philippe Poulin (Chargé de Recherches CNRS), Annie Colin (chargée de recherches CNRS), Sébastien Manneville (Chargé de Recherches CNRS), Chrystel Faure (Maître de conférences, Université Bordeaux I), Serge Ravaine (Maître de conférences, Université Bordeaux I), Olivier Mondain-Monval (Professeur, Université Bordeaux I), Cécile Zakri (Maître de conférences, Université Bordeaux I). Les centres d'intérêts développés en commun sont globalement représentés sur la Figure 35 et ont permis de réaliser, pour le moment, cinq brevets et 6 communications.

S'agissant de recherches actuelles certains de ces axes sont assez bien développés, d'autres le sont moyennement et certains ne le sont pas du tout, avec dans ce dernier cas, l'avantage d'y penser !

IV-1-a Morphogénèses minérales et fluides complexes

La mésostructuration de polymères inorganiques est un procédé extrêmement développé surtout depuis la découverte des MCM-41.^[54] Dans ce cadre, l'utilisation de systèmes moléculaires organisés est une approche versatile et attrayante car elle débouche sur un très bon contrôle des tailles de pores et de la répartition de ces derniers au sein du squelette minérale. Les applications de tels objets à porosité contrôlée sont considérables et on peut citer à titre d'exemple: catalyse^[55], extraction en phase solide et filtration^[56], électronique, optique, acoustique^[57-60] etc.

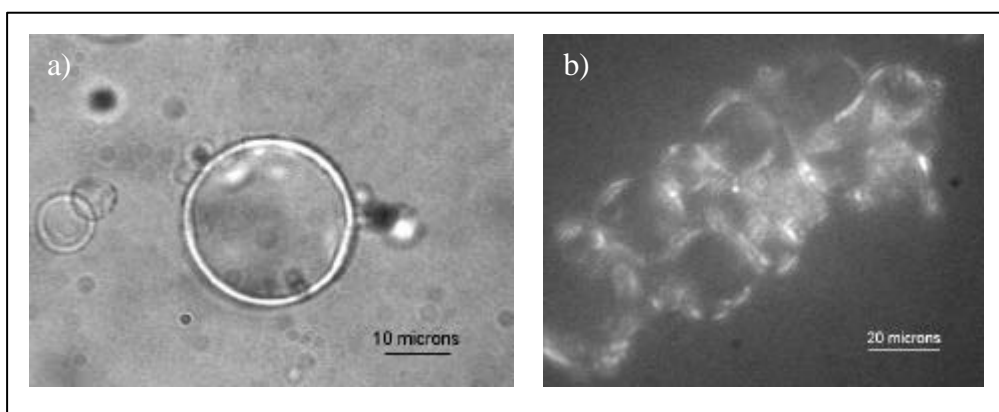


Figure 36. a) Photographie en microscopie optique d'une coque de silice obtenue en émulsion inverse, b) Photographie en microscopie optique entre polariseurs et analyseurs croisés de plusieurs capsules. La biréfringence des parois reflète une organisation régulière de la porosité du minéral.

Toutefois, il est nécessaire de pouvoir structurer et texturer les systèmes obtenus sur des échelles plus grandes (de l'ordre du micron à plusieurs dizaines de microns) pour espérer ajouter une spécificité à leurs applications (relargage contrôlé de produits pharmaceutiques ou décontamination en absorbant des hydrocarbures). Dans cette optique nous utilisons une interface eau-huile par le

biais d'une émulsion inverse (eau dans de l'huile). Une approche similaire a été proposée en 1996 par Schacht et al. [61] où les auteurs utilisent une émulsion directe (huile dans eau).

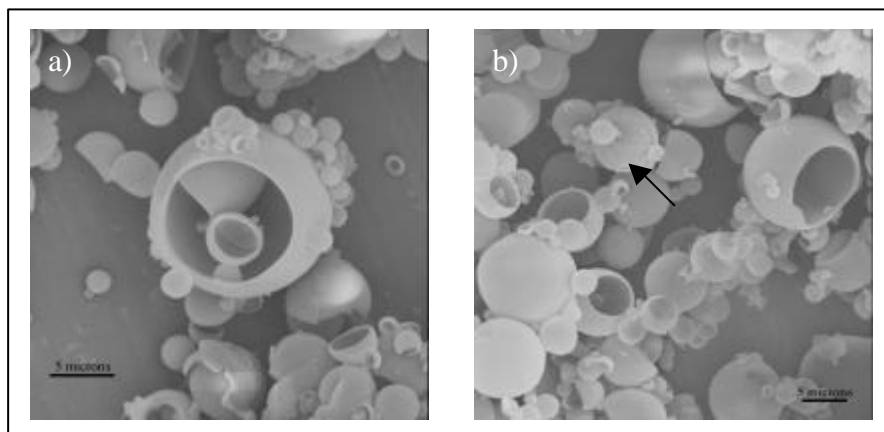


Figure 36a. Photographie en microscopie électronique à balayage de capsules minérales. Les échantillons sont mis sous vide pour l'observation. La mise sous vide et l'effet de charge électronique provoquent l'ouverture des coques (flèche de sur la figure b).

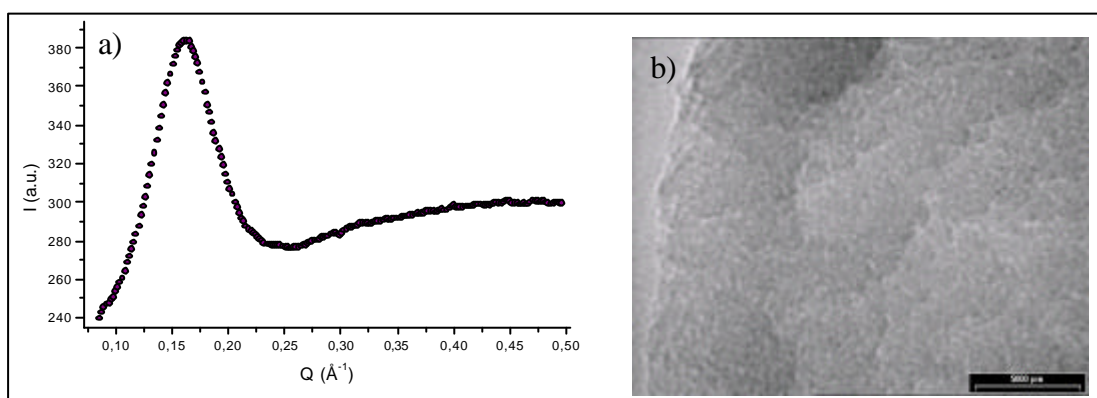


Figure 38. a) Diffractogramme de rayons X. La présence du pic reflète les corrélations spatiales entre les pores de la coque minérale. Nous pouvons déduire du vecteur d'onde correspondant au maximum d'intensité du pic de diffraction que la distance entre les pores est d'environ 4 nm. Aucun harmonique n'est observé, et ceci met en avant la caractère vermiculaire de la mésostructure, b) image de microscopie électronique à transmission.

Sur la figure 37 nous pouvons observer des objets sphériques et creux de diamètres compris entre 2 et 50 μm . La biréfringence des objets observés sur la figure 36 reflète une organisation de la mésostructure associée aux coques minérales. Cette organisation est confirmée par mesures de diffraction de rayons X (fig. 38-a). La mésostructure vermiculaire a été confirmée par microscopie électronique en transmission (fig. 38-b). Des études récentes de Giulia Fornasieri (stagiaire post-doctorale au CRPP), nous ont permis de corréler diamètres et épaisseurs des coques (figure 39).

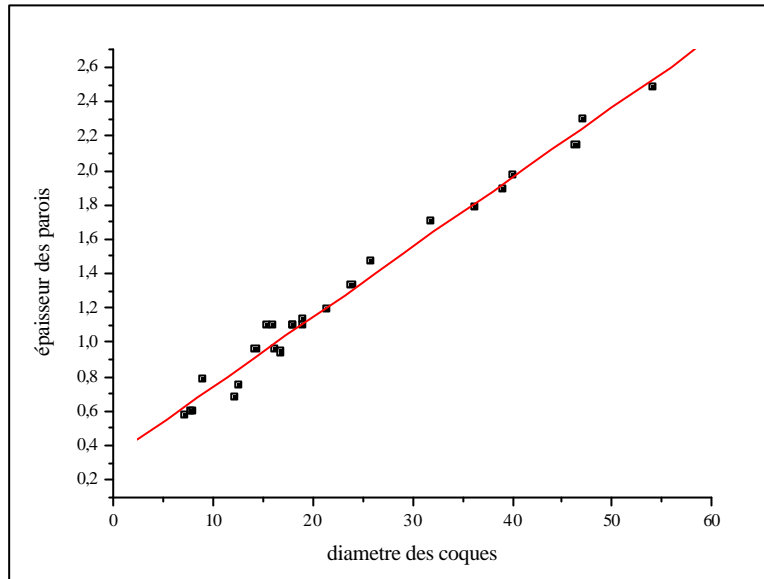


Figure 39. Relation entre diamètre des coques et épaisseurs des parois.

La relation linéaire décrite dans la figure ci-dessus est importante. En effet, dans le cas d'utilisation d'émulsions inverses monodisperses nous connaîtrions les corrélations existant entre tailles des gouttes utilisées et épaisseurs de parois associées aux objets formés *in fine*. Ces travaux sont en cours d'étude.

Egalement, nous sommes parvenus à transposer cette méthodologie à la réalisation de coque de TiO_2 , avec l'émergence d'une phase Anatase après traitement à 600°C .

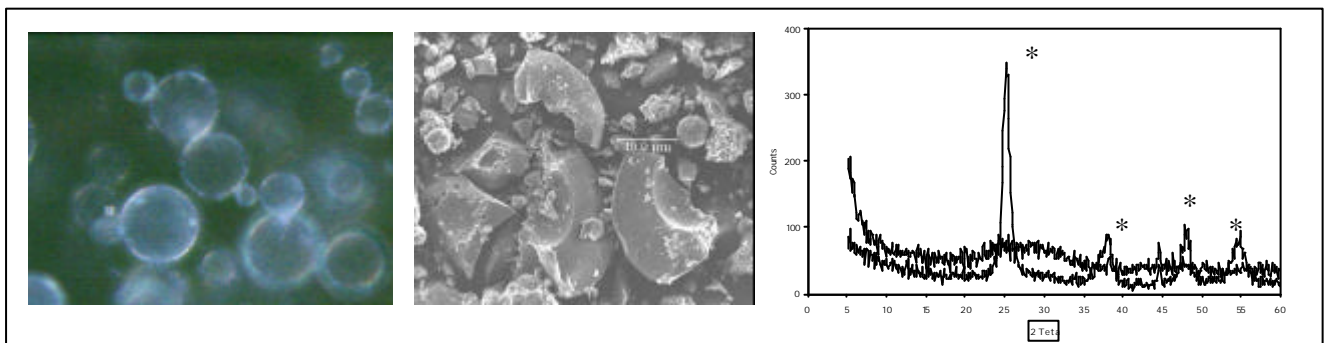


Figure 40. a) Coque de TiO_2 observée en microscopie optique sous polariseurs et analyseurs croisés b) coques de TiO_2 cassées observées par MEB, c) diffractogramme de RX avant et après traitement à 600°C (les raies caractéristique de la structure Anatase sont étoilées).

Des études sont en cours pour mieux contrôler la paroi des coquilles de TiO_2 en limitant l'hydrolyse du monomère utilisé par des effets chélatants. Nous nous focalisons également sur un meilleur contrôle de la mésostructure de ces coquilles de SiO_2 et TiO_2 . A terme, nous envisageons la réalisation de systèmes mixtes SiO_2 - TiO_2 .

IV-1-b Morphogenèses minérales sous cisaillement.

Des procédés de morphogenèses minérales sous cisaillement sont également étudiés au laboratoire. Dans cette approche un stress mécanique sous cellule de Couette se substitue à une

macrostructure organique ou à un procédé d'émulsification (système thermodynamique métastable). Dans ce contexte les matériaux hiérarchisés néoformés possèdent des morphologies anisotropes et exotiques. Cette approche mécanique de mise en forme aux grandes échelles ouvre de nouvelles voies de synthèse où la vitesse de cisaillement contrôle et dirige les processus de nucléation associés aux morphogénèses d'objets minéraux en croissance.

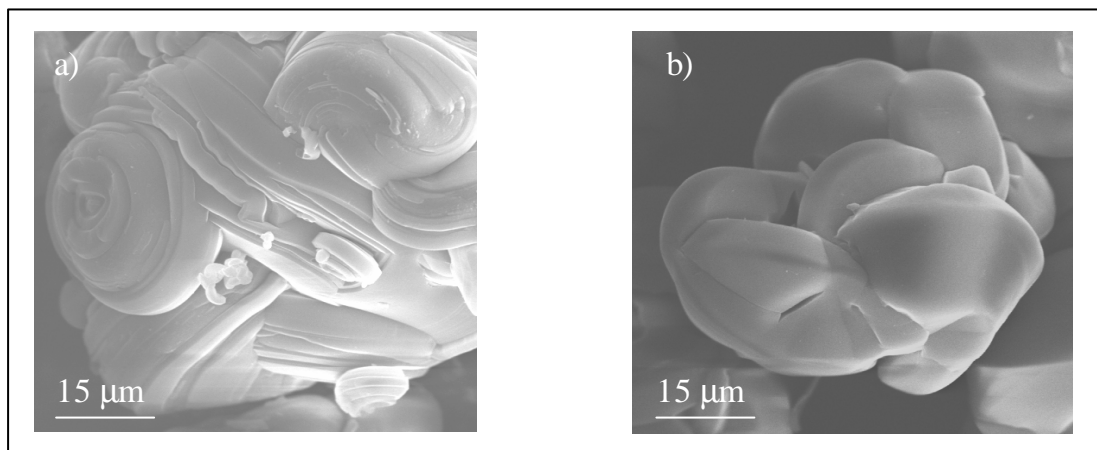


Figure 41. Mise en forme de silice mésoporeuse par cisaillement en cellule de Couette sous deux vitesses.

La mise en forme de matériaux minéraux en croissance peut être induite par l'effet d'empreinte d'un système moléculaire organisés (surfactants sous formes de micelles cylindriques, tubulaires, organisées en structures hexagonales, cubiques ou bien encore vermiculaires). La texturation aux grandes échelles émanant de cet effet "moulant" doit être forcément associée à un stress mécanique (induit par les structures caractéristiques du fluide réactionnel) extrinsèque au système hybride organique-inorganique en croissance. Le contrôle de la structure d'un fluide induite par l'agitation d'un barreau aimanté (fluide lamino-turbulent) est une tâche assez ardue. Les vitesses de cisaillement en cellule de Couette, peut être une manière élégante de contrôle de l'effet structurant d'un fluide sur un objet en croissance. Par exemple, sur la figure 41, nous pouvons constater que la morphologie, à grande échelle, d'un objet silicaté mésostructuré (présence de bromure de cétyltriméthylammonium) peut varier en passant d'un flux laminaire (figure 41-a) à un flux turbulent (figure 41-b). Ceci met d'ores et déjà en évidence le caractère coopératif existant entre l'effet texturant induit par la mésostructure et celui imposé par la structure du fluide réactionnel. Ces études viennent de commencer au CRPP et sont très prometteuses. A terme, différentes mésostructures (effet de chiralité, par exemple) seront associées à différentes structures de fluides (laminaires ou turbulents).

IV-1-c Minéralisation et mousses

Les mousses air-liquides sont des systèmes thermodynamiques et métastables dont la stabilité et les comportements rhéologiques sont étudiés au laboratoire depuis plusieurs années. A mon arrivée au CRPP, avec ma collègue Annie Colin, nous avons envisagé la minéralisation contrôlée de ces systèmes. Cette approche constitue actuellement la base du travail de thèse de Florent Carn.

Les mousses sont des systèmes thermodynamiquement métastables (coalescence d'Oswald et gravité détériorent leur texture) structurées par l'intermédiaire de bords de Plateau, nœuds et films. Ces mousses peuvent servir d'empreintes à un minérale en croissance. Des études ont commencé et ont permis d'obtenir toute une palette de morphologies en jouant simplement sur le pH des réactions sol-gel (figure 42).

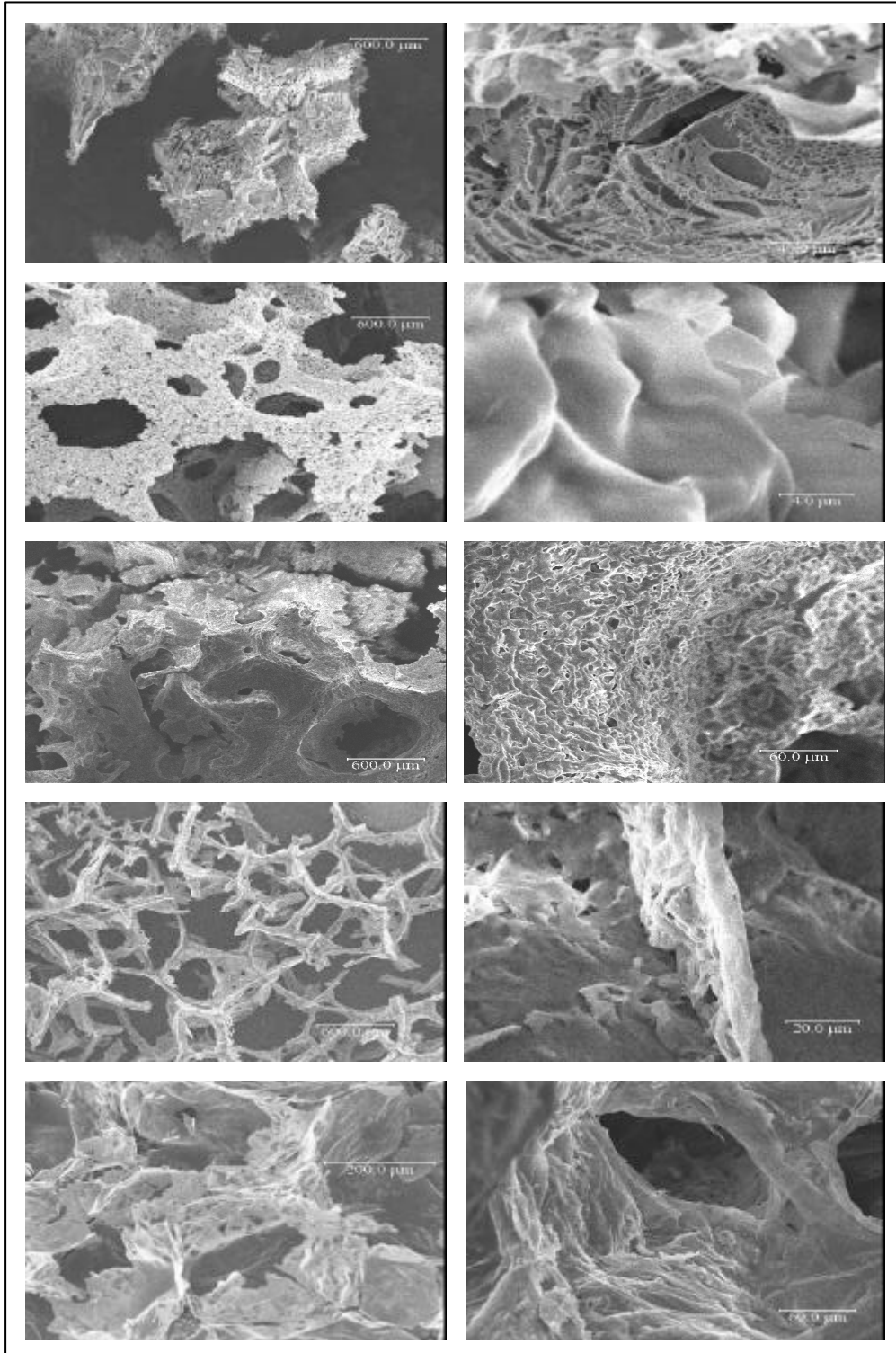


Figure 42. Mousses de silice obtenues sous différents pH réactionnels.

Nous pouvons donc constater qu'un contrôle des procédés de chimie sol-gel permet d'aboutir à des texturations contrôlées. Nous pouvons également minéraliser complètement bords de Plateau et films (figure 43).

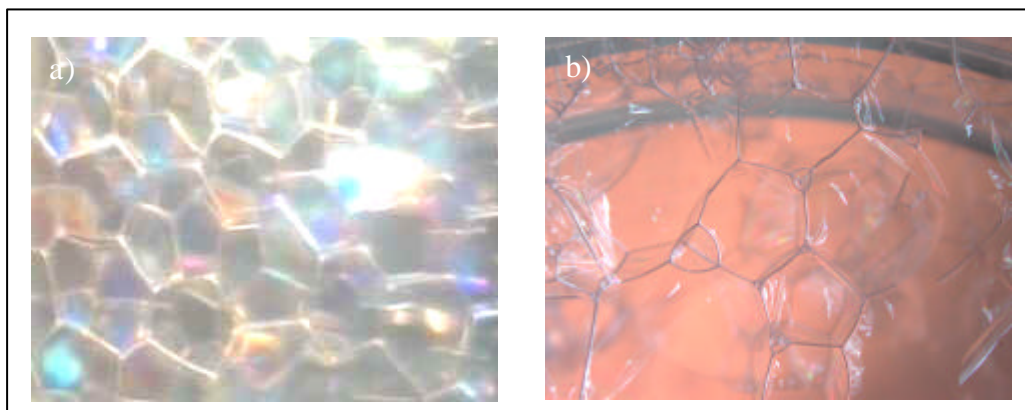


Figure 43. a) Mousse et b) mousse complètement minéralisée.

Le procédé de moussage utilisé permet également de contrôler le rapport de taille entre bords de plateaux et films. Ceci est développé à l'heure actuelle. La silice est un matériau inerte pouvant être utilisé comme substituant osseux. Dans ce contexte des études de bio-compatibilité sont prévues. A terme, nous nous tournerons également vers la minéralisation de mousses où l'hydroxyapatite sera utilisé comme support inorganique. Ces synthèses seront associées à des caractérisations des micro-, méso- et macrostructure. Les propriétés de porosité et de tenues mécaniques seront également envisagées.

IV-1-d Minéralisation et phases lamellaires

IV-1-d1- Minéralisation sur monocouches organiques

Dans un contexte de Biotectonique et biomimétisme, les monocouches de Langmuir apparaissent comme des modèles simples permettant de mimer les interfaces des membranes cellulaires (bicouches phospholipidiques). Au-delà de la volonté de réalisation de nouveaux matériaux, nous nous intéresserons à la compréhension des mécanismes intimes de nucléation et de croissance aux interfaces organiques-inorganiques. Un certain nombre de paramètres ont été identifiés :

- 1- Densité de charge anionique ou cationique à l'interface "monocouche/espèce en croissance".
- 2- Structure de la monocouche (la nucléation se résume-t-elle à une simple épitaxie?)
- 3- Fluidité des monocouches (la fluidité permet aux monocouches d'accommoder leurs paramètres de maille à ceux de l'espèce en croissance: commensurabilité)
- 4- Présence de défauts inhérents aux monocouches ou générés pendant le processus de nucléation.

A cette systématique permettant d'induire, d'appréhender et d'élucider les phénomènes de nucléation et de croissance aux interfaces, seront associées des études centrées sur des monocouches auto-assemblées sur substrat (SAMs). Dans ce cadre la fluidité est inhibée et seule la phénoménologie liée à l'épitaxie est exploitée.

IV-1-d2 Minéralisation en phases oignons

Les études de rhéophysique menées au CRPP ces dernières années ont permis la mise au point d'un procédé de préparation d'une phase de vésicules multilamellaires de tensioactifs et de lipides, baptisées "sphérulites" ou oignons.^[66] Dans cette optique les sphérulites peuvent jouer le rôle de microréacteurs chimiques dans lequel la réaction chimique est confinée. La possibilité de synthétiser des nanoparticules à l'intérieur de ces structures a été démontrée.^[67]

Dans ce cadre il s'agira d'étendre ces réalisations de matériaux hybrides organiques-inorganiques et d'y associer une caractérisation minutieuse permettant de mieux comprendre la spécificité des réactions aux interfaces. Dans ce contexte, par le biais d'un travail commun avec Chrystel Faure, les premières réalisations de nanoparticules d'or au sein de structures oignons ont été réalisées.

Globalement trois formulations à base de dipalmitoylphosphatidylcholine (DPPC)-simulsol, (DPPC)-monooléine et génamine. Les résultats obtenus sont résumés dans les lignes suivantes. Dans les trois cas, on hydrate les tensioactifs avec une masse identique d'une solution à 10^{-3} M de tétrachloro-orate(III) de potassium KAuCl_4 , afin que le complexe $[\text{AuCl}_4]^-$ soit présent dans la phase lamellaire. Dans une seconde étape, la phase lamellaire est cisailée manuellement donnant alors des "oignons". Ce principe de formation "d'oignons" par cisaillement d'une phase lamellaire lyotrope est très bien explicité dans la littérature et sera pas explicité dans ce document.^[62]

Dans le cas du système à base de phosphatidylcholine et de simulsol, l'insertion du complexe entraîne une augmentation de la distance entre bicouches lipidiques de 10\AA , le pas smectique passant de 55\AA à 66\AA comme le montrent des expériences de diffraction de rayons X aux petits angles. Le changement de couleur intervient également lorsque l'on disperse les oignons après cisaillement de la phase lamellaire dans une solution de KAuCl_4 à 10^{-3}M (figure 44). Notons, par ailleurs, que nous avons vérifié par microscopie à contraste de phase que les oignons sont intacts dans la dispersion et que, de ce fait la structure en vésicules multilamellaires n'est pas altérée par la formation des nano-objets.

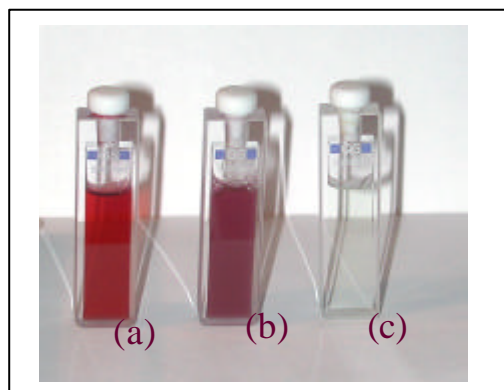


Figure 44. Cellules de quartz où les oignons ont été dispersés dans une solution de $\text{K}^+\text{AuCl}_4^-$ (10^{-3}M): a) Génamine + $\text{K}^+\text{AuCl}_4^-$ deux heures après dispersion b) DPPC + $\text{K}^+\text{AuCl}_4^-$ deux heures après dispersion, C) DPPC + $\text{K}^+\text{AuCl}_4^-$ juste après dispersion.

Cette coloration rouge-rubis, observée dans les trois formulations testées, est caractéristique de nanoparticules d'or et est associée à une bande plasmon se situant à 530 nm en UV-visible.^[63] De plus nous n'observons aucune absorption vers 650 nm en spectroscopie électronique (figure 45). L'absence de cette

absorption apporte deux informations importantes : les nanoparticules confinées dans la matrice organique ne sont pas agrégées, ^[64,63] les nano-objets synthétisés ont une faible anisotropie de forme. ^[63]

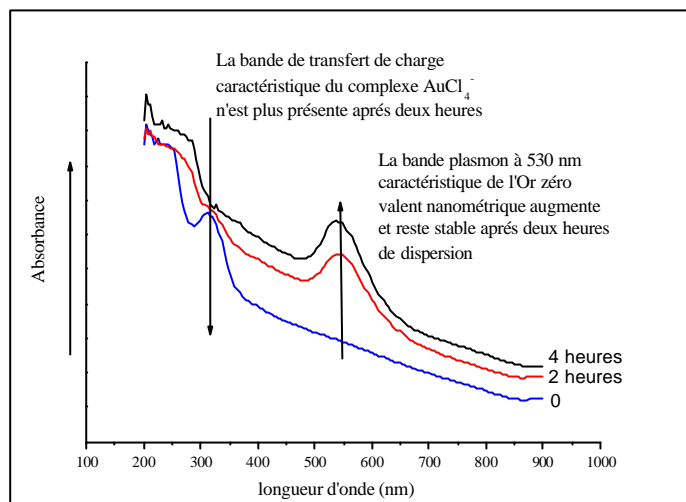


Figure 45 : Evolution des spectres d'UV visible d'une dispersion d'onions ($\text{PC}/\text{AuCl}_4^-$) dans AuCl_4^- (10^{-3}M) en fonction du temps. A $t=0$ la dispersion est achevée.

Ces spectres d'UV-visible mettent en évidence une diminution de la bande de transfert de charge associé à la consommation du complexe AuCl_4^- et l'augmentation d'une bande plasmon centrée à 530 nm caractéristique de la formation de nanoparticules d'or au degré d'oxydation zéro. ^[63] Le potentiel rédox du couple $\text{Au}^{\text{III}}/\text{Au}^0$ est très élevé. De ce fait, la réduction sans catalyse par rayonnement UV pourrait être induit par oxydation d'une fonction alcool en une fonction acide. ^[64], mais aucune vibration caractéristique d'une fonction acide n'a été détectée par spectroscopie infrarouge. Une autre explication pourrait être une diminution du potentiel rédox du couple $\text{Au}^{\text{III}}/\text{Au}^0$ par coordination bidentate des ions $\text{Au}^{\text{(III)}}$ par les groupements hydroxyles. ^[65] Il a été ainsi démontré que la réaction d'oxydo-réduction pouvait être possible dans ces conditions.

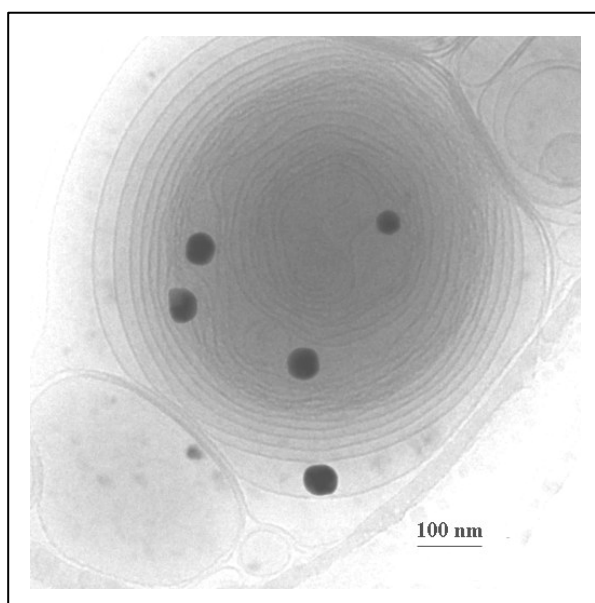


Figure 46. Image du système hybride organique-inorganique obtenu par cryo-TEM.

Le caractère métallique des nano-objets synthétisés est démontré directement par XPS. La valeur des bandes d'émission X des énergies associées aux électrons $4f_{5/2}$ et $4f_{7/2}$ respectivement à 87.9 eV et 84.1 eV est caractéristique de la présence d'or métallique.^[63-65] Ces pics ne sont pas dédoublés et donc il n'y a pas d'oxydes co-formés ou de complexes non consommés associés aux matériaux finals hybrides organiques-inorganiques. Par ailleurs, nous devons souligner que ces pics ont été obtenus après qu'un décapage (quelques Angström) de l'échantillon a été effectué : ceci confirme que la majorité des nanoparticules sont confinées dans la phase organique. Ce confinement présumé a été confirmé par la technique de cryo-TEM (figure 46).

Dans le but d'améliorer les propriétés de confinement et de mise en forme, les compositions seront modifiées avec l'adjonction de molécules amphiphiles à caractère amine ou thio. Egalement, la formation de nanoparticules métalliques au sein de structures oignons constituent une première étape. Nous souhaiterions, à terme nous tourner vers la réalisation *in situ* de nanoparticules magnétiques (ferrites, maghémites). La minéralisation de ces phases structurantes est également envisagée par utilisation de silicates.

IV-1-e Systèmes poreux et réactivité

Ce thème de recherche a été amorcé en 1998 via une collaboration entre Olivier Mondain-Monval et Hervé Deleuze (LCOO-Université Bordeaux-I). Cette double compétence "matière molle (émulsions) et chimie organique" a permis la réalisation de monolithes poreux organo-fonctionnalisés.^[68] Lors de mon arrivée, nous avons décidé d'utiliser de tels supports et d'y associer des procédés de nucléations hétérogènes induisant une nanofonctionnalisation inorganique ou métallique. Ce travail s'inscrit dans la thèse d'Alexandre Desforges co-encadrée par Olivier Mondain-Monval et moi-même.

Dans nos études, nous utilisons pour le moment des monomères polymérisables comme le divinylbenzène, le styrène ou bien encore toutes associations des deux. Pour améliorer la porosité de cette gamme de matériaux nous pouvons utiliser des entités porogènes, permettant d'établir une sous-porosité intra-parois (Figure 47).

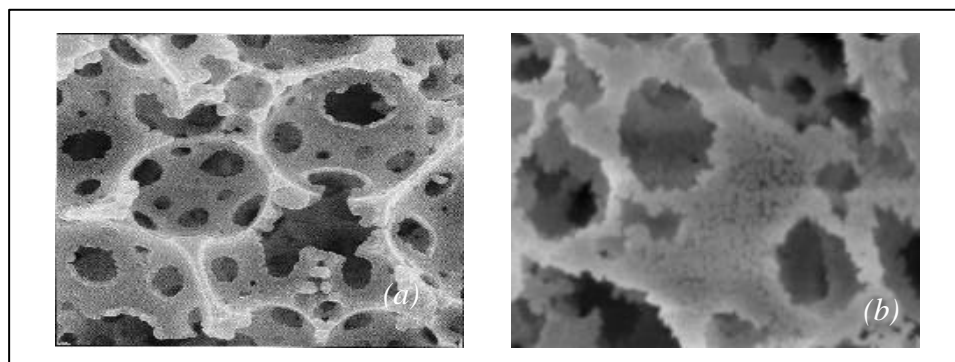


Figure 47. Photo de microscopie électronique à balayage (a) macro-structure poreuse, (b) sous-structure poreuse de parois.

Dans une seconde étape, nous utilisons ces matrices organiques poreuses comme substrats de nucléation hétérogène, *via* des synthèses *in-situ*, d'entités inorganiques. Dans une première étude, nous nous sommes intéressés à la formation de nanoparticules métalliques. Ces synthèses sont réalisées en utilisant des solutions (aqueuses ou non) de sels de complexes de métaux de transition (KAuCl_4 , K_2PtCl_4 , K_2PdCl_4 , etc.) à différentes concentrations. La réduction des ions transitionnels est assurée par la présence de radicaux mis en évidence par RPE (ΔH_{pp} d'une dizaine de Gauss typiquement). Ces réductions sont également catalysées par traitement UV. La valence nulle des nano-objets synthétisés est mise en évidence par XPS et est couplée par diffraction de RX en transmission.

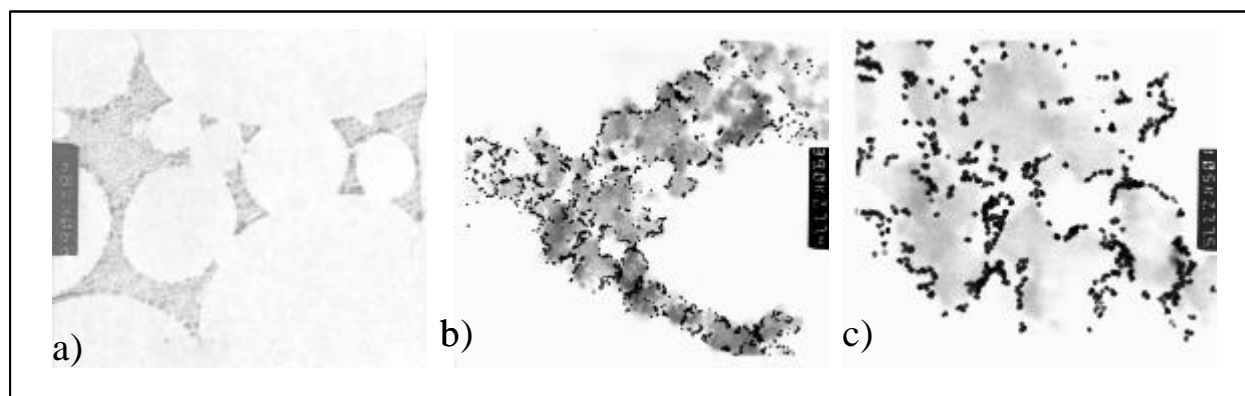


Figure 48. Clichés MET a) d'un polyHIPE sans porogène à un grossissement *9000, b) d'un système hybride organique-métallique (Pd) à un grossissement *40000, c) d'un système hybride organique-métallique (Pd) à un grossissement *100000

Sur la figure 48, nous pouvons constater la taille nanométrique des objets générés au sein de la matrice d'accueil organique, également nous pouvons constater que la réduction est dirigée à l'interface polymère-solution. En fonction des concentrations de sels d'ions complexes utilisés, nous sommes parvenus à contrôler la taille des nano-objets ainsi élaborés, deux histogrammes sont proposés sur la figure 49.

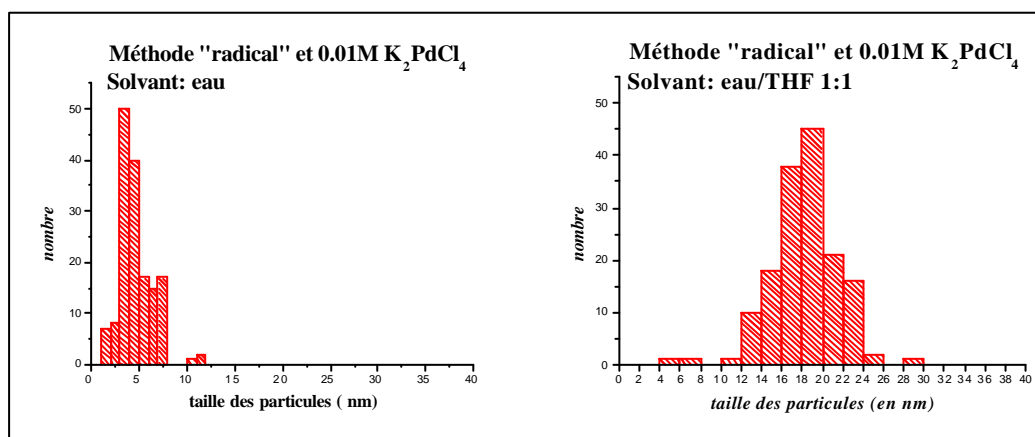


Figure 49. Histogrammes des tailles caractéristiques des nano-objets synthétisés en fonction des conditions de synthèse utilisés.

Nous avons donc réalisé des structures hybrides permettant de réaliser des réactions de catalyse hétérogène. En prenant une réaction de catalyse type (hydrogénation d'un alcène en alcane) nous avons comparé l'activité catalytique des objets hybrides synthétisés à celle d'un système

extrêmement employé en catalyse supportée (Pd/charbon). Nous pouvons constater que l'activité catalytique des matériaux présentés dans ce document est supérieure au système Pd/charbon (figure 50).

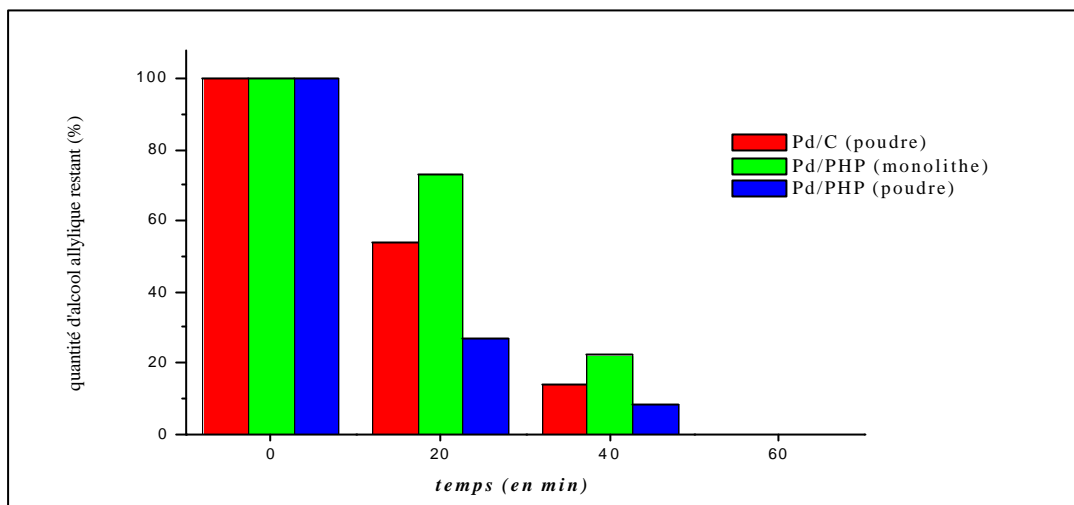


Figure 50. Activité catalytique de deux systèmes utilisés et comparés au système Pd/charbon.

D'autre part le système Pd/charbon dont la texture est une poudre très fine, ne permet pas la réalisation de catalyse cyclique. En effet, la poudre de Pd/charbon est très fine et s'agrège dans l'étape de séparation entre catalyseur et produit de catalyse. Les systèmes développés en ce moment, se présentant sous forme de monolithes, offrent la possibilité d'une ségrégation aisée où la texture du catalyseur n'est pas dénaturée dans l'étape de séparation ou filtration. Des réactions de catalyses cycliques peuvent donc être envisagées, comme l'indique la figure 51.

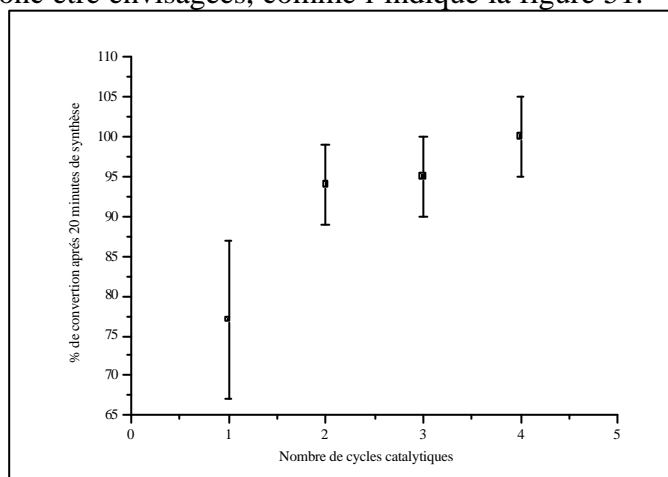


Figure 51. Catalyse supportée cyclique pour le système Pd/PHP (monolithe)

Nous constatons sur la figure 51, que le pourcentage de conversion ne diminue pas même après quatre cycles catalytiques. Nous observons même une légère augmentation de cette activité, très certainement lié à une meilleure imprégnation du solvant utilisé (et donc de l'espèce catalysée) avec le nombre de cycles imposés.

A terme, nos efforts seront centrés sur la spécificité des réactivités aux interfaces. Les surfaces des matrices organiques pourront être modifiées par des groupements, amino, thio, pour induire une stabilisation accrue des nano-objets néoformés. Egalement en fonction des temps d'irradiation UV et des concentrations de sels utilisés, nous aimerions élaborer des films métalliques

recouvrant toute la surface interne du polymère poreux. Nous envisageons l'utilisation de polymères biocompatibles en y associant des synthèses minérales de carbonate de calcium ou bien encore d'hydroxy-apatite.

V- PERSPECTIVES GLOBALES

Dans le cadre des recherches en cours et énoncées précédemment la première des perspectives, qui paraîtra raisonnable, sera de poursuivre les travaux commencés en se focalisant sur cette chimie des formes associant chimie douce et matière molle. Un aspect nouveau sera d'associer minéralisation et instabilités hydrodynamiques. En effet, Il existe dans la nature différentes façons d'organiser la matière. Les instabilités hydrodynamiques structurent l'espace d'un fluide. Lorsque l'on soumet un fluide à un gradient de température inversé, c'est à dire lorsqu'on chauffe le bas du fluide et que l'on refroidit sa partie haute, une instabilité de convection apparaît. Des rouleaux apparaissent dans le fluide. La taille de ces rouleaux est de l'ordre de grandeur de l'épaisseur du fluide.

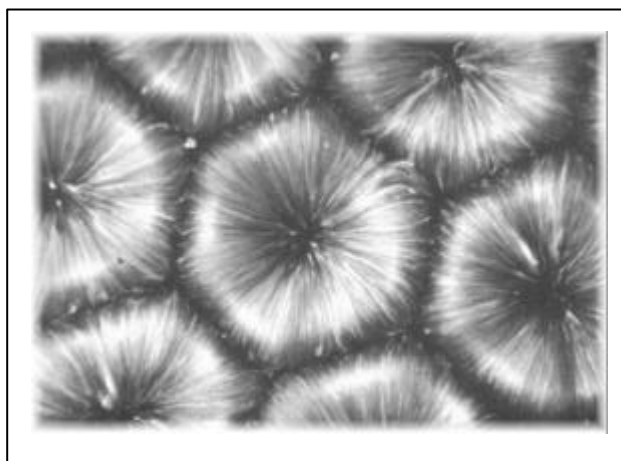


Figure 52. Exemple de défauts hydrodynamique de type Rayleigh-Bénard.

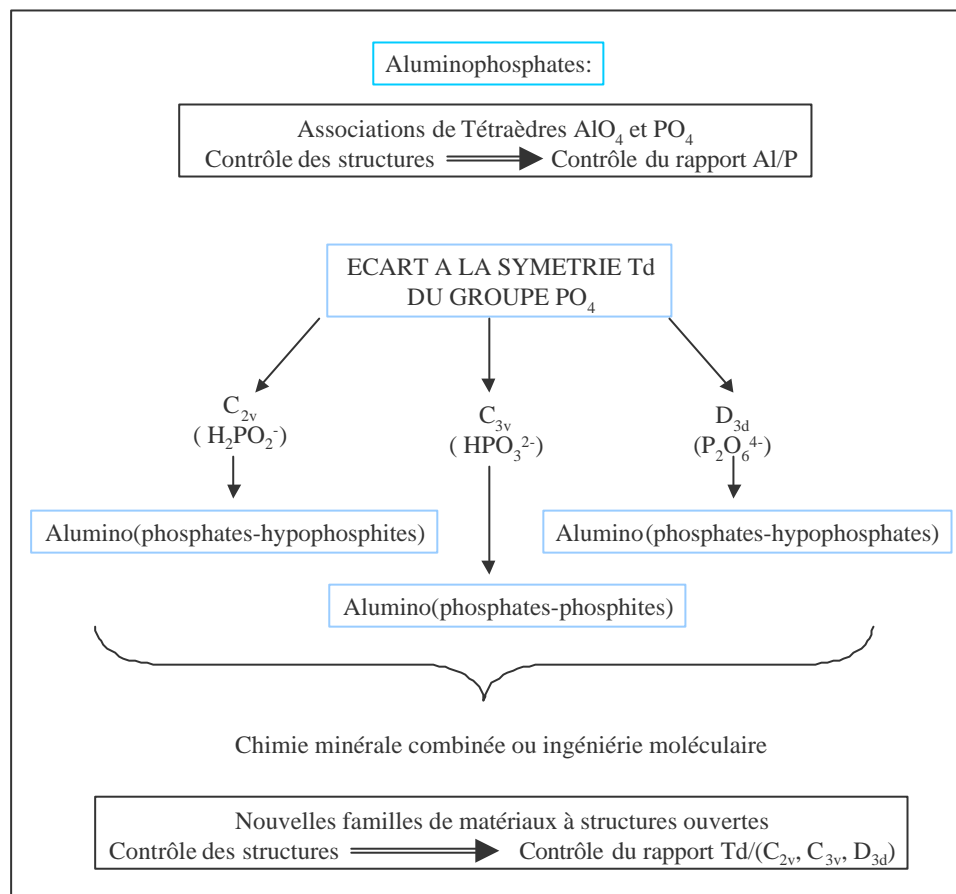
Nous souhaitons réaliser des réactions sol-gel dans ces écoulements, de façon à induire de nouvelles structures et textures, exotiques et contrôlées.

L'ensemble des études de morphogenèse associant chimie douce et matière molle mettent en avant, pour le moment, un seul type de polymère inorganique, la silice en l'occurrence. Ce choix est dicté par des processus d'hydrolyse-condensation très bien documentés et faciles d'application au laboratoire. A terme, nous nous tournerons également vers des morphosynthèses de polymères inorganiques complètement nouveaux. Dans une première approche nous essaierons de développer de nouvelles connectivités des polyèdres de base dans la familles des aluminophosphate. Les mécanismes impliqués dans la g n se des aluminophosphates sont encore mal explicit s, ceci  tant d    une cin tique de condensation assez rapide qui ne permet pas de s quencer ais ment les diff rentes  tapes condensation-hydrolyse associ es aux divers processus de croissance cristalline. N anmoins, la communaut  scientifique impliqu e dans cet art particulier de la chimie du solide s'efforce de comprendre et de rationaliser les processus r actionnels. Cette d marche  tant r alis e par le biais de synth ses en milieux quasi non-aqueux qui permettent de diminuer les cin tiques de condensation, tout en r alisant par ailleurs de nouveaux mat riaux. Cette conceptualisation des m canismes r actionnels est d duite   partir d' tudes minutieuses mettant en jeu des techniques de caract risation comme la diffraction de rayons X, la RMN (CP-MAS ou non) du ^{31}P , ^{27}Al , ^{13}C et toutes autres m thodes spectroscopiques (IRTF-Raman).

La microstructure min rale de ces aluminophosphates est compos e d'architectures anioniques (structures ouvertes). Ces structures poss dent notamment les compositions suivantes: $[\text{Al}_3\text{P}_4\text{O}_{16}]^{3-}$, $[\text{Al}_2\text{P}_3\text{O}_{12}\text{H}_x]^{(3-x)}$, $[\text{Al}(\text{HPO}_4)_2(\text{H}_2\text{O})_2]$, $[\text{AlP}_5\text{O}_{20}\text{H}]^{2-}$ et sont, dans la plupart des cas, constitu es par l'association de t tra dres PO_4 et AlO_4 . D'autre part, la balance d' lectronneutralit  est

obtenue en utilisant des espèces cationiques: alcalino-terreux, métaux transitionnels, ions ammoniums et surfactants cationiques.. Dans cette optique, nous nous attacherons à la réalisation de nouvelles architectures minérales. Cette approche sera centrée sur une substitution méthodique de l'ion phosphate en vue de se soustraire à l'influence de la symétrie T_d du groupe PO_4 dans les réactions de condensation. Cette systématique est explicitée avec le schéma 1.

Schéma 1. Différents écarts à la symétrie T_d du groupe PO_4 .



Comme l'indique ce schéma, d'autres motifs phosphates associés à différents groupes ponctuels pourraient être utilisés. Nous proposons par exemple de travailler avec l'ion phosphite (HPO_3^{2-} , C_{3v}), l'ion hypophosphite ($H_2PO_2^-$, C_{2v}), ou des dimères (sans pont oxo) comme l'ion hypophosphate ($P_2O_6^{4-}$, D_{3d}). Les différentes symétries associées à ces motifs de base devraient permettre de synthétiser de nouveaux matériaux, aluminophosphites, aluminohypophosphites, aluminohypophosphates. Lesdits motifs de base pourront réorienter les réactions de condensation, générant ainsi de nouveaux types de connectivités. Pour optimiser les propriétés de tel ou tel matériau, ces différents motifs pourraient être associés à travers de nouvelles synthèses minérales combinées. Dans le même ordre d'idée, certaines équipes de recherche ont commencé de nouvelles synthèses en substituant le groupe phosphonate au groupe phosphate.

Ces travaux demeurent "exotiques" comparés à la masse de ceux réalisés avec les aluminophosphates conventionnels. Ces concepts de chimie minérale combinatoire pourraient être étendus à la classe des aluminosilicates (cf. schéma 2).

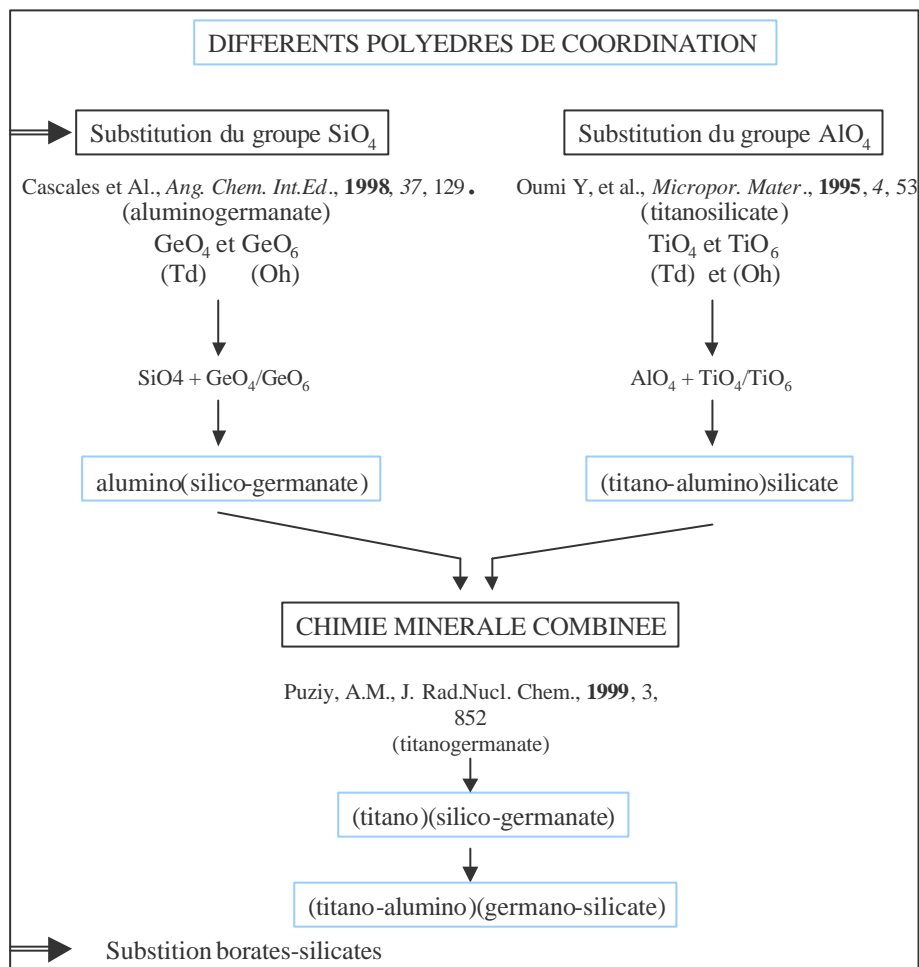


Schéma 2. Différents polyèdres de coordination.

Au-delà, il serait souhaitable de pouvoir intégrer une chimie un peu plus informée. En effet, avec les recherches décrites dans cette synthèse d'activité, les entités organiques impliquées, au niveau soit de la mésostructure soit de la macrostructure, n'apportent qu'un effet d'empreinte et sont sacrifiées par lavages ou calcinations ultérieures. Le premier outil vers lequel nous pourrions nous diriger serait d'utiliser des assemblages moléculaires apportant à la fois une aptitude à diriger les processus de morphosynthèse d'un squelette inorganique et une spécificité de propriété comme par exemple la reconnaissance moléculaire. Dans cet objectif, on reconnaîtra l'apport de la chimie supramoléculaire. Dans cette approche, structuration et information sont apportées aux composés de manière concomitante. Dans une autre approche, le procédé de mise en forme et l'apport d'une propriété pourront être non simultanés. A titre d'exemple, nous souhaiterions modifier les surfaces internes des matériaux macroporeux (mousses et HIPE organiques ou inorganiques) avec l'objectif de les rendre biocompatibles en utilisant des procédés de nucléation hétérogène d'hydroxyapatite (ceci mené en parallèle aux études sur monocouches de Langmuir et monocouches auto-assemblées sur substrats). A terme, nous aimerions appliquer à ces matériaux des tests de résistance mécanique, de cytotoxicité et de développements cellulaires dans un premier temps en nous efforçant d'optimiser ces caractéristiques au cours d'études ultérieures.

Toujours dans cette volonté d'associer une spécificité de propriété à un matériau à structure hiérarchisée nous pourrons faire appel à des procédés de nano-structuration, ce qui par ailleurs, a déjà commencé à être abordé avec les structures oignons et HIPE organiques.

A une autre échelle, et sans vouloir trop spéculer, nano-structuration et chimie supramoléculaire pourront être couplées pour essayer d'atteindre une synergie de propriétés d'où pourront émaner des processus de réponses à un stimulus externe, des procédés d'auto-réparations ou toute autre propriété collective. Dans ce cadre, les systèmes réalisés deviendront de plus en plus complexes où cette notion de complexité s'exprime comme le produit d'une multiplicité de propriétés, de procédés d'interactions et d'une capacité d'intégration. Dès lors, nous pouvons déceler l'interface grandissante et nécessaire entre physiques, chimie et biologie, interface vers laquelle nous aimerions converger.

Les activités de recherches citées dans les parties "Recherches actuelles" et "perspectives globales" de ce document sont couplées à des démarches extra-CRPP dans le but à la fois de valider, mais également de confronter et d'optimiser nos approches de recherches sur la mise en formes de matériaux hybrides organiques-inorganiques.

- Participation à une proposition d'ACI blanche jeunes chercheurs.2003 (dossier 4001-première évaluation positive): Modèles biomimétiques pour l'élaboration de matériaux à structures hiérarchisées. (*Coordinateur CRPP: R. Backov*)

- Participation à une proposition de thématique dans le cadre du réseau d'excellence Européen (PCRDT- 6): matériaux hybrides organiques-inorganiques et biomatériaux. Direction nationale : Clément Sanchez. (*Coordinateur CRPP : R. Backov*). *Proposition acceptée.*

VI- REMERCIEMENTS ET CONCLUSION

Nous avons abordé un ensemble de thématiques articulées autour de la matière organisée hybride organique-inorganique (figures 1 et 35). Chaque thème de recherche, brièvement décrits dans ce document, demande une spécificité des compétences, associée à la qualité nécessaire permettant d'envisager la phase de "diffusion scientifique". Ceci n'aurait jamais pu être réalisé sans de multiples collaborations. Je remercie donc l'ensemble des personnalités scientifiques associées à ces recherches, pour bien avoir accepté de partager leurs compétences, pour avoir consacré le temps nécessaire à la réalisation de ces travaux et au-delà je les remercie de la générosité qu'ils ont toujours mis en avant dans ces relations d'échanges et de partages des connaissances scientifiques.

A ce stade je tiens particulièrement à remercier *Frédéric Nallet*, professeur à l'Université Bordeaux I, pour avoir relu ce document et en avoir très certainement optimisé la qualité d'écriture.

Les thèmes de recherche associés aux hybrides organiques-inorganiques me placent dans une situation d'apprentissage permanent. De ce fait, mes connaissances actuelles, en cours de maturation, ne m'autorisent pas à tirer de grandes conclusions sur ces travaux, qui par essence ne sont qu'un début. Néanmoins, je me permettrai de terminer cet écrit sur des mots empruntés, traduisant tout de même un certain état d'esprit.

"Les hybrides permettent de créer et d'optimiser de nouveaux matériaux multifonctionnels.

Un optimiste peut se tromper, mais le plus souvent c'est lui qui a raison".

SANCHEZ Clément, Paris VI

VII- LISTE DE PUBLICATIONS CHOISIES

Dans le but d'illustrer la polyvalence des thèmes abordés, sept articles sont proposés. Ces documents s'articulent autour de la chimie des matériaux hybrides organiques-inorganiques, de la matière molle et des spécificités de réactivités aux interfaces organo-minérales, de la physique et enfin de la médecine (domaine de la néphrologie).

- 01-** Presence of lipids in urine, crystals and stones: Implication for the formation of kidney stones.
S. R. Khan, P. A. Glenton, **R. Backov** and D. R. Talham.
Kidney International **2002**, 62, 2062.
- 02-** Layered mixed-metal phenylphosphonates, $\text{Co}_x\text{Mn}_{1-x}(\text{O}_3\text{PC}_6\text{H}_5)\cdot\text{H}_2\text{O}$: Structure and magnetic properties.
J. T. Culp, G. E. Fanucci, B. C. Watson, **R. Backov**, H. Ohnuki, M. W. Meisel, D. R. Talham
J. Solid State Mat. **2001**, 159, 362.
- 03-** The magnetic spin ladder $(\text{C}_5\text{H}_{12}\text{N}_2)_2\text{CuBr}_4$: high field magnetization and scaling near quantum criticality.

B. C. Watson, V. N. Koto, M. W. Meisel, D. W. Hall, G. E. Granroth, W. T. Montfrooij, S. E. Nagler, D. A. Jensen, **R. Backov**, M. A. Petruska, G. E. Fanucci, D. R. Talham. *Phys. Rev. Letter* **2001**, *86*, 5168.

04- Multiple bilayer dipalmitoylphosphatidylserine (DPPS) LB films stabilized with transition metals ions.

G. E. Fanucci, **R. Backov**, R. Fu, D. R. Talham. *Langmuir* **2001**, *17*, 1660.

05- Calcium oxalate monohydrate precipitation at phosphatidylglycerol Langmuir monolayers.

R. Backov, C. M. Lee, S. R. Khan, C. Mingotaud, G. E. Fanucci, D. R. Talham. *Langmuir* **2000**, *16*, 6013.

06- Evidence of confinement of fullerene C₆₀ in microporous zeolite.

A. Lamrate, J. M. Jannot, A. Elmidaoui, **R. Backov**, J. Rozière, L. C. de Ménorval, J. L. B. Sauvajol, J. Allègre, P. Séta. *Chem. Phys. Lett.* **1998**, *295*, 257.

07- Rational design of macrocellular silica scaffolds obtained by a tunable sol-gel foaming process.

F. Carn, A. Colin, M.-F Achard, H. Deleuze, Z. Saadi, **R. Backov** *Adv. Mat.* **2004**, *16*, 140.

VIII- REFERENCES

[1] (a) C. Sanchez, G.J. de A.A. Soller-Illia, F. Ribot, T. Lalot, C.R. Mayer, V. Cabuil *Chem. Mater.* **2001**, *13*, 3061. (b) D. Avnir, D. Levy, R. Reisfield *J. Phys. Chem.* **1984**, *88*, 5956. (c) R.J.P. Corriu, D. Leclercq *Angew. Chem., Int. Ed. Engl.* **1996**, *35*, 1420. (d) A. Cheetnam, C.J. Brinker, M. Mac Cartney, C. Sanchez Eds. *Mater. Res. Soc. Symp. Proc.* **1994**, 364. (e) B. Lebeau, C. Sanchez *Curr. Opin. Solid State Mater. Sci.* **1999**, *4*, 11. (f) K. Moller, T. Bein, *Chem. Mater.* **1998**, *10*, 2950. (g) C. Rottman, G. Grader, Y de Hazan, S. Melchior, D. Avnir *J. Am. Chem. Soc.* **1999**, *121*, 8533.

[2] (a) J. Rouxel *Inorg. Chem.* **1979**, *1*, 245. (b) R. Schöllhorn *Chem. Mater.* **1996**, *8*, 1747. (c) J.M. Thomas *Angew. Chem., Int. Ed. Engl.* **1994**, *33*, 913. (d) M.S. Whittingham, A.J. Jacobson Eds. *Academic Press N.Y.*, **1982**, 315. (e) D.W. O'Hare *Wiley and Sons Eds. N.Y.* **1992**, 165. (f) E.P. Giannelis, V. Mehrota *Solid State Comm.* **1990**, *77*, 155. (g) P. Arenda, E. Ruiz-Hizky *Chem. Mater.* **1992**, *4*, 1395. (h) J.E. Pillion, M.E. Thompson *Chem. Mater.*, **1991**, *94*, 59. (i) M. G. Kanatzidis, C.G Wu, D.C. De Groot, J.L. Schindler, C.R. Kannewurf *Chem. Mater.* **1991**, *3*, 992.

[3] (a) J. Livage, J. Lemerle *Ann. Rev. Mat. Sci.*, **1992**, *12*, 103. (b) J. Livage, M. Henry, C. Sanchez, *Prog. Solid State Chem.* **1988**, *18*, 259. (c) C.J. Brinker *J. Non-Crystalline Solids* **1988**, *100*, 30. (d) R.J.P. Corriu, D. LeClercq, A. vioux, M. Pauthe, *Ultrastructure Proces. Adv. Ceramics. Eds J. Mackenzy and D.R. UlUlrich (Wiley NY)* **1988**, 113. (e) D.C. Bradley *Metal alkoxides (Academic Press, London)* 1978. (f) C.J. Brinker G.W Scherrer, *Sol-Gel Science(Academic Press, San diego)* 1990.

[4] (a) J.-M Lehn, *Leçon Inaugurale, Collège de France, Paris*, **1980**; *Le débat* **1982**, *18*, 46; *Interdisciplinarity Science Rev.* **1985**, *10*, 72. (b) J.-M Lehn *Angew. Chem.* 1988, *100*, 91. (c) J.-M Lehn *Angew. Chem., Int. Ed. Engl.* 1988, *27*, 89. (d) J.-M Lehn *Science* **1985**, *227*, 849. (e) B.

Dietrich, J.-M. Lehn, J.P. Sauvage, *J. Chem. Soc., Chem. Commun.* **1973**, 15. (f) S.R. Cooper, S.C. Rawle, *Struct. Bonding* 1990, 72, 1. (g) B. Dietrich, M.W. Hosseini, J.-M Lehn, R.B. Sessions *J. Am. Chem. Soc.* **1981**, 103, 1282. (h) A. Bencini, A. Bianchi, P. Dapporto, E. Garcia-Espanã, M. Micheloni, J.A. Ramirez, J.A. Ramirez, P. Paoletti, P. Paoli *Inorg. Chem.* **1992**, 31, 1902. (i) S. Boudon, A. DeCian, J. Fisher, M.W. Hosseini, J.-M. Lehn, G. Wipff *J. Coord. Chem.* **1991**, 23, 113.

[5] (a) S. Mann *Nature* **1988**, 332, 119. (b) L. Addabi, S. Weiner *Angew. Chem., Int. Ed. Engl.* **1992**, 31, 153. (c) G. Krampitz, G. Grazer *Angew. Chem., Int. Ed. Engl.* **1988**, 27, 1145. (d) G.H. Nancollas *VCH Verlagsgesellschaft, Weinheim (Eds. S. Mann, J. Webb, R.J.P. Williams)* **1989**, 157. (e) S. Raz, S. weiner, L. Addabi *Adv. Mater* **2000**, 12, 38. (f) B.R. Heywood, S. Mann *Adv. Mater.* **1994**, 6, 9.

[6] (a) D. Zhao, P. Yang, B.F. Chmelka, G.D. Stucky *Chem. Mater.* **1999**, 11, 1174. (b) D.D. Archibald, S. Mann *Nature* **1993**, 364, 430. (c) A. Imhof, D.J. Pine *Nature* **1997**, 389, 948. (d) P. Feng, X. Bu, G.D. Stucky, D.J. Pine *J. Am. Chem. Soc.* **2000**, 122, 994. (e) G.-R. Jun, J.H. Moon, V.T. Manoharan, D.J. Pine, S.-M. Yang, *J. Am. Chem. Soc.* **2002**, 124, 13354. (f) D. Walsh, J.D. Hopwood, S. Mann *Science* **1994**, 264, 1576. (g) S.-Y. Chang, L. Liu, S.A. Asher *J. Am. Chem. Soc.* **1994**, 116, 6745. (h) H. Yang, A. Kuperman, N. Coombs, S. Mamiche-Afara, G.A. Ozin *Nature* **1996**, 379, 703. (i) S. M. Yang, I. Sokolov, N. Coombs, C.T. Kresge, G.A. Ozin *Adv. Mater.* **1999**, 11, 1427.

[7] (a) S. Mann *Nature*, **1993**, 365, 499. (b) S. Mann *Biomimetic materials chemistry*, **1996**, VCH, New York. (c) S. Mann, *Angew. Chem., Int. Ed. Engl.* **2000**, 39, 3392. (d) S. Mann, G.A. Ozin *Nature*, **1996**, 382, 313. (e) S. Mann, J.P. Hannington, R.J.P. Williams *Nature*, **1986**, 324, 565. (f) S. Mann, S.L. Burkett, S.A. Davis, C.E. Fowler, N.H. Mendelson, S.D. Sims et al. *Chem. Mater.* **1997**, 9, 2300. (g) T. Ogasawara, W. Shenton, S.A. Davis, S. Mann *Chem. Mater.* **2000**, 12, 2835. (h) G.A. Ozin *Acc. Chem. Res.* **1997**, 30, 17. (i) M. Sarikaya, I.A. Aksay, *AIP Press Woodbury NY*, **1995**. (j) P.T. Tanev, T.J. Pinnavaia *Science* **1996**, 271, 1267.

[8] R. Backov, D.J. Jones, J. Rozière *J. Chem. Soc., Chem. Comm.* **1996**, 599.

[9] R. Backov, B. Bonnet, D.J. Jones, J. Rozière *Chem. Mater.* **1997**, 9, 1812.

[10] R. Backov, B. Bonnet, D.J. Jones, J. Rozière *Mol. Liq. Liq. Cryst.* **1998**, 311, 233.

[11] R. Backov, L. Binnet, J.M. Fabre, D.J. Jones, J. Rozière *Mol. Liq. Liq. Cryst.* **1998**, 311, 239.

[12] T. Corradin, R. Backov, D.J. Jones, J. Rozière, R. Clément, *Mol. Liq. Liq. Cryst.* **1998**, 311, 275.

[13] A. Lambrate, J.M. Jannot, A. Emidaoui, R. Backov, J. Rozière, L.C. de Ménorval, J.L. Sauvajol, J. Allègre, P. Séta *Chem. Phys. Lett.* **1998**, 295, 257.

[14] A. Lambrate, J.M. Jannot, L.C. de Ménorval, R. Backov, J. Rozière, J.L. Sauvajol, J. Allègre, P. Séta *Synth. Metals* **1991**, 103, 2426.

[15] (a) G. Alberti, U. Constantino, S. Alluli, N. Tomassini *J. Inorg. Nucl. Chem.* **1978**, 40, 1113. (b), *Solid State Ionics*, **1988**, 26, 63. (c) G. Cao, H. Lee, V.M. Lynch, T.E. Mallouk *Inorg. Chem.* **1988**, 27, 2781. (d) D. Cunningham, P.J. Hennesly, *Inorg. Chim. Acta*, **1979**, 37, 95. (e) Y. Ortiz-Avila, P.R. Rudolf, A. Clearfield, *Inorg. Chem.*, **1989**, 28, 2137.

- [16] (a) G.V. Rubenaker, D.P. Raffaell, J.E. Drumheller, K. Emerson, *Phys. Rev. B* **1988**, *37*, 3563. (b) K. Zemmyo, H. Kubo, *J. Phys. Soc. Jpn.* **1995**, *64*, 1320. (c) G.C. DeFotis, G.S. Coker, J.W. Jones, C.S. Branch, H.A. King, J.S. Bergman, S. Lee, J.R. Goodey, *Phys. Rev. B* **1998**, *58*, 12178. (d) G.C. DeFotis, E.M. Just, V.J. Pugh, G.A. Coffey, B.D. Hoggs, S.L. Fitzhenry, J.L. Marmorino, D.J. Krovich, R.V. Chamberlain, *J. Magn. Magn. Mater.* **1999**, *202*, 27. (e) G.C. DeFotis, D.S. Mantus, E.M. MpcGhee, K.R. Echols R.S. Weis, *Phys. Rev. B* **1988**, *38*, 11486.
- [17] L.J. de Jongh, in ‘*Magnetic Properties of Layered Transitional Metal Compounds*’ (L.J. de Jongh Ed.), pp.1-51 Kluwer Academic, Dordrecht, **1990**.
- [18] (a) G.E. Fanucci, J. Krystek, M.W. Meisel, L.-C. Brunel, D.R. Talham *J. Am. Chem. Soc.* **1998**, *120*, 5469. (b) J.T. Culp, G.E. Fanucci, B.C. Watson, A.N. Morgan, R. Backov, H. Ohnuhi, M.W. Meisel, D.R. talham *J. Solid States Chem.*, **2001**, *159*, 362.
- [19] S. Fishman, A. Aharony *Phys. Rev. B*, **1978**, *18*, 3507.
- [20] (a) C.G. Roberts *Langmuir-Blodgett Films*; Plenum Press: New York, **1990**. (b) M.C. Petty *Langmuir-Blodgett Films: An Introduction*; Cambridge University Pres: Cambridge, **1996**.
- [21] (a) C.T. Seip, G.E. Granroth, M.W. Meisel, D.R. Talham *J. Am. Chem. Soc.* **1997**, *119*, 7084. (b) G.E. Fanucci, D.R. Talham *Langmuir*, **15**, 3289.
- [22] (a) J. Le Bideau, D. Papoutsakis, J.E. Jackson, D. G. Nocera *J. Am. Chem. Soc.* **1997**, *119*, 1313 . (b) D. Papoutsakis, J.E. Jackson, D. G. Nocera *Inorg. Chem.* **1996**, *35*, 800. (c) D. Beltrán-Porter, A. Beltrán-Porter, P. Amorós, R. Ibáñez, R. Matinez, A. Le Bail, G. Ferey, G. Villeneuve, *J. Solid State Inorg. Chem.* **1991**, *28*, 131. (d) V. Laget, P. Hornick, P. Rabu, M. Drillon *J. Mater. Chem.* **1999**, *9*, 169.
- [
- 23] (a) O.M Yaghi, G. Li, H. Li *Nature* **1995**, *378*, 703. (b) M.J. Zaworotko *J. Chem. Commun.* **2001**, *1*. (c) R. Robson, B.F. Abrahams, S.R. Batten, R.W. Gable, B.F. Hoskins, J. Liu, *Supramolecular Architecture*; American Chemical society: Washington D.C., 1995. (d) F. Robinson, M.J. Zaworotko *J. Chem. Soc., Chem. Commmun.* **1995**, 213. (e) O.M. Yaghi, G. Li *Angew. Chem. Int. Ed. Engl.* **1995**, *34*, 207. (f) J. Lu, G. Crisci, T. Niu, A.J. Jacobson *Inorg. Chem.* **1997**, *36*, 5140. (g) T.L. Hennigar, D.C. MacQuarrie, P. Losier, R.D. Rogers, M.J. Zaworotko *Angew. Chem. Int. Ed. Engl.* **1997**, *36*, 972. (h) H. Li, M. Eddaoudi, M. O’Keefe, O.M. Yaghi *Nature*, **1999**, *402*, 276.
- [24] J.W. Woodward, PhD thesis dissertation: *Chemical and physical characterization of hybrid organic-inorganic low-dimensional coordination polymers*. University of Florida, **2002**.
- [25] O.M. Yaghi, H. Li, C. Davis, D. Richardson, T.L. Groy *Acc. Chem. Res.* **1998**, *32*, 474.
- [26] M.; Fujita, Y.J. Kwon, S. Washizu, K. Ogura *Inorg. Chem.* **1994**, *116*, 1151.
- [27] (a) L. Carlucci, G. Ciani, D.M. Propsperio, A. Sironi *J. Am. Chem. Soc.* **1995**, *117*, 4562. (b) B.F. Hoskins, R. Robson *J. Am. Chem. Soc.* **1990**, *112*, 1546.
- [28] (a) O.R. Evans, R.G. Xiong, Z. Wang, G.K. Wong, W. Lin *Angew. Chem. Int. Ed. Engl.* **1999**, *38*, 536. (b) C. Janiak, T.G. Scharman, P. Albrecht, F. Marlow, R. MacDonald *J. Am. Chem. Soc.* **1996**, *118*, 6307. (c) O. Lin, O.R. Evans, R.G. Wang *J. Am. Chem. Soc.* **1998**, *120*, 13272.

- [29] (a) M. Inoue, M. Kubo *Coord. Chem. Rev* **1976**, 27,1. (b) S. Kawata, s. Kitagawa, M. Kondo, I. Furuchi, M. Munakata *Angew. Chem. Int. Ed. Engl.* **1994**, 33, 1761. (c) W.R. Entley, G.S. Girolami *Inorg. Chem.* **1994**, 33, 5165. (d) J.L. Manson, C. Campana, J.S. Miller *Chem.Comm.* **1998**, 251.
- [30] (a) R. Manavalan, M.M. Patal *Makromol.Sci.Chem* **1983**, A19, 951. (b) W. Kobel, M. Hanack *Inorg. Chem.* **1986**, 25, 103. (c) K.Sinzger, S. Hining, M. Jopp, D. Bauer, W. Bietsch, J.U.V. Schutz, H.C. Wolf, H.C. Kremer, T. Metzenthin, R. Bau, S.I. Khan, A. Lindbaum, C.L. Langauer, E. Tillmanns *J. Am. Chem. Soc* **1993**, 115, 7696.
- [31] J.D Woodward, R. backov, K.A. Abboud, H. Ohnuki, M.W. Meisel, D.R. talham *polyhedron*, **sumis**.
- [32] (a) O. Khan *Molecular Magnetism*; VCH: New york, **1993**. (b) A. Bencini, D. Gatteschi *Inorg. Chim. Acta.* **1978**, 31, 11. (c) O. Khan *Inorg. Chim. Acta* **1982**, 62, 3.
- [33] G.E. Fanucci, R. Backov, R. Fu, D.R. Talham *Langmuir* **2001**, 17, 1660.
- [34] (a) J.M. Soletti, M. Botreua, F. Sommer, W.L. Brunat, S. Kasas, T.M. Duc, M.R. Celio *Langmuir* **1996**, 12, 5379. (b) J.P. Green, M.C. Phillips, G.G. Shipley *Biochim. Biophys. Acta*, **1993**, 330, 243. (c) H. Nakahara, K. Fukada, H. Akutsu, Y. Kyogoku, *J. Colloid. Interface Sci.* **1978**, 65, 517.
- [35] (a) T.D. Osborn, P. Yager, *Biophys. J.***1995**, 68, 1364. (b) M. Losche, C. Helm, H.D. Mattes, H. Mohwald *Thin Solid Films* **1985**, 133, 51. (c) A.P. Girard-Egrot, R.M. Morelis, P.R. Coulet *Langmuir* **2000**, 12, 778.
- [36] G.E. Fanucci, C.R. Bowers, D.R. Talham *J. Am. Chem. Soc.* **1999**, 121, 1088.
- [37] (a) S. Mann, D.D. Archibald, J.M. Didymus, T. Douglas, B.R. Heywood, F.C. Meldrum, N.J. reeves *Science* **1993**, 261, 1286. (b) S.J. Cooper, R.B. Sessions, S.D. Lubetkin *Langmuir* **1997**, 13, 7165. (c) S.J. Cooper, R.B. Sessions, S.D. Lubetkin *J. Am. Chem. Soc.* **1998**, 120, 2090.
- [38] S. Whipps, S.R., F.J. O’Palko, R. Backov, D.R. Talham *J. Cryst. Growth* **1998**, 192, 243.
- [39] R. Backov, C.M. Lee, S.R. Khan, C. Mingotaud, G.E. Fanucci, D.R. Talham *Langmuir* **2000**, 16, 6013.
- [40] R. Backov, S.R. Khan, C. Mingotaud, K. Byer, C.M. Lee, D.R. Talham *J. Am. Soc. Nephrol.* **1999**, 10, S359.
- [41] L.J. de Jongh (Ed.), *Physics and chemistry of metal cluster compounds*, Kluwer Publishers, Dordrecht, **1994**.
- [42] C.A. Foss, G.L. Horniak, J.A. Stokert, C.R. Martin *J. Phys. Chem.* **1994**, 98, 2963.
- [43] (a) M.P. Pileni *Cryst. Res. Technol.* **1998**, 33, 1155. (b) J.D. Hopwood, S. Mann *Chem. Mater.* **1997**, 9, 1819. (c) X. Zhang, K. Chan *Chem. Mater.*, **2003**, 15, 451.
- [44] (a) F.C. Meldrum, B.R. Heywood, S. Mann *J. Colloid Interface Sci.* **1993**, 161, 66. (b) C. Faure, R. Backov *Brevet Français 02-15153*, 2002.

- [45] (a) F.C. Meldrum, N.A. Kotov, J.H. Fendler *Langmuir* **1994**, *10*, 2035. (b) S. ravaine, G.E. Fanucci, C.T. Seip, J.H. Adair, D.R. Talham *Langmuir* **1998**, *14*, 708. (c) L. Petit, J.P. Manaud, C. Mingotaud, S. Ravaine, E. Duguet *Materials Letters* **2001**, *51*, 478.
- [46] G.W. Gray, P.A. Winsor Eds., Jon Wiley and Sons Inc. *Liquid Crystals and Plastic Crystals*, **1974**.
- [47] D. Demus, L. Richter, VEB Deutscher Verlag Für Grundstoffindustrie, Leipzig, Second Edition, *Texture of liquid crystals*, **1978**.
- [48] (a) H. Zocher *Z. Anorg. Allg. Chem.* **1925**, *147*, 91.
- [49] (a) P. Davidson, P. Batail, J.C.P. Gabriel, J. Livage, C. Sanchez, C. Bourgaux *Prog. Polym. Sci* **1997**, *22*, 913. (b) O. Pelletier, P. Davidson, C. Borgaux, C. Coulon, S. Regnault, J. Livage *Langmuir* **2000**, *16*, 5295. (c) B. Vigolo, C. Zakri, F. Nallet, J. Livage, C. Coulon *Langmuir*, **2002**, *18*, 9121.
- [50] (a) P. Davidson, J.C. Gabriel, A.M. Levelut, P. Batail *Adv. Mater.*, 1993, *5*, 665. (b) J.M. Tarascon, F.J. Disalvo, C.H. Chen, P.J. Carroll, W. Walsh, L. Rupp *J. Solid State Chem.*, **1985**, *58*, 290.
- [51] (a) H. Zocher, C. Török *Kolloid Z.*, **1960**, *173*, 1. (b) P.A. Buning, H.N.W. Lekkerkerker *J. Phys. Chem.*, **1993**, *97*, 11510.
- [52] (a) J.C. Gabriel, C. Sanchez, P. Davidson *J. Phys. Chem.* **1996**, *100*, 11139. (b) A.B.D Brown, C. Ferrero, T. Narayanan, A.R. Rennie *Eur. Phys. B*, **1999**, *11*, 481.
- [53] (a) J.C.P. Gabriel, F. Camerel, B.J. Lemaire, H. Desvaux, P. Davidson, P. Batail *Nature* **2001**, *413*, 504. (b) R. backov, A.N. Morgan, S. Lane, E.E. Perez-Cordero, K. Williams, M.W. meisel, C. sanchez, D.R. talham, *Mol. Cryst. Liq. Cryst.* **2002**, *376*, 127.
- [54] C. T. Kresge, M. E. Leonowicz, W. J. Roth, J. C. Vartuli, J. S. Beck, *Nature* **1992**, *359*, 710.
- [55] M.P. Harold and al., Catalysis with inorganic membranes, *MRS Bull.* **1994**, *19*, 34.
- [56] R.R. Bhave, Inorganic membranes synthesis, characteristics, and applications (Van Nostrand Reinhold, New York, **1991**).
- [57] [5] P. Feng, X. Bu, G.D. Stucky, D.J. Pine, *J. Am. Chem. Soc.* **2000**, *122*, 994.
- [58] M.T. Anderson, J.E. Martin, J.G. Odinek, P.P. Newcomer, J.P. Wilcoxon, *Microporous Mater.* **1997**, *10*, 13.
- [59] N.A. Melosh, P. Davidson, B.F. Chmelka, *J. Am. Chem. Soc.* **2000**, *122*, 823.
- [60] E. Litovsky, M. Shapiro, A. Shavit, *J. Am. Ceram. Soc.* **1996**, *79*, 1366.
- [61] S. Schacht, Q. Huo, I.G. Voigt-Martin, G.D. Stucky, F. Schüth *Science*, **1996**, *273*, 768.

[62] (a) O. Diat, D. Roux, D. *J. Phys. II*, **1993**, 9. (b) O. Diat, D. Roux, F. Nallet, *J. Phys. II*. **1997**, **3**, 1427

[63] (a) K.C. Grabar, R.G. Freeman, M.B. Hommer, M. J. Natan, *Anal. Chem.* **1995**, *67*, 735. (b) C.F. Bohren, D.R. Huffman eds., *Absorption and scattering of light by small particles*, New York, **1983**.

[64] K. Esumi, T. Hosoya, K. Torigoe *Langmuir* **2000**, *16*, 2978.

[65] T. Yokoyama, T. *et al J. Colloid Interf. Sci.* **2001**, *233*, 112.

[66] (a) O. Diat, D. Roux, F. Nallet, *J. Phys. II* **1993**, *3*, 1427. (b) O. Diat, D. Roux, *J. Phys. II*, **1993**, *9*. (c) D. Roux, T. Gulik, J. Dedieu, C. Degert, R. Laversanne, *Langmuir* **1996**, *12*, 4668.

[67] (a) F. Gauffre, D. Roux *Langmuir*, **1999**, *15*, 3738.(b) C. Faure, A. Derre, W. Neri *J. Phys. Chem. B* **2003**, *107*, 4738.

[68] A. Desforges, M. Arpontet, H. Deleuze, O. Mondain-Monval, *Reactive and functional polymers*, **2002**, *53*, 183.

Evidence of confinement of fullerene C₆₀ in microporous VPI-5 zeolite

Abdelaziz Lamrabte^{a,b}, Jean-Marc Janot^a, Azzeddine Elmidaoui^b, Patrick Seta^{a,*},
Louis-Charles de Ménorval^c, Rénal Backov^d, Jacques Rozière^d,
Jean-Louis Sauvajol^e, Jacques Allègre^f

^a Laboratoire des Matériaux et Procédés Membranaires, UMR CNRS 5635, 1919 route de Mende, F-34293 Montpellier Cedex 5, France

^b Laboratoire des Procédés de Séparation, Université Ibn Tofail, Faculté des Sciences, Kénitra, Morocco

^c Laboratoire de Matériaux Catalytiques et Catalyse en Chimie Organique, E.N.S.C.M., UMR CNRS 5618, 8 rue de l'École Normale, F-34296 Montpellier Cedex 5, France

^d Laboratoire des Agrégats Moléculaires et Matériaux Inorganiques (LAMMI), Université Montpellier II, place Eugène Bataillon, F-34095 Montpellier Cedex 5, France

^e Groupe de Dynamique des Phases Condensées URA-233, Université Montpellier II, place Eugène Bataillon, F-34095 Montpellier Cedex 5, France

^f Groupe d'Étude des Semiconducteurs (GES), Université Montpellier II, place Eugène Bataillon, F-34095 Montpellier Cedex 5, France

Received 7 June 1998; revised 27 August 1998

Abstract

Anderson's method of incorporation of C₆₀ within the cages of a VPI-5 zeolite has been used as well as a chemical vapor deposition procedure. ¹²⁹Xe nuclear magnetic resonance has confirmed that, starting from an organic solution of fullerene, C₆₀ was actually incorporated into the molecular cages of the inorganic matrix. Thermal analysis methods and X-ray diffraction show that the treatment does not affect the integrity of the crystalline structure of VPI-5. Photoluminescence experiments gave similar results to those already mentioned by other authors, indicating the probable confinement effect of the inorganic matrix on the C₆₀ isolated molecules. © 1998 Elsevier Science B.V. All rights reserved.

1. Introduction

Since the large-scale commercial production of fullerenes, which became possible due to efficient purification techniques [1–3], numerous attempts have been made to incorporate them into various molecules or media. Organic molecules or supramolecules such as cyclodextrins [4], or cal-

ixarenes [5] or more organized systems such as micelles or vesicles [6] are able to encapsulate C₆₀. Polymers [7] or inorganic solids, in particular silica gels [8] and zeolites [9], have been considered in order that new materials might be developed. Interesting electrical properties (electric conductivity and photoconductivity) and also optical properties have been brought out. The demonstration of photophysical properties of systems including fullerenes has promoted research work in areas as diverse as non-linear optics and biology. In the first area, optical

* Corresponding author.

limiting effects (reverse saturable absorption) have been shown [10] and, in the second, therapeutic applications are expected relying on the cytotoxic properties of C_{60} [11] which result from its excellent photosensitising capacities.

These photophysical properties derive from a yield of formation of the triplet state of C_{60} close to 1 and are extremely dependent on the environment of the molecule. It has been shown [6] that when C_{60} molecules aggregate (in non-solvating media, or in media which are strongly anisotropic in their interactions with C_{60}), the yield of formation of the triplet state considerably decreases, rendering these media useless for the purpose of these applications. In the same way, the lifetime of the photoexcited states depends on the relaxation modes and consequently on the nature and the organization of the surrounding medium, as has been shown by kinetic studies on the photoinduced electron transfer in doped polymers [12]. These data led to the conclusion that the ways of building materials including fullerenes should, as much as possible, preserve the molecular state of the molecules inside the host matrix. The intramolecular contacts between C_{60} molecules should be limited, and strong constraints possibly exerted in order to promote confinement effects [13]. The idea of incorporating C_{60} in porous materials, either during the synthetic process or a posteriori once the microstructured material is elaborated, appeared promising, as the remarkable results of Hamilton et al. on the photoluminescence of C_{60} incorporated in a zeolite VPI-5 [14] and further results in various confinement media [15] have shown.

Although the results show appreciable modifications of the photophysical properties of C_{60} , few conclusive elements have been brought concerning the nature of the insertion of C_{60} in the porosity of the materials. In this Letter we present data concerning the incorporation of C_{60} in a zeolite of the VPI-5 series, which corroborate the existence of properties linked to confinement. We characterize the doped material using several techniques; in particular, ^{129}Xe nuclear magnetic resonance (NMR) has unambiguously demonstrated that C_{60} really penetrates inside the zeolite supercages. Nevertheless, a small fraction of C_{60} shows characteristics similar to those of crystalline C_{60} and might be blocked in structural defects.

2. Experimental

VPI-5 was the generous gift of Dr. M. Davis. The compound was synthesized hydrothermally according to his method [16]. X-ray diffraction showed that the material was highly crystalline. For NMR experiments: (1) the zeolite sample was evacuated in a NMR tube (equipped with a re-sealable valve suited for attachment to a vacuum line) at room temperature for 24 h. The temperature was then increased to 110°C for 24 h ($0.5^\circ\text{C min}^{-1}$) and to 450°C for 24 h ($0.5^\circ\text{C min}^{-1}$), then the xenon was introduced at room temperature in the zeolite; and (2) the treated zeolite sample (0.25 g), under nitrogen pressure, was added to a solution of C_{60} (0.025 g) in benzene (30 ml) and stirred at 50°C for 24 h, then put into a hydrothermal reaction vessel, and maintained at 140°C for 96 h. The product was then centrifuged off and washed thoroughly with benzene to remove any surface species. The obtained product was transferred to the NMR tube and evacuated at 200°C for 10 h, then the xenon was added at room temperature.

VPI-5 and VPI-5 reacted with C_{60} were characterized by power X-ray diffraction (XRD) using a Philips generator (Cu $K\alpha$ radiation) and goniometer. Thermogravimetric (TG) and differential thermal analysis (DTA) were carried out in air on a Stanton Redcroft STA 781 thermobalance, with a heating rate of 2°C min^{-1} .

^{129}Xe -NMR spectra were obtained at room temperature on a Bruker AC 250 L spectrometer operating at a frequency of 69.9 MHz for ^{129}Xe . Typically, 10000–40000 signal acquisitions were accumulated for each spectrum with a recycle delay of 2 s between $\pi/2$ pulses. Chemical shift measurements are accurate to within 1 ppm and are expressed relatively to xenon gas at zero pressure [17]. Downfield (high frequency) chemical shifts are considered to be positive.

Static photoluminescence spectra were recorded with identical excitation ($\lambda = 514.5$ nm) and collection conditions (spectrometer ISA Jobin-Yvon T64000). Spectra were not corrected for the spectral response efficiency of the PM tube.

Time-resolved photoluminescence measurements were carried out using two different techniques. The single-photon counting technique has been used for experiments at room temperature and mostly for an

excitation set in the visible range (514.5, 590–620 nm). Some measurements using an excitation in the UV range (300 nm) were performed on a non-incorporated C_{60} powder sample. A Hamamatsu model C4334 synchroscan streak camera has been used for the experiments performed at 8 K. For these experiments the excitation was set to 272 nm. Some experiments at room temperature were performed on this device using 514.5 nm excitation wavelength. In photon counting experiments the 514.5 nm excitation wavelength was provided using a Spectra Physics model 2030, 82 MHz mode locked argon ion laser (pulses ~ 200 ps FWHM). The 600 nm visible excitation was obtained using the same argon laser pumping synchronously a cavity dumped Spectra Physics rhodamine 6G dye laser model 375 (pulses ~ 20 ps FWHM). The 300 nm excitation wavelength was obtained by doubling the fundamental 600 nm dye laser beam using a Spectra Physics model 390 frequency doubler. A Jobin-Yvon DH10 double monochromator (focal length 100 mm, 8 nm bandwidth) was used without cutoff filter to collect the fluorescence. A photomultiplier tube Hamamatsu model H5323 cooled at -20°C has been used for the detection (cathode S20, 160 ps transient time spread). The response function of the single-photon counting device (laser, PM tube, time-to-amplitude converter Ortec 457, multichannel analyzer Tracor Northern 1750) was in the range 200 ps (FWHM). The excitation energy was set in order to obtain a count rate of maximum 12 kHz. No special care for the samples has been used against oxygen. The emission spectra were not corrected for the sensitivity of the photocathode neither from the grating response.

Decay analysis was performed using a Levenberg–Marquardt algorithm. Lifetimes were calculated by iterative adjustment after convolution of the pump profile (scattered light) with a sum of exponentials. We assumed a Poissonian distribution of the counts in the calculation of the χ^2 criterion used to estimate the quality of the adjustment. The program has been written in order to correct automatically: (1) for the accumulation of background; (2) for the repetition rate of the laser; and (3) for the shift between the pump profile and the decay. A global analysis of the decays was performed using the same program. The spectral distribution of the lifetimes was calculated as the product of the yield of each

component with the corresponding amplitude of the emission spectrum at the same wavelength.

The 272 nm laser UV excitation wavelength (repetition frequency 80 MHz, 1.6 ps FWHM) was obtained after admixing in a non-linear BBO crystal of the second and fundamental harmonic 816 nm emission wavelength of a Spectra Physics Tsunami Ti:sapphire laser pumped with an argon ion laser Spectra Physics model 2040E. The excitation pulse was focused on the sample set in a helium cryostat. The emission was collected through a 0.5 m focal length spectrophotometer. The response function of the system has been estimated to 5 ps. The analysis of the decays was performed using the same kind of program as described previously. However, as the Poissonian distribution analysis can only be applied for counting experiments, the χ^2 criterion has not been corrected for the noise.

The absorption spectra were recorded on a Kontron Uvikon 940 absorption spectrophotometer, the C_{60} /VPI-5 sample being incorporated in a KBr pellet.

3. Results and discussion

3.1. X-ray diffraction, TGA and DTA

The thermogravimetric profiles of VPI-5 and C_{60} /VPI-5 samples recorded in air presented in Fig. 1a and b show a weight loss at 480–580°C of $\sim 16\%$ of the dry VPI-5, which we interpreted as breakdown and loss of C_{60} from the micropores. This weight loss is associated with an exothermic peak in the DTA curve (see Fig. 1b) due to a combustion of C_{60} . This exothermic peak is not observed on the DTA of the pure VPI-5. Such a concentration gives an approximate stoichiometry of one fullerene C_{60} for 35 AlPO_4 or in average one C_{60} molecule in the matrix every 15 Å; the channels are about two-thirds full. Furthermore the amount of occluded water is reduced by 11% as compared to the parent VPI-5. This is consistent with a reduced internal void volume owing to the presence of C_{60} within the pores. However, from such data it is not possible to say whether C_{60} is located inside the pores or simply adsorbed outside of the VPI-5.

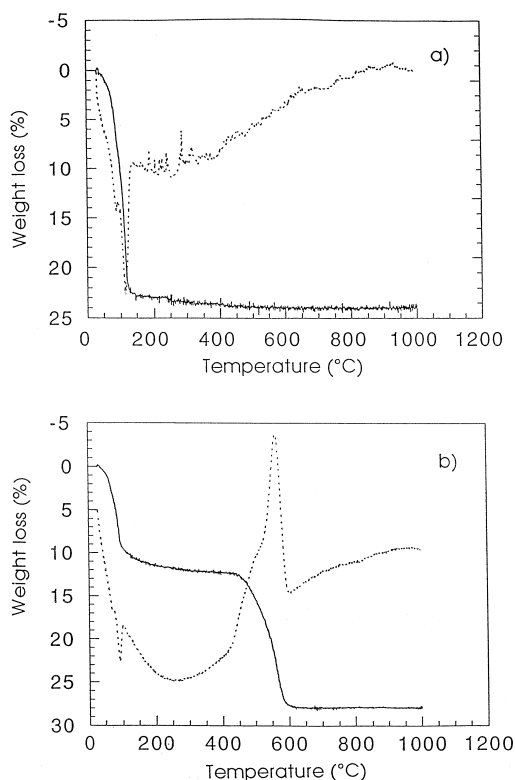


Fig. 1. Thermogravimetric and differential thermal analysis profiles of: (a) VPI-5 zeolite; and (b) C_{60} trapped VPI-5 sample prepared from a C_{60} benzene solution.

X-ray diffraction indicates that the product was still highly crystalline with the same structure and no superlattice reflections. This material is stable in air without any phase transition and therefore C_{60} , because of its size, stabilizes the VPI-5 structure.

3.2. ^{129}Xe -NMR

Fig. 2A shows the ^{129}Xe -NMR spectra of xenon adsorbed on treated VPI-5 zeolite (Fig. 2A, a), treated C_{60} /VPI-5 zeolite obtained by vapor deposition (Fig. 2A, b) and C_{60} /VPI-5 zeolite prepared in the presence of a C_{60} benzene solution (Fig. 2A, c). The spectra shown in Fig. 2A, a and b are similar. This means that the adsorbed xenon has the same environment in these two cases. We can suggest that the C_{60} cannot penetrate through the porosity of the VPI-5 zeolite during the C_{60} adsorption by vapor phase deposition. This observation is in accordance with

Refs. [18–20] concerning the adsorption of organic molecules in zeolite, where the chemical shift of adsorbed xenon increases only when the organic molecules are adsorbed in the porosity.

Fig. 2A, c shows a decrease of the intensity of the 60 ppm line, when the C_{60} was incorporated from a liquid phase, then the sample was desorbed under vacuum at 200°C in order to remove the benzene phase. In this case a decrease in the line intensity means that now C_{60} is actually incorporated in the porosity of VPI-5 and that the xenon can no longer penetrate into the porosity. In these conditions if benzene was still adsorbed in the VPI-5 porosity, an

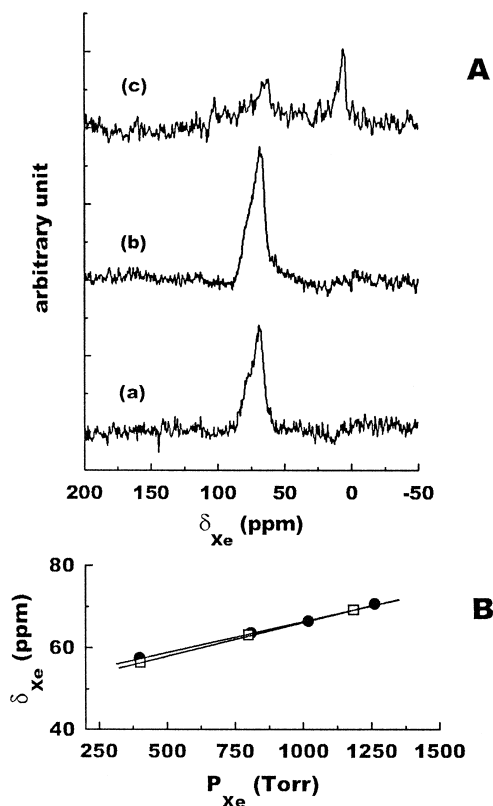


Fig. 2. (A) ^{129}Xe -NMR spectra of xenon adsorbed on: (a) VPI-5 zeolite treated under vacuum at 450°C ; (b) C_{60} /VPI-5 zeolite sample obtained by vapor-phase deposition and treated under vacuum at 450°C ; and (c) C_{60} /VPI-5 zeolite sample prepared from a C_{60} benzene solution and treated under vacuum at 200°C . (B) ^{129}Xe -NMR chemical shift variations with equilibrium xenon pressure of VPI-5 samples treated at 450°C (\bullet = VPI-5 zeolite; \square = C_{60} trapped VPI-5 sample prepared by C_{60} vapor deposition).

increase in the xenon chemical shift would be observed, in accordance with Refs. [18–21], instead of the decrease of the intensity of the corresponding line as described in this Letter. We observed the same behavior when organic molecules (HMB: hexamethyl-benzene) were introduced into a NaY zeolite, with a population of more than one molecule in the α -cage. The spectrum of Fig. 2A, a shows two lines; the main one, in the range 50–70 ppm, corresponds to the xenon adsorbed in the microporosity of VPI-5. Its chemical shift varies linearly with the xenon pressure as shown in Fig. 2B. This variation of δ_{Xe} is similar to that described in the work of Fraissard et al. [22]. This behavior confirms the open state of the porosity of VPI-5 zeolite. The second line when it exists, shifted by a few ppm, is independent of the xenon pressure. This signal corresponds probably to the xenon adsorbed on the outer surface of VPI-5, which has presumably a secondary mesoporosity formed by the agglomeration of zeolite grains.

3.3. Optical absorption measurements

Typical shapes of the absorption spectra are shown in Fig. 3. The spectra were corrected for light scattering. As a result of this correction the absorption

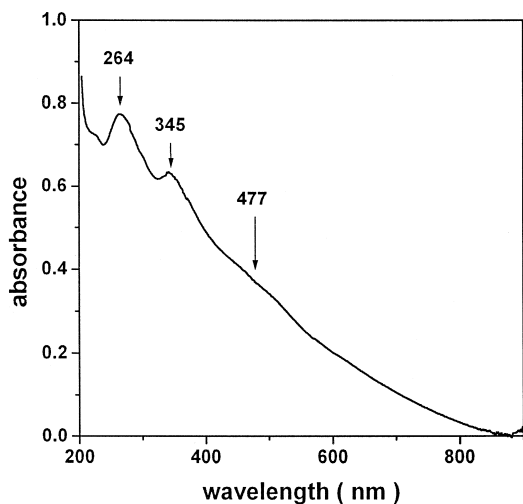


Fig. 3. C_{60} /VPI-5 in KBr pellet absorption spectrum. The absorption spectrum was corrected from scattered light assuming that the absorbance of C_{60} is close to zero for wavelengths longer than 800 nm.

maxima were better resolved, peaking at 264 and 345 nm with a shoulder around 477 nm. The absorption spectrum of the C_{60} /VPI-5 sample was broader than that of C_{60} in an organic solution [7] or even in solid C_{60} ; however, the main features are consistent with the classical absorption bands of C_{60} , the maxima being red-shifted by 8 and 17 nm as compared to hexane solution in which C_{60} is monomeric. The maxima are less red-shifted than those of C_{60} films on KBr [23]. Absorption studies in various media have shown a tendency for the main absorption peaks to be red shifted when C_{60} is located at the vicinity of polar interfaces [7]. The position of the maxima of C_{60} /VPI-5 are close to those of C_{60} incorporated in ultrathin membranes (liposomes), i.e. in systems where C_{60} is close to polar aqueous interfaces of dielectric constant higher than hydrophobic organic media. According to this observation, the environment of C_{60} incorporated within the cages of the zeolite can be considered as equivalent to a medium of high polarity. This result is not surprising, as the atoms of the matrix which form a solvent-type shell for the C_{60} molecules are mainly oxygen atoms. The latter may partly mix their electrons density with that of the fullerene, as in a charge transfer inclusion complex. This effect could explain the fact that the onset of the absorption spectrum of the C_{60} /VPI-5 is close to 900 nm. The constraints exerted by VPI-5 cages on C_{60} presumably lead to symmetry breaking [24] and correlatively to the occurrence of transitions which are forbidden in the case of isolated C_{60} molecules.

3.4. Static photoluminescence measurements

Photoluminescence spectra, plotted in arbitrary intensity units, of the VPI-5 and C_{60} /VPI-5 samples are shown in Fig. 4. The strong intensity of fluorescence of our zeolite sample (although lower than that of the C_{60} /VPI-5 sample) is an important problem for the resolution of the photoluminescence spectrum of the C_{60} /VPI-5 material. We were not able to understand the origin of the luminescence of the matrix and admit that this one is probably due to some contamination during the preparation. Nevertheless, the significant changes observed between the fluorescence measured for the C_{60} /VPI-5 material and the pure zeolite, unambiguously support the

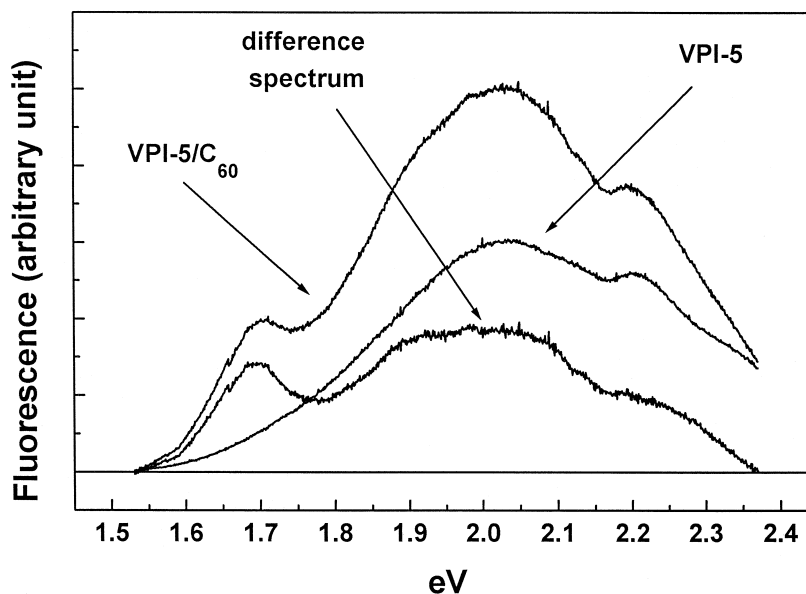


Fig. 4. Photoluminescence spectra of: (a) VPI-5; (b) C_{60} confined in VPI-5; and (c) pure C_{60} powder. Excitation wavelength 514.5 nm.

existence of an interaction between the C_{60} and the zeolite. This result is an additional evidence of the incorporation of C_{60} into the zeolite. A quantitative estimation of the quantum yield of fluorescence of both samples (VPI-5 and $C_{60}/VPI-5$) has not been possible because of the inherent difficulty of studies on solids. Nevertheless, as fluorescence signal cannot be negative, if we calculate the difference between both samples in order to have the minimum of positive contribution, we can have an idea of the shape of the emission spectrum of the incorporated C_{60} . This calculated spectrum is plotted in Fig. 4. This difference spectrum leads to a broad structure with mainly two bands. The less intense sharp peak in the 1.7 eV region could be attributed to the classical main emission band of the C_{60} powder. The broad emission peaking in the 2.0 eV region could be due to the matrix confinement effect. This broadening of the emission of the C_{60} is in accordance with the results previously published by Hamilton et al. [14] on C_{60} trapped in VPI-5 zeolite. Similar observations were published for C_{60} incorporated in other matrixes [25,26]. The discrepancy between the position of the maximum of emission of the C_{60} trapped we observed and with the previously published value of Hamilton et al. [14] can probably be

attributed to: (1) the way we calculated this spectrum; and (2) the fact that none of the original spectra were corrected for the response of the fluorescence device.

3.5. Time-resolved photoluminescence experiments

Uncorrected emission spectra of pure VPI-5 and $C_{60}/VPI-5$ recorded using the photon counting device are presented in Fig. 5. The difference spectrum calculated as previously discussed in Section 3.4 is shown Fig. 5c. On the basis of the arguments developed previously, the spectrum (Fig. 5a) of the $C_{60}/VPI-5$ is in agreement with the previously mentioned result [14] and with our static fluorescence measurements (Fig. 4). This spectrum shows clearly three peaks at 800 nm (1.55 eV), 730 nm (1.7 eV) and 540 nm (2.29 eV), respectively. Comparison of this spectrum with the one obtained under the same conditions for C_{60} powder (Fig. 5e) shows clearly that the peaks at 800 and 730 nm proceed from the contribution of C_{60} crystals.

Fluorescence decays recorded for the C_{60} powder show clearly a non-mono-exponential behavior. Whichever the excitation wavelength (300, 514.5 or 600 nm), two lifetimes, 180 and 450 ps, were neces-

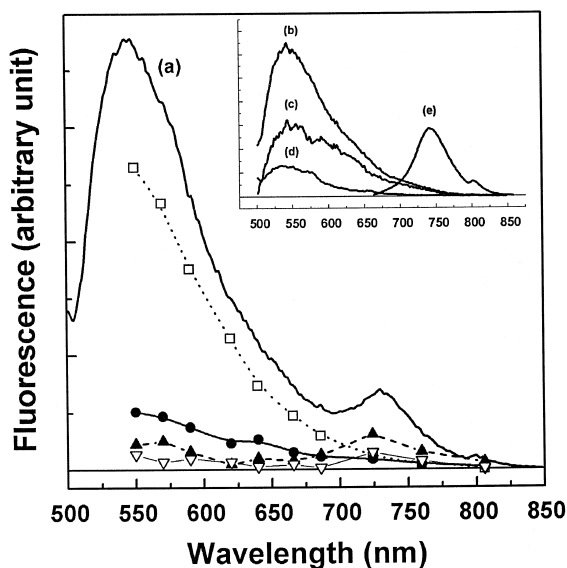


Fig. 5. C_{60} /VPI-5 emission spectra recorded under 496 nm excitation wavelength: (a) before washing the sample with benzene and (b) after being abundantly rinsed with benzene; (c) calculated difference spectrum of spectra (b) and (d), where (d) emission spectra of pure VPI-5; (e) spectrum of C_{60} powder recorded. Spectral distribution of lifetimes issued from global analysis of C_{60} /VPI-5 fluorescence decays (∇ = 180 ps; \blacktriangle = 450 ps; \bullet = 1.2 ns; \square = 4.6 ns). The lines between the points are just drawn in order to visualize the spectral distribution of the components.

sary in order to obtain a good adjustment. Under the same conditions, the value we measured for a solution of C_{60} in toluene was 1.2 ns as usually observed [27]. The result obtained for the C_{60} powder is clearly different from those published by other authors but seems to be in accordance with the fact that the dynamics of deactivation of the singlet $^1C_{60}$ state in the solution and in the solid are rather different. In solution, the yield of triplet state formation ($\Phi_{C_{60}}^3$) has been established to be close to unity [28]; in contrast in the solid state at room temperature almost no triplet state formation has been observed and the singlet $^1C_{60}$ state has been measured to decay in the picosecond timescale [29]. The explanation of the bi-exponential behavior that we noticed is not clearly understood. We observed that the contribution yield of both lifetimes to the emission spectrum also depends on the region where we excited the sample. This result could be interpreted assuming a heterogeneity of the sample, one emission originating from

the surface and the other from the core of the C_{60} crystal.

As for the powder sample, the lifetime analysis of the emission of the C_{60} /VPI-5 sample shows clearly a non-mono-exponential behavior of the emission. At least three lifetimes were necessary to achieve a good adjustment at each emission wavelength. The global analysis of decays ranging from 830 to 540 nm gave a solution involving five lifetimes (spectrally distributed), respectively: 10–80 ps, 180 ps, 450 ps, 1.2 ns and 4.6 ns. The contribution of each lifetime to the emission spectrum, calculated as the product of each component yield with the corresponding emission spectrum is presented Fig. 5. The fluorescence lifetime analysis of the pure VPI-5 sample leads to the conclusion that two of these lifetimes could be attributed to the matrix: the longer 4.6 ns component and at least in the 500 nm region the medium 450 ns component. The 10–80 ps lifetime (< 2% of the total fluorescence) was also observed in the matrix. Even if the use of this short component in the decay analysis is absolutely necessary, we decided to ignore it since: (1) it is at the limit of our possibility of detection; and (2) it could be an artifact of the convolution.

The contributions of the 180 and 450 ps lifetime emissions are in agreement with both lifetime and spectral signature of the C_{60} powder. The slight deviation at short wavelength of the yield of the 450 ps component from the spectrum of the C_{60} powder has been attributed as previously mentioned to the emission of the matrix. From these observations it seems to be clear that the contributions of the peaks at 800 and 730 nm originate from C_{60} aggregated molecules not incorporated in the pores, but mixed or adsorbed to the zeolite. In order to verify this assignment, we performed some other experiments on new samples abundantly rinsed with benzene. The emission spectrum of such a sample is presented in Fig. 5b. The lifetime analysis of the fluorescence of these samples shows an important decrease of the yield of the emission of both the 180 and 450 ps components (12% against 46% and 17% against 29% at 750 nm, respectively).

Finally, all these results suggest that the contribution of the C_{60} incorporated in the matrix can be attributed mainly to the 1.2 ns component. The shape of the calculated difference spectrum (Fig. 5c) is in

accordance with the calculated distribution of the 1.2 ns component. The discrepancy of the amplitude of these two spectra could be due to the way we calculate the difference between the VPI-5 and C₆₀/VPI-5 spectra but also to a heterogeneity of the sample. Effectively, the analysis of decays collected with an excitation set on a different part of the sample gave a different ratio of yield. This result suggests that the incorporation is not homogenous.

All these results are in agreement with those obtained using the streak camera device. On this system whichever the excitation domain and temperature (272 or 514.5 nm, 8 or 300 K) the emission spectra are broad and reveal as before a continuum like behavior with a smooth maximum around 500 nm (272 nm excitation, 8 K) or 540 nm (514.5 nm, 300 K). Two minor peaks at 730 and 800 nm are visible. These peaks can be associated with those of C₆₀ crystals as mentioned previously. At 8 K no fine structure was resolved. At this temperature the temporal luminescence analysis at 500 nm shows a tri-exponential decay with 200 ps, 940 ps and ~ 35 ns emission lifetimes, respectively. This result is in agreement with the values we found previously (80 ps, 180 ps, 450 ps, 1.2 ns and 4.6 ns) even if only three lifetimes are necessary for the fit. The adjustment using more than three exponential decays is more difficult in streak camera data analysis since the statistic of the noise of the signal is unknown in contrast to the photon counting technique where the Poissonian structure of the noise is used as a criterion. We think that the calculated value of 940 ps is in fact an average of the 450 ps and 1.2 ns components. At 8 K a decrease of the rate constant of internal conversion is expected and thus an increase of the emission lifetime should be observed. This could explain the longer lifetime (35 ns) and the lower yield of the longer component compared to what we observed in photon counting experiments at room temperature.

At room temperature under 514.5 nm excitation three lifetimes were estimated: 200 ps, 570 ps and 3.1 ns. These results, for the same reason as discussed above, are consistent with those obtained in the photon counting experiments.

As a conclusion from the whole photoluminescence analysis, solely the 1.2 ns lifetime, which is observed in a region where the C₆₀ in the solid state

does not emit, can be attributed to the fluorescence emission of the C₆₀ molecules incorporated in the pores of the VPI-5 zeolite. The 1.2 ns lifetime is similar to the one measured for organic solutions of C₆₀ where the C₆₀ molecules are in a solvent shell and do not interact each other like in aggregates or in the molecular fullerene crystal. In solution the photoluminescence spectrum is broadened too as compared to solid C₆₀, the maximum also being blue shifted. As already discussed by Zhu et al. [15], the symmetry lowering effect of C₆₀ insertion within the cages makes forbidden transition of C₆₀ allowed in the matrix because the momentum selection rules are broken.

This emission could be interpreted as a deactivation process which converts the upper levels of photoexcited C₆₀ in the matrix to ground states, these upper levels resulting from the confinement of C₆₀ in the zeolite cages.

The quenching of the upper excited states can be achieved by photoactivated electron transfer from the embedded C₆₀ molecules to the oxygen atoms of the inner shells of the zeolite cages. As already mentioned by Wang et al. [25] the formal oxidation state of C₆₀ interacting with oxygen (C₆₀⁺, O⁻) increases the gap between the HOMO and the LUMO as compared to crystalline C₆₀.

4. Conclusions

Our data confirm that the method of Anderson et al. [9] for incorporation of fullerene C₆₀ within the open molecular cages of the zeolite VPI-5 from a benzene solution following thermal treatment of the inorganic matrix was shown to be suitable for actual insertion of the spherical chromophore in the porous matrix. Evidence for the incorporation of C₆₀ into the supercages of the VPI-5 matrix was obtained unambiguously from the strong decrease of the ¹²⁹Xe-NMR signal when VPI-5 samples were treated with the C₆₀ in a benzene solution.

UV visible absorption and emission spectra are consistent with interaction of the surrounding matrix. The confinement effects, which lowers the high symmetry of the fullerene molecules might explain, the white continuum type photoluminescence, the broadening of the absorption spectrum and presumably

charge transfer processes between the C_{60} and the oxygen atoms of the surrounding matrix. This special polar environment is responsible of the shift of the absorption bands as has been shown for C_{60} small aggregates interacting with other polar interfaces [7].

Acknowledgements

We are very indebted to Dr. M. Davis for the gift of the VPI-5 sample.

References

- [1] M. Diack, R.L. Hettich, R.N. Compton, G. Guiochon, *Anal. Chem.* 64 (1992) 2143.
- [2] A. Gügel, K.J. Müllen, *Chromatography* 628 (1993) 23.
- [3] A. Gügel, K.J. Müllen, *Chromatography* 37 (1993) 387.
- [4] A. Buvári-Barcza, L. Barcza, T. Braun, I. Konkoly-Thege, K. Ludanyi, K. Vékely, *Fullerene Sci. Technol.* 5 (1997) 311.
- [5] A. Ikeda, M. Yoshimura, S. Shinkai, *Tetrahedron Lett.* 38 (1997) 2107.
- [6] R.V. Bensasson, E. Bienvenue, M. Dellinger, S. Leach, P. Seta, *J. Phys. Chem.* 98 (1994) 3492.
- [7] N.S. Sariciftci, L.S. Smilowitz, A.J. Heeger, F. Wuld, *Synth. Met.* 59 (1993) 333.
- [8] L. Zhu, Li.Y. Wang, J. Shen, *J. Appl. Phys.* 77 (1995) 2801.
- [9] M.W. Anderson, J. Shi, D.A. Leigh, A.E. Moody, F.A. Wade, B. Hamilton, S.W. Carr, *J. Chem. Soc., Chem. Commun.* (1993) 533.
- [10] J.E. Wray, K.C. Liu, C.H. Chen, W.R. Garrett, M.G. Payne, P. Codert, D. Templeton, *Appl. Phys. Lett.* 21 (1994) 2785.
- [11] A.W. Jensen, S. Wilson, D.I. Schuster, *Bioorg. Med. Chem. Lett.* 4 (1996) 767.
- [12] G. Sauvé, N.M. Dimitrijevic, P.V. Kamat, *J. Phys. Chem.* 99 (1995) 1199.
- [13] C. Zhang, X. Xiao, G. Weikun, M.M.T. Loy, W. Dazhi, Z. Qijin, Z. Jian, *Appl. Phys. Lett.* 68 (1996) 943.
- [14] B. Hamilton, J.S. Rimmer, M. Anderson, D. Leigh, *Adv. Mater.* 5 (1993) 583.
- [15] L. Zhu, Y. Li, J. Wang, J. Shen, *Chem. Phys. Lett.* 239 (1995) 393.
- [16] M.E. Davis, C. Montes, J.M. Garces, Zeolite synthesis, in: M.L. Occelli, H.E. Robson (Eds.), *ACS Symp Ser.*, Am. Chem. Soc., Washington, DC, 1989, p.291.
- [17] A.K. Jameson, C.J. Jamesson, H.S. Gutowsky, *J. Chem. Phys.* 53 (1970) 2310.
- [18] R. Ryoo, S.B. Liu, L.C. de Ménorval, K. Takegoshi, B. Chmelka, A. Pines, *J. Phys. Chem.* 91 (1987) 6575.
- [19] L.C. de Menorval, D. Raftery, S.B. Liu, K. Takegoshi, R. Ryoo, A. Pines, *J. Phys. Chem.* 94 (1990) 27.
- [20] B.F. Chmelka, J.G. Pearson, S.B. Liu, R. Ryoo, L.C. de Menorval, A. Pines, *J. Phys. Chem.* 95 (1991) 303.
- [21] J.F. Wu, T.L. Chen, L.J. Ma, M.W. Lin, S.B. Liu, *Zeolites* 12 (1992) 86.
- [22] Q.J. Chen, J. Fraissard, H. Gauffriez, J.L. Guth, *Zeolites* 11 (1991) 534.
- [23] T. Ichihashi, K. Tanigaki, T.W. Ebbesen, S. Kuroshima, S. Iijima, *Chem. Phys. Lett.* 190 (1992) 179.
- [24] S.Y. Wang, W.Z. Shen, X.C. Shen, *Appl. Phys. Lett.* 67 (1995) 783.
- [25] D. Wang, J. Zuo, Q. Zhang, Y. Luo, Y. Ruau, Z. Wang, *J. Appl. Phys. Lett.* 81 (1997) 1413.
- [26] G. Gu, W. Ding, G. Cheng, S. Zhang, Y. Du, S. Yang, *Chem. Phys. Lett.* 270 (1997) 135.
- [27] L. Yang, R. Dorsinville, *Opt. Commun.* 124 (1996) 45.
- [28] J.L. Anderson, Y.Z. An, Y. Rubin, C.S. Foote, *J. Am. Chem. Soc.* 116 (1994) 9763.
- [29] M. Ichida, M. Sakai, T. Tajima, A. Nakamura, *Prog. Cryst. Growth Charact.* 33 (1998) 125.

Layered Mixed-Metal Phenylphosphonates, $Mn_xCo_{1-x}(O_3PC_6H_5)\cdot H_2O$: Structure and Magnetic Properties

Jeffrey T. Culp,* Gail E. Fanucci,*¹ Brian C. Watson,† A. Nicole Morgan,† Rénal Backov,* Hitoshi Ohnuki,*² Mark W. Meisel,†³ and Daniel R. Talham*³

*Department of Chemistry; and †Department of Physics and Center for Ultralow Temperature Research, University of Florida, Gainesville, Florida 32611-7200
E-mail: talham@chem.ufl.edu

Received March 20, 2001; accepted March 21, 2001

IN DEDICATION TO THE LATE PROFESSOR OLIVIER KAHN FOR HIS PIONEERING CONTRIBUTIONS TO THE FIELD OF MOLECULAR MAGNETISM

Mixed metal phenylphosphonates of composition $Mn_xCo_{1-x}(O_3PC_6H_5)\cdot H_2O$ were prepared with $0 \leq x \leq 1$. Atomic absorption, X-ray powder diffraction, and electron paramagnetic resonance measurements indicate that the mixed-metal solid solutions are homogeneous and isostructural with the single-metal-parent compounds over the entire concentration range, with a small, systematic evolution of the a and c in-plane unit cell parameters. The temperature dependence of the magnetic data for the pure Mn^{2+} ($x = 1$) and pure Co^{2+} ($x = 0$) samples was fitted by standard 2D Heisenberg and 2D Ising models, respectively, yielding nearest-neighbor exchange interaction energies of $J = -2.27 \pm 0.02$ K for $Mn(O_3PC_6H_5)\cdot H_2O$ and $J = -2.43 \pm 0.05$ K for $Co(O_3PC_6H_5)\cdot H_2O$. The magnetic phase diagram, down to 2 K, was constructed over the entire composition range. Both dc and ac magnetic susceptibilities were used to identify the transitions to low temperature, long-range-ordered antiferromagnetic states. In the Mn^{2+} - and Co^{2+} -rich regions, the ordering temperature, T_N , decreases relative to the pure materials, as expected for magnetic ion impurity doping. For intermediate values of x , Mn^{2+} - Mn^{2+} interactions dominate, resulting in a minimum in T_N near $x = 0.25$. A weak negative magnetization was observed for $x < 0.25$. No evidence of spin glass behavior was observed for any concentration at any temperature. © 2001 Academic Press

Key Words: magnetic phase diagram; canted antiferromagnet; mixed-metal; solid solution; manganese; cobalt; phenylphosphonate; magnetism.

INTRODUCTION

Even before Clearfield's and Smith's elucidation of the structure of the prototype α -Zr(HPO₄)₂·H₂O (1), layered

¹ Current address: Department of Chemistry, University of Virginia, Charlottesville, VA 22904-4319.

² Current address: Tokyo University Mercantile Marine, Applied Physics Laboratory, Koto Ku, Etchujima 2-1-6, Tokyo 1358533, Japan.

³ To whom correspondence should be addressed.

metal phosphates were extensively studied primarily because of their ion exchange capabilities (2). This initial interest has been extended to metal phosphonates where similar architectures are found (3–7) and now includes organic networks that can be varied to further modify the properties of the layered solids (8–13). Recently, layered metal phosphates and phosphonates have been shown to exhibit interesting magnetic phenomena, including magnetic ordering, canted antiferromagnetism (14–21), and antiferromagnetic resonance (22), and they have been studied as models for two-dimensional (2D) magnetism. Our group has also extended these studies from the solid-state (22, 23), to monolayer (24–27) and multilayer thin films (28–33), where similar properties have been observed.

As part of our interest in 2D magnetism in metal phosphonate solids and thin films, we have investigated a series of mixed-metal Mn^{2+}/Co^{2+} and Mn^{2+}/Zn^{2+} phenylphosphonates. Two possibilities exist if mixed metal phases form, each giving rise to different magnetic behavior. If ions of a different spin state organize in an ordered fashion, then a new superstructure is formed, giving rise to the possibility of ferrimagnetism if the spin state of the two ions is different. Alternatively, if the ions distribute randomly, then a solid solution results. Historically, mixed-metal solid solutions have been extensively studied (34) because they exhibit altered magnetic behavior and provide an opportunity for studying the details of magnetic ordering mechanisms. Systems based on Mn^{2+}/Co^{2+} have been popular choices, as the materials cover a range of dimensions, from quasi-1D (35–37) to quasi-2D (38) to 3D (39), and in most cases an isotropic (Heisenberg-type) interaction describes the coupling between $S = \frac{5}{2}$ spins of Mn(II) ions, while an anisotropic (Ising-type) interaction describes the coupling between "effective" $S = \frac{1}{2}$ spins of Co(II). Consequently, upon dilution these materials experience an interesting blend of competing spin and lattice dimensions. Despite previous studies on mixed-metal solids, there are still some unanswered

questions. For example, in some cases, but not all, the combination of random mixing and magnetic frustration leads to spin glass behavior (40). In addition, some ferrimagnetic systems have exhibited the interesting effect of negative magnetization (41, 42). New examples of mixed-metal magnetic systems, either structurally ordered or as solid solutions, can provide the opportunity to further study some of these phenomena.

The divalent metal phenylphosphonates form an isostructural series (Fig. 1) (5), and we find that the mixed-metal analogues form as solid solutions of formula $Mn_xCo_{1-x}(O_3PC_6H_5) \cdot H_2O$ or $Mn_xZn_{1-x}(O_3PC_6H_5) \cdot H_2O$. At low temperature, the pure Mn^{2+} and pure Co^{2+} phenylphosphonates experience long-range antiferromagnetic order at $T_N \approx 12$ and 4 K, respectively. Upon dilution, the ordering temperatures are reduced compared to the values found for the pure compounds, and the resulting magnetic phase diagrams are reported here. For diamagnetic Zn^{2+} doping, i.e., Mn_xZn_{1-x} , the reduction of T_N follows the prediction of mean field theory for $x > 0.6$ and this magnetic phase diagram was reported previously (43). However, for the Mn_xCo_{1-x} compounds, the reduction of T_N with doping concentration is weaker than expected on the basis of mean field theory. For Mn_xCo_{1-x} at low temperatures, the magnetization of the Mn-rich specimens, i.e., $x > 0.25$, is characterized by canted antiferromagnetic behavior. On the other hand, the magnetization of the Co-rich specimens, i.e., $x < 0.25$, exhibits a very small negative magnetization behavior when the zero-field cooled and field-cooled data are compared. The magnetic phase diagram for $Mn_xCo_{1-x}(O_3PC_6H_5) \cdot H_2O$ is reported here.

EXPERIMENTAL

Materials used. Reagent grade $Mn(NO_3)_2 \cdot 4H_2O$, $CoCl_2 \cdot 6H_2O$ and phenylphosphonic acid ($C_6H_5PO_3H_2$, 95%) were purchased from Aldrich (Milwaukee, WI) and used without further purification. The water used in all reactions was purified with a Barnstead NANOpure purification system that produced water with an average resistivity of 18 M Ω cm. $Mn(O_3PC_6H_5) \cdot H_2O$ and $Co(O_3PC_6H_5) \cdot H_2O$ were synthesized by mixing equimolar amounts of the appropriate metal ion solution with a solution of phenylphosphonic acid (pH adjusted to 5–6 with 0.1 M KOH) both heated to 60°C prior to mixing. The solutions were allowed to stir for 2 h at this temperature. For each sample, the precipitate was filtered, washed with water and subsequently with acetone, and then dried under vacuum.

Preparation of $Mn_xCo_{1-x}(O_3PC_6H_5) \cdot H_2O$ compounds. The mixed-metal phenylphosphonates $Mn_xCo_{1-x}(O_3PC_6H_5) \cdot H_2O$ were prepared in a manner similar to that of the pure metal phenylphosphonates but with slight modification. In each case, aqueous solutions of the metal salts in

the desired molar ratios were heated to 60°C and added to a solution containing a slight excess of phenylphosphonic acid at pH 5–6. The resultant solutions were stirred for only 10 min. before filtering the precipitate. The products were washed with water and acetone, and finally dried under vacuum. In all cases, the final Mn:Co ratios (determined by atomic absorption) of the solid-state materials were similar, i.e., within 10%, to those of the starting metal salt solutions.

Instrumentation. Atomic absorption (AA) measurements were performed on a Perkin-Elmer Model 3100 atomic absorption spectrometer with a photomultiplier tube detector. For AA analysis, the solid-state samples were dissolved in a 1.0 M HCl solution. X-ray diffraction was done with a step scan (0.02° 2 θ /step, 2 s/step) using a Philips APD 3720 X-ray powder diffractometer with the $CuK\alpha$ line as the source. Electron paramagnetic resonance (EPR) spectra were recorded on a Bruker (Billerica, MA) ER 200D spectrometer modified with a digital signal channel and a digital field controller. Data were collected using a U.S. EPR (Clarksville, MD) SPEC300 data acquisition program and converted to ASCII format using a U.S. EPR EPRDAP data analysis program. Magnetization and ac susceptibility measurements were performed using a Quantum Design MPMS SQUID magnetometer. The dc measurements were made with a measuring field of 100 G or 1.0 kG when sweeping the temperature, or were made at 2 K while sweeping the field up to 50 kG. The ac susceptibility measurements used frequencies ranging from 17 Hz to 1.5 kHz and an ac field amplitude of 4.0 G. Additional low-frequency (19 Hz) ac susceptibility measurements were performed with a homemade mutual inductance coil of a standard design (44). High-frequency (14 MHz) studies were conducted in a homemade tank-circuit biased with tunnel diode (44, 45). For all of the magnetic studies, powder samples were contained in gelcaps or plastic vials, with the exception of the work performed at 14 MHz when the sample was loaded directly into the housing of the coil. The background signals arising from the gelcaps and vials were independently measured and were either negligible or subtracted from the data.

RESULTS AND DISCUSSION

Sample preparations. In order to encourage homogeneous solid solutions of composition $Mn_xCo_{1-x}(O_3PC_6H_5) \cdot H_2O$, and to prevent any annealing into a multiphased system, samples were quickly precipitated and collected immediately. This procedure resulted in a decreased crystallinity of the solid solutions, relative to what is possible with the pure phases, although it is sufficient for powder XRD analyses and does not appear to influence the magnetic properties. All attempts to prepare mixed-metal

samples of high crystallinity by slow-growth techniques resulted in the formation of physical mixtures and/or multi-phase materials.

Structural characterizations. The relative percentage of manganese and cobalt in the solid solutions was determined from AA analyses (Table 1). Although AA spectroscopy gives an average stoichiometry, it cannot provide information about the structural homogeneity of the samples. Therefore, X-ray diffraction was used to determine if the final product consists of single or multiple phases. The structures of the pure manganese and cobalt phenylphosphonate compounds consist of layers of quasi-two-dimensional metal-phosphorus-oxygen sheets that define the *ac* plane, while the organic moieties project between the layers, thus defining the *b* axis (Fig. 1) (4, 5). These materials are known to crystallize in the same space group, $Pmn2_1$, with slight modifications of the *ac* basal plane spacings (4, 5). However, the interplane distances are almost identical because both compounds contain the same organic phenyl group.

Due to the symmetry of the $Pmn2_1$ space group, the 100 and 001 reflections are systematically absent, so the highest order reflections containing in-plane structural information are the 110 and 011. Although both of these reflections contain an interplane contribution, this distance remains essentially constant for all compositions. The 110, 030, and 011 reflections conveniently occur consecutively over a small range of 2θ in the X-ray diffractogram, making them a practical series for monitoring variations in the *ac* lattice spacings. The position of the 030 reflection in all samples is an internal reference that confirms that the interplane distances do not change as a function of doping, allowing the 2θ values for the 110 and 011 reflections in the doped

TABLE 1
Concentration of Manganese in $Mn_xCo_{1-x}(O_3PC_6H_5) \cdot H_2O$ Determined from AA Spectroscopy and Unit Cell Parameters from the 110, 011, and 030 *hkl* Reflections in the Corresponding Powder XRD Patterns

Mol % Mn	$a \pm 0.01$	$b \pm 0.01$	$c \pm 0.01$
100	5.73	14.34	4.94
95	5.73	14.34	4.94
82	5.70	14.34	4.92
68	5.68	14.34	4.90
55	5.66	14.34	4.88
35	5.65	14.34	4.88
30	5.64	14.34	4.87
21	5.62	14.34	4.86
19	5.63	14.34	4.85
11	5.61	14.34	4.85
10	5.61	14.34	4.85
0	5.60	14.34	4.83

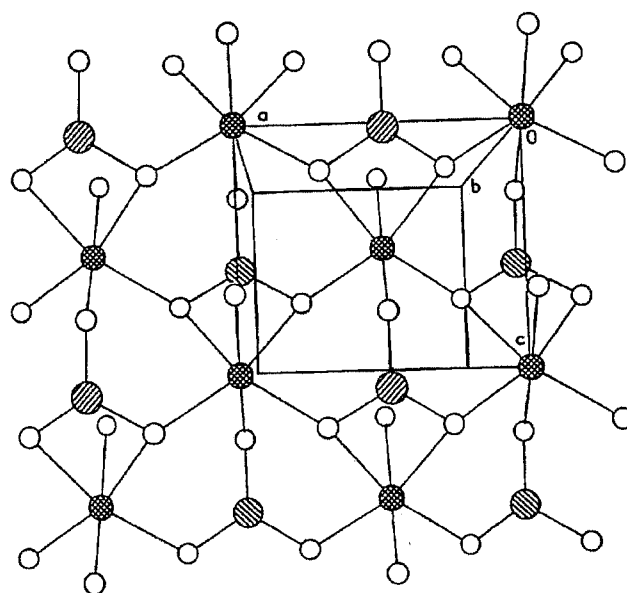


FIG. 1. In-plane and cross-sectional view of $Mn(O_3PC_6H_5) \cdot H_2O$. Crystallographic data are taken from Ref. (5). Key: oxygen, small open circles; manganese, cross-hatched circles; phosphorus, diagonal-hatched circles (phosphorus atoms above and below the plane are distinguished by hatches with different directions).

materials to be used to determine the in-plane lattice spacings.

Powder XRD patterns for the pure manganese and pure cobalt phenylphosphonates, as well as that of the $Mn_{0.35}Co_{0.65}$ sample, are shown in Fig. 2. The similarity of the patterns in Fig. 2A makes it clear that the mixed-metal systems are isostructural with the parent compounds. An expansion of the region between 2θ values of 16° – 20° in Fig. 2B shows the 110, 030, and 011 reflections for the same three compounds. For the mixed-metal example, discrete 110 and 011 reflections are observed at 2θ values between those of the pure Mn^{2+} and Co^{2+} phases, while the 030

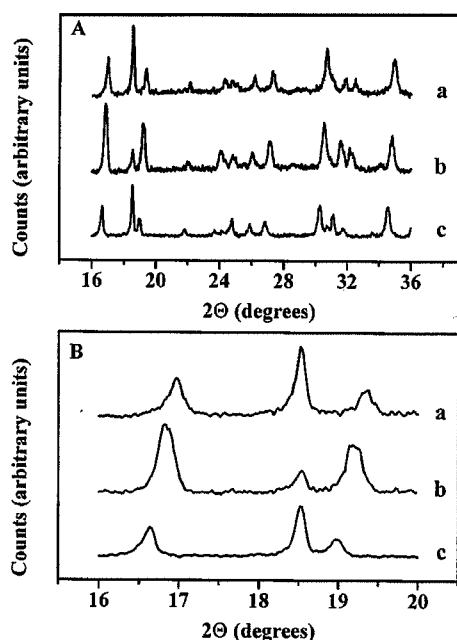


FIG. 2. (A) XRD powder patterns for (a) $\text{Co}(\text{O}_3\text{PC}_6\text{H}_5)\cdot\text{H}_2\text{O}$, (b) $\text{Mn}_{0.35}\text{Co}_{0.65}(\text{O}_3\text{PC}_6\text{H}_5)\cdot\text{H}_2\text{O}$, and (c) $\text{Mn}(\text{O}_3\text{PC}_6\text{H}_5)\cdot\text{H}_2\text{O}$. (B) Expansion showing, from left, 110, 030, 011 hkl reflections for (a) $\text{Co}(\text{O}_3\text{PC}_6\text{H}_5)\cdot\text{H}_2\text{O}$, (b) $\text{Mn}_{0.35}\text{Co}_{0.65}(\text{O}_3\text{PC}_6\text{H}_5)\cdot\text{H}_2\text{O}$, and (c) $\text{Mn}(\text{O}_3\text{PC}_6\text{H}_5)\cdot\text{H}_2\text{O}$.

reflection remains the same for all three samples. These observations are consistent with the formation of a single homogeneous solid solution. Similar results were seen for all compositions, and Table 1 lists the corresponding a , b , c cell parameters for the pure and doped materials as calculated from the 110, 030, and 011 reflections. The cell edge lengths systematically shift in value as a function of x . The absence of any reflections corresponding to the pure single-ion phenylphosphonates in the XRD patterns of the mixed-metal phenylphosphonates, combined with the observation that the detected reflections have 2θ values between those of the two pure compounds, provides convincing evidence that single-phase solid solutions have been formed.

Electron paramagnetic resonance. Evidence for microscopic homogeneity of the solid solutions comes from EPR. The cobalt phosphonate is EPR silent at X-band, while the manganese analog gives a broad line that is structureless as a result of dipolar interactions (Fig. 3) (46). The anisotropy of the EPR linewidth has previously been used to demonstrate the two-dimensional exchange pathways in the layered manganese phosphonates (23, 46). As the percentage of Co^{2+} in the solid solution increases, the Mn^{2+} signal broadens (Fig. 3), reflecting the randomization of the identity of the Mn^{2+} ion's nearest neighbors. In the solid solution, there is no signal due to crystallites of pure $\text{Mn}(\text{O}_3\text{PC}_6\text{H}_5)\cdot\text{H}_2\text{O}$.

Magnetic properties of $\text{Mn}(\text{O}_3\text{PC}_6\text{H}_5)\cdot\text{H}_2\text{O}$ and $\text{Co}(\text{O}_3\text{PC}_6\text{H}_5)\cdot\text{H}_2\text{O}$. The magnetic properties of several manganese and cobalt organophosphonates have been studied previously (15, 16, 18, 19, 22). The manganese phosphonates undergo a long-range ordering transition to a canted antiferromagnetic state at temperatures ranging from 12 to 18 K, depending on the identity of the organophosphonate. Pure $\text{Mn}(\text{O}_3\text{PC}_6\text{H}_5)\cdot\text{H}_2\text{O}$ orders at $T_N \approx 12$ K (22). The cobalt phosphonates also order antiferromagnetically, and for $\text{Co}(\text{O}_3\text{PC}_6\text{H}_5)\cdot\text{H}_2\text{O}$, we observe $T_N \approx 4$ K, as we describe later in this section.

The data in Fig. 4 show the temperature dependence of the static magnetic susceptibility of the pure Mn and Co materials, acquired by cooling the samples in zero magnetic field and measuring in a dc field of 1 kG. The broad maximum in the susceptibility, χ_{max} , is characteristic of low-dimensional antiferromagnetic interactions when short-range order correlations become greater than the thermal fluctuations of the spins. These short-range correlations are established by magnetic exchange interactions, J , which are typically considered to be limited to nearest neighbor spins. In other words, the Hamiltonian may be written as

$$\mathcal{H} = -J \sum_{mn} \mathbf{S}_i \cdot \mathbf{S}_j, \quad [1]$$

where \sum_{mn} runs over all pairs of nearest neighbor spins \mathbf{S}_i and \mathbf{S}_j . The susceptibility data for the manganese phosphonate may be fitted with a 2D high-temperature series expansion (47) for a quadratic layer of Heisenberg $S = \frac{5}{2}$ spins based on Eq. [1], and the solid line in Fig. 4A shows the best fit to the data with $J = -2.27 \pm 0.02$ K. The fit was restricted to $T > 20$ K since at lower temperatures the

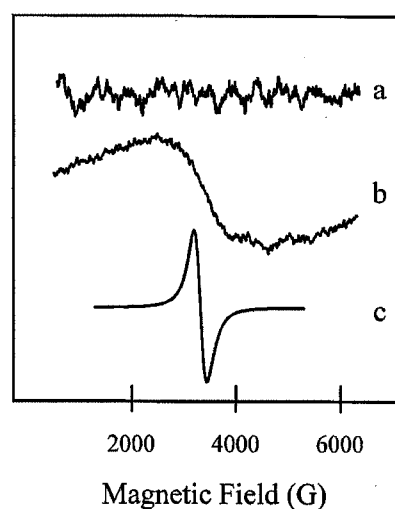


FIG. 3. Room temperature EPR signals for (a) $\text{Co}(\text{O}_3\text{PC}_6\text{H}_5)\cdot\text{H}_2\text{O}$, (b) $\text{Mn}_{0.84}\text{Co}_{0.16}(\text{O}_3\text{PC}_6\text{H}_5)\cdot\text{H}_2\text{O}$, and (c) $\text{Mn}(\text{O}_3\text{PC}_6\text{H}_5)\cdot\text{H}_2\text{O}$.

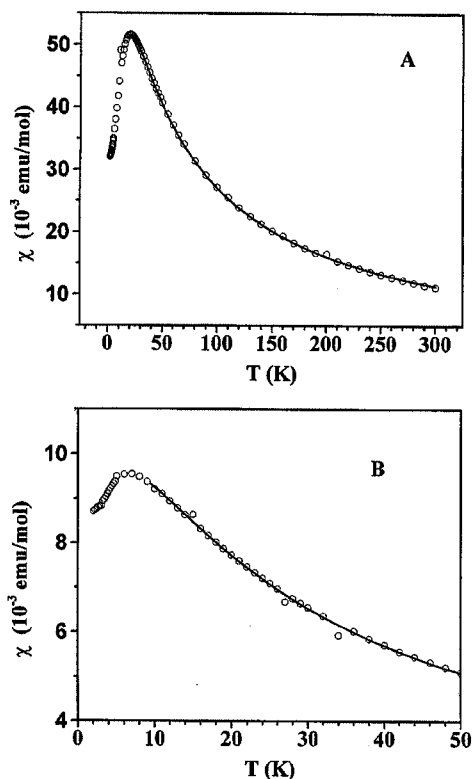


FIG. 4. (A) The temperature dependence of the DC magnetic susceptibility for $\text{Mn}(\text{O}_3\text{PC}_6\text{H}_5) \cdot \text{H}_2\text{O}$ after zero field cooling the specimen to 2 K and then measuring in a field of 1 kG. The results of a fit using a $S = \frac{5}{2}$ Heisenberg high-temperature expansion for $T > 20$ K are shown by the solid line with the result $J = -2.27 \pm 0.02$ K, as described in the text. (B) The temperature dependence of the DC magnetic susceptibility for $\text{Co}(\text{O}_3\text{PC}_6\text{H}_5) \cdot \text{H}_2\text{O}$ after zero-field cooling the sample to 2 K and then measuring in a field of 1 kG. The results of a fit using an $S = \frac{1}{2}$ Ising high-temperature expansion for $T > 9.5$ K are shown by the solid line with the result $J = -2.43 \pm 0.05$ K, as described in the text.

fitting procedure is not valid. In the case of the pure cobalt phenylphosphonate, Eq. [1] still describes the simplest interactions for the case of this 2D, $S = \frac{1}{2}$ Ising system when the spin operators are restricted to their z components (48). The solid line in Fig. 4B is a fit, for $T > 9.5$ K, to a 2D, $S = \frac{1}{2}$ Ising high-temperature series expansion (49), using an exchange constant of $J = -2.43 \pm 0.05$ K. It is noteworthy that the magnetic exchange parameters are very similar despite the significantly different spin values and spin dimension.

Previous studies (22) have identified the ordering in $\text{Mn}(\text{O}_3\text{PC}_6\text{H}_5) \cdot \text{H}_2\text{O}$ as a transition to a canted antiferromagnetic state in analogy to other manganese organophosphonates (15). The magnetic moments assume a noncollinear orientation that produces a weak ferromagnetic moment that lies within the plane of the manganese ions. This moment, and hence the transition from the paramagnetic to the canted antiferromagnetic state, can be ob-

served in a difference plot of the magnetization as a function of temperature for experiments performed in field-cooled (fc) and zero-field-cooled (zfc) conditions, $\Delta M_{\text{fc-zfc}}$ (Fig. 5). The ordering temperature, T_N , may be identified in the M_{fc} data as the temperature where the magnetization begins to deviate from its high-temperature paramagnetic behavior, and from Fig. 5, $T_N = 11.7$ K for $\text{Mn}(\text{O}_3\text{PC}_6\text{H}_5) \cdot \text{H}_2\text{O}$. Another parameter, T_N^* , is defined as the temperature at which $\Delta M_{\text{fc-zfc}}$ differs significantly from 0. These two temperatures, $T_N = 11.7$ K and $T_N^* = 11.5$ K, are identifiable in Fig. 5. The value of T_N^* changes as a function of the magnitude of the applied measuring field and as a result, for small values of T_N , it is best to acquire data with a smaller measuring field, typically 50–100 G. Due to this dependence upon the measuring field, it is important to realize that T_N^* will always be lower than T_N , but T_N^* is nevertheless evidence of an ordered state with a weak ferromagnetic moment. In contrast to the weakly ferromagnetic manganese compound, the pure cobalt compound is antiferromagnetic with $T_N = 3.9$ K, as determined from both dc magnetization and ac susceptibility measurements.

Magnetic properties of the solid solutions. Typical magnetization plots for the solid solutions $\text{Mn}_x\text{Co}_{1-x}(\text{O}_3\text{PC}_6\text{H}_5) \cdot \text{H}_2\text{O}$ with $0.25 < x < 1.00$ are shown in Fig. 6. The ordering temperatures identified in the magnetization vs temperature plots are consistent, within experimental

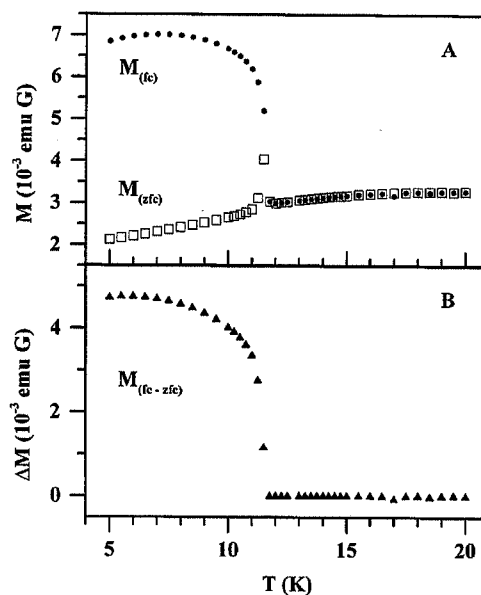


FIG. 5. (A) Field-cooled (FC) and zero-field-cooled (ZFC) magnetization data of manganese phenylphosphonate are shown as a function of temperature. Both data sets were acquired with a 100-G measuring field. (B) The difference between field-cooled and zero-field-cooled magnetization versus temperature for $\text{Mn}(\text{O}_3\text{PC}_6\text{H}_5) \cdot \text{H}_2\text{O}$ measured in a field of 100 G.

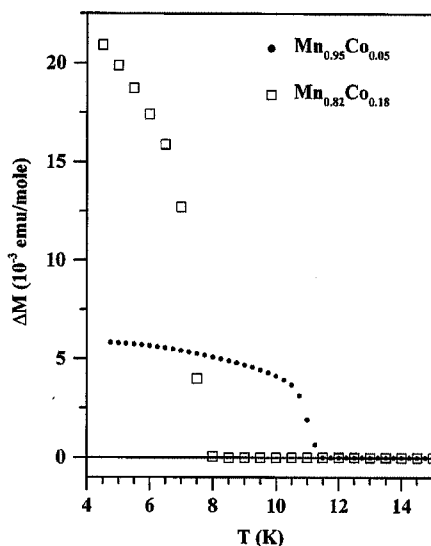


FIG. 6. The difference between the field-cooled and zero-field-cooled magnetization, ΔM , is shown as a function of temperature. Typical data from the Mn-rich (i.e., $x > 0.25$) samples are shown when the magnetic field, for measuring and field cooling, was 100 G.

resolution, with the temperatures of anomalies in the ac susceptibility studies. Like the pure $\text{Mn}(\text{O}_3\text{PC}_6\text{H}_5) \cdot \text{H}_2\text{O}$, the solid solutions with $x > 0.25$ form canted antiferromagnets in the low-temperature state. For $x < 0.25$, the $\Delta M_{f_c-zf_c}$ vs temperature plots still reveal the ordering temperature, but the magnitude of $\Delta M_{f_c-zf_c}$ is much smaller and negative, Fig. 7. This point is discussed further, later in this section. Nonetheless, the ordering temperatures were confirmed with ac susceptibility measurements, and they are included in Fig. 8.

The mixed Mn/Co phenylphosphonates can be thought of as magnetically doped pure manganese or pure cobalt lattices with the other metal ion as impurity. Consequently, a reduction of T_N from the pure systems is anticipated. Since the magnetic exchange interactions and lattices are similar, the primary differences are the spin values and the dimension of the spins (i.e., Ising-like or Heisenberg-like). Therefore, the reduction of T_N is not expected to be as strong as it is for the case of doping with diamagnetic spins, and these general tendencies are reflected in the phase diagram in Fig. 8. In the Mn-rich regime, $T_N(x)$ closely follows a linear function with an $x = 0$ intercept (solid line) at the T_N value obtained for the pure Co material. For $0.25 < x < 0.60$, the perturbation of the magnetic correlations is stronger as the percolation threshold is approached and the reduction of T_N follows a trend qualitatively represented by the dotted line. For the Co-rich samples, there is not sufficient resolution in the identification of T_N to allow a specific x dependence to be identified, so the general trend is sketched by the dashed line. The prediction of a tetracritical point at

$x = 0.25$ agrees well with a face-centered square planar lattice containing four nearest neighbors where one spin species dominates the magnetic exchange. In our case, the Mn^{2+} spins dominate the local magnetic environment. Tetracritical points (34, 50) have been observed previously in other doped magnetic systems containing competing magnetic anisotropies (51–54).

SEARCH FOR SPIN GLASS OR PRECURSOR PHASES

The assignment of the pure Mn^{2+} material as a canted antiferromagnetic $S = \frac{5}{2}$ Heisenberg-like system and the pure Co^{2+} system as a quantum antiferromagnetic $S = \frac{1}{2}$ Ising-like system opens the possibility of forming a spin-frustrated state in a randomly mixed Mn/Co system. In molecular magnetism, similar studies on layered materials have been reported. Thus, bimetallic oxalato layered mixed-metal compounds containing competing ferro- and antiferromagnetic interactions have been magnetically characterized and in some cases spin glass behavior has been observed (55). Spin-frustrated systems displaying magnetic properties characteristic of spin glasses have also been

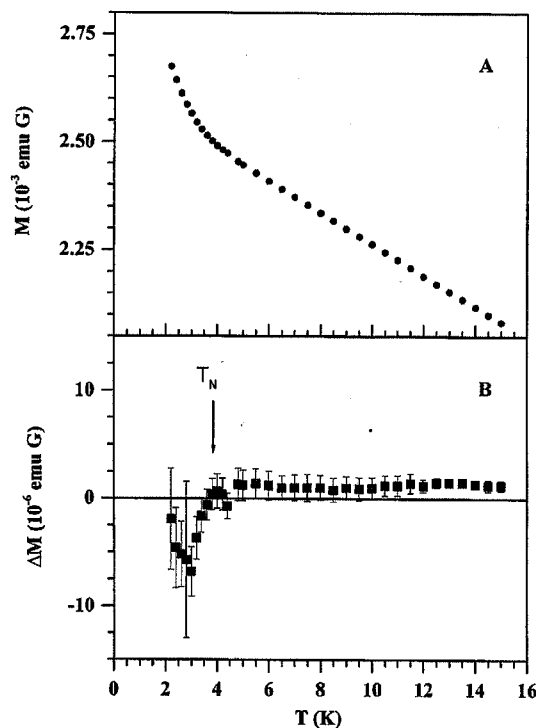


FIG. 7. (A) Field-cooled and zero-field-cooled dc magnetization for $x = 0.1$. Both data sets were acquired with a 100-G measuring field, and on this scale, the difference between the two data sets is not visually detectable. (B) The difference between field-cooled and zero-field-cooled magnetization from (A) is shown as a function of temperature. The onset of a negative magnetization occurs at T_N , and this signature is characteristic for all the Co-rich (i.e., $x < 0.25$) samples.

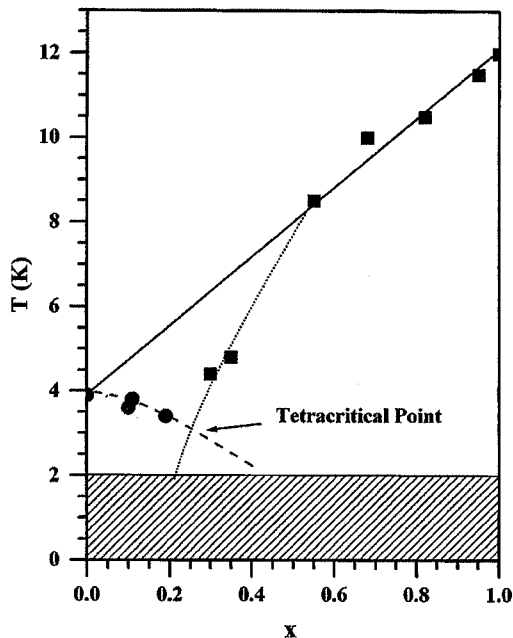


FIG. 8. The magnetic phase diagram of $\text{Mn}_x\text{Co}_{1-x}(\text{O}_3\text{PC}_6\text{H}_5) \cdot \text{H}_2\text{O}$ indicating the ordering temperature vs Mn^{2+} concentration. The phase diagram has a tetracritical point at $x = 0.25$, as described in the text. The present work was restricted to $T > 2$ K. The lines are guides for the eyes and are described in the text.

observed in doped magnetic materials possessing tetracritical points in their magnetic phase diagrams (35, 38, 56).

Time-dependent thermal remnant magnetization studies were performed with two samples, $x = 0.30$ and 0.68 . In one set of experiments, the samples were zero-field cooled from 300 K to 5, 7, and 12 K in three separate runs. The process of cooling from 300 K to the low-temperature fixed point required approximately 80 min. After equilibrium was established, a field of 1 kG was applied, and the magnetization was monitored for nominally 40 min. During this time, the magnetization was observed to relax toward an equilibrium value, and this process was easily fitted by a simple exponential function, yielding time constants ranging from 700 to 1100 s. In a different measurement, the magnetization relaxation rates of the sample holders were studied and were determined to be negligible. The total change of the signal during the measurement after achieving the equilibrium state, as defined by the thermometer of the instrument, was about 1%. Although these results may be suggestive of behavior associated with a spin glass state, we consider them to be related to the process of cooling the powder samples. A simple cooling model (57) provides a plausible explanation for the measured relaxation rates. It is noteworthy that the same type of behavior was observed for both samples and at all three of the temperatures that were studied. In other words, the experiments covered several of

the magnetic phases shown in Fig. 8, and in every instance, the behavior was always the same.

In a second set of studies, the ac susceptibility of samples was investigated. The temperature dependences of the real component of the ac susceptibility in applied magnetic fields of 0 and 1 kG are shown in Fig. 9 for $x = 0.82$. Our ac studies of all x reproduced, to within experimental resolution, the ordering temperatures seen in the dc magnetization data. However, when no external DC magnetic field was present, new peaks were observed in the ac susceptibility signals, and these features were not present in the dc magnetization data. Upon application of a 1 kG field, these features were suppressed and, therefore, can be attributed to the dynamics of the magnetic domains and the powder nature of the specimens. The temperatures of the transitions as measured by ac susceptibility did not appear to be frequency dependent from 17 Hz to 1.5 kHz. Therefore, no spin glass behavior was observed in any of the samples at any temperature $T > 2$ K.

In summary, no evidence of a spin glass state was obtained in our measurements. It is important to note, however, that a spin-flop transition has been observed in pure $\text{Mn}(\text{O}_3\text{PC}_6\text{H}_5) \cdot \text{H}_2\text{O}$ in magnetization vs field studies performed at 2 K (22), and a similar spin-flop transition is seen for the solid solution with $x = 0.84$. However, no spin-flop signatures were observed for samples with $x < 0.84$, where an increasing intrinsic background arising from competing magnetic spins may have masked the spin-flop transitions. Furthermore, we were particularly curious about the possibility of precursor behavior in the region near the tetracritical point, i.e., a region bounded by the solid, dotted, and

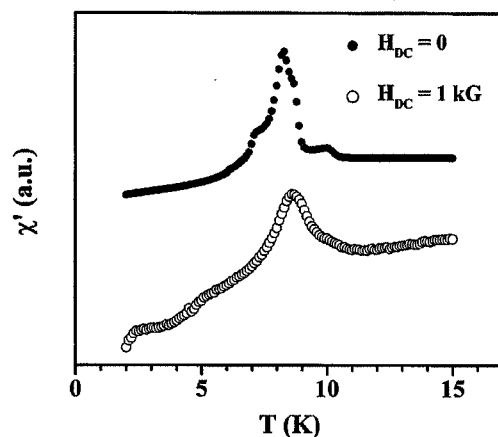


FIG. 9. The real component of the ac susceptibility for $\text{Mn}_{0.18}\text{Co}_{0.82}(\text{O}_3\text{PC}_6\text{H}_5) \cdot \text{H}_2\text{O}$ at 17 Hz and an amplitude of 4 G. The ac susceptibility was studied in an applied field of 0 and 1 kG, corresponding to the filled and open circles, respectively. The identification of T_N is consistent with the values determined by dc magnetization techniques. The ac response is understood as arising from the dynamics of the magnetic domains and the powder nature of the specimens, as described in the text.

broken lines in Fig. 8. However, as discussed at the beginning of this section, no magnetic glassy behavior was observed in this region. Finally, we note that for $x = 0.30$ and 0.35 , our studies down to 2 K did not reveal any anomalies indicative of crossing into an "intermediate" phase (34). Naturally, specific heat studies may provide additional information concerning the existence of and the identification of such a phase.

Negative magnetization in the cobalt-rich samples. For $x < 0.25$, ordering is observed, but the value of ΔM_{fc-zfc} is small and negative, Fig. 7. Features in the ac susceptibility are observed at the same temperatures, so we associate these temperatures with the transition to long-range antiferromagnetic order. The negative magnetization shifts observed for the Co-rich specimens contrast with the positive magnetization shifts detected for the Mn-rich materials. The phenomenon of negative magnetization has been identified previously in a variety of ferrimagnetic materials (41, 42). Naturally with the doped Co-rich specimens, similar arguments may be made if small regions of ferrimagnetic ordered phase are present. However, negative magnetization is also observed in the pure Co material, although it is even weaker than observed in the data shown in Fig. 7B. Negative magnetization has previously been observed in the canted antiferromagnet LaVO_3 (58), and the same phenomenon may be responsible for the behavior observed for the cobalt phase ($x < 0.25$).

CONCLUSION

A new series of mixed-metal phenylphosphonate solid solutions, $\text{Mn}_x\text{Co}_{1-x}(\text{O}_3\text{C}_6\text{H}_5) \cdot \text{H}_2\text{O}$, have been prepared and their magnetic properties investigated. Each composition undergoes long-range magnetic ordering to a canted antiferromagnetic state at temperatures, $T_N \leq 12$ K, and a magnetic phase diagram has been constructed based on individual dc and ac susceptibility measurements. For both the Mn^{2+} and Co^{2+} high concentration limits, T_N decreases relative to the pure single-ion phosphonates, consistent with what is expected for magnetic ion impurity doping. The phase diagram includes four phases with a tetracritical point at $x = 0.25$ K, indicating a competition between the Heisenberg-like Mn^{2+} and the Ising-like Co^{2+} spins, with the $S = \frac{5}{2}$ Mn^{2+} dominating the local environment. While prior studies on mixed-metal systems possessing competing spin types have shown evidence for spin glass behavior, no such state is observed in the $\text{Mn}_x\text{Co}_{1-x}(\text{O}_3\text{C}_6\text{H}_5) \cdot \text{H}_2\text{O}$ solid solutions.

ACKNOWLEDGMENTS

During the course of this work, we have benefited from conversations with A. Feher, M. Orendáč, and A. Orendáčova. This research was

supported by the National Science Foundation through Grants DMR-9900855 (D.R.T.), INT-9722935 (M.W.M), and DMR-9704225 (M.W.M). Special thanks are given to the Florida Major Analytical Instrumentation Center for use of XRD facilities and to Dr. Katherine Williams and Mr. Russell Pierce for use of the atomic absorption spectrometer.

REFERENCES

1. A. Clearfield and G. D. Smith, *Inorg. Chem.* **8**, 431–436 (1969).
2. A. Clearfield, *Chem. Rev.* **88**, 125–148 (1988).
3. G. Alberti, U. Costantino, S. Allulli, and N. Tomassini, *J. Inorg. Nucl. Chem.* **40**, 1113–1117 (1978).
4. G. Cao, H. Lee, V. M. Lynch, and T. E. Mallouk, *Solid State Ionics* **26**, 63–69 (1988).
5. G. Cao, H. Lee, V. M. Lynch, and T. E. Mallouk, *Inorg. Chem.* **27**, 2781–2785 (1988).
6. D. Cunningham and P. J. D. Hennelly, *Inorg. Chim. Acta* **37**, 95–102 (1979).
7. Y. Ortiz-Avila, P. R. Rudolf, and A. Clearfield, *Inorg. Chem.* **28**, 2137–2141 (1989).
8. G. Cao, H.-G. Hong, and T. E. Mallouk, *Acc. Chem. Res.* **25**, 420–427 (1992).
9. H. E. Katz, M. L. Schilling, C. E. D. Chidsey, T. M. Putvinski, and R. S. Hutton, *Chem. Mater.* **3**, 699–703 (1991).
10. H. E. Katz, G. Scheller, T. M. Putvinski, M. L. Schilling, W. L. Wilson, and C. E. D. Chidsey, *Science* **254**, 1485–1487 (1991).
11. H. E. Katz, W. L. Wilson, and G. Scheller, *J. Am. Chem. Soc.* **116**, 6636–6640 (1994).
12. M. B. Dines and P. M. DiGiacomo, *Inorg. Chem.* **20**, 92–97 (1981).
13. D. M. Poojary, L. A. Vermeulen, E. Vicenzi, A. Clearfield, and M. E. Thompson, *Chem. Mater.* **6**, 1845–1849 (1994).
14. D. Visser, S. G. Carling, P. Day, and J. Deportes, *J. Appl. Phys.* **69**, 6016–6018 (1991).
15. S. G. Carling, P. Day, D. Visser, and R. K. Kremer, *J. Solid State Chem.* **106**, 111–119 (1993), doi:10.1006/jssc.1993.1269.
16. S. G. Carling, P. Day, and D. Visser, *J. Phys.: Condens. Matter.* **7**, L109–L113 (1995).
17. S. G. Carling, P. Day, and D. Visser, *Inorg. Chem.* **34**, 3917–3927 (1995).
18. P. Rabu, P. Janvier, and B. Bujoli, *J. Mater. Chem.* **9**, 1323–1326 (1999).
19. J. Le Bideau, C. Payen, B. Bujoli, P. Palvadeau, and J. Rouxel, *J. Magn. Magn. Mater.* **140–144**, 1719–1720 (1995).
20. B. Bujoli, O. Pena, P. Palvadeau, J. Le Bideau, C. Payen, and J. Rouxel, *Chem. Mater.* **5**, 583–587 (1993).
21. P. Gerbier, C. Guerin, J. LeBideau, and K. Valle, *Chem. Mater.* **12**, 264–267 (2000).
22. G. E. Fanucci, J. Krzystek, M. W. Meisel, L.-C. Brunel, and D. R. Talham, *J. Am. Chem. Soc.* **120**, 5469–5479 (1998).
23. G. E. Fanucci, M. A. Petruska, M. W. Meisel, and D. R. Talham, *J. Solid State Chem.* **145**, 443–451 (1999), doi:10.1006/jssc.1999.8145.
24. H. Byrd, J. K. Pike, and D. R. Talham, *Chem. Mater.* **5**, 709–715 (1993).
25. H. Byrd, S. Whipps, J. K. Pike, J. Ma, S. E. Nagler, and D. R. Talham, *J. Am. Chem. Soc.* **116**, 295–301 (1994).
26. H. Byrd, J. K. Pike, and D. R. Talham, *Syn. Met.* **71**, 1977–1980 (1995).
27. G. E. Fanucci, C. M. Nixon, M. A. Petruska, C. T. Seip, D. R. Talham, G. E. Granroth, and M. W. Meisel, in "Supramolecular Engineering of Synthetic Metallic Materials" (J. Veciana and C. Rovira, Eds.), Vol. 518, pp. 465–475, 1998.
28. G. E. Fanucci, C. T. Seip, M. A. Petruska, S. Ravaine, C. M. Nixon, and D. R. Talham, *Thin Solid Films* **327–329**, 331–335 (1998).
29. G. E. Fanucci and D. R. Talham, *Langmuir* **15**, 3289–3295 (1999).

30. M. A. Petruska, G. E. Fanucci, and D. R. Talham, *Chem. Mater.* **10**, 177-189 (1998).
31. M. A. Petruska, G. E. Fanucci, and D. R. Talham, *Thin Solid Films* **327-329**, 131-135 (1998).
32. M. A. Petruska and D. R. Talham, *Chem. Mater.* **10**, 3673-3682 (1998).
33. M. A. Petruska and D. R. Talham, *Langmuir* **16**, 5123-5129 (2000).
34. L. J. de Jongh, in "Magnetic Properties of Layered Transition Metal Compounds" (L. J. de Jongh, Ed.), pp. 1-51. Kluwer Academic, Dordrecht, 1990.
35. G. V. Rubenacker, D. P. Raffaell, J. E. Drumheller, and K. Emerson, *Phys. Rev. B* **37**, 3563-3568 (1988).
36. K. Zenmyo and H. Kubo, *J. Phys. Soc. Jpn.* **64**, 1320-1325 (1995).
37. G. C. DeFotis, G. S. Coker, J. W. Jones, C. S. Branch, H. A. King, J. S. Bergman, S. Lee, and J. R. Goodey, *Phys. Rev. B* **58**, 12,178-12,192 (1998).
38. G. C. DeFotis, E. M. Just, V. J. Pugh, G. A. Coffey, B. D. Hogg, S. L. Fitzhenry, J. L. Marmorino, D. J. Krovich, and R. V. Chamberlain, *J. Magn. Magn. Mater.* **202**, 27-46 (1999).
39. G. C. DeFotis, D. S. Mantis, E. M. McGhee, K. R. Echols and R. S. Weis, *Phys. Rev. B* **38**, 11,486-11,499 (1988).
40. J. A. Mydosh, "Spin Glasses: An Experimental Introduction." Taylor & Franacis, London, 1993.
41. C. J. Nuttall and P. Day, *Chem. Mater.* **10**, 3050-3057 (1998).
42. H. C. Nguyen and J. B. Goodenough, *Phys. Rev. B* **52**, 8776-8787 (1995).
43. G. E. Fanucci, J. T. Culp, B. C. Watson, R. Backov, H. Ohnuki, D. R. Talham, and M. W. Meisel, *Physica B* **284-288**, 1499-1500 (2000).
44. P. J. C. Signore, Ph.D. thesis, University of Florida, 1994.
45. B. H. Ward, G. E. Granroth, K. A. Abboud, M. W. Meisel, P. G. Rasmussen, and D. R. Talham, *J. Mat. Chem.* **8**, 1373-1378 (1998).
46. C. T. Seip, H. Byrd, and D. R. Talham, *Inorg. Chem.* **35**, 3479-3483 (1996).
47. M. E. Lines, *J. Phys. Chem. Solids* **31**, 101-116 (1970).
48. M. F. Sykes and M. Fischer, *Physica* **28**, 919-938 (1962).
49. R. Navarro, in "Magnetic Properties of Layered Transition Metal Compounds" (L. J. de Jongh, Ed.), pp. 105-190. Kluwer Academic, Dordrecht, 1990.
50. S. Fishman and A. Aharony, *Phys. Rev. B* **18**, 3507-3520 (1978).
51. K. Katsumata, M. Kobayashi, T. Sato, and Y. Miyako, *Phys. Rev. B* **19**, 2700-2703 (1979).
52. L. Brevaart, E. Frikkee, and L. J. de Jongh, *Solid State Comm.* **25**, 1031-1033 (1978).
53. K. Katsumata, S. M. Shapiro, G. Shirane, and J. Tuchendler, *Phys. Rev. B* **46**, 14,906-14,908 (1992).
54. P. Wong, P. M. Horn, R. J. Birgeneau, and G. Shirane, *Phys. Rev. B* **27**, 428-447 (1983).
55. E. Coronado, J. R. Galán-Mascarós, C. J. Gómez-García, and J. M. Martínez-Agudo, *Adv. Mater.* **11**, 558-561 (1999).
56. G. C. DeFotis, P. Christoph, and P. A. Spencer, *J. Chem. Phys.* **80**, 2079-2086 (1984).
57. R. C. Richardson and E. N. Smith, "Experimental Techniques in Condensed Matter Physics at Low Temperatures," Sec 3.5. Addison-Wesley, Redwood City, CA, 1988.
58. H. C. Nguyen and J. B. Goodenough, *Phys. Rev. B* **52**, 324-334 (1995).

Presence of lipids in urine, crystals and stones: Implications for the formation of kidney stones

SAEED R. KHAN, PATRICIA A. GLENTON, RENAL BACKOV, and DANIEL R. TALHAM

Department of Pathology and Department of Chemistry, University of Florida, Gainesville, Florida, USA

Presence of lipids in urine, crystals and stones: Implications for the formation of kidney stones.

Background. Cell membranes and their lipids play critical roles in calcification. Specific membrane phospholipids promote the formation of calcium phosphate and become a part of the organic matrix of growing calcification. We propose that membrane lipids also promote the formation of calcium oxalate (CaOx) and calcium phosphate (CaP) containing kidney stones, and become a part of their stone matrix.

Methods. Human urine, crystals of CaOx and CaP produced in the urine of healthy individuals, and urinary stones containing struvite, uric acid, CaOx and CaP crystals for the presence of membrane lipids were analyzed. Crystallization of CaOx monohydrate at Langmuir monolayers of dipalmitoylphosphatidylglycerol (DPPG), dipalmitoylphosphatidylcholine (DPPC), dipalmitoylphosphatidylserine (DPPS), dioleoylphosphatidylglycerol (DOPG), palmitoyloleoylphosphatidylglycerol (POPG) and dimyristoylphosphatidylglycerol (DMPG) was investigated to directly demonstrate that phospholipid assemblies can catalyze CaOx nucleation.

Results. Urine as well as CaOx and CaP crystals made in the urine and various types of urinary stones investigated contained some lipids. Urine of both CaOx and uric acid stone formers contained significantly more cholesterol, cholesterol ester and triglycerides than urine of healthy subjects. However, urine of CaOx stone formers contained more acidic phospholipids. The organic matrix of calcific stones contained significantly more acidic and complexed phospholipids than uric acid and struvite stones. For each Langmuir monolayer precipitation was heterogeneous and selective with respect to the orientation and morphology of the CaOx crystals. Crystals were predominantly monohydrate, and most often grew singly with the calcium rich (10-1) face toward the monolayer. The number of crystals/mm² decreased in the order DPPG > DPPS > DPPC and was inversely proportional to surface pressure and mean molecular area/molecule.

Conclusions. Stone forming conditions in the kidneys greatly impact their epithelial cells producing significant differences in the urinary lipids between healthy and stone forming individuals. Altered membrane lipids promote face selective nucleation and retention of calcium oxalate crystals, and in the process become a part of the growing crystals and stones.

Key words: nephrolithiasis, calcium oxalate, phospholipids, phosphatidylserine, cell membrane.

Received for publication February 15, 2002
and in revised form May 22, 2002

Accepted for publication July 22, 2002

© 2002 by the International Society of Nephrology

Lipids are integral to the organic matrices of mineralized tissues as well as pathologic calcifications [1–3]. Even though they account for a relatively small proportion of the organic matrix; 7 to 14% in bone, 2 to 6% in dentin, 12 to 22% in newly mineralized enamel [2], approximately 9.6% in submandibular salivary gland calculi and 10.2% in supragingival calculi [4–6], lipids are proposed to play a significant role in the calcification process. They promote crystal nucleation and become incorporated in the growing calcifications.

Our investigations of calcium oxalate (CaOx), struvite and uric acid stones showed that all of them contain some lipids [7] and that lipid matrix is a good nucleator of CaOx crystals from a metastable solution [8]. In addition, we have shown that membranes of renal epithelial cells are involved in crystallization of CaOx and CaP *in vivo* in kidneys of male and female rats, respectively [9, 10] and renal brush-border membrane vesicles isolated from rat kidneys can induce CaOx crystallization *in vitro* [11, 12]. Lipids that participate in crystallization of calcium phosphate form complexes with calcium and bind tightly to the crystals [13–15]. The current study was undertaken to elucidate further the role of lipids in CaOx nephrolithiasis and identify membrane lipids most likely involved in nucleation of CaOx crystals. We analyzed lipids of CaOx, CaP, struvite and uric acid stones and separated complexed and non-complexed lipids. We also isolated and analyzed urinary lipids from uric acid and calcium oxalate/phosphate stone formers and investigated the lipids associated with the CaOx and CaP crystals induced in the human urine. In addition, we used monolayers at the air/water interface for *in vitro* studies to directly demonstrate that phospholipid assemblies can nucleate CaOx. These monolayers, called Langmuir monolayers or films, have been used extensively to investigate the nucleation and growth of biominerals at organized interfaces [16]. The monolayer studies also were used to compare the CaOx nucleating potential of various phospholipids.

METHODS

Collection of human urine

Twenty-four-hour urine samples were collected from male and female uric acid and calcium oxalate stone formers (33 to 83 years) and healthy people with no evidence of kidney disease (31 to 54 years). Individuals were classified as uric acid or CaOx stone formers based on their history and composition of their stones. Individuals with hyperparathyroidism and primary or enteric hyperoxaluria were excluded. Urinary protein was determined using a protein-assay kit (Bio-Rad Laboratories, Hercules, CA, USA). Absence of proteinuria, overt crystalluria and blood cells in the urine were considered symbolic of the absence of kidney disease. In the case of calcium oxalate stone formers, renal functions were further evaluated by determining the rate of creatinine clearance. During collection, the specimens were maintained at room temperature, approximately 24°C. Prior to collection, 1 mL of 20% sodium azide, an antibacterial agent, was placed in the collection bottles. The pH and total urinary volume were recorded. The total urinary protein was determined using dipsticks and/or a Bio-Rad protein assay kit. Urine was examined microscopically.

Induction of calcium oxalate crystals in the human urine

Previously reported procedures were utilized [17]. The urine samples were allowed to warm to 37°C in a shaking water bath (Fisher Scientific, Norcross, GA, USA) and divided into 250 mL aliquots. CaOx and CaP crystals were induced by the addition of 15 mL/L of 0.1 mol/L sodium oxalate or 0.1 mol/L sodium phosphate, followed by incubation for three hours. At the end of the incubation period, the urine specimens were centrifuged at $10,000 \times g$ for 25 minutes, and the supernatant was aspirated. The crystal-containing pellet was placed in a micro-centrifuge tube, washed three times and then dried for 24 hours in the Flexi-Dry lyophilizer.

Isolation, identification and quantification of lipids

The methods for isolation, identification and quantification of lipids from urine and stones are described in detail in earlier publications [7, 18]. Here we will provide only a brief account using urine as an example.

Urinary lipids. To isolate the lipids, 400 mL of urine was mixed with 1.2 L of 2:1 chloroform:methanol. The mixture was shaken and placed on an end-over-end mixer for 24 hours at 4°C and then centrifuged at 7000 rpm to achieve phase separation. The top portion was removed and set aside as the aqueous layer, the middle layer was recovered as the interface, and the lower phase was collected as the organic layer. After evaporation to a smaller volume, the organic sample was Folch-washed twice, pooling the respective phases with the previous

ones. The pooled organic phase consisting of the total lipids was then lyophilized, weighed and reconstituted with 2:1 chloroform:methanol to a final volume of 1 mL with 0.1% butyl hydroxytoluene (BHT) as a preservative, blanketed with dry nitrogen and stored in the dark at -70°C until further analysis. Lyophilized organic phase provided the dry weight for total lipid.

The organic extract was separated into various lipid classes using Bio Sil A silicic acid column. The sample was applied to a 1.5×15 cm column equilibrated with chloroform. Neutral lipids were eluted with 230 mL of chloroform, glycolipids with 900 mL of acetone and phospholipids with 230 mL of methanol. Each lipid class was concentrated with a rotary evaporator, dried under nitrogen gas, lyophilized, weighed, and re-suspended in a known volume of chloroform:methanol (2:1) with 0.1% BHT and stored at -70°C .

Phospholipids were further quantified using ammonium ferrothiocyanate (AMF) and Victorian Blue R (VBR) methods. The AMF method is suitable primarily for the determination of phosphatidylcholine (PC), phosphatidylethanolamine (PE) and sphingomyelin (SM) while VBR method is appropriate for detecting phosphatidylserine (PS), phosphatidylinositol (PI), phosphatidylglycerol (PG), phosphatidic acid (PA) and cardiolipin. Neutral lipids were analyzed for total and free cholesterol, cholesterol esters and triglycerides. The amount of glycolipids was determined by analyzing for glucose. The lipid classes were further analyzed for identification of individual lipids by one-dimensional thin layer chromatography (TLC). Neutral lipid standards were purchased from Nu Chek Prep (Elysian, MN, USA); glycolipid standards from Sigma Chemical Ltd. (St. Louis, MO, USA), and phospholipid standards from Avanti Polar Lipids (Birmingham, AL, USA). Individual lipid spots were visualized by exposure to iodine vapor for 30 minutes and identified by comparison to known standards. Individual phospholipids were quantified by scraping the spots from the iodine-stained plates and analyzing them for phosphate using Bartlett's method.

Lipids of crystal matrix. The crystals were weighed and then demineralized by treatment with 5 mL of 0.25 mol/L ethylenediaminetetraacetic acid (EDTA) at pH 8.0 and 4°C for three days with continuous stirring. The extract was centrifuged at $10,000 \times g$ for five minutes. The supernatant was dialyzed against water for 24 hours at 4°C using dialysis tubing with a 6 to 8 kD cut-off (Spectrum Medical Industries, Gardena, CA, USA). Protein concentration in the crystal matrix was determined by the Lowry method using bovine serum albumin as the standard. Lipids were extracted by treating the crystal matrix with chloroform/methanol as described above.

Lipids of urinary stones. The specific purpose of this study was to further investigate the differences between stone types with respect to various lipids and determine

the amounts of complexed and non-complexed lipids in stone matrices. Calcium lipid complexes have been suggested to play a critical role in the nucleation of calcium phosphate [13–15]. To isolate complexed and non-complexed lipids from the same stones, we followed the procedures developed by Boyan and Boskey [14].

Urinary struvite, CaOx and uric acid stones were obtained from our departmental surgical pathology practice and stored at -80°C . Stone fragments were analyzed using x-ray diffraction and were classified according to their composition. For example, stones with 70% or more of CaOx were considered CaOx. Approximately 4 g of each stone were thoroughly washed and sonicated to remove blood and surface debris. After drying, stones were ground to a fine powder. Lowry's method was used to determine the protein contents of the stone matrix. The lipids were extracted from the stone powder with ice-cold chloroform:methanol:0.05 mol/L Tris-HCl, pH 7.4 (2:1:1); 30 mL of extraction solvent to 1 g of stone using sonication at 4°C . Sonication was carried out for 10 minutes, after which the sample was centrifuged to phase separate and pellet the residue. The upper and lower phases were removed separately and pooled as aqueous and organic substances, respectively. Fresh extraction solvent was added to the pellet and the process repeated several times pooling the respective phases. Pooled organic phases were extracted with ethanol:ether (3:1) and then centrifuged. Non-complexed lipids were isolated from the supernatant. Complexed lipids were recovered from the pellet.

Langmuir monolayers

Details of the experimental procedures are given in previous articles [19–21] and, therefore, only a brief description of the experimental methods is given here. The effects of changing head group, mean molecular area and surface pressure were investigated. Six different phospholipid interfaces, with different head groups and alkyl tails, were investigated. Monolayers of dipalmitoylphosphatidylglycerol (DPPG), dipalmitoylphosphatidylcholine (DPPC), dipalmitoylphosphatidylserine (DPPS), dioleoylphosphatidylglycerol (DOPG), palmitoyl-oleoylphosphatidylglycerol (POPG) and dimyristoylphosphatidylglycerol (DMPG) were prepared at the air/water interface by spreading the lipid from a chloroform/methanol solution and compressing the films to the targeted surface pressure using opposing moveable barriers. The subphase was a metastable calcium oxalate solution of relative supersaturation (RS) 5. The RS values, specifically for the COM "whewellite" crystals, were computed using Finlayson's EQUIL v1.3 [22]. The Langmuir monolayers were held at the desired pressure at the solution/air interface at 25°C for a specified period of time (typically 4 h). Monolayers were then analyzed, either in situ, using Brewster angle microscopy (BAM), or ex situ, using SEM,

Table 1. Comparison of urinary excretion of proteins and lipids between healthy, calcium oxalate and uric acid stone formers

	Uric acid stone formers mg/24 hr (N = 3)	Normal mg/24 h (N = 8)	Calcium oxalate stone formers mg/24 h (N = 12)
Total proteins	71.35 ± 15.29 ^a	28.09 ± 2.47	42.43 ± 5.18 ^b
Glycolipids	8.57 ± 1.64 ^a	3.93 ± 0.85	5.35 ± 1.01
Cholesterol	3.86 ± 0.34 ^a	1.98 ± 0.28	3.39 ± 0.40 ^b
Cholesterol ester	2.43 ± 0.35 ^a	1.18 ± 0.20	2.23 ± 0.25 ^b
Triglycerides	34.70 ± 2.22 ^a	8.99 ± 2.24	18.08 ± 3.59 ^b
Phospholipid (VBR)	0.402 ± 0.14	0.351 ± 0.05	0.718 ± 0.13 ^b
Phospholipid (NH ₄)	1.60 ± 0.59	1.10 ± 0.17	2.08 ± 0.56

N is the number of stone patients.

^aP < 0.05 between normal and uric acid stone formers

^bP < 0.05 between normal and calcium oxalate stone formers

TEM or optical microscopy. The BAM sees only what is taking place at the monolayer/water interface by measuring differences in refractive indices at the surface [21]. For ex situ analyses, Langmuir monolayers were deposited onto a solid support by carefully draining the trough to lower the monolayer onto a substrate that had been placed in the subphase before the monolayer was applied. To be sure that nucleation occurred only in the presence of the Langmuir monolayer, a control was performed for each experiment by placing a solid support outside the barriers where there was no monolayer. For each of the experiments described here, no COM crystals were observed on the control substrates.

Statistical analysis

Statistical analysis of the data was performed using Microsoft EXCEL's version of the Student *t* test. Results are presented as ± SD.

RESULTS

Urinary lipids

The mean creatinine clearance rate for calcific stone formers was 84 ± 22.19 mg/mL/min. The urine from stone formers contained higher amounts of total and individual phospholipids than urine from healthy subjects. Quantitative determination of phospholipids using the VBR method showed significantly more phospholipids in the calcium oxalate stone formers' urine than in the urine from healthy individuals or uric acid stone formers (Table 1). Thin-layer chromatography detected SM, PC, PE, as well as PS in all urinary samples investigated. In addition some urine samples from both stone formers and healthy subjects contained PI, cardiolipin (CL), and PA. Occasionally lyso (L)-PC, -PE, and -PA were detected also. More calcium oxalate stone formers' urine contained cardiolipin, and PA than urine from healthy individuals or uric acid stone formers. Densitometric quantification of individual phospholipids showed that urine from cal-

Table 2. Average protein and lipid contents of kidney stone as percent of the matrix

Stone type	Protein	Lipids
	%	
Struvite (<i>N</i> = 5)	74 ± 33.9	26 ± 3.9
Calcium oxalate (<i>N</i> = 5)	20 ± 6.3	80 ± 7.5
Calcium phosphate (<i>N</i> = 3)	33 ± 11.1	67 ± 5.6
Uric acid (<i>N</i> = 5)	75 ± 3.9	25 ± 6.6

cium oxalate stone formers contained higher amounts (mg/24 h) of SM (1.57 ± 0.76 vs. 0.98 ± 0.6), PC (1.66 ± 1.6 vs. 0.56 ± 0.34), and PS (0.72 ± 0.63 vs. 0.45 ± 0.16) than urine from the healthy subjects.

The urine of both uric acid and calcium oxalate stone formers contained significantly higher amounts of cholesterol, cholesterol ester and triglycerides than did the urine obtained from healthy subjects. Urine also contained glycolipids consisting of sulfatides, gangliosides, sphingosine, as well as glucocerebrosides. Even though urine from calcium oxalate stone formers contained more glycolipids, differences in the total or individual glycolipids between urine from healthy subjects and calcium oxalate stone formers were not significant.

Lipids of the matrix of urinary stones

As expected, the matrix of all stones investigated including struvite, uric acid, calcium oxalate and calcium phosphate contained both proteins and lipids (Table 2). The protein-to-lipid ratio, however, appeared higher in the matrix of struvite and uric acid stones than the matrix of calcium oxalate and calcium phosphate stones. Even though there were no significant differences in various types of lipids encountered in the stones (Table 3), there were some clear dissimilarities between struvite stones associated with infection and other non-infectious stones on the one hand and between calcium containing and uric acid stones on the other. Matrix of struvite stones contained more cholesterol and triglycerides than others. Calcific stones contained more phospholipids than uric acid stones. One-dimensional thin layer chromatography was used to separate and identify various phospholipids and glycolipids. SM, PC, PE, CL and trace amounts of PS were detected in matrices of all stones (Table 4). Matrix of struvite stones also contained quantifiable PS and PA. Occasionally the organic matrix of various stones showed the presence of PI, lyso-PC, lyso-PA and lyso-PE. Glycolipids identified in all stones included gangliosides, D-sphingosine, and glucocerebrosides (Table 5). Struvite stone matrix also contained sulfatides and digalactodiglycerides, while matrices of calcium oxalate and calcium phosphate stones contained cerebrosides 1 and 2 and digalactodiglycerides.

The matrices of all stones contained both complexed

and non-complexed lipids (Table 6). The amount of complexed lipids was highest in calcium phosphate stones and lowest in the uric acid stones. Both complexed and non-complexed lipids contained cholesterol, triglycerides, phospholipids and gangliosides.

Lipids of the matrix of crystals induced in healthy human urine

Both calcium oxalate and calcium phosphate crystals induced in the urine contained lipids (Table 7). There were no significant differences in either the nature of lipid constituents or the lipid amounts/g of crystals between two types of crystals. Glucocerebrosides were the most common glycolipids, while SM was the most common phospholipid. Gangliosides were the second most common glycolipids and PC and PE the most common phospholipids.

Crystallization at Langmuir monolayers

Observation of nucleation at phospholipid interfaces. Crystal growth was monitored under Langmuir monolayers of each lipid held at 20 mN/m (Fig. 1A). In all experiments the majority of the crystals nucleated with the (10-1) face toward the phospholipid monolayer (Figs. 2 and 3). While the overall selectivity in crystal habit remained the same for each of the lipids, the number of crystals observed under the monolayers changed, decreasing in the order: DPPG > DPPS ≥ DPPC (Fig. 1A). Even under lower surface pressure (Fig. 1B), the DPPG subphase produced more crystals than either the DPPS or DPPC.

Effects of monolayer fluidity on nucleation. In the Langmuir monolayer experiments, changing the surface pressure applied by the moveable barriers altered the fluidity and the local order within the model membranes. Increased pressure brought the molecules close together and decreased phospholipid fluidity. Lowering the surface pressure increased the number of crystals/mm² (Figs. 1A and B) without having a significant effect upon crystal orientation. Crystals with the (10-1) face oriented toward the monolayer still predominated except for a somewhat higher incidence of agglomerates under the DPPG monolayer. The effect of packing density of the headgroup on crystal formation was probed by employing DPPG, DMPG, POPG and DOPG monolayers. At surface pressure of 20 mN/m, mean molecular area increases in the order of DPPG < DMPG < POPG < DOPG ranging from 40 to 90 Å²/molecule because different lipophilic tails had different sizes even though the headgroup remained the same. Clearly more crystals formed at lower mean molecular area (Fig. 1A). Still, most crystals formed with their (10-1) face toward the monolayer. When DPPG, DMPG, POPG and DOPG monolayers were held at the same mean molecular area

Table 3. Lipid constituents of the organic matrix

Stone type	Total cholesterol	Cholesterol ester	Triglycerides	Glycolipids	Phospholipids (AMF)	Phospholipids (VBR)
	<i>mg/g stone</i>					
Struvite	1.53 ± 0.72	0.21 ± 0.25	10.71 ± 9.17	0.13 ± 0.05	0.57 ± 0.5	0.06 ± 0.04
Calcium oxalate	0.64 ± 0.27	0.37 ± 0.10	1.64 ± 0.6	0.16 ± 0.06	0.18 ± 0.1	0.05 ± 0.03
Calcium phosphate	0.76 ± 0.5	0.37 ± 0.26	1.45 ± 0.13	0.17 ± 0.1	0.31 ± 0.23	0.05 ± 0.02
Uric acid	0.2 ± 0.07	0.11 ± 0.04	1.6 ± 0.34	0.09 ± 0.03	0.08 ± 0.03	0.03 ± 0.01

Number of stones is listed in Table 2.

Table 4. Major phospholipids of stone matrix quantified by the Bartlett method

Stone type	SM	PC	PE	CL	PS	PA
	<i>% of total phospholipids</i>					
Struvite	30.4 ± 12.9	11.4 ± 10.3	8.7 ± 6.8	19.6 ± 16.6	7.1 ± 2.4	21.9 ± 29.0
Calcium oxalate	32.6 ± 6.6	16.8 ± 4.9	34.7 ± 7.6	11.2 ± 3.0		
Calcium phosphate	32.2 ± 18.0	15.0 ± 12.4	22.4 ± 8.6	12.7 ± 5.7		
Uric acid	20.5 ± 11.2	28.3 ± 5.5	29.8 ± 1.7	19.6 ± 11.6		

Abbreviations are: SM, sphingomyelin; PC, phosphatidylcholine; PE, phosphatidylethanolamine; CL, cardiolipin; PS, phosphatidylserine; PA, phosphatidic acid.

Table 5. Major glycolipids of stone matrix quantified by densitometric analysis of the spots after chromatography

Stone type	Gangliosides	D-sphingosine	Sulfatides	Digalactodiglycerides	Cerebrosides	Glucocerebrosides
	<i>% of total glycolipids</i>					
Struvite	14.7 ± 3.9	3.0 ± 0.6	9.6 ± 4.4	13.8 ± 1.6		58.73 ± 3.7
Calcium oxalate	18 ± 7.6	1.9 ± 0.6		2.6 ± 2.3	36.7 ± 11.7	48.2 ± 23.1
Calcium phosphate	3.0 ± 2.3				40.8 ± 6.2	50.0 ± 0.5
Uric acid	52.0 ± 33.4					47.0 ± 36.2

Table 6. Complexed and non-complexed lipids of the stone matrix

Stone type	Non-complexed lipids	Complexed lipids
	<i>mg/g stone</i>	
Struvite	3.5 ± 2.53	0.7 ± 0.50
Calcium oxalate	9.93 ± 3	2.34 ± 0.82
Calcium phosphate	5.06 ± 1.2	2.76 ± 2.8
Uric acid	4.19 ± 1.45	0.76 ± 0.18

N is the same as in Table 2.

of 95 Å²/molecule (Fig. 1B), again most crystals formed with their 10-1 face toward the monolayer.

DISCUSSION

Human urine usually contains only very small amounts of lipids. However, under certain nephrotic syndromes the urinary excretion of cholesterol, cholesterol esters, triglycerides, free fatty acids and phospholipids is considerably increased [23]. Many of these lipids originate from the plasma. In some diseases urinary excretion of specific lipids is increased. Patients with mitochondrial encephalomyopathy, for example, excrete PE, PS and cardiolipin derived from mitochondria and sulfatides specific to re-

nal epithelial cells [24]. Increased lipiduria is caused also by intake of a variety of drugs and some common chemicals. Aminoglycoside antibiotics like gentamicin injure the proximal tubular epithelial cells inducing myeloid bodies in their lysosomes [25]. These bodies are later extruded out of the cells and cause an increase in urinary levels of phospholipids such as PE, PC, PS and PI. Nephrotoxins such as mercuric chloride [25] or ethylene glycol [9, 10] induce shedding of the microvillous brush border of the renal epithelium reflected in increased urinary excretion of phospholipids such as sphingomyelin. Thus, phospholipiduria is often an indication of membranuria.

Animal model and tissue culture studies have shown that an exposure to high levels of oxalate and/or CaOx crystals challenges the renal epithelial cells. Production of proteins such as osteopontin [26, 27], bikunin [28, 29] and Tamm-Horsfall protein [30] is increased. Cholesterol contents of proximal tubular cells are known to increase also when they are injured [31]. Prolonged exposure to oxalate and CaOx crystals results in cellular damage, resulting in shedding of microvillous brush border and ultimately in sloughing of the cells into the urine [9, 10]. These changes in membrane lipids must manifest as increases in their urinary contents. Thus, our results show-

Table 7. Lipids present in the matrix of calcium oxalate and calcium phosphate crystals produced in normal human urine

Crystal type	Total cholesterol	Cholesterol ester	Triglycerides	Glycolipids	Phospholipids (AMF)	Phospholipids (VBR)
	mg/total crystal/24 h					
Calcium oxalate	0.37 ± 0.09	0.20 ± 0.04	3.11 ± 2.9	1.15 ± 1.2	0.06 ± 0.04	0.09 ± 0.04
Calcium phosphate	0.27 ± 0.1	0.21 ± 0.03	2.51 ± 2.4	1.35 ± 1.04	0.07 ± 0.03	0.02 ± 0.01

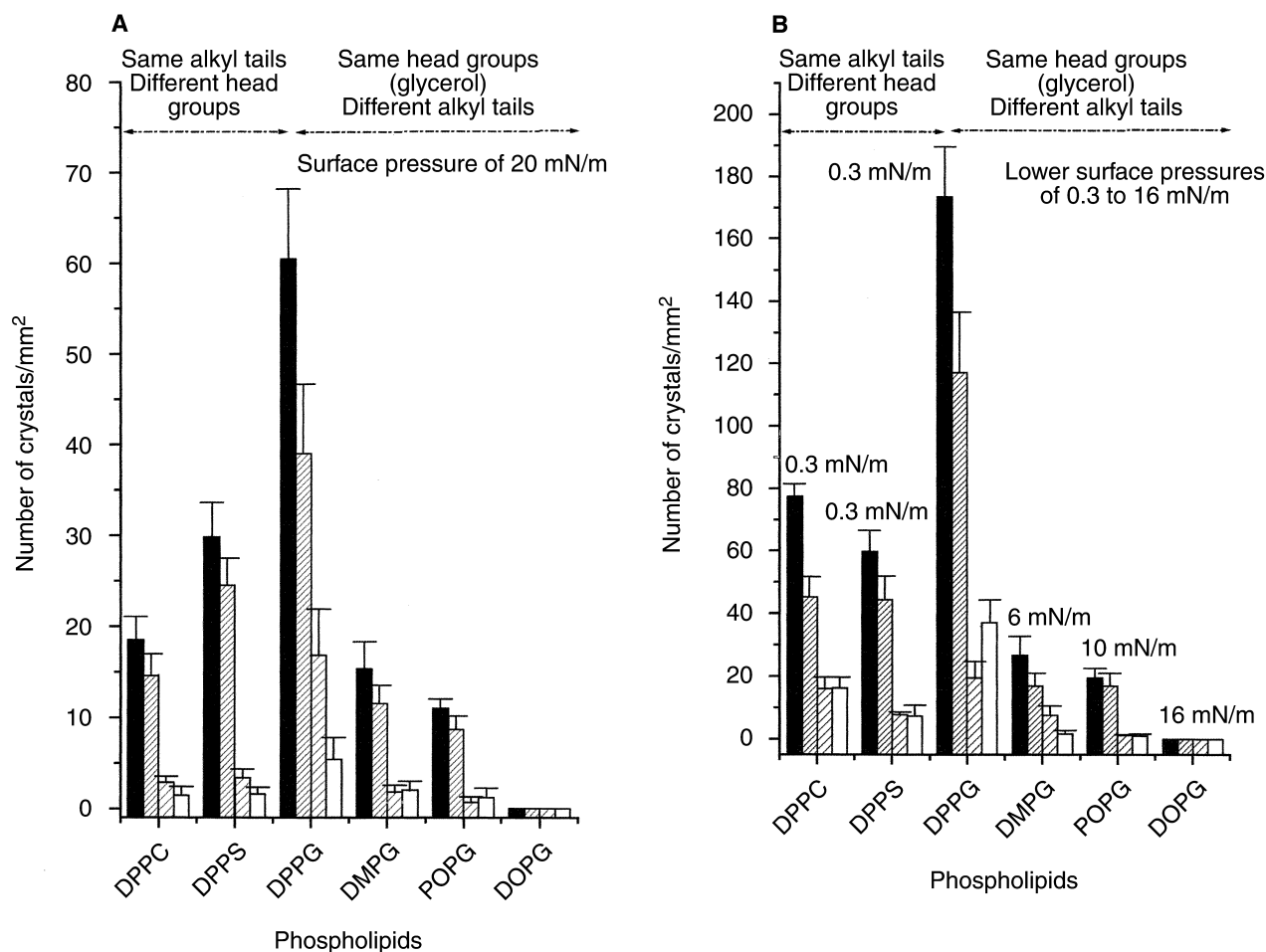


Fig. 1. Histograms showing the distribution of the observed COM crystal orientations under Langmuir monolayers of six different phospholipid interfaces from a calcium oxalate subphase of relative supersaturation of 5. Data are shown for high (A) and low (B) surface pressure. The number of densities reported, are on average over at least 40 mm². Note that DPPC, DPPS, DPPG, have different polar headgroups, while the series DPPG, DMPG, POPG, and DOPG has the same headgroup but different lipophilic tails. Symbols are: (■) total crystals; (▨) faces 10-1; (▩) faces 101; (□) agglomerates.

ing significantly increased urinary excretion of proteins and lipids by stone formers may be indicative of a renal response to prolonged exposure to oxalate and/or deposition of CaOx/CaP/uric acid crystals in the tubules. Lipiduria alone may be a non-specific reaction of the kidneys to various challenges, but in the case of stone formers, it is perhaps a surrogate marker for crystallization in the kidneys.

According to the current concepts on calcification, initial deposition of calcium phosphate (CaP) occurs on

cellular membranes that are present at the calcification site either as a limiting membrane of the so-called matrix vesicles or as cellular degradation products [2, 32]. Even biomaterial associated calcification, such as that of bio-prosthetic heart valves fabricated from porcine aortic valves or bovine pericardium, is associated with cellular membrane fragments derived from the pig cusp cells in the case of porcine valves and from connective tissue cells in the case of bovine pericardium [33]. Calcification of intrauterine devices also appears to be initiated by cellu-

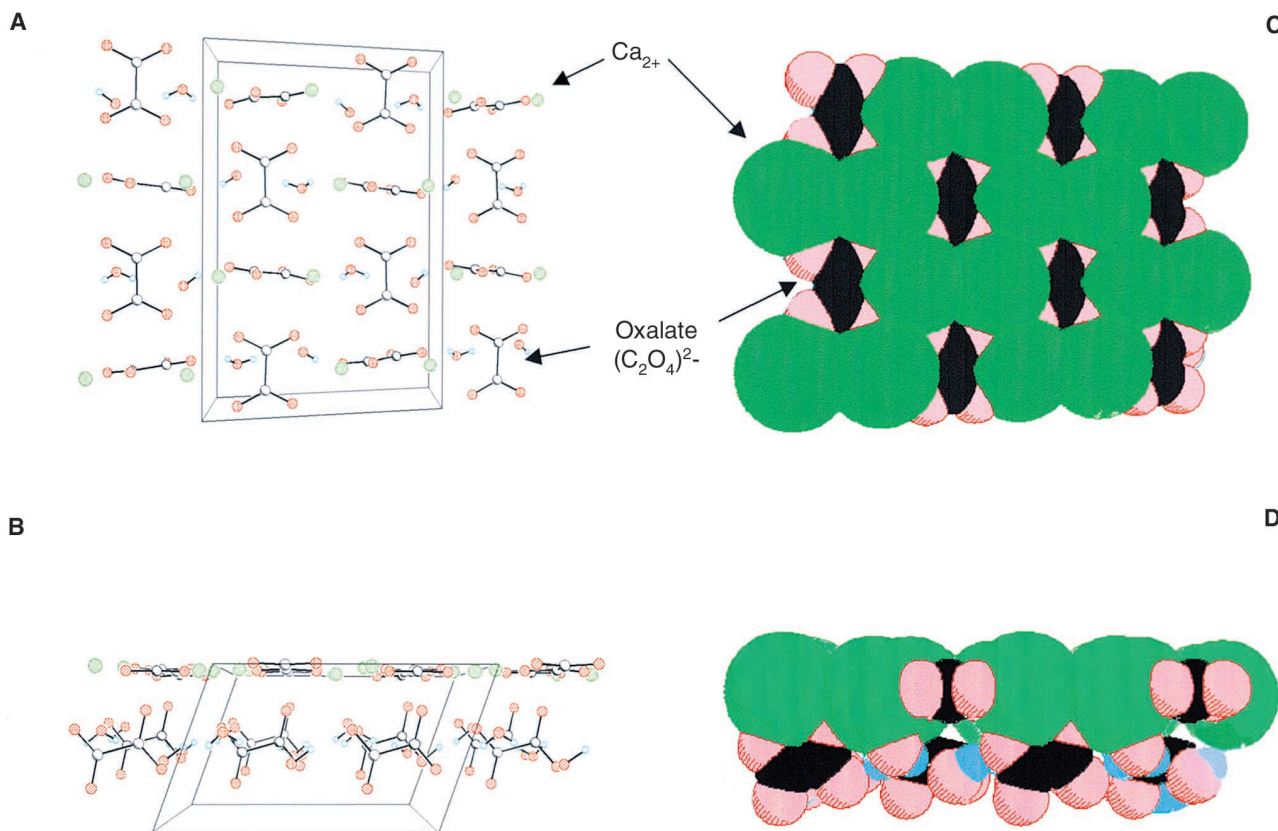


Fig. 2. Views of the calcium oxalate monohydrate (COM) crystal structure perpendicular (A and C) and parallel (B and D) to the (10-1) face. Views C and D are space-filling representations, showing the different sizes of the ions. Calcium ions and oxalate ions are indicated. The structure consists of sheets parallel to the (10-1) face that alternate between calcium-rich and oxalate-rich. Anionic additives are expected to stabilize the calcium-rich layers, giving the surface shown in C. The large ionic radius of Ca^{2+} causes it to project well beyond the oxalate ion (view D) and dominate the surface. Key to atom coloring: calcium is green; oxygen, red; carbon, black; hydrogen, blue.

lar membranous material that is deposited on the devices during their exposure to the uterine fluid [34]. Dental plaque and calculus formation is yet another example of calcification initiated by cellular membranes [4-6]. Membranes of microorganisms present in the dental plaque nucleate calcium phosphate and thus initiate calculus formation. One of the main reasons for cellular membranes to act as specific nucleators of calcium phosphate is proposed to be the presence of lipids and particularly the acidic phospholipids therein. We have proposed that membranes and their phospholipids are similarly involved in nucleation of calcium oxalate crystals and formation of kidney stones [11, 12, 35].

Our results show that lipids are present in stone matrices of all stones irrespective of the inorganic nature of their major crystalline components, be they calcium oxalate, calcium phosphate, struvite or uric acid. However, calcium oxalate and calcium phosphate stones contained 2 to 4 times more lipids than proteins (Table 2), while uric acid and struvite stones contained fewer lipids than proteins. Furthermore, calcium oxalate and calcium phosphate stones contained more complexed lipids than

struvite and uric acid stones (Table 6). Formation of a complex between calcium and acidic phospholipids is considered the initial step in calcification [13-15]. Phosphatidylserine is one of the key membrane lipids involved in the formation of such complexes and, as reported here and earlier [7], was detected in matrices of all stones examined. However, PS amounts were so small that we were unable to quantify it in all samples and thus it was not included in Table 4. Lipid matrix of struvite stones contained comparatively higher amounts of triglycerides, cholesterol (Table 3) and sulfatides (Table 5), which may be a result of bacterial infection associated with struvite stone formation. In addition, cardiolipin constituted a higher percentage of phospholipids in the matrix of struvite stones. Cardiolipin is a significant part of bacterial membranes. The presence of cardiolipin in other stones is most likely a result of mitochondrial inclusion in the matrix. Mitochondrial membranes also contain significant amounts of cardiolipin. Ultrastructural examination of calcium oxalate stones has shown their matrix to contain cellular degradation products including mitochondria [35].

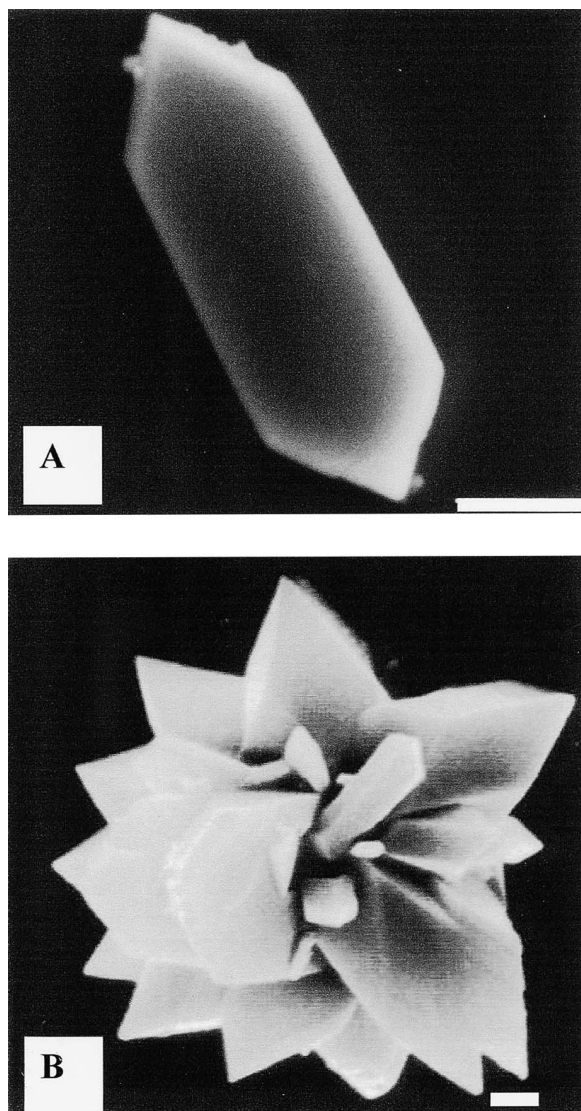


Fig. 3. Scanning electron micrograph of the CaOx crystals growing on a Langmuir monolayer. Bar = 1 μm . (A) A single CaOx monohydrate growing with 10-1 face toward the monolayer. (B) An aggregate of CaOx monohydrate crystals growing on the monolayer.

We propose that membrane lipids present in the urine promote crystallization of CaP and CaOx and then become a part of growing stones. It is possible, however, that cellular membranes and lipids found in stone matrix are accidentally incorporated by binding to surfaces of growing and aggregating crystals, since crystals and stones form in urine rich with these entities. Moreover, crystals and growing stones can physically damage the renal cells causing increased sloughing of cells into the urine. Similar arguments have been made about the accidental inclusion of urinary proteins. To deal with this issue, it is now customary to generate crystals in the healthy urine and study the macromolecules, which become associated with the induced crystals [17]. Our results demonstrate

that both CaP and CaOx crystals induced in vitro in healthy human urine contained neutral lipids, phospholipids as well as glycolipids. Moreover, cholesterol, cholesterol esters, triglycerides, glucocerebrosides, gangliosides, sphingomyelin, phosphatidylcholine and phosphatidylethanolamine were identified, lipids that are the major constituents of renal cell membranes [36].

Langmuir monolayers of various membrane phospholipids were used to investigate their potential involvement in the crystallization of CaOx [19–21]. While the monolayer experiments are not physiological, they provide direct physical evidence that CaOx can be nucleated at phospholipid interfaces. Previous studies have shown that nucleation at a monolayer from a low supersaturation calcium oxalate solution is heterogeneous and selective with respect to the nature, orientation and morphology of the precipitated crystal [19–21, 37]. The rate of crystallization is higher at monolayers of acidic phospholipids. Crystals are mostly CaOx monohydrate and the majority nucleate as single cuboidal structures with their (10-1) face oriented toward the monolayer (Figs. 2 and 3). As seen in Figure 2, layers of the cations alternate with layers of anions parallel to the (10-1) direction so that this crystal surface either can be rich in calcium ions or rich in oxalate ions. In the presence of anionic phospholipids, it is reasonable to envision the layer of calcium ions at the interface as the point of interaction and crystal nucleation. Once the crystal forms, the anionic phospholipid will remain adsorbed to the surface, stabilizing the calcium layer and making the (10-1) face prominent in the observed crystal habit.

Monolayer studies can be extended to explore further the variables that can influence nucleation. For example, the effect of the fluidity of the monolayer was studied by maintaining the same head group with different alkyl tails and under different applied surface pressures. When comparing the same headgroups under different conditions, CaOx monohydrate crystals were observed to form at both high and low pressures (Fig. 1). Despite the significantly different mean molecular area/headgroup represented in the experiments, the selectivity for the (10-1) face relative to the other faces remained nearly constant. The monolayers held at 20 milliNewton/m cannot all present the same template because the lipophilic tails have different sizes, yet they show similar selectivity (Figs. 1A). Even though more crystals were observed under DPPG, the selectivity for the (10-1) and (010) COM faces was similar for DMPG and POPG, which cannot achieve the same packing geometry as DPPG. It appears that the highest density of crystals resulted under the phospholipids that have the potential to achieve the smallest mma in association with the higher anionic density.

The monolayer does not have to be held in a compressed state to nucleate CaOx, but if it is capable of organizing in a smaller area, the crystal precipitation in-

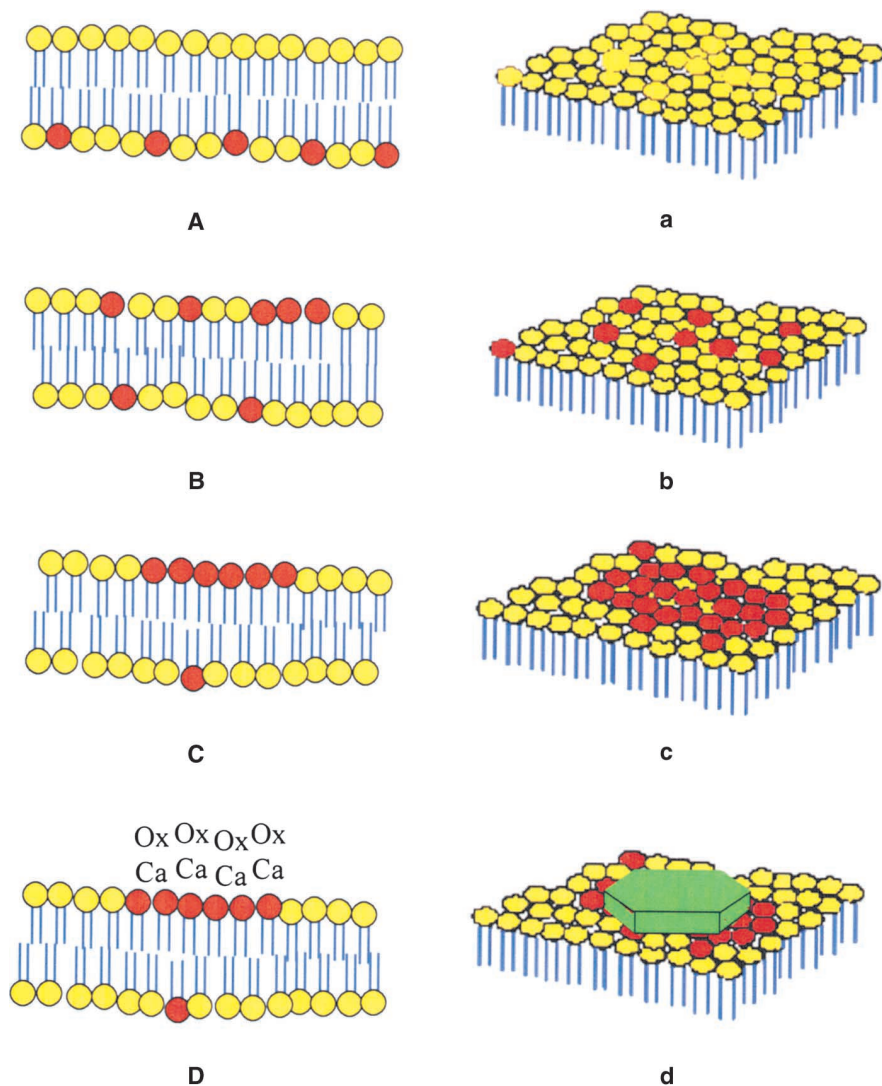


Fig. 4. Schematic presentation of changes in cell membrane phospholipids and nucleation of calcium oxalate crystals based on Wiessner et al [49] and Khan [50]. Two-dimensional (A–D) and three-dimensional (a–d) views. (A, a) Normal membrane with only the neutral phospholipids (yellow circles) on the outer surface. (B, b) Movement of acidic phospholipids (red circles) from inside to the outside. (C, c) Lateral movement of acidic phospholipids into specific domains and concentration of calcium ions. (D, d) Interaction between calcium and oxalate ions and nucleation of CaOx crystal.

creases. It is clear from Figure 1 that crystallization was enhanced at lower applied surface pressures. For each of the monolayers, crystal numbers increased as the monolayer expanded. Also, when the DPPG, DMPG, DOPG and POPG monolayers were compared at the same area (Fig. 1B), those at the lower corresponding surface pressure generated more crystals. These observations are consistent with the concept that crystal formation is enhanced if the interface is more fluid, or has the ability to rearrange to accommodate the nucleating or growing crystal.

Crystal attachment to the inner medullary collecting duct cells has previously been correlated with membrane fluidity [38]. Results of other tissue culture studies also indicate that dynamic regions at the lipid interface lead to increased chances of crystal nucleation and or crystal attachment [39–41]. Membrane damage, which is so prevalent after exposure to oxalate and CaOx crystals,

may lead to exceptionally fluid sites that can catalyze crystal nucleation and adhesion.

Templating by organic interfaces is often invoked in biomineralization. However, there does not appear to be a direct lattice match between closely packed phospholipid monolayers and CaOx monohydrate [19–21]. More likely, there is a more complex process involving concentration of Ca^{2+} ions at the phospholipid interface followed by reorganization of the lipids to stabilize the nascent crystal face. The (10-1) face of CaOx monohydrate can be calcium-rich (Fig. 2), and the tendency of the phospholipids to bind Ca^{2+} may provide a mechanism to sufficiently concentrate calcium ions, mimicking the calcium-rich face, to lead to specific nucleation. Since the structure is layered in the (10-1) direction, the phospholipid anions do not need to be displaced to bind oxalate beneath the calcium layer (Fig. 2B). The phospholipids stabilize this face, making it the predominant

facet in the observed crystals. The calcium rich (10-1) crystal face has been implicated also in adhesion of CaOx monohydrate crystals to membranes in lipid enriched cell culture studies [38]. The calcium-rich face of CaOx dihydrate crystals has similarly been implicated in their attachment to renal epithelial cells in culture [39].

The influence of the lipid headgroups on precipitation of CaOx monohydrate correlates with the anionic character of the head group (glycerol > serine ≥ choline). Most crystals were observed at the DPPG interface, which has an anionic headgroup, while fewer crystals were observed at the negatively charged zwitterionic DPPS interface and the neutral zwitterionic DPPC interface. The observations further suggest that calcium binding at the interface, either electrostatic or specific, plays a role in CaOx monohydrate nucleation. All three lipids are known to bind Ca²⁺ from aqueous solution and concentrate ions at lipid interfaces. However, calcium binding is greater at the negatively charged lipids.

Increased urinary excretion of oxalate and calcium are the major risk factors for stone formation. Exposure to both high calcium and oxalate induces several changes in the renal epithelial cells [42–49]. Catastrophic changes can induce lateral and *trans*membrane migration of phospholipids, sequestering them in specific domains (Fig. 4). Oxalate exposure induces a redistribution of phosphatidylserine from the inner leaflet of the plasma membrane to the outside [43, 45, 47] and promotes adhesion of CaOx crystals to the epithelium. Membranous vesicles derived from such cells with phosphatidylserine on the surface can promote crystallization of calcific crystals. Partitioning of acidic lipids in specific domains available to calcium and oxalate ions will attract them and nucleate CaOx crystals.

This study demonstrates the presence of lipids in human urine, CaOx crystals generated therein, and in both, the calcium as well as and non-calcium containing urinary stones. Since millions of tubular epithelial cells are discarded daily into the urine, it is highly likely that membranes of some of these cells accidentally become incorporated into the growing stones. We also provide evidence that membrane phospholipids promote heterogeneous nucleation of CaOx crystals, and suggest the possibility that their aggregation may be promoted also by an interaction with the cell membranes. Negatively charged phospholipids may be involved also in crystal attachment to the cell membranes. Thus, cell membranes and their lipids, by virtue of their involvement in crystal nucleation, aggregation and retention, and accidental incorporation become a part of the organic matrix of growing stones.

ACKNOWLEDGMENTS

This study was partially supported by NIH grants RO1 DK41434, DK53962, DK59765. We thank Mrs. Patricia Khan for reviewing the

manuscript and generating Figure 4, and Mr. Jonathan D. Woodward for producing Figure 2.

Reprint requests to Saeed R. Khan, Ph.D., Department of Pathology, Box 100275, College of Medicine, University of Florida, Gainesville, Florida 32610-0275, USA.
E-mail: khan@pathology.ufl.edu

APPENDIX

Abbreviations used in this article are: AMF, ammonium ferrioxalate; BAM, Brewster angle microscopy; CaOx, calcium oxalate; CaP, calcium phosphate; CL, cardiolipin; COM, calcium oxalate monohydrate; DMPG, dimyristoylphosphatidylglycerol; DOPG, dileophosphatidylglycerol; DPPC, dipalmitoylphosphatidylcholine; DPPG, dipalmitoylphosphatidylglycerol; DPPS, dipalmitoylphosphatidylserine; PA, phosphatidic acid; PC, phosphatidylcholine; PE, phosphatidylethanolamine; PG, phosphatidylglycerol; PI, phosphatidylinositol; POPG, palmitoyloleoylphosphatidylglycerol; PS, phosphatidylserine; RS, relative supersaturation; SEM, scanning electron microscopy; SM, sphingomyelin; TEM, transmission electron microscopy; TLC, thin layer chromatography; VBR, Victorian Blue R.

REFERENCES

1. WUTHIER RE: Lipids of mineralizing epiphyseal tissues in the bovine fetus. *J Lipid Res* 9:68–79, 1968
2. BOSKEY AL: Current concepts of physiology and biochemistry of calcification. *Clin Orthop* 157:225–257, 1981
3. ANDERSON HC: Calcific diseases. *Arch Pathol Lab Med* 107:341–348, 1983
4. SLOMIANY BL, MURTY VLN, AONO M, et al: Lipid composition of the matrix of human submandibular salivary gland stones. *Arch Oral Biol* 27:673–677, 1982
5. BOSKEY AL, BURSTEIN LS, MANDEL ID: Phospholipids associated with human parotid gland sialoliths. *Arch Oral Biol* 28:655–657, 1983
6. BOSKEY AL, BOYAN-SALYERS BD, BURSTEIN LS, MANDEL ID: Lipids associated with mineralization of human submandibular gland sialoliths. *Arch Oral Biol* 26:779–785, 1981
7. KHAN SR, SHEVOCK PN, HACKETT RL: Presence of lipids in urinary stones: Results of preliminary studies. *Calcif Tissue Int* 42:91–96, 1988
8. KHAN SR, SHEVOCK PN, HACKETT RL: In vitro precipitation of calcium oxalate in the presence of whole matrix or lipid components of the urinary stones. *J Urol* 139:418–422, 1988
9. KHAN SR, HACKETT RL: Calcium oxalate urolithiasis in the rat: Is it a model for human stone disease? A review of recent literature. *Scanning Microsc* 2:759–774, 1985
10. KHAN SR: Animal models of kidney stone formation: An analysis. *World J Urol* 15:236–243, 1997
11. KHAN SR, WHALEN PO, GLENTON PA: Heterogeneous nucleation of calcium oxalate crystals in the presence of membrane vesicles. *J Crystal Growth* 134:211–218, 1993
12. FASANO JM, KHAN SR: Intratubular crystallization of calcium oxalate in the presence of membrane vesicles: An in vitro study. *Kidney Int* 59:169–178, 2001
13. BOSKEY AL: Role of calcium-phospholipid-phosphate complexes in tissue mineralization. *Met Bone Dis Relat Res* 1:137–142, 1978
14. BOYAN BD, BOSKEY AL: Co-isolation of proteolipids and calcium-phospholipid-phosphate complexes. *Calcif Tissue Res* 36:214–218, 1984
15. BOSKEY AL, ULLRICH W, SPEVAK L, GILDER H: Persistence of complexed acidic phospholipids in rapidly mineralizing tissues is due to affinity for mineral and resistance to hydrolytic attack: In vitro data. *Calcif Tissue Int* 58:45–51, 1996
16. MANN S, HEYWOOD BR, RAJAM S, BIRCHALL JD: Controlled crystallization of calcium carbonate under stearic acid monolayers. *Nature* 334:692–694, 1988
17. ATMANI F, GLENTON PA, KHAN SR: Identification of proteins isolated from calcium oxalate and calcium phosphate crystals induced

- in the urine of healthy and stone forming subjects. *Urol Res* 26:201–207, 1998
18. KHAN SR, GLENTON PA: Increased urinary excretion of lipids by patients with kidney stones. *Br J Urol* 77:506–511, 1996
 19. WHIPPS S, KHAN SR, OPALCO FJ, et al: Growth of calcium oxalate monohydrate at phospholipid Langmuir monolayers. *J Crystallogr Growth* 192:243–249, 1998
 20. BACKOV R, KHAN SR, MINGOTAUD C, et al: Precipitation of calcium oxalate monohydrate at phospholipid monolayers. *J Am Soc Nephrol* 10(Suppl):S359–S363, 1999
 21. BACKOV R, LEE CM, KHAN SR, et al: Calcium oxalate monohydrate precipitation at phosphatidylglycerol langmuir monolayers. *Langmuir* 16:6013–6019, 2000
 22. WERNES P, BROWN C, SMITH L, FINLAYSON B: EQUIL 2: Basic computer program for the calculation of urinary saturation. *J Urol* 134:1242–1244, 1985
 23. MARTIN RS, SMALL DM: Physicochemical characterization of the urinary lipid from humans with nephrotic syndrome. *J Lab Clin Med* 103:798–810, 1984
 24. UYAMA E, KITSUKAKE Y, HARA A, et al: Abnormal excretion of urinary phospholipids and sulfatides in patients with mitochondrial encephalomyopathies. *Biochem Biophys Res Comm* 194:266–273, 1993
 25. JOSEPOVITZ C, LEVINE R, LANE B, KALOYANIDES J: Contrasting effects of gentamicin and mercuric chloride on urinary excretion of enzymes and phospholipids in the rat. *Lab Invest* 52:375–386, 1985
 26. LIESKE JC, HAMMES MS, HOYER JR, TOBACK FG: Renal cell osteopontin production is stimulated by CaOx monohydrate crystals. *Kidney Int* 51:679–686, 1997
 27. GOKHALE JA, GLENTON PA, KHAN SR: Immunocytochemical Tamm-Horsfall. *Nephron* 73:456–461, 1996
 28. IIDA S, PECK AB, JOHNSON-TARDIEU J, et al: Temporal changes in mRNA expression for bikunin in the kidneys of rats during CaOx nephrolithiasis. *J Am Soc Nephrol* 10:986–996, 1999
 29. IIDA S, PECK AB, BYER KJ, KHAN SR: Expression of bikunin mRNA in renal epithelial cells after oxalate exposure. *J Urol* 162:1480–1486, 1999
 30. GOKHALE JA, GLENTON PA, KHAN SR: Characterization of Tamm-Horsfall protein in a rat nephrolithiasis model. *J Urol* 166:1492–1497, 2001
 31. ZAGER RA, BURKHART KM, JOHNSON ACM, SACKS BM: Increased proximal tubular cholesterol content: Implications for cell injury and acquired cytoresistance. *Kidney Int* 56:1788–1797, 1999
 32. BOSKEY AL: Phospholipids and calcification, in *Calcified Tissue*, edited by HUKINS DWL, Boca Raton, CRC Press, 1989, pp 215–243
 33. SCHOEN FJ, HARASAKI H, KIM KM, et al: Biomaterial-assisted calcification: Pathology, mechanisms, and strategies for prevention. *J Biomed Mater Res* 22:11–36, 1988
 34. KHAN SR, WILKINSON EJ: Scanning electron microscopy, x-ray diffraction, and electron microprobe analysis of calcific deposits on intrauterine contraceptive devices. *Hum Pathol* 16:732–738, 1985
 35. KHAN SR: Heterogeneous nucleation of calcium oxalate crystals in mammalian urine. *Scanning Microsc* 9:597–616, 1995
 36. MOLITORIS BA, SIMON FR: Renal cortical brush-border and basolateral membranes: Cholesterol and phospholipid composition and relative turnover. *J Membr Biol* 83:207–215, 1985
 37. LETELLIER SR, LOCHHEAD MJ, CABELL AA, VOGEL V: Oriented growth of calcium oxalate monohydrate crystals beneath phospholipid monolayers. *Biochim Biophys Acta* 1380:31–45, 1998
 38. MANDEL NS: Crystal-membrane interaction in kidney stone disease. *J Am Soc Nephrol* 5(Suppl):S37–S45, 1994
 39. LIESKAE JC, TOBACK FG, DEGANELLO S: Face-selective adhesion of calcium oxalate dihydrate crystals to renal epithelial cells. *Calcif Tissue Intl* 58:195–200, 1996
 40. LIESKE JC, TOBACK FG, DEGANELLO S: Direct nucleation of calcium oxalate dihydrate crystals onto the surface of living epithelial cells in culture. *Kidney Intl* 54:796–803, 1998
 41. LIESKE JC, HUANG E, TOBACK FG: Regulation of renal epithelial cell affinity for calcium oxalate monohydrate crystals. *Am J Physiol* 278:F130–F137, 2000
 42. TRUMP BF, BEREZESKI IK: Calcium-mediated cell injury and cell death. *FASEB J* 9:219–228, 1995
 43. KHAN SR, BYER KJ, THAMILSELVAN S, et al: Crystal-cell interaction and apoptosis in oxalate-associated injury of renal epithelial cells. *J Am Soc Nephrol* 10(Suppl):S457–S463, 1999
 44. KOUL H, KENNINGTON L, NAIR G, et al: Ox-induced initiation of DNA synthesis in LLC-PK1 cells, a line of renal epithelial cells. *Biochem Biophys Res Comm* 205:1632–1637, 1994
 45. WIESSNER JH, HASEGAWA AT, HUNG LY, MANDEL NS: Oxalate-induced exposure of PS on surface of renal epithelial cells in culture. *J Am Soc Nephrol* 10(Suppl):S441–S445, 1999
 46. JONASSEN JA, COONEY R, KENNINGTON L, et al: Ox-induced changes in the viability and growth of human renal epithelial cells. *J Am Soc Nephrol* 10(Suppl):S446–S451, 1999
 47. KOUL HK, KOUL S, FU S, et al: Oxalate: From crystal formation to crystal retention. *J Am Soc Nephrol* 10:S417–421, 1999
 48. CAO L-C, JONASSEN J, HONEYMAN TW, SCHEID C: Oxalate-induced redistribution of phosphatidylserine in renal epithelial cells, implication for kidney stone disease. *Am J Nephrol* 21:69–77, 2001
 49. WIESSNER JH, HASEGAWA AT, HUNG LY, et al: Mechanisms of calcium oxalate crystal attachment to injured renal collecting duct cells. *Kidney Int* 59:637–644, 2001
 50. KHAN SR: Interactions between stone forming calcific crystals and macromolecules. *Urol Int* 59:59–71, 1997

Calcium Oxalate Monohydrate Precipitation at Phosphatidylglycerol Langmuir Monolayers

Réal Backov,[†] Christine M. Lee,[†] Saeed R. Khan,[‡] Christophe Mingotaud,[§]
Gail E. Fanucci,[†] and Daniel R. Talham^{*,†}

Department of Chemistry, University of Florida, Gainesville, Florida 32611-7200,
CNRS, Centre de Recherches Paul Pascal, F-33600 Pessac, France, and Department of
Pathology, College of Medicine, University of Florida, Gainesville, Florida 32610

Received December 31, 1999. In Final Form: April 6, 2000

Calcium oxalate monohydrate (COM) has been crystallized beneath Langmuir monolayers of four different phosphatidylglycerol lipids, allowing investigation of the influence of the density of headgroup packing and monolayer compressibility on heterogeneous precipitation. The COM crystals were nucleated from metastable solutions at Langmuir monolayers of the phospholipids dipalmitoylphosphatidylglycerol (DPPG), dioleoylphosphatidylglycerol (DOPG), palmitoyloleoylphosphatidylglycerol (POPG), and dimyristoylphosphatidylglycerol (DMPG). Crystal formation was monitored at the air/water interface using Brewster angle microscopy, and in transferred films with scanning electron microscopy. For each Langmuir monolayer it was observed that precipitation is heterogeneous and is selective with respect to the orientation and morphology of the precipitated crystals, with a majority of crystals having the (101) face oriented toward the monolayer interface. When the phospholipid monolayers are held at the same pressure, more crystals are observed under DPPG, which is the film with the smallest area per molecule. However, in apparent contrast, nucleation rates increase when the films are expanded. Also, when the four monolayers are held at the same area, nucleation occurs preferentially beneath films at lower surface pressures. The results suggest that the compressibility of the monolayer and the potential of the monolayer to achieve a small area per molecule are more important characteristics that lead to heterogeneous crystallization of COM than is providing a prearranged template. We also observe some evidence that domain boundaries between different monolayer phases can act as nucleation sites.

Introduction

Calcium oxalate and calcium phosphate are the principal crystalline materials found in human urinary stones. In these calcific deposits, inorganic crystals are mixed with an organic matrix of urinary macromolecules that includes proteins, lipids, and carbohydrates.^{1,2} In the kidney, oxalate and phosphate are concentrated, resulting in supersaturation with respect to their calcium salts. Heterogeneous precipitation is normal, and in nonstoneformers the effects are minimized by the production of protein and small molecule inhibitors. In stoneformers, it is often found that the production of inhibitors is unusually small, or that there are high levels of nucleation promoters.³ Among the promoters are acidic phospholipids, originating as cellular degradation products, that have been shown to catalyze calcium oxalate and calcium phosphate precipitation.^{4–6} It has been hypothesized that transmembrane movement can result in an unusually high concentration, or partitioning, of acidic phospholipids at outer membrane surfaces, leading to nucleation or adhesion sites for the inorganic crystals.^{7,8}

An important part of the study of urinary stone formation is to develop an understanding of the interactions between the stone crystals and the components of the organic matrix. We recently began a series of studies looking at calcium oxalate precipitation at phospholipid interfaces prepared as Langmuir monolayers, where the organic film serves as a model for domains of like lipids found at the outer surface of a membrane bilayer.^{9,10} Initial studies by our group^{9,10} and by Letellier et al.¹¹ have shown that phospholipid monolayers can indeed catalyze heterogeneous precipitation of calcium oxalate from metastable solutions. There is a strong selectivity for the calcium oxalate monohydrate (COM) over the other common calcium oxalate phase, the dihydrate, which parallels observations on urinary stones.^{7,12} A comparison of different phospholipids showed an increased rate of COM crystal formation under negatively charged phospholipids, implicating a mechanism whereby COM nucleation is promoted by the concentration of calcium ions at the interface.^{9–11} Consistent with this mechanism is the observation that the majority of crystals orient with the calcium-rich (101) face parallel to the phospholipid monolayer.^{7,13}

* To whom correspondence should be addressed.

[†] Department of Chemistry, University of Florida.

[‡] College of Medicine, University of Florida.

[§] CNRS.

(1) Khan, S. R.; Hackett, R. L. *J. Urol.* **1993**, *150*, 239–245.

(2) Khan, S. R.; Atmani, F.; Glenton, P.; Hou, Z.-C.; Talham, D. R.; Khurshid, M. *Calcif. Tissue Int.* **1996**, *59*, 357–365.

(3) Khan, S. R. *Urol. Int.* **1997**, *59*, 59–71.

(4) Khan, S. R.; Whalen, P. O.; Glenton, P. A. *J. Cryst. Growth* **1993**, *134*, 211–218.

(5) Boskey, A. L.; Posner, A. S. *Calcif. Tissue Res.* **1976**, *22S*, 197–201.

(6) Boyce, W. H.; Garvey, F. K. *J. Urol.* **1956**, *76*, 213–217.

(7) Mandel, N. *J. Am. Soc. Nephrol.* **1994**, *5*, S37–S45.

(8) Bigelow, M. W.; Wiessner, J. H.; Kleinman, J. G.; Mandel, N. S. *Calcif. Tissue Int.* **1997**, *60*, 375–379.

(9) Whipps, S.; Khan, S. R.; O'Palko, F. J.; Backov, R.; Talham, D. R. *J. Cryst. Growth* **1998**, *192*, 243–249.

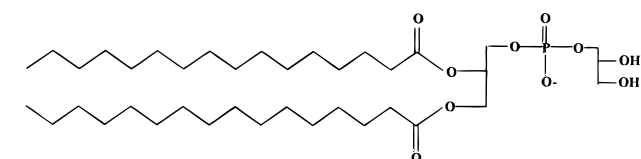
(10) Backov, R.; Khan, S. R.; Mingotaud, C.; Byer, K.; Lee, C. M.; Talham, D. R. *J. Am. Soc. Nephrol.* **1999**, *10*, S359–S363.

(11) Letellier, S. R.; Lochhead, M. J.; Cambell, A. A.; Vogel, V. *Biochim. Biophys. Acta—Gen. Subjects* **1998**, *1380*, 31–45.

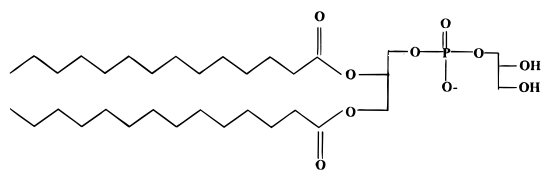
(12) Khan, S. R.; Cockrell, C. A.; Finlayson, B.; Hackett, R. L. *J. Urol.* **1984**, *132*, 153–157.

(13) Deganello, S.; Piro, O. E. *N. Jb. Miner. Mh.* **1981**, *2*, 81–88.

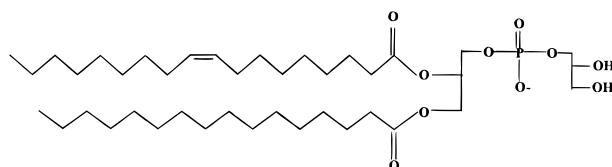
Chart 1



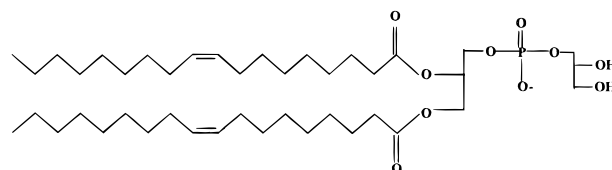
Dipalmitoylphosphatidylglycerol (DPPG)



Dimyristoylphosphatidylglycerol (DMPG)



1-Palmitoyl-2-oleoylphosphatidylglycerol (POPG)



Dioleoylphosphatidylglycerol (DOPG)

In the present study, we further explore the features of phospholipid monolayers that contribute to heterogeneous precipitation of calcium oxalate. While the chemical identity of the phospholipid headgroups has already been shown to influence precipitation, other variables have been proposed to regulate inorganic nucleation at organic monolayers, including the packing density and packing geometry of the amphiphiles,^{14,15} and the monolayer compressibility.^{16,17} To explore these variables, we have chosen to investigate calcium oxalate growth at monolayers of four phosphatidylglycerols possessing different lipophilic tails. The four amphiphiles, shown in Chart 1, are dipalmitoyl-*L*- α -phosphatidyl-DL-glycerol (DPPG), dimyristoyl-*L*- α -phosphatidyl-DL-glycerol (DMPG), β -oleoyl- γ -palmitoyl-*L*- α -phosphatidyl-DL-glycerol (POPG), and dioleoyl-*L*- α -phosphatidyl-DL-glycerol (DOPG). By studying this series, the effect of the packing density of the headgroup on crystal formation can be probed while maintaining the monolayers at the same applied pressure. Similarly, crystal growth under monolayers with the same mean molecular area, but at different surface pressures, allows comparison of the influence of monolayer compressibility. In the course of these experiments we also

observed evidence that phase boundaries in the Langmuir monolayer can promote formation of calcium oxalate crystals.

Experimental Section

Materials. DPPG (98%), DOPG (98%), POPG (98%), and DMPG (98%) were purchased from Sigma (St. Louis, MO) and used as received without further purification. Calcium chloride (97%), sodium oxalate (99.99+%), and tris(hydroxymethyl)-aminoethane hydroxychloride (Tris·HCl) (99+%) were used as received from Aldrich Chemical Co. (Milwaukee, WI). The water used in LB experiments was purified via a Sybron/Barnstead Nanopure system (Boston, MA) and had a resistivity of 18 M Ω cm. Glass microscope coverslips, used as substrates for SEM analyses, were cleaned using a piranha etch (1 h immersion in freshly prepared 3:1 H₂SO₄/H₂O (*Caution: piranha solution can react violently*)), then sonicated, and rinsed carefully with H₂O.

Instrumentation. Langmuir–Blodgett experiments were carried out on a custom-made Teflon double barrier trough measuring 12.8 cm \times 75 cm and controlled with a KSV Instruments (Stratford, CT) model 3000 LB system. Surface pressure was measured with a platinum Wilhelmy plate suspended from a KSV microbalance. Scanning electron microscopy (SEM) was performed using a JEOL (Peabody, MA) 35C microscope at an accelerating voltage of 15 kV. Brewster angle microscopy (BAM) was performed using a laboratory-made instrument.¹⁸

Methods. Film balance parameters include a linear compression rate of 5 (mN/m)/min and a barrier speed of 1.6 ($\text{\AA}^2/\text{mol}$)/min to achieve target pressures or target mean molecular areas. All lipids were dissolved in a 5:1 chloroform/methanol spreading solvent at concentrations near 1.0 mg/mL. Typically a volume of 100 μ L of the corresponding phospholipid solutions was spread onto the subphase. The transfer of Langmuir monolayers to solid supports for analysis by SEM was accomplished by carefully draining the subphase from the trough to lower the monolayer onto a substrate that had been placed in the subphase before the monolayer was applied. Substrates were positioned at an angle of approximately 35° with respect to the bottom of the trough to allow for better drainage.

Supersaturated calcium oxalate monohydrate subphases were prepared as follows. An aqueous solution that was 150 mM NaCl and 5 mM Tris·HCl buffer was adjusted to pH 7.0 by adding the appropriate volume of 0.05 M KOH(aq). This solution was split into two equal volumes before adding the appropriate amounts of CaCl₂ to one and Na₂C₂O₄ to the other (0.35 and 0.5 mM of each component for relative supersaturation (RS) 5 and 10, respectively). The RS values were calculated using Finlayson's computer program EQUIL v.1.3.¹⁹ The completely dissolved solutions were mixed together just prior to their use to generate the subphase solutions.

For Brewster angle microscopy experiments, DPPG was spread on either pure water or RS5 or RS10 calcium oxalate subphases. The monolayers were compressed to a target area or target pressure and allowed to stand for periods of 4–12 h and images collected. For the calcium oxalate subphases, bright birefringent spots were observed after several hours that correspond to calcium oxalate crystals. These features were not observed on the pure water subphases. The resolution of the BAM is not sufficient to focus an image of the crystals, so the bright spots that originate from the crystals appear much larger than their actual size.

Crystal Counting Procedures. For each crystal growth experiment, 1.2 mm² on each of eight glass coverslips was carefully examined using SEM. Each experiment was reproduced four times; thus, the reported crystal surface densities for each experimental condition are averaged over nearly 40 mm².

Results

Monolayer Experiments. Langmuir monolayers of the phospholipids DPPG, DMPG, POPG, and DOPG were

(14) Mann, S. *Nature* **1993**, *365*, 499–505.

(15) Mann, S.; Archibald, D. D.; Didymus, J. M.; Douglas, T.; Heywood, B. R.; Meldrum, F. C.; Reeves, N. J. *Science* **1993**, *261*, 1286–1292.

(16) Cooper, S. J.; Sessions, R. B.; Lubetkin, S. D. *Langmuir* **1997**, *13*, 7165–7172.

(17) Cooper, S. J.; Sessions, R. B.; Lubetkin, S. D. *J. Am. Chem. Soc.* **1998**, *120*, 2090–2098.

(18) Cuvillier, N.; Bernon, R.; Doux, J.-C.; Merzeau, P.; Mingotaud, C.; Delhaes, P. *Langmuir* **1998**, *14*, 5573–5580.

(19) Werness, P.; Brown, C.; Smith, L.; Finlayson, B. *J. Urol.* **1985**, *134*, 1242–1244.

each prepared at the air/water interface by spreading the lipid from a chloroform/methanol solution and compressing the films using opposing moveable barriers. Surface pressure vs area isotherms were measured on 0.35 and 0.5 mM Ca^{2+} subphases, which correspond to the Ca^{2+} ion concentration in the RS 5 and RS 10 calcium oxalate solutions, respectively. The isotherms are similar to those previously published.^{20–24} The inclusion of oxalate ion to form the RS 5 and RS 10 calcium oxalate subphases does not change the isotherms relative to those on pure Ca^{2+} subphases, and there are no significant differences in the isotherms recorded at the two subphase concentrations. The isotherms of DPPG, DMPG, POPG, and DOPG on RS 5 subphases are shown in Figure 1. The lipids DMPG, POPG, and DOPG each form liquid expanded (LE) phases as they are compressed, with no transition to a liquid condensed (LC) phase. For a given surface pressure, the area per molecule in the LE phase varies in the order $\text{DMPG} < \text{POPG} < \text{DOPG}$, reflecting the presence of zero, one, and two olefinic groups, respectively, in the lipid tails. The DPPG isotherm is much richer than the others, as at room temperature on Ca^{2+} -containing subphases both LE and LC phases are formed. As the monolayer is compressed, the pure LE phase onsets near $100 \text{ \AA}^2/\text{molecule}$, and between approximately 45 and $80 \text{ \AA}^2/\text{molecule}$, the LE and LC phases coexist in equilibrium. Below $45 \text{ \AA}^2/\text{molecule}$, the film is in the pure LC phase.²²

Crystal Nucleation Experiments. Calcium oxalate precipitation under each monolayer was studied using procedures described previously.^{9,10} Monolayers were held at either constant pressure or constant area over the supersaturated subphases for 4 h, at which point the subphases were slowly drained to lower the monolayers onto prepositioned glass supports for SEM analysis. Earlier studies,^{9–11} including observations by Brewster angle microscopy⁹ and optical microscopy,¹¹ showed that COM crystallization occurs at the phospholipid interfaces, and that this deposition procedure allows observation of crystals formed at the Langmuir monolayer interface. In addition, for each experiment described in the present study, control glass supports were placed outside the barriers, where there was no monolayer, to be sure that neither homogeneous precipitation nor water evaporation during the deposition procedure was a significant source of COM formation. No COM crystals were observed on the control slides by SEM.

Crystal formation at the four lipid monolayers was compared in two series of experiments. First, the monolayers were studied at a common surface pressure of 20 mN/m (Figure 2). Film “creep” at 20 mN/m was less than 2%/h during the course of the experiments. At this surface pressure, the mean molecular area (mma) increases in the order $\text{DPPG} < \text{DMPG} < \text{POPG} < \text{DOPG}$, ranging from $40 \text{ \AA}^2/\text{molecule}$ for DPPG to $90 \text{ \AA}^2/\text{molecule}$ for DOPG. In this same-pressure series of experiments, the area per molecule of the glycerol headgroup can be changed while keeping the mobility of the amphiphiles within the monolayers approximately the same. In the second series of experiments, the monolayers were held at a common mma of $95 \text{ \AA}^2/\text{molecule}$. At this area, the applied surface

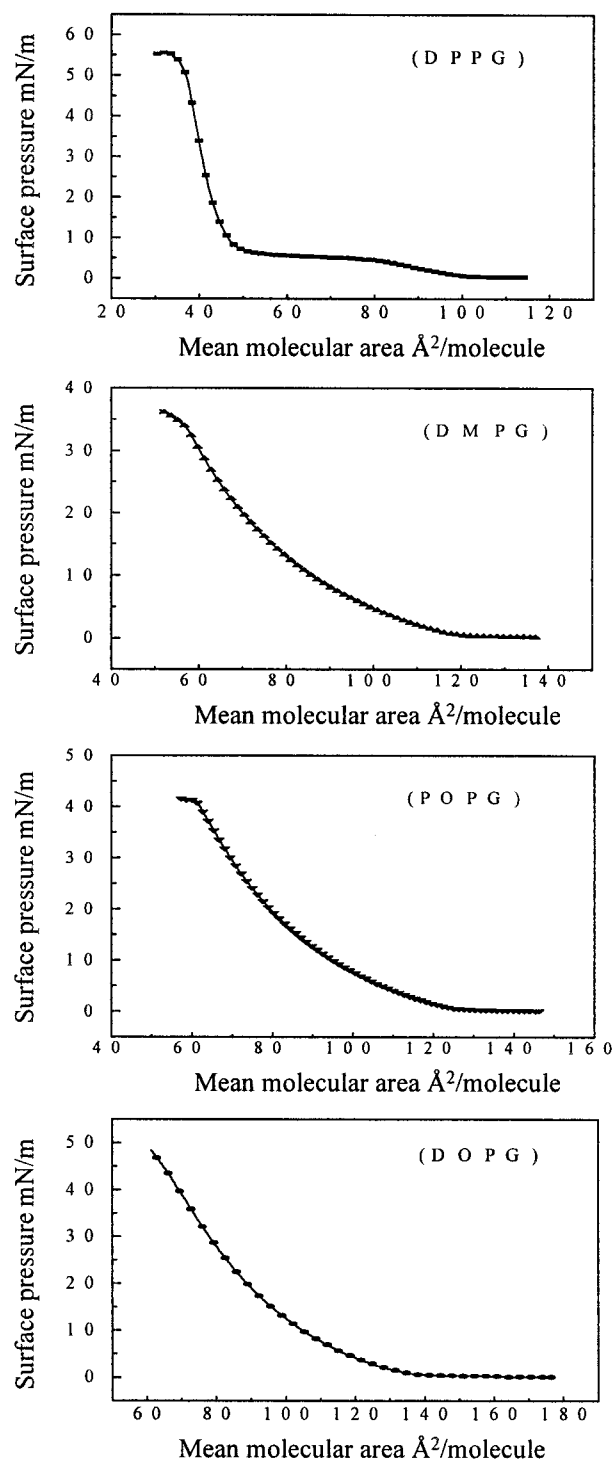


Figure 1. Pressure vs area isotherms of the phospholipids DPPG, DMPG, POPG, and DOPG at $25 \pm 0.5^\circ \text{C}$ on RS 5 calcium oxalate aqueous solutions at pH 7. The isotherms were recorded under linear compression, with maximum forward and backward barrier speeds of $1.6 (\text{Å}^2/\text{mol})/\text{min}$. DPPG exhibits both LE and LC phases, while DMPG, POPG, and DOPG form only LE phases at increased surface pressure.

pressure increases in the order $\text{DPPG} < \text{DMPG} < \text{POPG} < \text{DOPG}$, and ranges from 1.3 to 15 mN/m. The same-area-per-molecule experiment allows comparison of crystal growth under monolayers with the same average headgroup spacing, but with different molecular mobility and film compressibility. The two series of experiments also allow each monolayer to be compared at two different surface pressures (and corresponding mma). For the three phospholipids DMPG, POPG, and DOPG, all of the

(20) Mingotaud, A.-F.; Mingotaud, C.; Patterson, L. K. *Handbook of Monolayers*, 1st ed.; Academic Press: London, 1993; Vol. 1.

(21) Mombers, C.; Degier, J.; Demel, R. A.; Deenen, L. L. V. *Biochim. Biophys. Acta* **1980**, 52–62.

(22) El Mashak, E. M.; Tocanne, J.-F. *Biochim. Biophys. Acta* **1980**, 596, 165–179.

(23) Tamm, L. K. *Biochemistry* **1986**, 23, 7470–7476.

(24) Mingotaud, C.; Chauvet, J. P.; Patterson, L. K. *J. Phys. Chem.* **1996**, 100, 18554–18567.

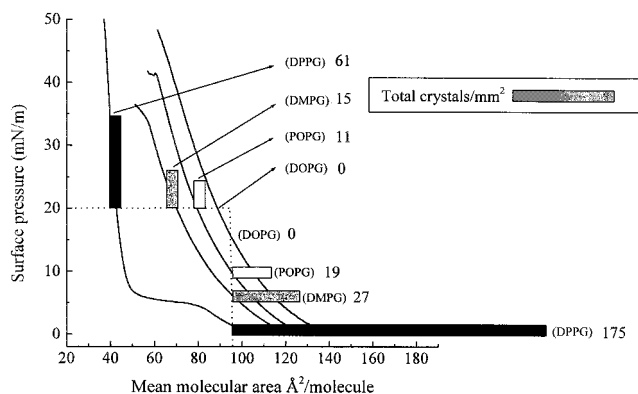


Figure 2. Histogram showing the average number of COM crystals (all formations) observed under each monolayer, held at the conditions indicated. The subphase is RS 5 calcium oxalate at 25 °C and pH 7. Samples were removed from the LB trough after 4 h, and the reported surface densities are averages over nearly 40 mm², as described in the Experimental Section.

comparisons are with the monolayer in the same LE phase. Phospholipid DPPG is more complicated because at high pressure the monolayer is in the LC phase while at 95 Å²/molecule, the monolayer is in the LE phase.

The total number of crystals (all formations) observed under each monolayer in the same-pressure and same-area comparisons is indicated by the histograms in Figure 2. The three COM crystal formations that are commonly observed during those studies are shown in Figure 3. These facets also grow when COM is precipitated homogeneously, but the crystal shapes differ when COM is formed from bulked solutions due to extensive twinning. Earlier electron diffraction studies⁹ have confirmed that each of these crystal formations is COM, and they are easily identified from SEM images by visual inspection of the crystal habit. As Figure 2 indicates, no crystals were observed under the DOPG monolayer; however, COM was observed under the other three phospholipid layers. The breakdown of the incidence of each type of crystal formation within each experiment is shown in Figures 4–6 for the DPPG, DMPG, and POPG monolayers, respectively, where the data are compared for each phospholipid at the two different points on their isotherms. In the experiments where COM was precipitated, between 60% and 90% of the observed crystals formed with the (101) face toward the interface. The other habit of the single crystal that was observed is oriented with the (010) face toward the surface. Agglomerates of crystals were also observed and usually accounted for about 10% of the crystal formations. The one exception was under the DPPG monolayer at low surface pressure where over 20% of the crystals were agglomerates. In earlier studies,^{9,11} electrostatic arguments were used to account for the highly specific crystal orientation that is observed. The (101) face of COM is calcium rich^{7,13} and has a slight positive charge surplus. The atomic arrangements in the (101) and (010)^{11,13} faces of COM are shown in Chart 2. The calculated calcium densities are 0.04 and 0.03 ions/Å², respectively. Each of the lipid assemblies is known to bind Ca²⁺, thereby providing a mechanism to sufficiently concentrate calcium ions, mimicking the calcium-rich face, and lead to specific nucleation. Such a mechanism was proposed previously by Heywood et al.^{25,26} for the crystallization of calcium carbonate at fatty acid monolayers. The calcium-rich (101)

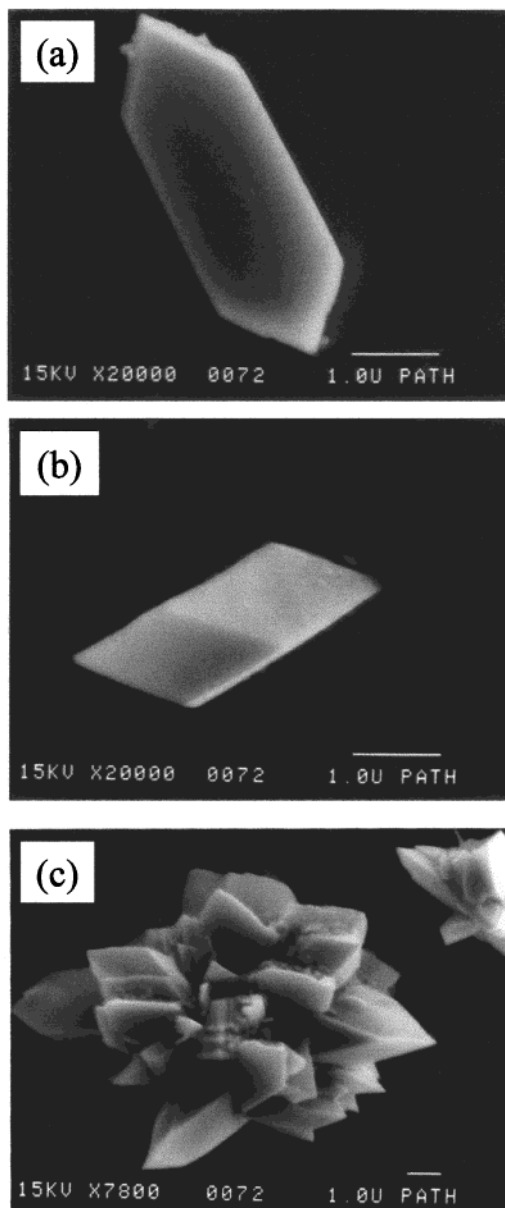


Figure 3. SEM images of commonly observed crystal formations of COM grown at a DPPG interface from a calcium oxalate subphase of RS 5: (a) the crystal is oriented with the (101) face toward the monolayer, (b) the (010) face is toward the monolayer, (c) an agglomeration of crystals. The scale bar corresponds to 1 μm.

crystal face has also been implicated in studies of adhesion of COM to membranes in lipid-enriched cell culture studies.⁷

Same Pressure/Different Area. Figure 2 indicates the total number of crystals observed under each monolayer while held at 20 mN/m. The general trend is that more crystals are generated at the monolayers with smaller corresponding mma. It should be remembered that the DPPG monolayer is in the LC phase at this pressure, while the other three lipids are in the LE phase, although the trend still applies to the three LE monolayers alone. The distributions of the types of crystal formations are described in Figures 4–6, and comparison of the 20 mN/m data indicates that the breakdown is similar in each case, with a slightly higher incidence of (010) orientation under the DPPG monolayer. In this comparison, we expect the mobility of the phospholipids to be similar within each monolayer, while the spatial distribu-

(25) Heywood, B. R.; Mann, S. *Langmuir* **1992**, *8*, 1492–1498.

(26) Heywood, B. R.; Mann, S. *J. Am. Chem. Soc.* **1992**, *114*, 4681–4686.

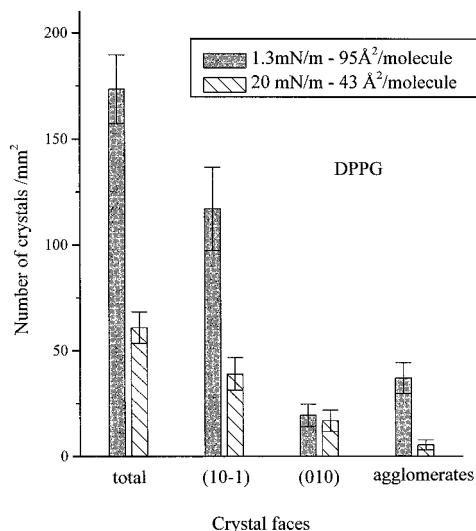


Figure 4. Histogram showing the distribution of COM crystal formations grown under DPPG from an RS 5 calcium oxalate subphase after 4 h. The filled bars correspond to the experiment where the monolayer was held at 95 Å²/molecule and the dashed rectangles correspond to the monolayer held at 20 mN/m.

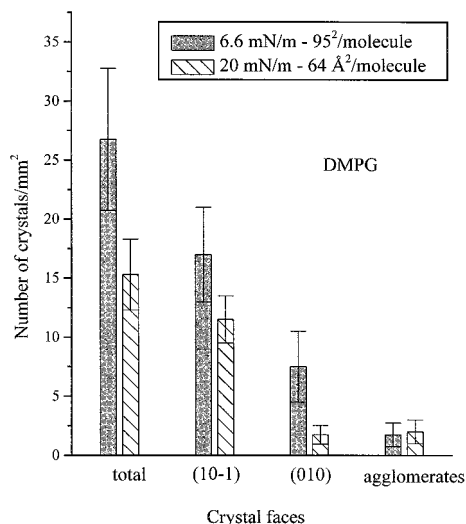


Figure 5. Histogram showing the distribution of COM crystal formations grown under DMPG from an RS 5 calcium oxalate subphase after 4 h. The filled bars correspond to the experiment where the monolayer was held at 95 Å²/molecule and the dashed rectangles correspond to the monolayer held at 20 mN/m.

tion of the headgroups and charge density at the interface are variable. This experiment suggests that when the monolayers are held at the same pressure, a higher charge density at the monolayer leads to an increase in crystal formation.

Same Area/Different Pressure. In this series of experiments, each monolayer was held at 95 Å²/molecule, where the resulting surface pressures range from a high of near 15 mN/m for the DOPG monolayer to 1.3 mN/m for DPPG. From Figure 2, the general trend is that more crystals are formed at lower surface pressure. The distribution in the type of observed crystal formations is again similar (Figures 5–7), except for a somewhat higher incidence of agglomerates under the DPPG monolayer. At this area per molecule, all monolayers are in the LE phase. In this same-area/different-pressure comparison, we expect the average charge density at the monolayers to be similar, while the mobility of the phospholipid molecules within the monolayers changes as a result of the different applied surface pressure. The result from

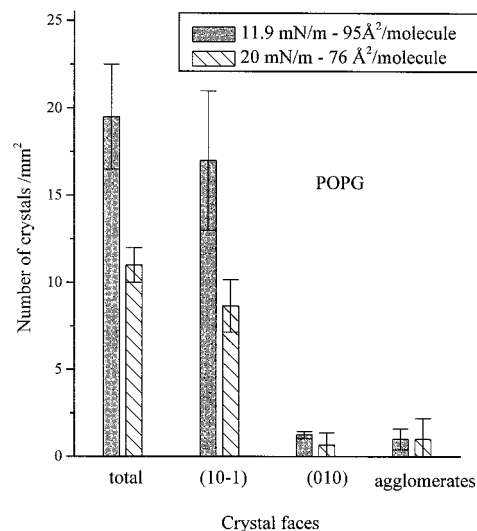
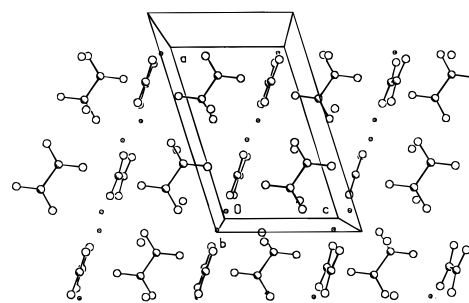


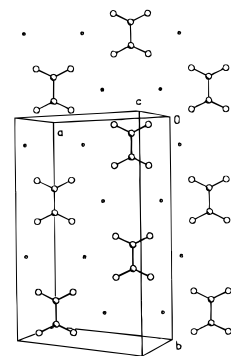
Figure 6. Histogram showing the distribution of COM crystal formations grown under POPG from an RS 5 calcium oxalate subphase after 4 h. The filled bars correspond to the experiment where the monolayer was held at 95 Å²/molecule and the dashed rectangles correspond to the monolayer held at 20 mN/m.

Chart 2

(010) Face of COM



(10-1) Face of COM



this experiment suggest that when the monolayers are compared at a common mean molecular area, a lower applied surface pressure leads to an increased incidence of crystal formation.

Same Phospholipid/Different Pressure and Area. After completing the same-pressure and same-area studies described above, we can now compare crystal growth under each monolayer held at two different sets of conditions. As seen in Figures 2 and 5–7, with the exception of the DOPG film where no crystals are observed, there is an increase in crystal formation as the monolayers are expanded. Expansion leads to a decrease in the average charge density at the monolayer, and an increase in the

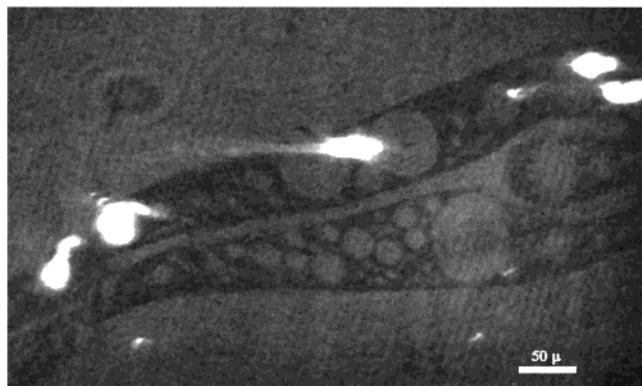


Figure 7. BAM image of a DPPG monolayer on a calcium oxalate subphase of RS 5 held near $100 \text{ \AA}^2/\text{molecule}$, just before the surface pressure begins to increase. The gray areas are the LE phase that is in equilibrium with the gas analogous phase, which appears as the darkest regions. Calcium oxalate crystal formations are observed as the bright white features. The BAM cannot focus on the crystals, so they can appear larger than they are. It is interesting to note that the crystals commonly appear at the interface between the two phases.

mobility of the phospholipid amphiphiles. For the DMPG and POPG monolayers, there is no phase change as these films are expanded from 20 mN/m. For the DPPG monolayer, however, expansion results in a phase change from the LC phase at 20 mN/m to the LE phase at $95 \text{ \AA}^2/\text{molecule}$ and 1.3 mN/m, and the increase in COM crystallization is significantly larger for the DPPG monolayer than for the others.

Discussion

Studies on crystal growth at organized monolayers have elucidated a number of factors that govern the monolayer's role in controlling nucleation and growth.^{27–29} A widely cited mechanism is direct templating of the crystal by the organized monolayer.^{11,15,27,28} Here, the packing of molecules in a close-packed monolayer mimics a face of the nucleating crystal and catalyzes nucleation relative to bulk precipitation. Templating often leads to high selectivity for a specific crystal orientation, or even a specific crystal polymorph,^{14,27,30} as nucleation takes place when a crystal face “recognizes” the organic interface. The mechanism has parallels in the epitaxial growth of inorganic solids at inorganic surfaces. Related to this are examples where the stereochemistry of the monolayer is transferred to a growing crystal.³¹ Direct templating is achieved through specific interaction between the template and the growing crystal face that occurs when the monolayer packing has the right geometry and the individual molecules within the monolayer have the right orientation²⁷ to interact with the inorganic crystal face.

Even when direct templating is not possible, organic interfaces can catalyze nucleation by concentrating interfacial charge. This mechanism is commonly invoked in protein-induced biomineralization, where the long-range translational symmetry necessary for direct templating is not possible, although the protein can sufficiently concentrate specific ions so that nucleation is induced.¹⁵

(27) Mann, S.; Heywood, B. R.; Rajam, S.; Walker, J. B. A. *J. Phys. D Appl. Phys.* **1991**, *24*, 154–164.

(28) Mann, S.; Heywood, B. R.; Rajam, S.; Birchall, J. D. *Proc. R. Soc. London, A* **1989**, *423*, 457–471.

(29) Mann, S.; Heywood, B. R. *Chem. Br.* **1989**, 98–101.

(30) Mann, S.; Heywood, B. R.; Rajam, S.; Birchall, J. D. *Nature* **1988**, *334*, 692–695.

(31) Landau, E. M.; Levanon, M.; Leiserowitz, L.; Lahav, M.; Sagiv, J. *Nature* **1985**, *318*, 353–356.

This mechanism has also been observed in studies of nucleation at organic monolayers. In fact, it was previously suggested that the concentration of calcium ions by the phospholipid monolayers is responsible for COM precipitation at the Langmuir monolayers.^{9,11}

Studies demonstrating the direct templating and interfacial charge mechanisms of particle nucleation at organized monolayers have generally been performed at high surface pressure where the organic interface is close-packed and rigid.^{11,27,32,33} Recent studies by Cooper et al.^{16,17} and by Ahn et al.³³ have indicated that a highly organized monolayer is not necessary to promote nucleation, and that monolayers at low or medium pressure can lead to higher nucleation rates. The greater dynamical freedom and compressibility at low or medium pressure allows the monolayer to reorganize itself to accommodate (optimize the geometrical and stereochemical fit) the nucleating or growing crystal. Cooper^{16,17} has pointed out a parallel with conventional epitaxial growth theory where a compressible inorganic substrate can more easily accommodate an overlayer because it can adjust to small lattice mismatches. When applied to organic interfaces, the surface can still template nucleation, but the process is cooperative and the template does not need to be preformed and rigid.

We can now review our experimental observations on the formation of COM crystals in the context of these mechanisms. It is clear from Figure 2 that crystallization is enhanced at lower applied surface pressures. For each of the monolayers where crystals are observed, the numbers increase as the monolayer is expanded. Also, when the different monolayers are compared at the same area, those at the lower corresponding surface pressure generate more crystals. These observations are consistent with ideas that crystal formation is enhanced if the interface has the ability to rearrange to accommodate the nucleating or growing crystal.

The next question is whether the monolayer rearranges to “template” the crystal growth, or does it induce crystallization by concentrating ions at the interface. Previous work by Letellier et al.¹¹ and by our own group^{9,10} looking at COM nucleation under different phospholipid headgroups failed to find a direct lattice match between close-packed phospholipid monolayers and the adsorbed faces of COM. In each of those studies, it was suggested that crystal formation was promoted by concentration of Ca^{2+} ions at the phospholipid interfaces. In the present study, COM is observed to form under three of the phosphatidylglycerols at both high and low pressures (Figure 2). Despite the significantly different mma per headgroup represented in those experiments, the selectivity for the (10 $\bar{1}$) face relative to the (010) (or any other face) remains nearly constant (Figures 4–6). This observation is especially evident for the three monolayers held at 20 mN/m that cannot all present the same template, yet show similar selectivities (Figures 4–6). Although there are more crystals observed under DPPG, the selectivity for the (10 $\bar{1}$) and (010) COM faces are similar for the other two monolayers that cannot achieve the same packing geometry as DPPG.

Considering all of the experimental results together, we observe that the highest density of crystals results under the phospholipids that have the *potential* to achieve the smallest mma (at the temperature studied). The monolayer does not need to be held in a compressed state,

(32) Zhao, X. K.; Yang, J.; McCormick, L. D.; Fendler, J. H. *J. Phys. Chem.* **1992**, *96*, 9933–9939.

(33) Ahn, D. J.; Berman, A.; Charych, D. *J. Phys. Chem.* **1996**, *100*, 12455–12461.

but if it is capable of organizing in a smaller area, the crystal precipitation is increased. For any set of conditions, more crystals form under the DPPG monolayer than under any of the others. DPPG can form an LC phase at room temperature, while the other phospholipids do not. Although DMPG also has two saturated alkyl tails, the shorter chains do not condense at room temperature, prohibiting this monolayer from achieving the same close packing as DPPG. The smaller *mma* results in a higher density of Ca^{2+} ions at the interface, which might account for the increased incidence of COM crystallization. In parallel, the stability gained through adsorption of the organic film to the growing crystal face will be greater as the *mma* decreases because it can achieve a higher surface coverage of the phosphatidylglycerol headgroup. While the observation holds true with or without including DPPG in the comparison, the highest crystal densities were observed under this monolayer, which can form a LC phase at room temperature, and is therefore capable of organizing at a much lower *mma*.

At this point in time, we cannot determine whether the influence of the monolayer on crystal formation is more important at the nucleation event, or during crystal growth. The SEM and BAM techniques employed detect mature crystals on the order of $1-10\ \mu\text{m}$ in size. To observe the crystals, they must grow, and nucleated crystals that do not mature will not be observed. While it is likely that similar factors affect both events, it is also possible that the factors we have identified influence COM crystal growth alone.

Finally, we have also observed COM crystallization at higher areas where the LE and gas analogous phases of DPPG are in equilibrium, suggesting an additional mechanism for heterogeneous crystallization, not observed under the single-phase monolayers. Figure 7 shows a BAM image of the DPPG monolayer just before the onset of pressure ($> 100\ \text{\AA}^2/\text{molecule}$). Crystals are observed as very bright spots at the interface between the gaseous regions (very dark) and the LE regions (slightly lighter). The BAM experiment does not have sufficient resolution to focus on the crystals, and they appear larger than they actually are because of their high refractive index. The crystals in Figure 7 are seen in regions where there is a boundary between LE and gaseous regions of the films. It is possible that nucleation of a crystal will cause a defect in the film, leading to a phase boundary. However, the features in Figure 7 are of too large a scale to have been caused by the crystals, and they are typical of the film dynamics during a compression cycle. It is more likely that the crystals form at these phase boundaries, and that high-energy sites at the interface may catalyze crystallization. Several factors might be responsible. The line tension between the LE and gaseous phases is large, and potentially reduced by crystal formation. A large gradient in the dipole electric field and increased fluidity at the phase boundary may also be important factors.

Similar interface effects are more difficult to observe in the LE/LC coexistence region of DPPG. Crystals are observed by BAM, and they are most often associated with LC regions of the film. However, we cannot differentiate the order of events. It is possible that the LC domain is formed first and COM nucleates at the LC domain or at the edge of the domain. Alternatively, it is COM nucleation that condenses phospholipids at the crystal surface, catalyzing the formation of adjacent LC domains.

Although we cannot yet quantify the nucleation mechanism, the observation of enhanced crystal formation at phase boundaries may have some relevance to phospholipid domains in bilayer membranes. Animal studies have demonstrated increased calcium oxalate crystallization in the kidneys following injuries to cells lining the renal tubules.³⁴ The crystals appeared to form in association with membranes of the vesicles produced during cellular degradation. Lipids in bilayer membranes are mobile, and lipid domains are dynamic. The results of the monolayer studies suggest that dynamic regions at the organic interface may lead to an increased chance of particle nucleation. Similarly, defects, such as those caused by membrane rupture, may lead to high-energy sites that can catalyze nucleation.

Conclusions

This study used phospholipid Langmuir monolayers to further explore the features of organic interfaces that lead to heterogeneous precipitation of the biomineral calcium oxalate monohydrate. A series of four phosphatidylglycerol lipids were chosen to investigate how variables including the density of headgroup packing, monolayer compressibility, and monolayer phase influence COM precipitation. The results suggest that there are a number of factors that contribute to formation of COM at the organic monolayer interface.

First, the monolayer must have the *potential* to form an arrangement that favors the incipient crystal face. The monolayer does not need to be preorganized, but the amphiphiles must be able to achieve a packing necessary to sufficiently concentrate charge and contribute to surface stabilization through adsorption.

Second, increased molecular mobility and film compressibility lead to enhanced crystal precipitation. This suggests that the interaction between the organic layer and the inorganic crystal face is cooperative. A dynamic monolayer can achieve an organization that is favorable for nucleation. A rigid monolayer might be able to template a crystal face, but if the lattice match is not perfect, it may actually suppress nucleation and growth. And finally, phase boundaries can be favorable sites for crystallization. The phospholipid molecules at boundary sites are the most likely to rearrange to accommodate an incipient crystal.

Langmuir monolayer studies continue to prove useful for elucidating the mechanisms of heterogeneous nucleation of inorganic particles at organic interfaces. The principal benefit is the ability to control specific variables that influence crystal formation. Future studies on COM precipitation will attempt to quantify the influence of monolayer phase boundaries, and we will also explore the effects that additives to the Langmuir monolayer have on crystal nucleation.

Acknowledgment. We thank the National Aeronautics and Space Administration, Grant NAG8-1244 (D.R.T.), and the National Institutes of Health, Grant RO1-DK41434 (S.R.K.), each for partial support of this work. D.R.T. thanks the CNRS for supporting his stay as a Visiting Scientist at the Centre de Recherches Paul Pascal, during which time part of this work was performed.

LA991684V

Assembly of Partially Oxidized Tetrathiafulvalene in Layered Phosphates. Formation of Conducting Organic–Inorganic Hybrids by Intercalation[†]

Rénal Backov, Bernard Bonnet, Deborah J. Jones, and Jacques Rozière*

Laboratoire des Agrégats Moléculaires et Matériaux Inorganiques, ESA CNRS 5072, Université Montpellier II, Place E. Bataillon, 34095 Montpellier Cedex 5, France

Received February 10, 1997. Revised Manuscript Received June 4, 1997[®]

Intercalation and ion-exchange reactions have been used for the synthesis of novel inorganic–organic hybrid materials comprised of tetrathiafulvalene (TTF) conducting chains interleaved with insulating zirconium phosphate layers. Two different synthetic strategies are described. In the first approach, we have attempted the oxidative insertion of neutral TTF into a $\text{Zr}(\text{PO}_4)(\text{HPO}_4)_2 \cdot 2\text{H}_2\text{O}$ host preexchanged with Cu^{2+} . In the second method, surfactant or long-chain alcohols have been used to expand the layers of the host structure, allowing the intercalation of partially charged TTF molecules. This latter approach produced materials with metal-like conductivity that exceeds by a factor of 10^7 that of the precursors. These compounds have been characterized by vibrational, UV–vis, and EPR spectroscopies, and transport properties (conductivity and thermoelectrical power) have been measured as a function of the temperature from -150 to 50 °C. The properties observed show marked similarity with those displayed by mixed valence TTF halides and pseudohalides. The reactions occur topotactically, and the increase in interlayer distance is compatible with an orientation of TTF perpendicular, or nearly, to the host layers.

1. Introduction

Compounds having a two-dimensional structure provide a specific environment that can be used for the spatial organization or confinement of organic molecules.¹ The nature of the guest, its concentration, the charge density, and electron-transfer properties of the host layers are factors decisive in the conception of new materials. Polymer layered host nanocomposites² are just one example of the growing family of hybrid organic inorganic materials derived from layered solids.³

It was first recognized some 15 years ago that layered solids could be used to provide the means of separating stacks of organic π -donor molecules,⁴ emulating the organization often observed in organic metals prepared in a one-step reaction.⁵ The best examples to date are

provided by bis(ethylenedithio)tetrathiafulvalene– FeOCl^6 and by TTF– FePS_3^7 systems, which have room-temperature conductivities of 0.26 and 3 S cm^{-1} , respectively. In general, the use of a redox-active host matrix can be considered to restrict the range of materials that can be prepared insofar as the reaction between a structural ion and TTF is “all or nothing”, since there is no control over the ultimate partial oxidation state of TTF. The aims of the study presented here were to make use of techniques of intercalation chemistry—ion exchange, preexpansion, exfoliation and flocculation around a guest ion, etc.—so as to both assemble and spatially organize partially oxidized TTF ^{δ^+} within the interlayer gallery of an appropriate inorganic host while, at the same time, exercising a degree of control over the extent of electron transfer.

Zirconium phosphate (ZrP) is a well-known layered solid which crystallizes in two forms known as α and γ . These differ in the structural arrangement in the layers, the surfaces carrying O_3POH groups in the former^{8a,b} and $\text{O}_2\text{P}(\text{OH})_2$ groups in the latter.^{8c,d} α -structured metal(IV) phosphates have, in particular, been exten-

[†] Dedicated to Professor Dr. Walter Siebert on the occasion of his 60th birthday.

[®] Abstract published in *Advance ACS Abstracts*, July 15, 1997.

(1) (a) *Intercalation Chemistry*, Whittingham, M. S., Jacobson, A. J., Eds.; Academic Press: New York, 1982. (b) Schöllhorn, R. *Chem. Mater.* **1996**, *8*, 1747. (c) Costantino, U. *Inorganic Ion Exchange Materials*, Clearfield, A., Ed.; CRC Press: Boca Raton, FL, 1982; pp 111–132. (d) *Comprehensive Supramolecular Chemistry*, Alberti, G., Bein, T., Eds.; Pergamon: New York, 1996; Vol. 7.

(2) (a) Ding, Y.; Jones, D. J.; Maireles-Torres, P.; Rozière, J. *Chem. Mater.* **1995**, *7*, 562. (b) Costantino U.; Marmottini, F. *Mater. Chem. Phys.* **1993**, *35*, 193. (c) Wang, Z.; Lan, T.; Pinnavaia, T. J. *Chem. Mater.* **1996**, *8*, 2200. (d) Hutchinson, J. C.; Bissessur, R.; Shriver, D. F. *Chem. Mater.* **1996**, *8*, 1597. (e) Wu, C.-G.; DeGroot, D. C.; Marcy, H. O.; Schindler, J. L.; Kannewurf, C. R.; Liu, Y.-J.; W. Hirpo, Kanatzidis, M. G. *Chem. Mater.* **1996**, *8*, 1992. (f) Messersmith, P. B.; Giannelis, E. P. *Chem. Mater.* **1993**, *5*, 1064. (g) Aranda, P.; Ruiz-Hitzky, E. *Chem. Mater.* **1992**, *4*, 1395. (h) Yanagisawa, T.; Yokoyama, C.; Kuroda, K.; Kato, C. *Bull. Chem. Soc. Jpn.* **1990**, *63*, 47. (i) Mehotra, V.; Giannelis, E. P. *Solid State Ionics* **1992**, *51*, 115. (j) Ruiz-Hitzky, E. *Adv. Mater.* **1993**, *5*, 334.

(3) O'Hare, D. *New J. Chem.* **1994**, *18*, 989.

(4) (a) Antonio, M. R.; Averill, B. A. *J. Chem. Soc., Chem. Commun.* **1981**, 382. (b) Bringley, J. F.; Averill, B. A.; Fabre, J.-M. *Mol. Cryst. Liq. Cryst.* **1988**, *170*, 215. (c) Van Damme, H.; Obrecht, F.; Letellier, M. *Nouv. J. Chim.* **1984**, *8*, 681. (d) Averill B. A.; Kauzlarich, S. M. *Mol. Cryst. Liq. Cryst.* **1984**, *107*, 55.

(5) (a) Munakata, M.; Kuroda-Sowa, T.; Maekawa, M.; Hirota, A.; Kitagawa, S. *Inorg. Chem.* **1995**, *34*, 2705. (b) Inoue, M. B.; Inoue, M.; Bruck, M. A.; Fernando, Q. *J. Chem. Soc., Chem. Commun.* **1992**, 515. (c) Pénicaud, A.; Boubekeur, K.; Batail, P.; Canadell, E.; Auban-Senzio, P.; Jérôme, D. *J. Am. Chem. Soc.* **1993**, *115*, 4101. (d) Batail, P.; Boubekeur, K.; Fourmigué, M.; Dolbecq, A.; Gabriel, J.-C.; Guirauden, A.; Livage, C.; Uriel, S. *New J. Chem.* **1994**, *18*, 999. (e) Geiser, U.; Wang, H. H.; Donega, K. M.; Anderson, B. A.; Williams, J. M.; Kwak, J. F. *Inorg. Chem.* **1986**, *25*, 401. (f) Urayama, H.; Yamochi, H.; Saito, G.; Nozawa, K.; Sugano, T.; Kinoshita, M.; Sato, S.; Oshima, K.; Kawamoto, A.; Tanaka, J. *Chem. Lett.* **1988**, 55.

(6) (a) Bringley, J. F.; Fabre, J.-M.; Averill, B. A. *J. Am. Chem. Soc.* **1990**, *112*, 4577. (b) Bringley, J. F.; Fabre, J.-M.; Averill, B. A. *Chem. Mater.* **1992**, *4*, 522.

(7) Léaustic, A.; Audière, J. P.; Lacroix, P. G.; Clément, R.; Lomas, L.; Michalowicz, A.; Dunham, W. R.; Francis, A. H. *Chem. Mater.* **1995**, *7*, 1103.

sively used in the recent past for the assembly of inorganic⁹ and organic^{1c,10} species. Both are known as ion-exchangers and materials appropriate for the insertion of basic molecules and polymers and as media for interlayer reactivity, properties that are based on proton-transfer characteristics of the hydrogen phosphate. Although the acid protons of zirconium phosphate have been shown to oxidize neutral molecules such as cobaltocene,¹¹ electron-transfer properties can be more readily induced by making use of the above ion-exchange characteristics to preinsert a redox center into the interlayer region, in an approach first developed for the intercalative redox polymerization of aniline.¹²

We describe below two original methods for the insertion/formation of partially charged TTF in layered zirconium phosphates. The first of these is based on the use of varying amounts of the ion-exchange capacity of γ -ZrP for Cu(II) to create an oxidizing precursor matrix then used in reaction with neutral TTF. It allows the degree of charge transfer and amount of inserted TTF to be directly related to the associated electrical properties, and preliminary results have been briefly reported.¹³ In the second method, long-chain alcohols and surfactants have been used to expand the interlayer distance and increase the hydrophobicity of the interlayer region, so facilitating insertion of partially charged TTF. The choice of a specific expanding agent enables modulation of the proportion of protons transferred or exchanged, so defining an effective ion-exchange capacity for the modified zirconium phosphate precursor. This approach leads to materials that have by far the highest conductivity of any phase based on zirconium phosphate.

2. Experimental Section

2.1. Synthesis. γ -ZrPO₄·H₂PO₄·2H₂O (γ -ZrP) and α -Zr(HPO₄)₂·H₂O (α -ZrP) were synthesized according to the methods described by Alberti.^{14,15}

Precursor Phases. Cu(II) exchanged forms were prepared by suspending γ -ZrP (0.2 g) in an aqueous solution of Cu(OAc)₂ (100 mL, 0.005–0.0125 mol dm⁻³) to give γ -ZrPO₄·(H₂-_{2x}PO₄)·Cu_x·nH₂O with $x = 0.035, 0.11, 0.21, 0.33,$ and 0.50 and $n = 2-4$ (Cu determined by atomic absorption spectroscopy and water content by thermogravimetric analysis).

γ -ZrPO₄·[HO(CH₂)₇CH₃]_{0.87}(H₂PO₄)·1.22H₂O was prepared by contacting the solid (1 g) with octanol (100 mL) in a closed vessel for 24 h with stirring. Powder X-ray diffraction (XRD)

indicated expansion to 29.0 Å and TGA analysis effected rapidly after centrifugation confirmed the above composition.

α -Zr(H_{1-_{2x}}PO₄)₂(H₃C)₃N(CH₂)₁₁CH₃]_x·1.3H₂O, $x = 0.65-0.8$. Expansion of α -ZrP with trimethyldecylammonium (TMDDA) ion cannot be achieved by direct ion exchange. α -ZrP (1 g) was preexpanded by contact overnight with propylamine vapor (50 mL, closed vessel), and the propylammonium ion exchanged in a second stage for TMDDA (dispersion of 1 g of [Zr(PO₄)₂(CH₃CH₂CH₂NH₃)₂] in a solution of 4 g of TMDDABr in 200 mL of ethanol/water 1/1 v/v). Over several syntheses, single-phase materials of interlayer spacing 20–26 Å were obtained containing 0.6–0.8 TMDDA/Zr.

Synthesis of (TTF)₃(BF₄)₂.¹⁶ TTF (0.875 g) was dissolved in acetonitrile (30 mL) and a solution of 48% aqueous fluoroboric acid (0.542 g) and 30% hydrogen peroxide (0.162 g; addition of hydrogen peroxide to ice-cold fluoroboric acid) was added. On cooling over an ice-bath, the solution afforded black crystals. (TTF)₃(BF₄)₂ (784) calcd: C 27.6, H 1.53, S 49.0%. Found: C 28.1, H 1.64, S 49.7%. (TTF)₃(BF₄)₂ contains both fully ionized and neutral TTF in its structure.¹⁷

Synthesis of TTFBr_{0.76}.¹⁸ A stoichiometric amount of Br₂ in CH₃CN (1.22 mol dm⁻³) was added dropwise to a solution of TTF (0.5 g) in CH₃CN (100 mL). The violet-black precipitate was recovered on a glass frit and washed with acetonitrile. TTFBr_{0.76} was separated from any other bromide salts by recrystallization in warm ethanol. The violet crystals which precipitated from the red-violet ethanol solution gave a single Raman line at 1444 cm⁻¹, corresponding to the presence of TTF^{0.76+} (see below).

Insertion of TTF⁺. γ -ZrP (0.2 g) or α -ZrP–TMDDA (0.2 g) was dispersed in solution of (TTF)₃(BF₄)₂ in acetonitrile (0.3 mol dm⁻³, 50 mL) and stirred at 40 °C for 6 days. The solid was recovered by centrifugation, washed, and dried. γ -ZrPO₄·(H_{1.2}PO₄)(TTF)_{0.80}·2H₂O (480) calcd: C 11.9, H 1.38, S 21.2%. Found: C 11.9, H 1.73, S 21.3%. α -Zr(H_{0.65}PO₄)₂(TTF)_{0.7}·1.1H₂O (446) calcd: C 11.1, H 1.43, S 20.1%. Found: C 12.5, H 1.63, S 21.4%.

Insertion of TTF. All manipulation was performed under flowing nitrogen.

Insertion in Cu(II)-Exchanged Phases. A TTF solution (acetonitrile, 0.03 mol dm⁻³, 50 mL) was added to samples of γ -ZrPO₄·(H₂-_{2x}PO₄)Cu_x·nH₂O (0.1 g) dispersed in acetonitrile (30 mL). After stirring at 40 °C for 6 days, the solid phase was recovered by centrifugation, washed, and dried.

Insertion in γ -ZrP–Octanol and α -ZrP–TMDDA. The precursor phase of ZrP (α or γ , 0.3 g) was dispersed in a solution of TTF (1 g, 0.004 89 mol) in ethanol (200 mL) with stirring. A stoichiometric amount of bromine in acetonitrile (0.002 44 mol of Br₂ mL⁻¹) was added drop by drop over a period of 6 h, with gentle heating to 40 °C. The coffee-colored solid phase was then recovered by centrifugation and washed three times with 50 mL volumes of ethanol/acetonitrile.

2.2. Characterization. Host α - and γ -ZrP and all intercalation compounds derived from them were characterized by powder X-ray diffraction (XRD) using a Philips generator (Cu K α radiation) and goniometer. Elemental (CHS) analysis was performed using an Erba Science 1108 instrument, and analysis for Cu (both before and after the insertion reaction with TTF) used atomic absorption spectrometry (AAS). Thermogravimetric (TGA) and differential thermal analyses (DTA) were carried out in air on a Stanton Redcroft STA 781 thermobalance. The heating rate was 2 °C min⁻¹. Infrared spectra were recorded in transmittance mode at room temperature on KBr disks using a Bomem DA8 FTIR spectrometer. Raman spectra were obtained either on pressed disks using grazing incidence or on powders contained within a thin-walled capillary tube and spun in a rotating cell, with a Spectraphysics Ar laser ($\lambda = 514.5$ nm) and Dilor spectrometer. Use of higher energy lines (488.0 nm) leads to rapid degradation of all samples by progressive oxidation of TTF^{δ+} as seen

(8) (a) Clearfield, A.; Smith, G. D. *Inorg. Chem.* **1969**, *8*, 431. (b) Albertsson, J.; Oskarsson, A.; Tellgren, A.; Thomas, J. O. *J. Phys. Chem.* **1977**, *81*, 574. (c) Christiansen, A. N.; Krogh Andersen, A.; Krogh Andersen, I. G.; Alberti, G.; Nielsen, M.; Lehmann, M. S. *Acta Chem. Scand.* **1990**, *44*, 865. (d) Poojary, D. M.; Shpeizer, B.; Clearfield, A. *J. Chem. Soc., Dalton Trans.* **1995**, 111.

(9) (a) Olivera-Pastor, P.; Maireles-Torres, P.; Rodríguez-Castellón, E.; Jiménez-López, A.; Cassagneau, T.; Jones, D. J.; Rozière, J. *J. Chem. Mater.* **1996**, *8*, 1759. (b) Clearfield, A. In *Multifunctional Mesoporous Inorganic Solids*; Sequeira, C. A. C., Hudson, M. J., Eds.; NATO ASI; Kluwer Academic: Dordrecht, 1993; Vol. 400, pp 159–178.

(10) (a) Alberti, G.; Casciola, M.; Costantino, U.; Viviani, R. *Adv. Mater.* **1996**, *8*, 291. (b) Clearfield, A. *Curr. Opin. Solid State Mater. Sci.* **1996**, *1*, 268. (c) Garcia, M. E.; Naffin, J. L.; Deng, N.; Mallouk, T. E. *Chem. Mater.* **1995**, *7*, 1968.

(11) Johnson, J. W. *J. Chem. Soc., Chem. Commun.* **1980**, 263.

(12) Jones, D. J.; El Mejjad, R.; Rozière, J. *Supramolecular Architecture: Synthetic Control in Thin Films and Solids*; Bein, T., Ed.; ACS Symp. Ser. **1992**, *499*, 220–230.

(13) Backov, R.; Jones, D. J.; Rozière, J. *J. Chem. Soc., Chem. Commun.* **1996**, 599.

(14) Alberti, G.; Bernasconi, M. G.; Casciola, M. *Reactive Polym.* **1989**, *11*, 245.

(15) Alberti, G.; Torracca, E. *J. Inorg. Nucl. Chem.* **1968**, *30*, 317.

(16) Wudl, F. *J. Am. Chem. Soc.* **1975**, *97*, 1962.

(17) Legros, J.-P.; Bousseau, M.; Valade, L.; Cassoux, P. *Mol. Cryst. Liq. Cryst.* **1983**, *100*, 181.

(18) La Placa, S. J.; Corfield, P. W. R.; Thomas, R.; Scott, B. A. *Solid State Commun.* **1975**, *17*, 635.

Table 1. Oxidative Insertion of TTF in Cu²⁺-Exchanged γ -ZrP: Effect of the Stoichiometry of the Precursor Phase on the Uptake of TTF and Its Charge

mol of preexchanged Cu ^{II} ZrH _{2-2x} Cu _x (PO ₄) ₂ ·yH ₂ O ^a	charge on TTF ^b	empirical formula ^c	relationship Cu ^{II} exchanged TTF insertion and charge ^d	conductivity at 25°C/S cm ⁻¹
0.035	0.78	Zr(PO ₄) ₂ (TTF) _{0.1} (H) _{1.92} ·0.9H ₂ O	1.11	10 ^{-3.5}
0.11	0.90	Zr(PO ₄) ₂ (TTF) _{0.24} (H) _{1.78} ·0.9H ₂ O	0.98	10 ^{-3.6}
0.21	0.94	Zr(PO ₄) ₂ (TTF) _{0.46} (H) _{1.57} ·1.1H ₂ O	1.03	10 ^{-3.9}
0.33	0.96	Zr(PO ₄) ₂ (TTF) _{0.75} (H) _{1.28} ·0.9H ₂ O	1.09	10 ^{-3.9}
0.5	0.98	Zr(PO ₄) ₂ (TTF) _{1.05} (H) _{1.0} ·1.9H ₂ O	1.03	10 ^{-4.5}

^a From atomic absorption spectrometry. ^b From Raman spectroscopy. ^c From elemental analysis C, H, S. ^d TTF content × partial charge/meq Cu(II) in precursor = $bd/2a$. The expected value of d is 1.

by the displacement to lower wavenumbers of the position of the line corresponding to the $\nu(\text{C}=\text{C})$ mode of TTF, which is sensitive to the degree of charge transfer on the ion. Transmission UV-vis-NIR spectra were recorded on KBr disks between 310 and 2500 nm on a Varian spectrometer. Direct current electrical conductivity and thermopower measurements were performed on pressed disks (thickness 0.5 mm). Conductivity measurements were made between -180 and 80 °C using the "four-point method" of Van der Pauw and fine (50 μm) gold needles for the current and voltage electrodes. Thermoelectric power was measured from -140 to 25 °C using a slow ac technique and copper electrodes. Electron spin resonance (4–298 K) spectra were recorded using a Bruker ER 200D spectrometer operating at 9 GHz (X-band).

3. Results and Discussion

3.1. Assembly of TTF under Controlled Oxidation Conditions. Direct ion exchange of TTF⁺ from a solution of (TTF)₃(BF₄)₂ occurs with protons of the (HO)₂PO₂ groups of γ -ZrP, giving a new compound of interlayer distance 19.7 Å. TGA and elemental analysis concur to provide a formula of ZrPO₄(H_{1.2}PO₄)(TTF)_{0.80}·2H₂O. Facile exchange also takes place with α -ZrP-TMDDA to give α -Zr(H_{0.65}PO₄)₂·(TTF)_{0.7}·1.1H₂O of basal spacing 15 Å.

When α - or γ -ZrP is contacted with a solution containing neutral TTF, however, neither ion exchange nor acid-base mechanisms can operate, and no reaction occurs. Nevertheless, oxidative intercalation becomes possible with neutral TTF if the γ -ZrP matrix is preexchanged with Cu(II). The exchange of Cu(II) into γ -ZrP has been studied by Clearfield.¹⁹ He showed that the system is mono- or biphasic, depending on the degree of copper loading, although the interlayer distance is invariant, 12.4 Å. In this work, γ -ZrPO₄·(H_{2-2x}PO₄)·Cu_x·nH₂O with $x = 0.035, 0.11, 0.21, 0.33,$ and 0.50 and $n = 2-4$ was used, the second and third of these samples lying in the biphasic region. Figure 1 shows the XRD patterns of γ -ZrP, γ -ZrPO₄·(H_{2-2x}PO₄)·Cu_x·nH₂O and the material recovered after redox ion exchange with TTF. The interlayer distance observed, independent of the copper content of the precursor, is 19.7 Å, identical with that given by materials prepared by direct ion exchange with TTF⁺. The expansion of 10–11 Å corresponds to the long dimension of the TTF molecule and so may indicate an orientation with the long axis perpendicular to the plane of the ZrP sheets; this point is addressed in greater detail in section 3.3.

The results of chemical analyses of the products of the redox ion-exchange reaction are given in Table 1. It is noted that no copper could be detected in any of the products after reaction with TTF. Copper is therefore reduced and eliminated, presumably as colloidal Cu⁰.

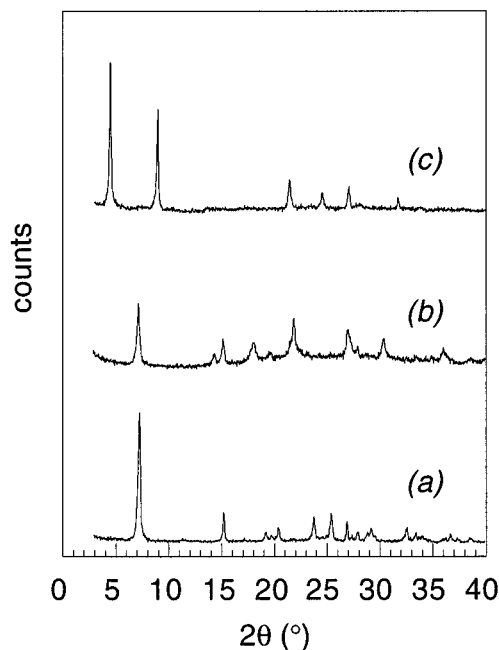
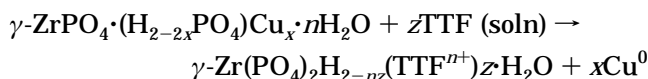


Figure 1. XRD patterns of (a) γ -ZrP, (b) γ -ZrPO₄·(H_{2-2x}PO₄)·Cu_x·nH₂O, (c) γ -Zr(PO₄)₂H_{2-nz}(TTFⁿ⁺)_z·H₂O.

The stoichiometries of Table 1 derived from analytical data show that the amount of TTF inserted in copper-exchanged γ -ZrP closely depends on the degree of copper loading of the precursor phase, with precursors of low copper loading leading to phases containing little TTF, and vice versa. Moreover, the copper content of the precursor influences also the degree of oxidation of inserted TTF as determined by Raman spectroscopy and described below. The equation for the reaction may then be written



and the number of meq of Cu(II) in precursor Cu(II)-exchanged γ -ZrP is equal to the product of the partial charge, n^+ , on the TTF taken up, z .

The positions of bands and lines in the vibrational spectra of TTF are sensitive to its degree of partial charge. The position of the stretching vibration $\nu(\text{C}=\text{C})$ in Raman spectroscopy is particularly useful, since it has been shown to vary linearly between 1520 cm^{-1} for the neutral molecule and 1415 cm^{-1} for the fully ionized species.²⁰ For the intercalated zirconium phosphates, only the compound prepared by direct ion exchange with TTF⁺ gave a signal corresponding to the presence of a

(19) Clearfield, A.; Kalnins, J. M. *J. Inorg. Nucl. Chem.* **1978**, *40*, 1933.

(20) Matsuzaki, S.; Moriyama, T.; Toyoda, K. *Solid State Commun.* **1980**, *34*, 857.

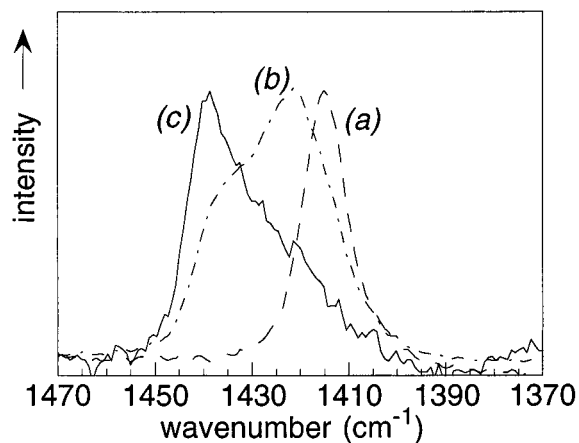


Figure 2. Raman spectra of TTF⁺ (a) and of redox intercalates obtained using Cu(II)-exchanged precursors with $x = 0.21$ (b) and 0.035 (c). Partial charges are 1+, 0.94+, and 0.78+, respectively.

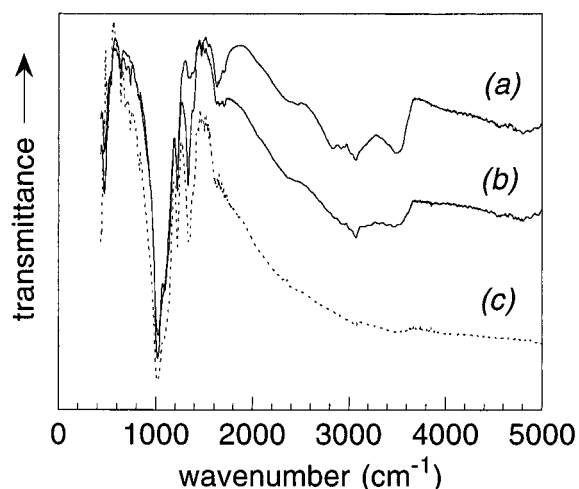


Figure 3. IR spectra of TTF⁺ (a) and of redox intercalates obtained using Cu(II)-exchanged precursors with $x = 0.21$ (b) and 0.035 (c). Partial charges are 1+, 0.94+, and 0.78+, respectively.

fully ionized species, all those prepared via Cu(II)-exchanged precursors are characterized by the presence of partially oxidized TTF (Figure 2). For example, for $\gamma\text{-ZrPO}_4 \cdot (\text{H}_{2-2x}\text{PO}_4)_x \cdot n\text{H}_2\text{O}$ with $x = 0.035$, the line at 1440 cm^{-1} indicates the presence of TTF with partial oxidation state 0.78, and for that with $x = 0.21$ (biphasic precursor), the Raman line is asymmetric, with a maximum at 1422 cm^{-1} and a shoulder at 1438 cm^{-1} , positions which correspond to charges of 0.94+ (dominant) and 0.78+ (minor; Table 1). At loadings higher than ca. 0.4 Cu/Zr, almost complete oxidation of TTF occurs.

The IR spectra (Figure 3) are superpositions of bands arising from the inorganic matrix and from intercalated TTF. Two factors are worthy of particular comment. First, that the spectral baseline is significantly affected by increasing absorption toward high frequencies, due to a band of maximum at ca. 4900 cm^{-1} . Materials for which the lowest degree of charge transfer to TTF has occurred give IR spectra having greatest increasing background absorption, evidence for an increasing presence of charge-transfer stacks (see below). Second, the intensity of the IR absorption at 1340 cm^{-1} increases inversely with the partial charge on TTF (and hence inversely with the TTF content of the intercalate). This

vibration corresponds to the IR component of the $\nu(\text{C}=\text{C})$ mode and its enhanced intensity, which has also been reported for the MPS₃/TTF system,²¹ originates in a vibronic interaction with the mixed-valence charge-transfer transition seen in NIR.²²

The electrical resistivity was measured using the four-point technique. The use of gold electrodes ensured that any transport properties observed result from electronic rather than ionic (protonic) charge carriers. The polarization effect was monitored by applying the dc current over an extended period of time (no change observed over 30 min). The use of disks of compacted powder provides a value for the electronic conductivity which is averaged over all crystallographic directions, although anisotropy of electrical properties is to be expected. The resistivities observed are clearly a function of the degree of charge transfer and of TTF content of the intercalates. Thus the compound prepared by direct ion exchange with TTF⁺ has conductivity of $10^{-5.5}\text{ S cm}^{-1}$, whereas materials prepared by redox ion exchange are increasingly less resistive as the initial Cu(II) content of the precursor phase decreases. The most conductive phase has a conductivity of $10^{-3.5}\text{ S cm}^{-1}$, a 100-fold increase. There is therefore a direct relationship between the degree of copper loading on $\gamma\text{-ZrP}$, the subsequent uptake of TTF and its partial charge, and the electronic conductivity. The lowest partial charge on TTF gives the most highly conducting phase, which suggests, given the limited uptake under these conditions (0.1 TTF/Zr), that TTF^{0.78+} must be stacked in islets sufficiently close to allow orbital overlap. The conductivity of this material still lies, however, in the semiconductor range. Any further increase requires the low partial charge on TTF to be maintained, while increasing the TTF uptake. Such a result seems difficult to achieve using the redox intercalation method, in view of the observed interchange between the Cu(II) content, TTF uptake, and partial charge. This led us to develop the approach described below designed to separate the electron transfer and insertion reactions into consecutive steps.

3.2. Assembly of TTF^{0.72+} in $\alpha\text{-ZrP}$ and $\gamma\text{-ZrP}$.

3.2.1. X-ray Diffraction, Chemical, and Thermal Analysis. In the precursor phases the interlayer distance is consistent with a double layer of octanol molecules in $\gamma\text{-ZrP}$ ($d_{002} = 29.0\text{ \AA}$) and a single layer of TMDDA ions in $\alpha\text{-ZrP}$ ($d_{002} = 22.6\text{ \AA}$). For the latter, the intercalation reaction could be achieved only by ion exchange with propylammonium, while for the former the driving force for the reaction is probably hydrogen-bond formation with the protons on the internal layers. The stoichiometry of these precursor phases is limited by the covering effect to $\alpha\text{-Zr}(\text{H}_{1.30}\text{PO}_4)_2[(\text{H}_3\text{C})_3\text{N}(\text{CH}_2)_{11}\text{CH}_3]_{0.70} \cdot 1.3\text{H}_2\text{O}$ ($\alpha\text{-ZrP-TMDDA}$) and, for intercalation of octanol, by the ion-exchange capacity of $\gamma\text{-ZrP}$ to $\gamma\text{-ZrPO}_4 \cdot [\text{HO}(\text{CH}_2)_7\text{CH}_3]_{0.87}(\text{H}_2\text{PO}_4) \cdot 1.2\text{H}_2\text{O}$ ($\gamma\text{-ZrP-octanol}$). Reaction of TTF oxidized in situ by bromine with preexpanded phases of α - and γ -ZrP leads to materials in which the interlayer distance, given by the d_{002} diffraction line, is lowered in each case compared with that of its immediate precursor. Thus $\gamma\text{-ZrP-octanol}$ gives a TTF-inserted phase of interlayer distance 19.4 \AA , and $\alpha\text{-ZrP-}$

(21) Miyazaki, T.; Matsuzaki, S.; Ichimura, K.; Sano, M. *Solid State Commun.* **1993**, *85*, 949.

(22) Bozio, R.; Zanon, I.; Girlando, A.; Pecile, C. *J. Chem. Phys.* **1979**, *71*, 2282.

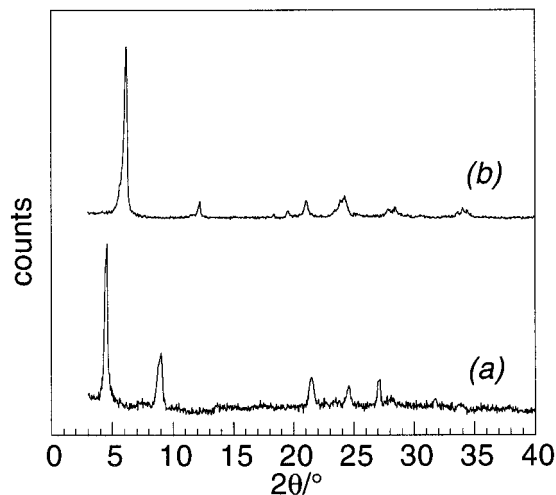


Figure 4. XRD patterns of γ -ZrP-(TTF^{0.72+})_{1.22} (a) and α -ZrP-(TTF^{0.72+})_{0.93} (b).

TMDDA to a compound of interlayer spacing 14.3 Å (Figure 4). The results of chemical analyses and TGA are in good agreement and indicate compositions of α -Zr(PO₄)₂H_{1.33}TTF^{0.72+}_{0.93}·1.2H₂O [α -ZrP-(TTF^{0.72+})_{0.93}] and γ -ZrPO₄·(H_{1.1}PO₄)(TTF^{0.72+})_{1.22}·1.2H₂O [γ -ZrP-(TTF^{0.72+})_{1.22}], where the partial charge on TTF was determined from the position of the ν (C=C) line in Raman spectroscopy (see section 3.2.2). TGA shows water to be lost up to 150 °C, while TTF is then eliminated in two distinct stages below 550 °C, with a change in rate of loss of TTF at ca. 375 °C.

3.2.2. Vibrational and UV-Vis-NIR Spectroscopy. The Raman spectra of TTF-intercalated phases prepared by insertion from Br₂-oxidized TTF solutions show a single line in the region 1400–1550 cm⁻¹ with a maximum at 1447 cm⁻¹. This position corresponds to a partial oxidation state of 0.72+, in the range reported for salts prepared by bromine oxidation of TTF in ethanol, TTFBr_{0.71–0.76}.²⁰ Compared with the spectra of Figure 2, where the compounds were prepared by redox intercalation with a Cu(II)-containing matrix, the Raman line is less broad and more symmetrical, inferring that the TTF species inserted has a rather limited range of, or indeed a unique, partial charge.

As for γ -ZrP-TTF^{δ+} prepared via Cu(II) exchanged phases, IR spectra of α -ZrP-(TTF^{0.72+})_{0.93} and γ -ZrP-(TTF^{0.72+})_{1.22} show the formally IR-inactive ν (C=C) stretch at 1360 cm⁻¹, and a strikingly broad absorption which increases in intensity from 1600 to 5000 cm⁻¹. This feature is notably absent from either of the precursors γ -ZrP-octanol or α -ZrP-TMDDA and is a direct result of the presence of intercalated TTF^{0.72+}.

Figure 5 shows the UV-vis-NIR spectra over the range 4000–32000 cm⁻¹ (2500–310 nm; 0.5–4.0 eV) given by α -ZrP-(TTF^{0.72+})_{0.93} and γ -ZrP-(TTF^{0.72+})_{1.22}. Four absorption peaks are observed, with maxima near 4600, 12400, 18400, and 25100 cm⁻¹ (0.57, 1.54, 2.28, and 3.11 eV) for γ -ZrP-(TTF^{0.72+})_{1.22}. A slight shift of the broad band in the NIR region to higher energies ($\Delta\nu$ = 200 cm⁻¹) is observed for α -ZrP-(TTF^{0.72+})_{0.93}. Using the notation of Torrance²³ developed for mixed-valence TTF halides, these features will be referred to as bands A–D, respectively. Bands C and D are intramolecular

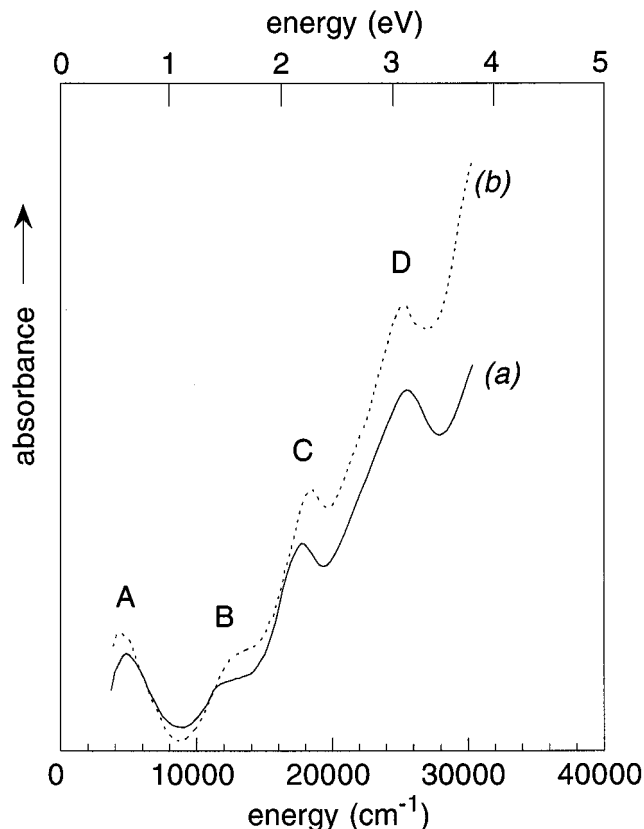


Figure 5. UV-vis-NIR spectra of γ -ZrP-(TTF^{0.72+})_{1.22} (a) and α -ZrP-(TTF^{0.72+})_{0.93} (b).

excitations of charged TTF which are generally observed for both monovalence and mixed valence salts of TTF. Their maxima are shifted to higher frequency when TTF is not structurally isolated, as for (TTF⁺)₂ or in TTF-Br_{0.79}. Bands C and D are observed at positions close to those reported for this latter compound. At lower energy, B and A are charge-transfer bands, and A described as a mixed-valence charge-transfer band, due to the presence of mixed valence stacks. The presence of this peak, which is the origin of the continuum seen in IR, has been related to the high dc conductivity of organic metals.²³

3.2.3. Transport Properties. Four probe electrical conductivity measurements were made on pressed pellets of powdered samples over the temperature range -150 to 30 °C. The room-temperature conductivity recorded for various preparations of α -ZrP-(TTF^{0.72+})_{0.93} and γ -ZrP-(TTF^{0.72+})_{1.22} lies between 3 and 5 S cm⁻¹, significantly above that of any other intercalation compound derived from ZrP.²⁴ Most interestingly, the temperature dependence of the conductivity is different for the two compounds. Near 25 °C, γ -ZrP-(TTF^{0.72+})_{1.22} behaves as a metallic conductor, its conductivity increasing slowly as the temperature is lowered. Over the same range, the conductivity of α -ZrP-(TTF^{0.72+})_{0.93} is still weakly thermally activated, suggesting that this phase has metal-like semiconductor behavior. Furthermore, a plot of the logarithm of the conductivity of γ -ZrP-(TTF^{0.72+})_{1.22} as a function of temperature shows a distinct hump, indicative of a phase transition, at 235 ± 10 K (Figure 6). Below 230 K, the conductivity of both TTF^{0.72+} intercalates drops rapidly, with a thermal

(23) Torrance, J. B.; Scott, B. A.; Welber, B.; Kaufman, F. B.; Seiden, P. E. *Phys. Rev. B* **1979**, *19*, 730.

(24) Pillion, J. E.; Thompson, M. E. *Chem. Mater.* **1991**, *3*, 779.

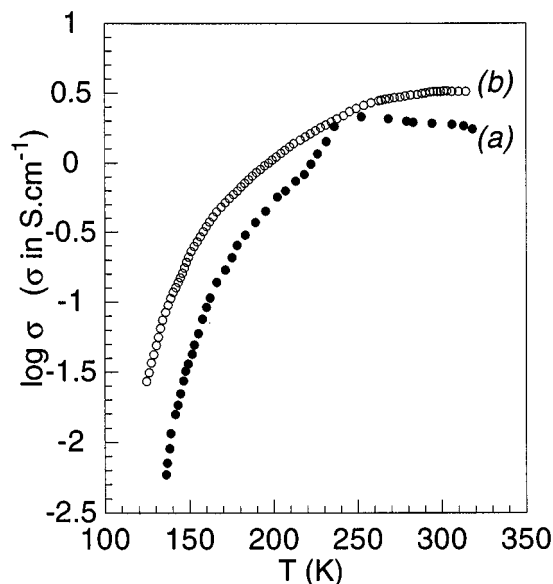


Figure 6. Electrical conductivity of TTF^{0.72+} intercalates. $\log \sigma$ vs T for γ -ZrP-(TTF^{0.72+})_{1.22} (a) and α -ZrP-(TTF^{0.72+})_{0.93} (b).

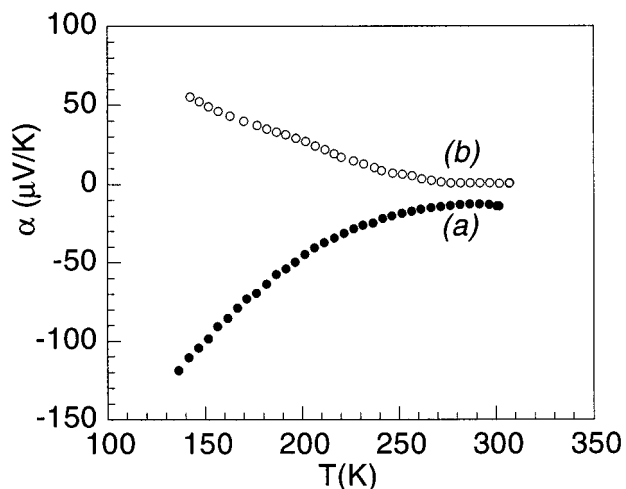


Figure 7. Temperature dependence of Seebeck coefficient of γ -ZrP-(TTF^{0.72+})_{1.22} (a) and α -ZrP-(TTF^{0.72+})_{0.93} (b).

activation similar to that observed for mixed-valence TTF halides.^{25,26} Attempts were made to fit the conductivity data to hopping models based on 2- or 3-dimensional hopping, but the results were inconclusive due to the limited temperature range of the data.

The electrical behavior has been further characterized by thermoelectric power measurements (Figure 7). The small negative value of the Seebeck coefficient of γ -ZrP-(TTF^{0.72+})_{1.22}, $-13 \mu\text{V K}^{-1}$ at 25°C , and its slightly negative temperature dependence near room temperature, suggest an n-type metal-like behavior. At lower temperature, the thermopower becomes strongly negative, characteristic of a semiconducting gap. Different behavior is observed for the TTF intercalate derived from α -ZrP, where the Seebeck coefficient is slightly positive at room temperature, $0.061 \mu\text{V K}^{-1}$, and shows

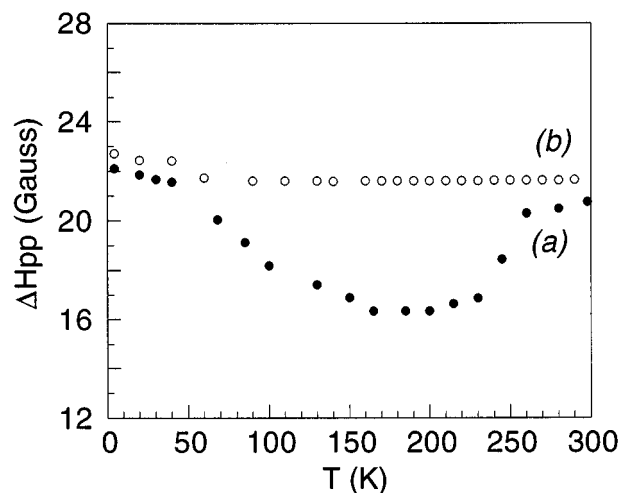


Figure 8. Temperature dependence of EPR line width of γ -ZrP-(TTF^{0.72+})_{1.22} (a) and α -ZrP-(TTF^{0.72+})_{0.93} (b).

a marked upturn at 275 K and then almost linear dependence on temperature down to 150 K. Opposing sign and temperature dependence has also been observed for other, apparently closely related, systems, notably the mixed-valence TTF halides, where TTFBr_{0.76}²⁶ shows the characteristics of an n-type semiconductor, while TTFI_{0.71}²⁵ has p-type and metallic behavior.

3.2.4. Electron Paramagnetic Resonance. Splitting of the EPR signal into two distinct absorption lines is observed for both compounds, even at room temperature, and persists down to the lowest temperature measured (~ 4 K). Since spectra were recorded on nonaligned samples, the splitting might arise simply from anisotropic g values. At 300 K, g_{\parallel} and g_{\perp} are 2.0040(5) and 2.0088(5) for γ -ZrP-(TTF^{0.72+})_{1.22} [2.0039(5) and 2.0089(5) at 87 K] and 2.0030(3) and 2.0079(3) for α -ZrP-(TTF^{0.72+})_{0.93}, in good agreement with values given by other mixed valence salts of TTF.²⁷

Despite the similarity between the room-temperature line widths of both compounds (22–23 G), their temperature dependence is quite different (Figure 8). Whereas the line width of α -ZrP-(TTF^{0.72+})_{0.93} shows practically no variation in the range 4–300 K, that of γ -ZrP-(TTF^{0.72+})_{1.22} decreases steeply below 250 K, a temperature close to the transition temperature observed in the $\log \sigma$ vs T plot of Figure 6. The line width then gradually broadens again below 150 K to regain its room-temperature value of 22 G at 4 K.

3.3. Discussion. The synthesis of electronically conducting ZrP phases by redox insertion depends on the ability of the Cu(II)-exchanged matrix to assemble partially charged TTF species. The results described in section 2.1 and summarized in Table 1 demonstrate that this objective is attained only by the use of precursor phases of low Cu(II) loading and within the monophasic region defined by Clearfield.¹⁹ In the range $x = 0.08$ – 0.3 in γ -ZrPO₄(H_{2-2x}PO₄)Cu_x· n H₂O, the copper-exchanged phases are biphasic, and above this region, TTF is almost completely oxidized to the 1+ state. Indirectly, information is obtained on the nature of the biphasic character in the intermediate range by reaction of γ -ZrPO₄(H_{1.58}PO₄)Cu_{0.21}· n H₂O with TTF. The Raman spectrum of this product (Figure 2b) in the range of the $\nu(\text{C}=\text{C})$ vibration has two components corre-

(25) (a) Somoano, R. B.; Gupta, A.; Hadek, V.; Datta, T.; Jones, M.; Deck, R.; Hermann, A. M. *J. Chem. Phys.* **1975**, *63*, 4970. (b) Wudl, F.; Schaefer, D. E.; Walsh, W. M., Jr.; Rupp, L. W.; DiSalvo, F. J.; Waszczak, J. V.; Kaplan, M. L.; Thomas, G. A. *J. Chem. Phys.* **1977**, *66*, 377.

(26) Chaikin, P. M.; Craven, R. A.; Etemad, S.; La Placa, S. J.; Scott, B. A.; Tomkiewicz, Y.; Torrance, J. B.; Welber, B. *Phys. Rev. B* **1980**, *22*, 5599.

(27) Tomkiewicz, Y.; Taranko, A. R. *Phys. Rev. B* **1978**, *18*, 733.

sponding to the presence of TTF in partial oxidation states 0.78+ and 0.94+ and probably reflecting the existence of phases in the precursor respectively poorer and richer in copper(II). The monophasic region at low copper loading is limited to $x < 0.08$, under which conditions the amount of TTF oxidized and taken up is low.

In a modification to the synthesis, therefore, we developed a different approach, in which partial oxidation states of TTF known to be stabilized in the bulk state as, e.g., mixed-valence halides $\text{TTFX}_{0.69-0.78}$ are preferentially formed and inserted into a preconditioned ZrP matrix. Appropriate precursor phases have an increased interlayer distance and hydrophobicity, and an effective ion-exchange capacity which results from the activation of a proportion of the sites on the ZrP surface (through proton transfer to the guest or hydrogen bonding interactions). The effective ion-exchange capacity of a given precursor should match the overall charge transfer to the TTF units; indeed, the product of stoichiometry and partial charge is 0.67+ in $\alpha\text{-ZrP}-(\text{TTF}^{0.72+})_{0.93}$, close to that of its immediate precursor $\alpha\text{-ZrP}-(\text{TMDDA}^+)_{0.70}$, and the charge \times stoichiometry product is 0.87+ in $\gamma\text{-ZrP}(\text{TTF}^{0.72+})_{1.22}$, identical with the number of activated sites in $\gamma\text{-ZrP}(\text{octanol})_{0.87}$.

For intercalation reactions occurring topotactically and in the absence of exploitable powder X-ray diffraction patterns, structural interpretation is necessarily speculative. However, the mixed-valence nature of the TTF stacks implies that the organic and inorganic layers are not in register, i.e., maximum occupation of the available surface area is independent of the charge distribution on the layers. The surface area available to inserted TTF then defines the stoichiometry of the phases formed. Considering that the structural features of a layer of TTF stacks in mixed-valence halides^{18,28} can be transposed into the interlayer region of zirconium phosphates with an average surface area per $\text{TTF}^{0.72+}$ of 27.9 \AA^2 (mixed valence bromide^{18,28}), the ratio of the occupied surface area/available surface area in $\gamma\text{-ZrP}$ is then 1.25 ($27.9/35$), rationalizing the experimentally observed stoichiometry. This is an indication that the arrangement of $\text{TTF}^{0.72+}$ between the layers of $\gamma\text{-ZrP}$ might indeed be similar to that in $\text{TTFBr}_{0.76}$ or $\text{TTFI}_{0.71}$, where the long axis of TTF is arranged alternatively perpendicular and parallel ("edge-on") to layers of halide ions, allowing the stacks to develop in the interlayer space. The implication then is that the interlayer distance of $\gamma\text{-ZrP}-(\text{TTF}^{0.72+})$ should be approximately equal to the sum of the thickness of the layers (9 \AA) and the long dimension of TTF, 10.7 \AA ; in agreement, the observed interlayer distance of $\gamma\text{-ZrP}-(\text{TTF}^{0.72+})_{1.22}$ is 19.4 \AA . A schematic representation of the possible spatial arrangement in such a hybrid organic-inorganic system is given in Figure 9. At this stage, any orientation of the TTF layers parallel to those of the host matrix can be envisaged. Additional information could be obtained from profile refinement²⁹ of the diffraction patterns, as previously reported for TTF-FeOCl .

Insertion of TTF into other layered matrixes is accompanied by lesser expansion. Neutron profile refinement of FeOCl-TTF^{29} shows TTF to be oriented

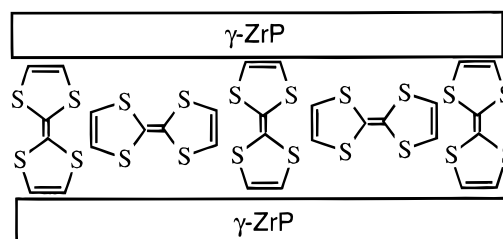


Figure 9. Schematic representation of the proposed arrangement of $\text{TTF}^{0.72+}$ in $\gamma\text{-ZrP}$.

edge-on, compatible with the 5.7 \AA gallery height. Here, as with FePS_3 ,⁷ where an identical expansion of 5.7 \AA is observed, TTF is inserted via a redox process with metal ions in the layers. Possibly the specific assembly of $\text{TTF}^{0.72+}$ in the present case allows the layered structure adopted in $\text{TTF}_{0.71-0.78}$ mixed halides to be retained in layered γ -zirconium phosphate. For $\alpha\text{-ZrP}$, the ratio between the surface occupied by TTF and the available surface area (24 \AA^2) is 0.86, lower than the observed stoichiometry, 0.93. In addition, the interlayer spacing of 14.3 \AA (layer thickness in $\alpha\text{-ZrP}$ ca. 6.3 \AA) suggests that the TTF stacks make an angle of ca. 50° with the plane formed by zirconium phosphate, in an arrangement that effectively increases the occupation of the ZrP surface per TTF. These factors lead us to consider that the packing of TTF in $\alpha\text{-ZrP}$ may involve tilted, end-on TTF ions only.

The similarity between mixed-valence TTF halides and zirconium phosphates goes beyond structural factors. The conductivity of both $\gamma\text{-ZrP}-(\text{TTF}^{0.72+})_{1.22}$ and $\text{TTFBr}_{0.76}$ show a similar dependence on temperature and evidence for a phase transition, although the room-temperature conductivity of $\text{ZrP}-(\text{TTF}^{0.72+})$ is lower by a factor 3–4 that of compacted powders of $\text{TTFBr}_{0.76}$ measured under identical conditions (100 times lower than that of single crystals). In addition, similar values of the Seebeck coefficient are measured for $\alpha\text{-ZrP}-(\text{TTF}^{0.72+})_{0.93}$ as for $\text{TTFI}_{0.71}$,²⁶ small and positive, and for $\gamma\text{-ZrP}-(\text{TTF}^{0.72+})_{1.22}$ as for $\text{TTFBr}_{0.76}$,^{25a} small and negative.

The synthetic method has the particular advantage of versatility and can probably be generalized to the insertion of partially oxidized TTF in other layered hosts. The use of appropriate precursors allows maximization of the packing density in the interlayer region and control of the oxidation state of TTF. The $\text{ZrP}-(\text{TTF}^{0.72+})$ phases reported here display properties not observed previously in any of the hundreds of ZrP intercalates known. The drawback, of course, is that the preparation of single crystals is precluded, so excluding the evaluation of the expected marked anisotropy of electrical and spectroscopic properties. As a step in this direction, we are currently making use of new methods of exfoliation of ZrP and reprecipitating in the presence of $\text{TTF}^{0.72+}$. Self-assembly in this way leads to oriented, and self-supporting films, the full characterization of which will be reported subsequently.

Acknowledgment. We thank Dr. Gérard Brun for his assistance with thermoelectric power measurements. We have enjoyed discussions with Professor Jean-Marc Fabre and Dr. Bernard Mula throughout the course of this work.

CM970083R

(28) Scott, B. A.; La Placa, S. J.; Torrance, J. B.; Silverman, B. D.; Welber, B. *J. Am. Chem. Soc.* **1977**, *99*, 6631.

(29) Kauzlarich, S. M.; Stanton, J. L.; Faber, J., Jr.; Averill, B. A. *J. Am. Chem. Soc.* **1986**, *108*, 7946.

Multiple Bilayer Dipalmitoylphosphatidylserine LB Films Stabilized with Transition Metal Ions

Gail E. Fanucci,^{†,‡} Rénal Backov,[†] Riqiang Fu,[‡] and Daniel R. Talham^{*,†}

Department of Chemistry, University of Florida, Gainesville, Florida 32611-7200, and National High Magnetic Field Laboratory, Tallahassee, Florida 32310

Received July 10, 2000

Langmuir–Blodgett films of dipalmitoyl-DL- α -phosphatidyl-L-serine (DPPS) have been transferred from aqueous subphases containing the 0.1 mM transition metal compounds K_2PdCl_4 , K_2PtCl_4 , $K_2Pt(CN)_4$, $KAuCl_4$, and $Cd[ClO_4]_2$. This report provides a detailed description of the formation and structural characterization of the multiple bilayer films of DPPS that are formed. The films were characterized through a combination of attenuated total reflectance Fourier transform infrared spectroscopy, X-ray diffraction, X-ray photoelectron spectroscopy, and solid-state ^{31}P NMR. The results show that the films are layered, there are two types of DPPS molecule in the films, and the metals are incorporated as positive ions that bridge phospholipids by complexing amines of the serine headgroups. Water molecules likely occupy the remaining coordination sites of the metal complexes, leading to a proposed stoichiometry of $[Pt(DPPS^-)_2(OH_2)_2](DPPS)_4$. The metal ions stabilize film formation by screening repulsive interactions between the serine headgroups through the formation of coordinate covalent bonds.

Introduction

The Langmuir–Blodgett (LB) technique is a useful way of forming sequential layers of ultrathin organic films.^{1–4} Organized assemblies of functionalized molecules have been prepared using this method for applications such as energy transfer in controlled geometries, molecular electronics, nonlinear optics, coatings, and sensing.^{4,5} However, one of the most obvious features of the structure of LB films is their similarity to biological membranes.^{4,6} In this respect, many have studied Langmuir monolayers of lipids or lipid–sterol mixtures in attempts to understand the role these components play in the structure and function of biological membranes.^{4,6,7} Others have used floating monolayers of lipids to study membrane mimetic processes, such as templated particle growth.^{8,9} Although most studies of this nature have been confined to the examination of monolayers on the water surface, there are reasons to study the structure of transferred lipid bilayers. These studies typically include the transfer of a monolayer of a pure or mixed lipid system for investigation by FTIR, atomic force microscopy (AFM), or scanning

electron microscopy (SEM).^{10–12} In a few cases, successful transfer of single bilayers of phospholipids onto solid substrates has been reported;^{12–14} however, for a number of spectroscopic techniques, one or two bilayers may not provide enough material to obtain adequate signals, thus making multiple-bilayer samples necessary.

In general, the deposition of phospholipid bilayers by LB techniques is a difficult task. Apart from a few reports of success with phosphatidylethanolamine derivatives,^{12,15,16} usually no more than three layers can be deposited. The use of “horizontal dipping” has resulted in very useful studies of lipid monolayers and bilayers,^{4,6,11} but again, it is difficult to transfer well-organized multiple bilayer phospholipid samples with this technique. The poor transfer of lipid bilayers with traditional vertical deposition techniques has been attributed to the weakly attractive and sometimes repulsive interactions between the lipid headgroups.^{14,17,18} Some success has been achieved transferring dipalmitoylphosphatidic acid (DPPA) or mixed phospholipid films that include DPPA with calcium or uranyl ions present in the subphase.^{19–21} This approach incorporates ionic interactions between the negatively charged DPPA molecules and the positively charged calcium/uranyl ions to help stabilize film formation.

[†] University of Florida.

[‡] Current address: Department of Chemistry, University of Pennsylvania, Philadelphia, PA 19104.

[‡] National High Magnetic Field Laboratory.

* To whom correspondence should be addressed.

(1) Blodgett, K. B. *J. Am. Chem. Soc.* **1935**, *57*, 1007–1022.

(2) Blodgett, K. B.; Langmuir, I. *Phys. Rev.* **1937**, *51*, 964–982.

(3) Gaines, G. J. *Insoluble Monolayers at Liquid–Gas Interfaces*; Wiley-Interscience: New York, 1966.

(4) Roberts, G. G. *Langmuir–Blodgett Films*; Plenum Press: New York, 1990.

(5) Ulman, A. *An Introduction to Ultrathin Organic Films: From Langmuir–Blodgett to Self-Assembly*; Academic Press: Boston, 1991.

(6) Petty, M. C. *Langmuir–Blodgett Films. An Introduction*; Cambridge University Press: Cambridge, 1996.

(7) Lafont, S.; Rapaport, H.; Somjen, G. J.; Renault, A.; Howes, P. B.; Kjaer, K.; Als-Nielsen, J.; Leiserowitz, L.; Lahav, M. *J. Phys. Chem. B* **1998**, *102*, 761–765.

(8) (a) Mann, S. *Nature* **1993**, *365*, 499–505. (b) Mann, S.; Archibald, D. D.; Didymus, J. M.; Douglas, T.; Heywood, B. R.; Meldrum, F. C.; Reeves, N. J. *Science* **1993**, *261*, 1286–1292.

(9) (a) Whipps, S.; Khan, S. R.; O Palko, F. J.; Backov, R.; Talham, D. R. *J. Cryst. Growth* **1998**, *192*, 243–249. (b) Backov, R.; Lee, C. M.; Khan, S. R.; Mingotaud, C.; Fanucci, G. E.; Talham, D. R. *Langmuir* **2000**, *16*, 6013–6019.

(10) Tang, Z.; Jing, W.; Wang, E. *Langmuir* **2000**, *16*, 1696–1702.

(11) Parikh, A. N.; Beers, J. D.; Shreve, A. P.; Swanson, B. I. *Langmuir* **1999**, *15*, 5369–5381.

(12) Solletti, J. M.; Botreua, M.; Sommer, F.; Brunat, W. L.; Kasas, S.; Duc, T. M.; Celio, M. R. *Langmuir* **1996**, *12*, 5379–5386.

(13) Bahng, M. K.; Cho, N. J.; Park, J. S.; Kim, K. *Langmuir* **1998**, *14*, 463–470.

(14) Osborn, T. D.; Yager, P. *Biophys. J.* **1995**, *68*, 1364–1373.

(15) Green, J. P.; Phillips, M. C.; Shipley, G. G. *Biochim. Biophys. Acta* **1973**, *330*, 243–353.

(16) Nakahara, H.; Fukada, K.; Akutsu, H.; Kyogoku, Y. *J. Colloid Interface. Sci.* **1978**, *65*, 517–526.

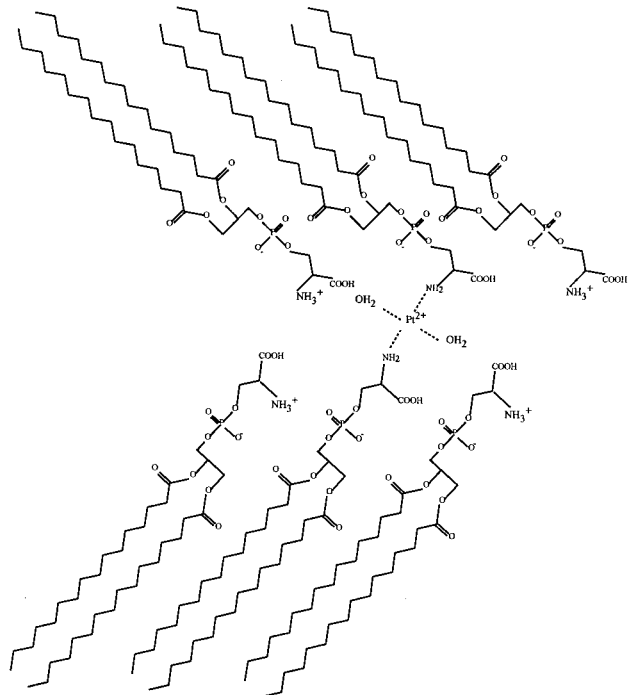
(17) Losche, M.; Helm, C.; Mattes, H. D.; Mohwald, H. *Thin Solid Films* **1985**, *133*, 51–64.

(18) Girard-Egrot, A. P.; Morelis, R. M.; Coulet, P. R. *Langmuir* **2000**, *12*, 778–783.

(19) Cui, D. F.; Howarth, V. A.; Petty, M. C.; Ancelin, H.; Yarwood, J. *Thin Solid Films* **1990**, *192*, 391–396.

(20) Hasmonay, H.; Caillaud, M.; Dupeyrat, M. *Biochim. Biophys. Res. Commun.* **1979**, *89*, 338–344.

(21) Peng, B. J.; Prakash, M.; Macdonald, R.; Dutta, P.; Ketterson, J. B. *Langmuir* **1986**, *3*, 1096–1097.

Scheme 1. Idealized Representation of the Structure of the DPPS–Pt Bilayers

However, there has been less success in transferring single-component LB bilayers of zwitterionic phospholipids such as phosphatidylcholine, and almost no mention of phosphatidylserine LB bilayers can be found in the literature.

In this article, we describe the successful transfer of bilayers of dipalmitoylphosphatidylserine (DPPS) from subphases containing late transition metal ions, originating from the salts K_2PdCl_4 , K_2PtCl_4 , $K_2Pt(CN)_4$, $KAuCl_4$, and $Cd[ClO_4]_2$. Films with up to 100 bilayers have been formed. Infrared spectroscopy, X-ray diffraction (XRD), X-ray photoelectron spectroscopy (XPS), and solid-state ^{31}P NMR spectroscopy combine to show that the starting metal complexes are decomposed, and the metal ions are incorporated into the film by complexing the amine groups of two proximal serine phospholipids (Scheme 1). Not all of the DPPS molecules coordinate metal ions, and the films contain a mixture of anionic and neutral DPPS. Water molecules likely occupy the remaining coordination sites of the metal complexes, leading to a proposed stoichiometry of $[Pt(DPPS)_2(OH_2)_2](DPPS)_4$. The metal ions stabilize film formation by screening repulsive interactions between the serine headgroups through the formation of coordinate covalent bonds. The deposition process is facile, and the observation could lead to the study of other examples of phospholipid LB multilayers.

Experimental Section

Materials. Dipalmitoyl-DL- α -phosphatidyl-L-serine (DPPS, 98%) was purchased in powdered form from Sigma (St. Louis, MO) and used as received without further purification. Potassium tetrachloroplatinate(II) (99.99%), potassium tetracyanoplatinate(II) trihydrate (98%), potassium tetrachloroaurate(III) (99.999%), potassium tetrachloropalladate(II) (99.99%), cadmium perchlorate hydrate, calcium chloride, and octadecyltrichlorosilane (OTS, $C_{18}H_{37}SiCl_3$, 95%) were purchased from Aldrich (Milwaukee, WI). The water used in all LB experiments was purified via a Sybron/Barnstead Nanopure system (Boston, MA) and had a resistivity of $18 M\Omega \cdot cm$. HPLC grade chloroform, stabilized with amylene, was used as received from Acros (Pittsburgh, PA). In all experiments the subphase pH was adjusted by adding the appropriate amount of a 0.1 M HCl solution.

Substrate Preparation. Single crystal (100) silicon wafers, purchased from Semiconductor Processing Co. (Boston, MA), were used as deposition substrates for XPS. XRD samples were prepared on petrograph slides that were purchased from Buehler Ltd. (Lake Bluff, IL). Germanium single crystals, $50 mm \times 10 mm \times 3 mm$ with 45° faces, purchased from Wilmad Glass (Buena, NJ), were used as substrates for attenuated total reflectance (ATR) FTIR experiments. Mylar film, purchased from DuPont (Wilmington, DE), was used as a substrate for the NMR sample. The Mylar was cleaned by sonication in ethanol and water. The silicon and glass substrates were cleaned with the RCA process²² and dried under nitrogen. Substrate surfaces were made hydrophobic by the deposition of a layer of OTS.^{22,23} Germanium ATR crystals were cleaned by oxygen plasma etch and washed with chloroform in a Soxhlet extractor before coating with OTS.

Instrumentation. Langmuir–Blodgett films were prepared on a KSV 3000 (Statford, CT) trough modified to operate with double barriers having surface area of $960 cm^2$ ($12.8 cm \times 75 cm$). Surface pressure was measured with a platinum Wilhelmy plate suspended from a KSV microbalance. Infrared spectra were recorded on a Mattson Instruments (Madison, WI) Research Series I FTIR spectrometer with a deuterated triglycine sulfate (DTGS) detector. LB films were deposited onto OTS-coated Ge ATR parallelograms, and a Harrick (Ossining, NY) TMP stage was used to hold the substrate during ATR experiments. All ATR-FTIR spectra consist of 500 scans at $4 cm^{-1}$ resolution and were referenced to the appropriate background. X-ray diffraction was performed with a Phillips APD 3720 X-ray powder diffractometer with the $Cu K\alpha$ line, $\lambda = 1.54 \text{ \AA}$, as the source. XPS was performed on a Perkin-Elmer (Eden Prairie, MN) PHI 5000 series spectrometer. The $Mg K\alpha$ line at $1253.6 eV$ was used as the anode source with voltage and power settings of 15 kV and 300 W, respectively. All XPS spectra were recorded with a 45° takeoff angle. XPS survey scans consisted of five scans performed with 0.5 eV/step, 20 ms/step, and 89.45 eV pass energy, and multiplex scans consisted of 80 scans per region taken in 10 sweeps/cycle operating at 0.1 eV/step, 50 ms/step, and 37.75 eV pass energy. To calculate elemental ratios, sensitivity factors provided by the manufacturer in the operating software were used. All ^{31}P NMR spectra were recorded at room temperature on a Bruker DMX-600 NMR spectrometer ($B_0 = 14 T$) with Larmor frequencies of 243 MHz for ^{31}P and 600 MHz for 1H , equipped with a Bruker double-resonance magic angle spinning (MAS) probe with 4 mm rotor. In the experiments, the ^{31}P magnetization was generated by conventional cross-polarization (CP)²⁴ ($7 \mu s$ $^1H 90^\circ$ pulse length and 600 μs contact time) and then detected under high-power proton decoupling with TPPM.²⁵ A recycle delay of 5 s was used for signal accumulation. The number of scans varied for each sample. For instance, 60 000 scans were used for the DPPS film. This sample consisted of 100 bilayers of DPPS, transferred from a 0.1 M K_2PtCl_4 subphase, onto a $35 mm \times 60 mm$ piece of Mylar. The sample was cut into irregularly shaped pieces and packed within the rotor with no preferential orientation. An 8 kHz spinning rate was used throughout the experiments. The spinning rate was controlled within $\pm 3 Hz$ by a Bruker pneumatic MAS unit. Phosphorus chemical shifts are referenced with respect to external $NH_4H_2PO_4$.

Results and Discussion

Formation of DPPS Films. Langmuir Monolayers. The pressure vs area isotherm of DPPS on a 0.5 mM $PtCl_4^{2-}$ subphase at pH 3.7 is shown in Figure 1. DPPS on the metal complex subphase forms a liquid condensed phase at the air–water interface with a mean molecular area (MMA) at film collapse of $44 \pm 0.5 \text{ \AA}^2$, which is consistent with the presence of two alkyl chains in the hydrophobic part of the molecule.²⁶ The isotherm is similar to that of

(22) Kern, W. *J. Electrochem. Soc.* **1990**, *137*, 1887–1892.

(23) Maoz, R.; Sagiv, J. *J. Colloid Interface Sci.* **1984**, *100*, 465–496.

(24) Pines, A.; Gibby, M. B.; Waugh, J. S. *J. Chem. Phys.* **1973**, *59*, 569–590.

(25) Bennett, A. E.; Rienstra, C. M.; Auger, M.; Lakshmi, K. V.; Griffin, R. G. *J. Chem. Phys.* **1995**, *103*, 6951–6958.

(26) Mingotaud, A.-F.; Mingotaud, C.; Patterson, L. K. *Handbook of Monolayers*, 1st ed.; Academic Press: London, 1993; Vol. 1.

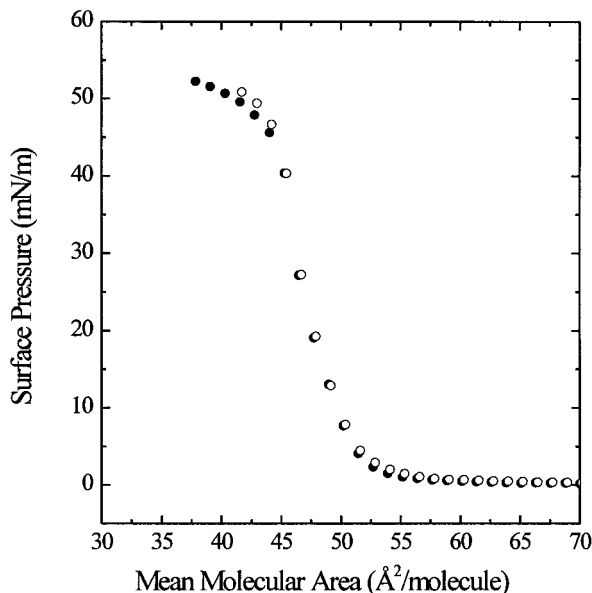


Figure 1. Pressure vs area isotherms for DPPS on a 0.1 M K_2PtCl_4 subphase, pH 3.7 (open circles), and DPPS on a pure water subphase, pH 3.7 (solid circles).

Table 1. Deposition Conditions for DPPS LB Films from Subphases Containing 0.1 mM Metal Ions^a

subphase complex	target press. (mN/m)	pH	d_{001} (± 0.1 Å)
K_2PtCl_4	37	3.7	55.5
$K_2Pt(CN)_4$	35	3.0	55.8
K_2PdCl_4	30	2.3	55.3
$KAuCl_4$	33	2.7	55.3
$Cd[ClO_4]_2 \cdot xH_2O$	20	3.0	55.5

^a For all depositions, films were compressed with a barrier speed of 10 mm/min. Hydrophobic substrates were dipped down and up with speeds of 8 and 6 mm/min, respectively.

DPPS on a pure water subphase at the same pH (Figure 1), indicating that it is the alkyl tails that regulate molecular packing. Similar isotherms were obtained for DPPS on subphases containing the other metal complexes.²⁷

Transfer onto Solid Supports. It is well-known that it is difficult to form multiple bilayer films of phospholipids using LB deposition methods, and only a few successful reports of films formed in this way can be found in the literature. However, multilayer films comprised of Y-type bilayers (head-to-head, tail-to-tail) of DPPS can readily be deposited from aqueous $PtCl_4^{2-}$ subphases. Films containing up to 100 bilayers have been formed. This phenomenon is not specific to $PtCl_4^{2-}$, as transfers with other complexes in the subphase such as $Pt(CN)_4^{2-}$, $PdCl_4^{2-}$, $AuCl_4^-$, and Cd^{2+} were also successful. In contrast, DPPS could not be transferred with the hard ion Ca^{2+} .

The conditions for depositing each of the films are summarized in Table 1. In general, a single Y-type DPPS bilayer film is transferred onto a hydrophobic substrate by compressing the Langmuir monolayer to the desired surface pressure (Table 1) and letting the film stabilize on the water surface for 5–10 min before deposition begins. Deposition onto a hydrophobic surface begins on the downstroke, and a bilayer is completed on the upstroke.

It is important to note that poor transfer ratios (~ 0.5 – 0.7) normally result for the first two bilayers of the DPPS–Pt films. To facilitate deposition, the first two bilayers

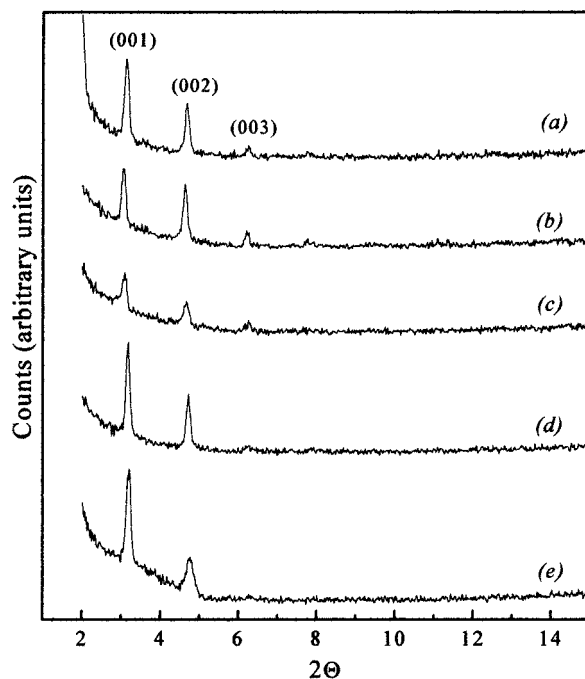


Figure 2. XRD patterns from 20-bilayer DPPS films deposited from subphases containing (a) $K_2Pt(CN)_4$, (b) K_2PdCl_4 , (c) $KAuCl_4$, (d) $Cd(ClO_4)_2$, and (e) K_2PtCl_4 .

were annealed at 45 °C for 10–12 h. Bilayers that were deposited after this treatment had transfer ratios of 0.95 ± 0.05 in all cases. Additionally, it is found that continuous deposition procedures do not produce very good bilayers, as the film becomes rigid on the water surface over time, suggesting that the DPPS molecules are gradually cross-linked by the metal complexes. Therefore, a deposition method was adopted whereby after two bilayers are deposited, the monolayer on the water surface is removed and a new monolayer compressed for the next two deposition cycles. During this cleaning and reapplication period of about 20 min, the sample is placed in an oven at 45 °C. The deposition procedure is similar to methods that have been successfully used to prepare metal phosphonate LB films.^{28,29}

Characterization of DPPS–Pt Bilayers. The layered nature of the deposited films was established by XRD, and diffractograms from 20-bilayer DPPS samples deposited from $PtCl_4^{2-}$, $Pt(CN)_4^{2-}$, Cd^{2+} , $AuCl_4^-$, and $PdCl_4^{2-}$ subphases are shown in Figure 2. An interlayer distance of 55 ± 0.2 Å is determined from the Bragg reflections, and this value is consistent with a bilayer structure. The interlayer distances for DPPS films deposited in the presence of the other metal complexes are similar, and these values are summarized in Table 1. For each film, FTIR confirmed that DPPS was indeed deposited, and XPS survey scans confirmed the presence of the respective metal ion in the transferred films. More detailed structural characterization was performed on the DPPS–Pt films, deposited from both K_2PtCl_4 and $K_2Pt(CN)_4$, and these results are presented next.

X-ray Photoelectron Spectroscopy. The elemental compositions of the DPPS–metal complex films were determined by XPS. For the DPPS–Pt film formed with either the chloroplatinate or cyanoplatinate ions in the subphase, XPS shows that C, O, P, N, and Pt are the only elements present in the film. Multiple XPS samples have been

(27) Ravaine, S.; Fanucci, G. E.; Seip, C. T.; Adair, J. A.; Talham, D. R. *Langmuir* **1998**, *14*, 708–713.

(28) Seip, C. T.; Granroth, G. E.; Meisel, M. W.; Talham, D. R. *J. Am. Chem. Soc.* **1997**, *119*, 7084–7094.

(29) Fanucci, G. E.; Talham, D. R. *Langmuir* **1999**, *15*, 3289–3295.

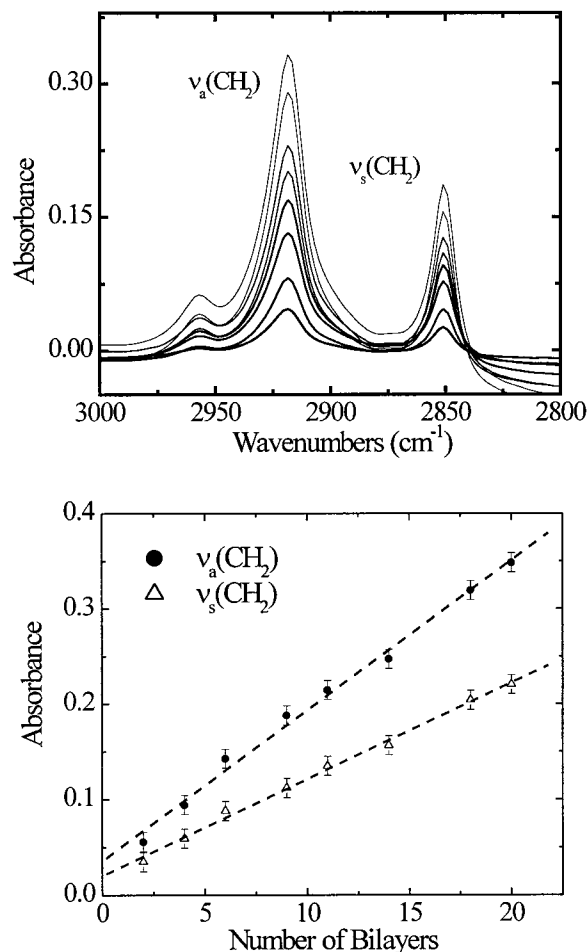


Figure 3. (top) ATR-FTIR spectra of the methylene stretching vibrations as a function of the number of deposited bilayers. (bottom) Plot of the absorbance intensity of the asymmetric and symmetric methylene vibrations for the DPPS-Pt film as a function of the number of transferred bilayers. Data are shown for the DPPS-Pt film that was transferred from the chloroplatinate subphase. Similar spectra and results were obtained for the DPPS-Pt film transferred from the cyanoplatinate subphase.

studied, each consisting of six bilayers, and similar results have been obtained in each case. There is no chloride observed in films deposited from the chloroplatinate subphase, indicating that the metal ions are incorporated into the film as positive ions and not as negatively charged complexes. (Similarly, IR results discussed below indicate that there is no cyanide present in films deposited in the presence of the cyanoplatinate.)

Although most commonly used to obtain qualitative data about the composition of LB and self-assembled monolayer thin films,^{12,30,31} XPS has also been used to obtain quantitative information about the relative percentages of elements within the films.^{32–35} In particular, we have been successful using XPS to measure the relative percentages of metal ions and phosphorus atoms in metal

(30) Akhter, S.; Lee, H.; Hong, H.-G.; Mallouk, T. E.; White, J. M. *J. Vac. Sci. Technol.* **1989**, *7*, 1608–1613.

(31) Connor, J. A. *XPS Studies of Inorganic and Organometallic Compounds*; Heyden & Son Ltd.: London, 1977.

(32) Seah, M. P.; Dench, W. A. *Surf. Interface Anal.* **1979**, *1*, 1–11.

(33) Wagner, C. D.; Davis, L. E.; Zeller, M. V.; Taylor, J. A.; Raymond, R. M.; Gale, L. H. *Surf. Interface Anal.* **1981**, *3*, 211–225.

(34) Pike, J. K.; Byrd, H.; Morrone, A. A.; Talham, D. R. *Thin Solid Films* **1994**, *243*, 510–514.

(35) Pike, J. K.; Byrd, H.; Morrone, A. A.; Talham, D. R. *Chem. Mater.* **1994**, *6*, 1757–1765.

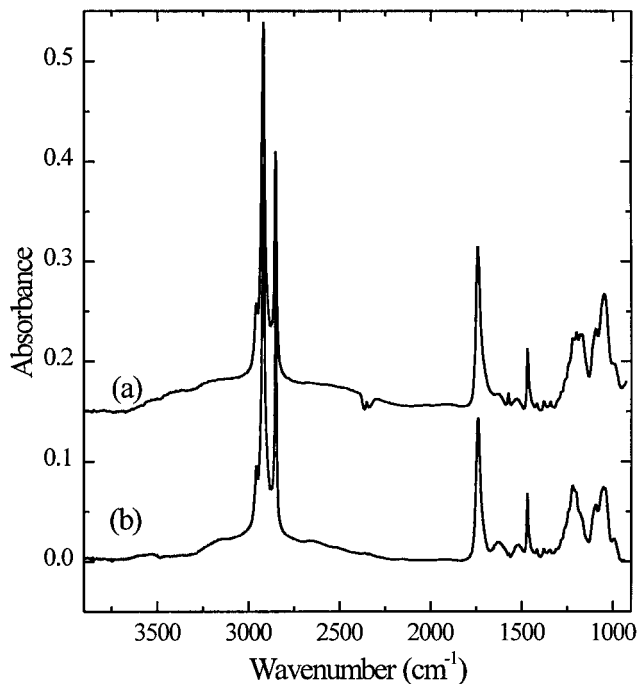


Figure 4. Comparison of (a) ATR-FTIR spectrum of a 20-bilayer DPPS-Pt film that was transferred from the cyanoplatinate subphase and (b) transmission FTIR spectrum of powdered DPPS ground into KBr. The absorbance scale applies to the LB film.

phosphonate LB films.^{28,29,34} Applied here to the DPPS-Pt films, the experimentally observed relative percentages of Pt (using the 4f 77 and 74 eV lines) and P (2p 134.5 eV) are $14 \pm 3\%$ and $86 \pm 3\%$, respectively, independent of the source of Pt^{2+} in the subphase. The results correspond well to a Pt:P ratio of 1:6, which implies the following film composition: $[(\text{DPPS}^-)_2\text{Pt}](\text{DPPS})_4$. Furthermore, according to XPS, the ratio of phosphorus to nitrogen is equal to 0.9, close to the expected value of 1.0, indicating that the serine headgroups are intact and that no hydrolysis of the lipid has occurred during the deposition process.³⁶

Infrared Analysis. Figure 3 shows the C-H stretching bands for DPPS-Pt films with increasing numbers of bilayers, deposited from a PtCl_4^{2-} subphase. The frequency and full width at half-maximum of both the $\nu_s(\text{CH}_2)$ and $\nu_a(\text{CH}_2)$ bands indicate that the alkyl chains are well-organized and close-packed.⁵ As additional layers are deposited, the position and line shape of each band remain the same, and the intensity increases linearly with number of layers. This linear dependence in Figure 3 demonstrates that the same amount of film is transferred during each deposition cycle and that the organization and structure of the alkyl chains do not change during the repeated cycles.³⁷

Perhaps the most significant feature in the IR spectrum of the DPPS-Pt film deposited from $[\text{Pt}(\text{CN})_4]^{2-}$ is the absence of a cyanide stretch, further suggesting that platinum in the film is not electrostatically bound in the form of a negatively charged complex, but rather coordinated by the phospholipid. The most likely coordination site is the amine of the serine headgroup.^{38,39} In Figure 4, a strong carbonyl stretch at 1750 cm^{-1} and the absence

(36) The P/N ratio of 1 helps confirm that the XPS analysis reasonably accounts for photoelectron attenuation through the lipophilic region of the film.

(37) Tilt angle analyses of the alkyl chains, determined from polarized infrared spectroscopy, are provided as Supporting Information.

(38) Khokhar, A. R.; Lumetta, G. J. *J. Coord. Chem.* **1992**, *26*, 251–257.

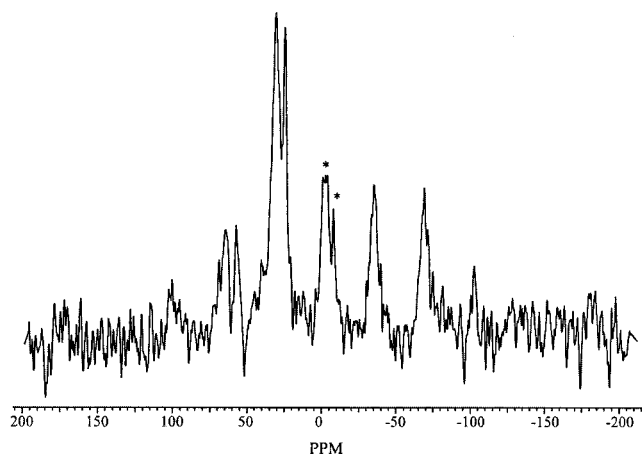


Figure 5. $^1\text{H}/^{31}\text{P}$ cross-polarized MAS NMR spectrum of a 100-bilayer DPPS-Pt film. This film was deposited from the chloroplatinate subphase. The two isotropic resonances are designated with asterisks.

of any carboxylate ion stretches signifies that all of the carboxylic acid groups in the films are fully protonated and that these groups are not interacting with the incorporated Pt^{2+} ions.^{38–41} Furthermore, little difference is discernible in the energy of phosphate stretching modes ($1020\text{--}1200\text{ cm}^{-1}$) between the films and a solid sample of DPPS (Figure 4), indicating that the phosphate groups are also not interacting with the Pt^{2+} ions.^{42,43} Differences in intensity could be attributed to the orientational effect present in the film and absent in the solid. Finally, subtle changes in the N–H stretch modes are consistent with metal binding by a portion of the amine groups.^{38–40} The N–H stretch modes are superimposed over a broad adsorption centered around 3500 cm^{-1} that likely results from water molecules hydrogen bonding in the hydrophilic network. Poorly resolved bands occurring near 3220 and 3530 cm^{-1} in the DPPS starting material are also present in the DPPS-Pt films. In addition, a new band appears near 3400 cm^{-1} , indicating a change in some of the amine groups, consistent with coordination to the metal ion.

³¹P NMR Analysis. It has recently been demonstrated that ^{31}P MAS NMR in combination with IR results can be used to study the structure and organization of phosphorus-containing LB films.⁴⁴ Here, application of this technique is extended to the DPPS phospholipid films. Figure 5 shows the CP MAS NMR spectrum of the DPPS-Pt LB film, deposited from K_2PtCl_4 , acquired at a spinning rate of 8.2 kHz . In this spectrum, two signals can be discerned with isotropic peaks at $\delta_{\text{iso}} = -2.9 \pm 0.2$ and $\delta_{\text{iso}} = -7.7 \pm 0.1\text{ ppm}$ (referenced to $\text{NH}_4\text{H}_2\text{PO}_4$). Although ^{31}P is a nucleus of almost 100% natural abundance, CP was used to enhance the sensitivity because of the small sample size. Data were collected over 72 h with a recycle delay that was 6 times shorter than that needed with direct detection methods.

The presence of two ^{31}P NMR signals indicates that the transferred film is composed of two types of DPPS

molecules. The signal with $\delta_{\text{iso}} = -2.9\text{ ppm}$ has similar position, shape, and spinning sideband pattern as that of a powder sample of DPPS, indicating that most of the DPPS molecules in the film have the serine headgroups in a state that is similar to the zwitterionic powdered lipid. However, the breadth of the signal is almost twice that of the solid, suggesting some structural disorder in the film. The narrower peak at $\delta_{\text{iso}} = -7.7\text{ ppm}$ corresponds to the second type of DPPS molecules. This narrow signal has a spinning sideband pattern that is similar to that of the broader signal. At first thought, it may be possible that the second type of phospholipid originates from hydrolysis of the serine headgroup. However, there is no evidence for the hydrolyzed phospholipid in the FTIR spectrum (Figure 4). In addition, the spinning sideband pattern that is observed differs significantly from that of a hydrolyzed lipid, such as dipalmitoylphosphatidic acid, DPPA. For DPPA, a phospholipid with a PO_3H^- headgroup, no spinning sideband pattern is detected at similar and slower spinning rates, and its isotropic chemical shift occurs at -1.7 ppm . Hence, this second type of DPPS in the film does not correspond to hydrolyzed lipid, but instead the NMR data are consistent with a portion of the DPPS molecules interacting with the incorporated Pt^{2+} ions. Furthermore, the narrow signal suggests enhanced structural organization of the phospholipids that might occur as a result of linking the amphiphiles through an inorganic complex.⁴⁴

Conclusions

The observations presented here indicate that the transfer of DPPS LB films is facilitated by ionic/covalent interactions between the serine headgroup and the late transition metal ions. These interactions are evident at the air/water interface through changes in the pressure vs area isotherm and are also detected in the transferred film. It has often been observed that metal ions facilitate the transfer of Langmuir monolayers by screening electrostatic repulsions between anionic headgroups and adding ionic lattice energy to the LB film structure. Traditionally, hard ions are used and the interactions are predominantly electrostatic. However, LB transfer of DPPS with the hard ion Ca^{2+} has not been successful. In the case of DPPS with late transition metals, the interaction appears to be coordinate covalent binding of the headgroup to the metal ion.

The metal ion appears to bridge serine groups, although not all DPPS molecules in the transferred films are coordinating. For the Pt^{2+} -containing films, ^{31}P NMR and FTIR data suggest two types of DPPS molecules, consistent with XPS results that predict a 6:1 DPPS:Pt ratio. If each Pt^{2+} ion is coordinated by the amines of two DPPS⁻ headgroups, then charge neutrality leaves four uncoordinated DPPS molecules. It is likely the H_2O molecules finish out the Pt^{2+} coordination sphere, giving a proposed formula of $[\text{Pt}(\text{DPPS}^-)_2(\text{OH}_2)_2](\text{DPPS})_4$, as depicted in Scheme 1. The coordinated water molecules may help form a hydrogen-bonding network that would enhance the cohesion within the hydrophilic layer. It is interesting that despite the large excess of metal complex available in the subphase, in each case, the metal ions are incorporated into the film in substoichiometric ratios.

Finally, DPPS multilayers are easily deposited using the conditions reported here. The process should readily be adaptable to other phospholipid monolayers, including those with functionalized lipophilic tails. Studies on transferred films should help complement the numerous studies of phospholipid Langmuir monolayers.

(39) Condrate, R. A.; Nakamoto, K. *J. Chem. Phys.* **1965**, *42*, 2590–2598.

(40) Aletras, V.; Hadjiliadis, N.; Lymberopoulou-Karaliota, A.; Rombeck, I.; Lippert, B. *Inorg. Chim. Acta* **1994**, *227*, 17–23.

(41) Caubet, A.; Moreno, V.; Molins, E.; Miravittles, C. *J. Inorg. Biochem.* **1992**, *48*.

(42) Hartwig, J. F.; Lippard, S. J. *J. Am. Chem. Soc.* **1992**, *114*, 5646–5654.

(43) Navarro, R.; Garcia, J.; Urriolabeitia, E. P.; Cativiela, C.; Diaz-de-Villegas, M. D. *J. Organomet. Chem.* **1995**, *490*, 35–43.

(44) Fanucci, G. E.; Bowers, C. R.; Talham, D. R. *J. Am. Chem. Soc.* **1999**, *121*, 1088–1089.

Acknowledgment. This work was supported in part by NASA (NAG8-1675) and the National Science Foundation.

Supporting Information Available: Polarized infrared data that include dichroic ratios and alkyl chain tilt angles for the DPPS-Pt film are provided; additionally, a cartoon

representation of the film structure determined from IR, XPS, XRD, and NMR including molecular distances and orientations along with calculated distances. This material is available free of charge via the Internet at <http://pubs.acs.org>.

LA000971S

Magnetic Spin Ladder $(\text{C}_5\text{H}_{12}\text{N})_2\text{CuBr}_4$: High-Field Magnetization and Scaling near Quantum Criticality

B. C. Watson, V. N. Kotov, and M. W. Meisel

Department of Physics and The Center for Condensed Matter Sciences, University of Florida, P.O. Box 118440, Gainesville, Florida 32611-8440

D. W. Hall

National High Magnetic Field Laboratory, Florida State University, Tallahassee, Florida 32310

G. E. Granroth, W. T. Montfrooij, and S. E. Nagler

Oak Ridge National Laboratory, Building 7692, MS 6393, P.O. Box 2008, Oak Ridge, Tennessee 37831

D. A. Jensen, R. Backov, M. A. Petruska, G. E. Fanucci, and D. R. Talham

Department of Chemistry, University of Florida, P.O. Box 117200, Gainesville, Florida 32611-7200
(Received 9 August 2000)

The magnetization, $M(H \leq 30 \text{ T}, 0.7 \leq T \leq 300 \text{ K})$, of $(\text{C}_5\text{H}_{12}\text{N})_2\text{CuBr}_4$ has been used to identify this system as an $S = 1/2$ Heisenberg two-leg ladder in the strong-coupling limit, $J_\perp = 13.3 \text{ K}$ and $J_\parallel = 3.8 \text{ K}$, with $H_{c1} = 6.6 \text{ T}$ and $H_{c2} = 14.6 \text{ T}$. An inflection point in $M(H, T = 0.7 \text{ K})$ at half saturation, $M_s/2$, is described by an effective XXZ chain. The data exhibit universal scaling behavior in the vicinity of H_{c1} and H_{c2} , indicating that the system is near a quantum critical point.

DOI: 10.1103/PhysRevLett.86.5168

PACS numbers: 75.10.Jm, 75.40.Cx, 75.50.Ee, 75.50.Xx

Magnetic spin ladders are a class of low dimensional materials with structural and physical properties between those of 1D chains and 2D planes. In a spin ladder, the vertices possess unpaired spins that interact along the legs via J_\parallel and along the rungs via J_\perp , but are isolated from equivalent sites on adjacent ladders, i.e., interladder $J' \ll J_\parallel, J_\perp$. Recently, a considerable amount of attention has been given to the theoretical and experimental investigation of spin ladder systems as a result of the observation that the microscopic mechanisms in these systems may be related to the ones governing high temperature superconductivity [1,2]. The phase diagram of the antiferromagnetic spin ladder in the presence of a magnetic field is particularly interesting. At $T = 0$ with no external applied field, the ground state is a gapped, disordered quantum spin liquid. At a field H_{c1} , there is a transition to a gapless Luttinger liquid phase, with a further transition at H_{c2} to a fully polarized state. Both H_{c1} and H_{c2} are quantum critical points [2]. Near these points, the magnetization has been predicted to obey a universal scaling function [3], but until now, this behavior has not been observed experimentally.

A number of solid-state materials have been proposed as examples of spin ladder systems, and an extensive set of experiments have been performed on $\text{Cu}_2(\text{C}_5\text{H}_{12}\text{N}_2)_2\text{Cl}_4$, referred to as $\text{Cu}(\text{Hp})\text{Cl}$ [4]. The initial work identified this material as a two-leg $S = 1/2$ spin ladder [4–12]. Although quantum critical behavior has been preliminarily identified in this system near H_{c1} , this assertion is based on the use of scaling parameters identified from the experimental data rather than the ones predicted theoretically [11,12]. Furthermore, more recent work

has debated the appropriate classification of the low temperature properties [13–19]. Clearly, additional physical systems are necessary to experimentally test the predictions of the various theoretical treatments of two-leg $S = 1/2$ spin ladders.

Herein, we report evidence that identifies bis(piperidinium)tetrabromocuprate(II), $(\text{C}_5\text{H}_{12}\text{N})_2\text{CuBr}_4$ [20], hereafter referred to as BPCB, as a two-leg $S = 1/2$ ladder that exists in the strong-coupling limit, $J_\perp/J_\parallel > 1$. High-field, low-temperature magnetization, $M(H \leq 30 \text{ T}, T \geq 0.7 \text{ K})$, data of single crystals and powder samples have been fit to obtain $J_\perp = 13.3 \text{ K}$, $J_\parallel = 3.8 \text{ K}$, and $\Delta \sim 9.5 \text{ K}$, i.e., at the lowest temperatures finite magnetization appears at $H_{c1} = 6.6 \text{ T}$ and saturation is achieved at $H_{c2} = 14.6 \text{ T}$. An unambiguous inflection point in the magnetization, $M(H, T = 0.7 \text{ K})$, and its derivative, dM/dH , is observed at half the saturation magnetization, $M_s/2$. This feature is symmetric about $M_s/2$, consistent with expectations for a simple spin ladder. Any presence of asymmetry, as was observed in $\text{Cu}(\text{Hp})\text{Cl}$ [5–8], most likely arises from other factors. Our $M_s/2$ feature cannot be explained by the presence of additional exchange interactions, e.g., diagonal frustration J_F , but is well described by an effective XXZ chain, onto which the original spin ladder model (for strong coupling) can be mapped in the gapless regime $H_{c1} < H < H_{c2}$ [21]. After determining H_{c1} and with no additional adjustable parameters, the magnetization data are observed to obey a universal scaling function [3]. This observation supports our identification of BPCB as a two-leg $S = 1/2$ Heisenberg spin ladder with $J' \ll J_\parallel$.

The crystal structure of BPCB has been determined to be monoclinic with stacked pairs of $S = 1/2$ Cu^{2+} ions forming magnetic dimer units [20]. The CuBr_4^{-2} tetrahedra are cocrystallized along with the organic piperidinium cations so that the crystal structure resembles a two-leg ladder, Fig. 1. The rungs of the ladder are formed along the c^* axis (19.8° above the c axis and $+23.4^\circ$ away from the a - c plane [20]) by adjacent flattened CuBr_4^{-2} tetrahedra related by a center of inversion. The ladder extends along the a axis with 6.934 \AA between Cu^{2+} spins on the same rung and 8.597 \AA between rungs. The magnetic exchange, J_\perp , between the Cu^{2+} spins on the same rung is mediated by the orbital overlap of Br ions on adjacent Cu sites. The exchange along the legs of the ladder, J_\parallel , is also mediated by somewhat longer nonbonding ($\text{Br}\cdots\text{Br}$) contacts and possibly augmented by hydrogen bonds to the organic cations. A frustrating diagonal exchange, J_F , is possible, although it should be weak ($J_F \ll J_\parallel$), and so the potential of a finite J_F on the short diagonal was considered in our analysis.

Shiny, black crystals of BPCB were prepared by slow evaporation of solvent from a methanol solution of [(pipdH)Br] and CuBr_2 , and milling of the smallest crystals was used to produce the powder samples. The stoichiometry was verified using CHN analysis, and 9 GHz ESR measurements were completely consistent with the previously reported data, i.e., $g(\text{powder}) = 2.13$ [20]. In addition, deuterated specimens were produced and used in neutron scattering studies performed at the HFIR at Oak Ridge National Laboratory. No evidence for long-range magnetic order or structural transitions was observed down to 11 K by powder diffraction and 1.5 K for single crystal diffraction in the $[h\ 0\ 1]$ scattering plane. The low-field magnetic measurements were performed using a SQUID magnetometer. The high-field work was conducted

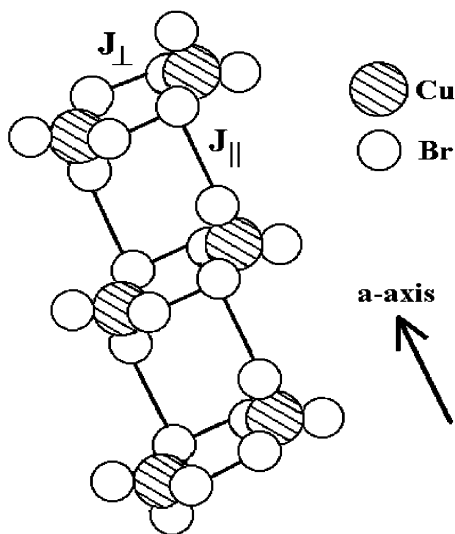


FIG. 1. Schematic of the crystal structure of BPCB. The legs (rungs) are along the a axis (c^* axis); see text.

at the NHMFL using a 30 T, 33 mm bore resistive magnet and a vibrating (82 Hz) sample magnetometer equipped with a Cernox thermometer [22].

The low-field, 0.1 T, magnetic susceptibility, χ , of a powder sample, 166.7 mg, is shown as a function of temperature in Fig. 2. The data from single crystals, with the magnetic field oriented along the a , b , and c axes in separate measurements, are indistinguishable from the results obtained with the powder specimen. The general shape of the curve is typical of low-dimensional magnetic systems, and more specifically, it possesses a rounded peak at $\approx 8 \text{ K}$ and an exponential temperature dependence below the peak. Consistent with the neutron scattering results, no evidence of long-range ordering was observed down to 2 K. A small extrinsic Curie-like impurity contribution ($=1.5\%$ of the total number of Cu spins) and a temperature-independent diamagnetic term ($\chi_{\text{dia}} = -2.84 \times 10^{-4} \text{ emu/mol}$, which is the sum of the core diamagnetism, estimated from Pascal's constants to be $-2.64 \times 10^{-4} \text{ emu/mol}$, and the background contribution of the sample holder) were subtracted from the data in Fig. 2. The Curie-Weiss temperature θ , and the Curie constant C , can be extracted from a fit [$\chi(T) = \chi_{\text{dia}} + C/(T + \theta)$, $50 \text{ K} < T < 300 \text{ K}$], and we find $C = 0.433 \pm 0.002 \text{ emu K/mol}$ and $\theta = 5.3 \pm 0.1 \text{ K}$ [23]. These values are close to $C = 0.425 \text{ emu K/mol}$ ($S = 1/2$, $g = 2.13$) and $\theta \approx (J_\perp + 2J_\parallel)/4 = 5.2 \text{ K}$ [24].

Initially, using exact diagonalization methods with 12 spins, the $\chi(T)$ data were fit to obtain the values $J_\perp = 13.3 \text{ K}$, $J_\parallel = 3.8 \text{ K}$ for a ladder Hamiltonian and

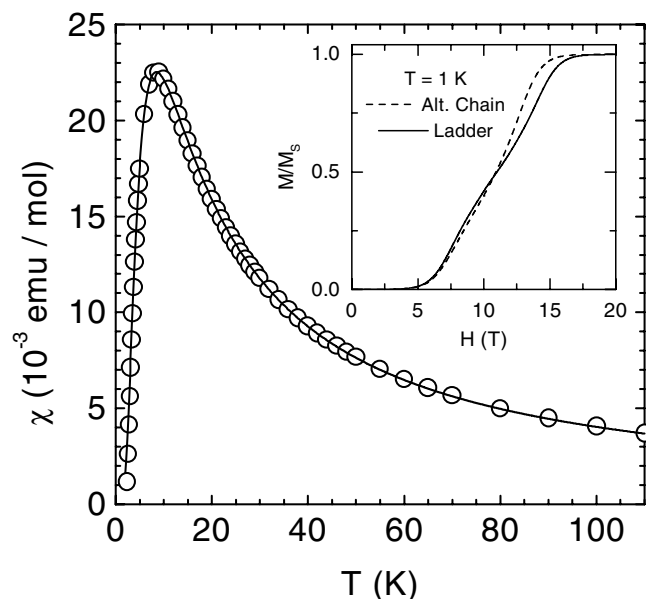


FIG. 2. The $\chi(T)$ of a powder sample (166.7 mg) in 0.1 T. The line is the result of an exact diagonalization of a ladder Hamiltonian with 12 spins when $J_\perp = 13.3 \text{ K}$ and $J_\parallel = 3.8 \text{ K}$; see text. The inset shows the $M(H, T = 1 \text{ K})$ expectations of an exact diagonalization of the alternating chain and ladder Hamiltonians with the exchange values given in the text.

$J_1 = 13.7$ K, $J_2 = 5.3$ K for an alternating chain Hamiltonian. Both fits are indistinguishable from the solid line shown in Fig. 2. Therefore, using only the low-field $\chi(T)$ data, we were unable to distinguish between the ladder and alternating chain models, and this situation was not improved by fitting the $M(H \leq 5$ T, $T = 2$ K) data. However, in extensions up to the saturation magnetization, M_s , the alternating chain model generated $M(H, T < J_{\parallel})$ curves that were asymmetric about $M_s/2$, as reported for Cu(Hp)Cl [8,23], and the spin ladder description predicted symmetric behavior; see Fig. 2 inset. Since our experimental resolution was estimated to be sufficient to allow us to differentiate between the two models, the high magnetic field studies were initiated.

The high-field, $H \leq 30$ T, magnetization of a powder sample, 208.2 mg, is shown in Fig. 3. Since M_s was reached in our studies, we were able to directly measure and subtract a small, temperature-independent contribution ($\chi_{\text{dia}} \approx -2.84 \times 10^{-4}$ emu/mole), which is the same value obtained in our low-field work. Measurements were also made on a single crystal, 18.9 mg, with $H \parallel a$ -axis and for $T \geq 1.6$ K. Within the resolution, the data are the same for the powder and single crystal samples. Furthermore, the data were acquired while ramping the field in both directions, and no hysteresis was observed.

The low energy states of the spin ladder Hamiltonian can be mapped, in the strong-coupling limit, onto the $S = 1/2$ XXZ chain [21], allowing $M(H, T)$ to be modeled. The

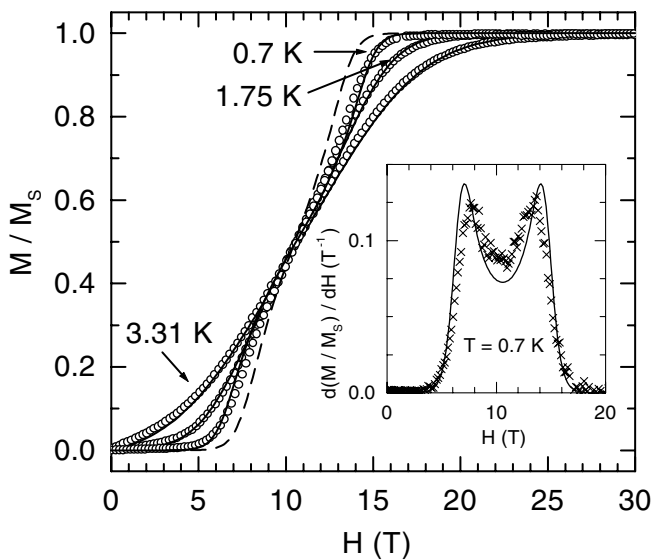


FIG. 3. The normalized magnetization, M/M_s , of a powder sample (208.2 mg). The data traces are limited to ≈ 150 (of ≈ 3000) points for clarity. The lines are spin ladder predictions of an effective XXZ chain when $J_{\perp} = 13.3$ K and $J_{\parallel} = 3.8$ K. At $T = 0.7$ K, the inflection point at $M_s/2$ is clearly visible, and the inset shows the derivative of this data. The dashed line is the alternating chain model prediction for 0.7 K when J_1, J_2 are taken to be the values obtained from fitting the data in Fig. 2; see text.

solid lines in Fig. 3 were obtained by numerical integration of the Bethe ansatz equations for the effective XXZ chain [25], using the parameters describing the spin ladder fit for $\chi(T)$. All of the data, Figs. 2 and 3, are reproduced by one set of exchange values when using the ladder model. On the other hand, the alternating chain model fails to fit all of the data with a single set of parameters. For example, the dashed line in Fig. 3 is $M/M_s(H, T = 0.7$ K) calculated from the alternating chain mapping onto the XXZ chain when $J_1 = 13.7$ K and $J_2 = 5.3$ K, i.e., the values obtain from fitting $\chi(T)$, Fig. 2, by an alternating chain model. In addition, our data were analyzed with a ladder model that also incorporated a frustrating interaction, J_F [26], and we can estimate an upper bound of $J_F < 0.5$ K. Consequently, all of the data are consistent with a strongly coupled ladder description for BPCB, where $J_{\perp} = 13.3 \pm 0.2$ K, and $J_{\parallel} = 3.8 \pm 0.1$ K.

To leading order, $g\mu_B H_{c1} = J_{\perp} - J_{\parallel}$, and $g\mu_B H_{c2} = J_{\perp} + 2J_{\parallel}$ [26,27]. Using the previously mentioned parameters, we obtain $H_{c1} = 6.6$ T and $H_{c2} = 14.6$ T, identical with the experimental results. The inset in Fig. 3 shows the derivative curve, $d(M/M_s)/dH$, of our data at the lowest temperature. The symmetric double bump structure and its evolution with temperature has been studied theoretically [17] but has not been observed previously in $S = 1/2$ two-leg ladder materials. Even though our theoretical curve somewhat overestimates the sharpness of $d(M/M_s)/dH$, the overall agreement between theory and experiment, including the evolution of $M(H, T)$, Fig. 3, is excellent, and involves no adjustable parameters once H_{c1} is defined. Furthermore, the fact that we see only one feature at $M_s/2$ between H_{c1} and H_{c2} is evidence that our strongly interacting dimers are not coupling to form 2D [28] or 3D [29,30] networks.

At H_{c1} , BPCB undergoes a transition from gapped dimer pairs to a gapless Luttinger liquid phase with fermionic excitations, where the magnetization is proportional to the fermion density [3,31,32]. This transition can be described as a condensation of a dilute gas of bosons (dimers), and quasiparticle interactions are irrelevant at the transition point. At H_{c2} , an analogous situation exists where the transition is between the Luttinger liquid and spin polarized phases. When $T, g\mu_B|H - H_{c1}|$, and $g\mu_B|H_{c2} - H|$ are $\lesssim J_{\parallel}$, the 1D magnetization is predicted to obey the universal scaling law (assuming $J_{\perp}/J_{\parallel} \gg 1$) that may be written as

$$\frac{M(H, T)}{M_s} = \sqrt{2k_B T/J_{\parallel}} \mathcal{M}(g\mu_B[H - H_{c1}]/k_B T),$$

$$1 - \frac{M(H, T)}{M_s} = \sqrt{2k_B T/J_{\parallel}} \mathcal{M}(g\mu_B[H_{c2} - H]/k_B T),$$

where the universal function \mathcal{M} is the fermion density [3]. This theoretically predicted scaling behavior is compared to the data in Fig. 4, where the agreement is impressive. It is important to stress that the scaling shown in Fig. 4

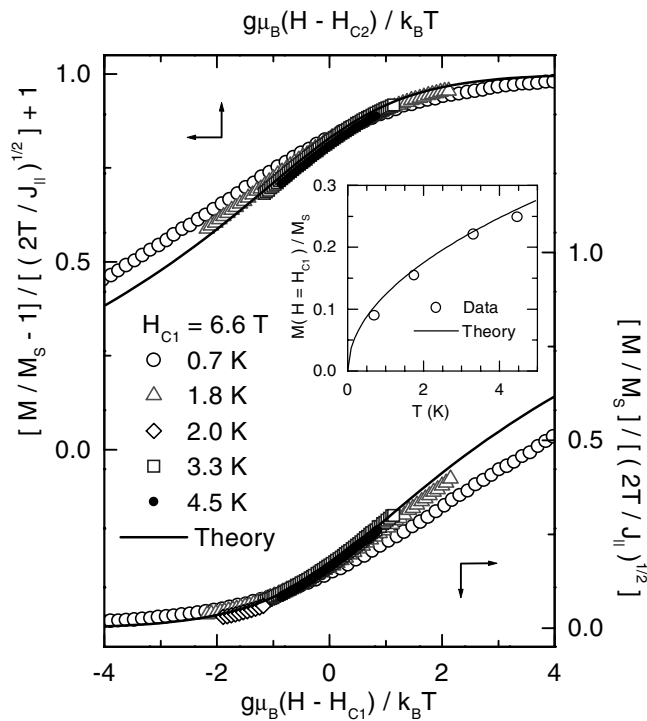


FIG. 4. The scaled data in the vicinity of H_{c1} and H_{c2} . The solid lines are the predictions of the theory when H_{c1} is fixed. The inset shows the $T^{1/2}$ scaling behavior at H_{c1} .

has been theoretically predicted [3] and is not a result of extracting scaling variables on the basis of the data [12]. In an isolated spin ladder, scaling is expected at the lowest temperatures, $T \lesssim J_{||}$. A deviation from scaling is observed for $T = 0.7$ K, which suggests that other weak interactions, such as J_F or J' , may begin to have a subtle influence, while the data up to 4.47 K appear to obey the scaling theory. The $T^{1/2}$ scaling of the magnetization at the critical point $H = H_{c1}$, Fig. 4, is further evidence that BPCB is a two-leg spin ladder with $J' \ll J_{||}$ [33].

In summary, analysis of $M(H \leq 30$ T, $T \geq 0.7$ K) has allowed us to identify BPCB as a two-leg $S = 1/2$ spin ladder in the strong-coupling limit, $J_{\perp}/J_{||} \sim 3.5$. A single set of exchange constants, $J_{\perp} = 13.3$ K and $J_{||} = 3.8$ K, are able to accurately describe all of the data. The $M(H \approx H_{c1}$ or H_{c2} , 1 K $< T < 4.5$ K) data exhibit scaling behavior in the universality class of the 1D dilute Bose gas transition [2,3]. Although we have considered the potential existence of additional exchange interactions J_F and J' , effects arising from these parameters are not prominent in the present data. However, since subtle differences arise between the theoretical predictions and the data at the lowest temperature, additional perturbing interactions may be present.

We have enjoyed input from many colleagues, including J.H. Barry, A. Feher, M. Orendáč, A. Orendáčova,

F. Mila, and A. Yashenkin. We thank G. Chaboussant for sending Ref. [8]. This work was supported, in part, by the NSF through DMR-9704225 (B.C.W. and M.W.M.), DMR-9357474 (V.N.K.), the NHMFL via DMR-9527035, DMR-9900855 (D.R.T. and co-workers), and by the State of Florida. Oak Ridge National Laboratory is managed for the DOE by UT-Battelle, LLC, under Contract No. DE-AC05-00OR22725.

- [1] E. Dagotto, Rep. Prog. Phys. **62**, 1525 (1999).
- [2] S. Sachdev, Science **288**, 475 (2000); *Quantum Phase Transitions* (Cambridge University Press, Cambridge, 1999).
- [3] S. Sachdev, T. Senthil, and R. Shankar, Phys. Rev. B **50**, 258 (1994).
- [4] B. Chiari *et al.*, Inorg. Chem. **29**, 1172 (1990).
- [5] P.R. Hammar and D.H. Reich, J. Appl. Phys. **79**, 5392 (1996).
- [6] C. A. Hayward, D. Poilblanc, and L. P. Lévy, Phys. Rev. B **54**, R12 649 (1996).
- [7] G. Chaboussant *et al.*, Phys. Rev. B **55**, 3046 (1997).
- [8] G. Chaboussant, Ph.D. thesis, Université Joseph Fourier, Grenoble, 1997 (unpublished).
- [9] Zheng Weihong, R. R. P. Singh, and J. Oitmaa, Phys. Rev. B **55**, 8052 (1997).
- [10] G. Chaboussant *et al.*, Phys. Rev. Lett. **79**, 925 (1997).
- [11] G. Chaboussant *et al.*, Phys. Rev. Lett. **80**, 2713 (1998).
- [12] G. Chaboussant *et al.*, Eur. Phys. J. B **6**, 167 (1998).
- [13] P.R. Hammar *et al.*, Phys. Rev. B **57**, 7846 (1998).
- [14] N. Elstner and R. R. P. Singh, Phys. Rev. B **58**, 11 484 (1998).
- [15] R. Calemczuk *et al.*, Eur. Phys. J. B **7**, 171 (1999).
- [16] H. Ohta *et al.*, J. Phys. Soc. Jpn. **68**, 732 (1999).
- [17] X. Wang and L. Yu, Phys. Rev. Lett. **84**, 5399 (2000).
- [18] H. Mayaffre *et al.*, Phys. Rev. Lett. **85**, 4795 (2000).
- [19] M. B. Stone *et al.*, cond-mat/0103023 (unpublished).
- [20] B. R. Patyal, B. L. Scott, and R. D. Willett, Phys. Rev. B **41**, 1657 (1990).
- [21] K. Totsuka, Phys. Rev. B **57**, 3454 (1998).
- [22] B. L. Brandt, D. W. Liu, and L. G. Rubin, Rev. Sci. Instrum. **70**, 104 (1999).
- [23] A complete analysis is given by B. C. Watson, Ph.D. thesis, University of Florida, 2000 (unpublished).
- [24] D. C. Johnston *et al.*, cond-mat/0001147 (unpublished).
- [25] M. Takahashi and M. Suzuki, Prog. Theor. Phys. **48**, 2187 (1972).
- [26] F. Mila, Eur. Phys. J. B **6**, 201 (1998).
- [27] M. Reigrotzki, H. Tsunetsugu, and T. M. Rice, J. Phys. Condens. Matter **6**, 9235 (1994).
- [28] H. Kageyama *et al.*, Phys. Rev. Lett. **82**, 3168 (1999).
- [29] W. Shiramura *et al.*, J. Phys. Soc. Jpn. **67**, 1548 (1998).
- [30] B. Kurniawan *et al.*, Phys. Rev. Lett. **82**, 1281 (1999).
- [31] A. M. Tsvelik, Phys. Rev. B **42**, 10 499 (1990).
- [32] I. Affleck, Phys. Rev. B **43**, 3215 (1991).
- [33] T. Giamarchi and A. M. Tsvelik, Phys. Rev. B **59**, 11 398 (1999).